

# **Particle Size Distribution**



ACS SYMPOSIUM SERIES **332**

# **Particle Size Distribution**

## **Assessment and Characterization**

**Theodore Provder, EDITOR**  
*The Glidden Company*

Developed from a symposium sponsored by  
the Division of Polymeric Materials: Science and Engineering  
at the 190th Meeting  
of the American Chemical Society,  
Chicago, Illinois,  
September 8-13, 1985



American Chemical Society, Washington, DC 1987



### Library of Congress Cataloging-in-Publication Data

Particle size distribution.

(ACS symposium series, ISSN 0097-6156; 332)

“Developed from a symposium sponsored by the Division of Polymeric Materials: Science and Engineering at the 190th meeting of the American Chemical Society, Chicago, Illinois, September 8-13, 1985.”

Includes bibliographies and index.

I. Particle size determination—Congresses.

I. Provder, Theodore, 1939- II. American Chemical Society. Division of Polymeric Materials: Science and Engineering. III. American Chemical Society. Meeting (190th: 1985: Chicago, Ill.) IV. Series.

TA418.8.P33 1987 620.1'1299 86-32185  
ISBN 0-8412-1016-0

Copyright © 1987

American Chemical Society

All Rights Reserved. The appearance of the code at the bottom of the first page of each chapter in this volume indicates the copyright owner's consent that reprographic copies of the chapter may be made for personal or internal use or for the personal or internal use of specific clients. This consent is given on the condition, however, that the copier pay the stated per copy fee through the Copyright Clearance Center, Inc., 27 Congress Street, Salem, MA 01970, for copying beyond that permitted by Sections 107 or 108 of the U.S. Copyright Law. This consent does not extend to copying or transmission by any means—graphic or electronic—for any other purpose, such as for general distribution, for advertising or promotional purposes, for creating a new collective work, for resale, or for information storage and retrieval systems. The copying fee for each chapter is indicated in the code at the bottom of the first page of the chapter.

The citation of trade names and/or names of manufacturers in this publication is not to be construed as an endorsement or as approval by ACS of the commercial products or services referenced herein; nor should the mere reference herein to any drawing, specification, chemical process, or other data be regarded as a license or as a conveyance of any right or permission, to the holder, reader, or any other person or corporation, to manufacture, reproduce, use, or sell any patented invention or copyrighted work that may in any way be related thereto. Registered names, trademarks, etc., used in this publication, even without specific indication thereof, are not to be considered unprotected by law.

PRINTED IN THE UNITED STATES OF AMERICA

**American Chemical Society**  
**Library**

1155 16th St. N.W.  
In Particle Size Distribution: Provder, T.;

ACS Symposium Series; American Chemical Society: Washington, DC, 1987.

# ACS Symposium Series

**M. Joan Comstock, *Series Editor***

## *1987 Advisory Board*

**Harvey W. Blanch**  
University of California—Berkeley

**Vincent D. McGinniss**  
Battelle Columbus Laboratories

**Alan Elzerman**  
Clemson University

**W. H. Norton**  
J. T. Baker Chemical Company

**John W. Finley**  
Nabisco Brands, Inc.

**James C. Randall**  
Exxon Chemical Company

**Marye Anne Fox**  
The University of Texas—Austin

**E. Reichmanis**  
AT&T Bell Laboratories

**Martin L. Gorbaty**  
Exxon Research and Engineering Co.

**C. M. Roland**  
U.S. Naval Research Laboratory

**Roland F. Hirsch**  
U.S. Department of Energy

**W. D. Shults**  
Oak Ridge National Laboratory

**G. Wayne Ivie**  
USDA, Agricultural Research Service

**Geoffrey K. Smith**  
Rohm & Haas Co.

**Rudolph J. Marcus**  
Consultant, Computers &  
Chemistry Research

**Douglas B. Walters**  
National Institute of  
Environmental Health

## Foreword

The ACS SYMPOSIUM SERIES was founded in 1974 to provide a medium for publishing symposia quickly in book form. The format of the Series parallels that of the continuing ADVANCES IN CHEMISTRY SERIES except that, in order to save time, the papers are not typeset but are reproduced as they are submitted by the authors in camera-ready form. Papers are reviewed under the supervision of the Editors with the assistance of the Series Advisory Board and are selected to maintain the integrity of the symposia; however, verbatim reproductions of previously published papers are not accepted. Both reviews and reports of research are acceptable, because symposia may embrace both types of presentation.

# Preface

THE FIELD OF PARTICLE SIZE DISTRIBUTION ANALYSIS has experienced a renaissance over the past five years and is now a rapidly growing and lively area of scientific and technological activity. This revitalization has been driven by advances in electronics and computer technology in conjunction with the market pull for particle size distribution analysis methods that cover a wide dynamic particle size range and have improved resolution. These technological advances are embodied in computer-aided, user-friendly, reliable, and cost-effective instrumentation. Three activities characterize this renaissance.

The first activity is the commercial use of instrumental methods used previously in a few academic and industrial laboratories by individuals with a high level of skill and expertise. Examples of such methods are hydrodynamic chromatography (HDC) and sedimentation field-flow fractionation (SFFF). HDC, first reported in 1976<sup>1</sup>, was invented in an industrial laboratory by Hamish Small to fulfill an analysis need. It has taken about 10 years for HDC to be transformed from a laboratory method requiring a high degree of skill into a commercial instrument requiring a moderate degree of skill. SFFF, a more extreme case, was invented by J. Calvin Giddings and co-workers and reported in 1967<sup>2,3</sup>. The technology transfer of SFFF from academic laboratory method to viable commercial instrument has taken almost 20 years to occur.

The second activity is characterized by the revitalization of older instrumental methods such as gravitational and centrifugal sedimentation methods. Redesign, modernization with advanced electronics, and user-friendly, computer-aided analysis have extended the instrument product life cycle. A good example is disc centrifuge photosedimentometry (DCP), the subject of three chapters in this volume.

The third activity is the evolution of a research instrument into a low-cost instrument that requires a minimum degree of skill to use. An excellent example of this process is the transformation of research-grade photon correlation spectrometers into low-cost, easy-to-use, limited-function instruments for routine analysis applications.

The activity in the field of particle size analysis has produced an explosion of papers. A useful review of recent literature is provided by H. G. Barth and S.-T. Sun in *Analytical Chemistry*<sup>4</sup>. This survey covers papers, books, and reviews from late 1981 to late 1984. A monograph published in 1984 and edited by H. G. Barth<sup>5</sup> gives excellent overviews of most new

methods, emphasizing those that provide distribution information. Barth's monograph is an excellent companion text to this volume.

The papers in this book reflect current activity in the field and emphasize measurement techniques, methodology, and application to a variety of particulate systems. The topics are divided into four sections. The first section deals with image analysis methodology and application, an area in which technology is in a state of flux. This area benefits significantly from advances in computer technology. The second section examines photon correlation spectroscopy and light-scattering methods. It presents refinements in classical light-scattering data analysis methodologies that involve angular light scattering and turbidity. Advances in and limitations of photon correlation spectroscopy with respect to data analysis and its application to emulsion and latex systems also are discussed. The third section deals with sedimentation techniques. Recent improvements in DCP instrumentation, experimental methodology, and data analysis procedures are reported. It presents the applicability of SFFF, a hybrid technique that combines centrifugal sedimentation with liquid chromatography, to colloid systems. Of special interest is a particle size analysis study that compares the results of SFFF, DCP, HDC, microscopy, and light-scattering methods for a common latex system. The fourth section emphasizes the use of column chromatography methods, HDC, and size-exclusion chromatography for latex systems.

Because of the commercial availability of new, revitalized, and low-cost routine instrumental methods, the field of particle size distribution analysis will continue to grow. I hope that this book will spur further activity.

I thank the authors for their effective oral and written communications and the reviewers for their critiques and constructive comments. I also acknowledge the book jacket design concepts provided by Ann F. Kah.

THEODORE PROVIDER  
The Glidden Company  
Dwight P. Joyce Research Center  
Strongsville, OH 44136

November 5, 1986

<sup>1</sup>Small, H. J. *Colloid Interface Sci.* **1976**, *57*, 337.

<sup>2</sup>Thompson, G. H.; Meyers, M. N.; Giddings, J. C. *Sep. Sci.* **1967**, *2*, 797.

<sup>3</sup>Giddings, J. C. *J. Chem. Phys.* **1968**, *49*, 81.

<sup>4</sup>Barth, H. G.; Sun, S.-T. *Anal. Chem.* **1985**, *57*, 151R.

<sup>5</sup>*Modern Methods of Particle Size Analysis*; Barth, H. G., Ed.; Wiley: New York, 1984.



# Chapter 1

## Size, Shape, and Texture Analysis

J. K. Beddow

Center for Particulate Material Processing Sciences, Department of Chemical and Materials Engineering, The University of Iowa, Iowa City, IA 52242

This paper is a brief review of original basic engineering research in morphological analysis applied to particle characterization which has been conducted during the last 20 years at the University of Iowa, Center for Particulate Material Processing Sciences. The topics discussed include definitions, theory, instrumental and experimental aspects of size, shape and texture measurements of particulate material.

### Morphological Analysis

Morphological analysis is concerned with particle characterization in the case of particle size, particle shape and particle texture. Particle texture may deal with the particle surface characteristics and also with the particle microstructure. Particle size and shape influence physical and chemical properties of particulate materials. Morphological analysis is being developed in order to facilitate a more accurate description of the properties and behavior of particulate systems from a fundamental knowledge of the characteristics of the particles of the system [1,2].

Shape is defined as the pattern of relationships among all of the points of the surface or profile of the particle. The development of this operational definition has in turn led to the development of morphological analysis.

### Experimental

An image of the particle is obtained, the profile of that image is converted to a set of  $x,y$  pairs, a process known as digitizing. The  $x,y$  set is then converted to polar coordinates,  $(R,\theta)$ . The curve in the  $R,\theta$  space is converted to a Fourier equation, the coefficients of which are extracted, and then mathematically transformed to morphic terms which themselves constitute the shape features of the particle. A sample usually consists of 100 particles, upwards of 150 profile points are extracted from each particle, giving a total of 15,000  $x,y$  points per analysis. Once the morphic terms are obtained, the data analysis can be carried out in order to facilitate the

0097-6156/87/0332-0002\$08.25/0  
© 1987 American Chemical Society

solution of the problem at hand. Morphological analysis is carried out using an instrument known as a Shape Analyzer [3], which consists essentially of a high quality graphic system and computer plus sophisticated software and peripherals [2].

The Shape Analyzer is a scientific instrument which is used to analyze the shape, size, and texture of objects. The item for analysis may be the object itself, its photograph, optical or electron micrograph, etc. The shape-size analysis is achieved by converting the profile to a set of shape and size descriptors which are complete, unequivocal and invariant. The texture analysis converts the full image of the object into a set of textural descriptors which are unequivocal, complete and invariant. These shape, size and texture descriptors can be used in research, in quality control, in process control and specifications. Additional details are given in Table 1 and the Appendix.

The morphological features measured in the Shape Analyzer include the following:

Table 1. Morphological Analysis

| <u>Topic</u> | <u>Feature</u>  | <u>Application</u>  |
|--------------|---|---|
| Size         | Equivalent radius<br>Mean radius/diameter                         | Hydraulic radius<br>Sedimentation<br>Correlations with other particle size analysis methods                                   |
| Shape        | Not-roundness<br>L2(2)<br>L2(3)<br>L2(4)<br>Roughness<br>Symmetry | Wear analysis<br>Dust explosions<br>Particle characterization<br>Settling<br>Bulk properties<br>Slurry flow<br>Fluidized beds |
| Texture      | Mean texture<br>Standard deviation<br>Symmetry                    | Microstructure analysis<br>Cancer cell identification and differentiation   |
| Mixtures     | Cross-over points   | Particle mixture and blend analysis   |

### Strategy

The shape and texture features are invariant, unique and unequivocal. They are associated with indications of physical meaning. The used form of the Fourier equation is

$$R(\theta) = a_0 + (a_n \sin n\theta + b_n \cos n\theta)$$

the raw Fourier coefficients not useful to describe the profile because they change in value as the profile is rotated. For this reason they are transformed into invariant morphological size and shape descriptor in the following way:

#### Theory of Morphological Analysis [4]

Size and Shape Descriptors. The following size and shape terms are defined. These are rotationally invariant and related to the amplitudes,  $a_n$  and  $b_n$ , as follows.

The size term is defined as

$$R_o = \sqrt{a_o^2 + \frac{1}{2} \sum_{n=1}^z (a_n^2 + b_n^2)} \quad (1)$$

in which  $R_o$  is termed "equivalent radius" and is the radius of a circle having the same area as that of the particle profile, and  $n$  is the order of the coefficient.

The shape terms are defined as

$$L_o = a_o/R_o \quad (2)$$

$$L_{1,n} = 0 \quad \text{for all } n$$

$$L_{2,n} = \frac{1}{2R_o^2} (a_n^2 + b_n^2) \quad (3)$$

$$L_{3,n} = \frac{3}{4R_o^3} (a_n^2 a_{2n} - b_n^2 a_{2n} + 2a_n b_n b_{2n}) \quad (4)$$

$a_o$  is the mean radius.

Equation (2) defines the value of the size normalized mean radius of the particle. Equation (3) defines the size normalized sum of the squares of the Fourier coefficients. Equation (4) defines the sum and differences of the multiples. It has been shown that these size and shape descriptors can be used to regenerate the original particle profile. This indicates that the descriptors together contain all of the size and shape information contained in the original profile.

The morphological descriptors described above will be examined later for their physical interpretation. But first their very interesting relationship to the statistical properties of the particle profile radial distribution will be considered.

Statistical Properties of Descriptors.

$$\mu_0 = L_o R_o \quad (\text{mean radius})$$

$$\mu_1 = R_o \sum_{n=1}^z L_{1,n} = 0 \quad L_{1,n} = 0 \quad \text{for all } n \quad (5)$$

$$\mu_2 = R_o^2 \sum_{n=1}^z L_{2,n} \quad (6)$$

$$\mu_3 = R_o^3 \sum_{n=1}^z \sum_{m=1}^z L_{3,m,n} \quad (7)$$

where  $\mu_2$  is the radial standard deviation (the NR not-roundness) and  $\mu_3$  is the radial skewness (SKE).

Symmetry Operations [5]

In crystallography one is accustomed to the idea that a structure either has a particular symmetry element or it does not. The membership is thus either 1 or zero. In morphological analysis the symmetry has a value of zero through 1 depending upon how closely the profile approaches the symmetry being considered. The definitions of the symmetry operations are shown below:

Rotation

$$C_m = \frac{\sum L_2(m \cdot n)}{\sum L_2(n)} \quad (m=1,2,3,\dots,M) \quad (8)$$

Reflection

$$\sigma_1 = \frac{\sum L_2(n) \cos^2(\alpha_n - n\beta - 2n\pi)}{\sum L_2(n)} \quad (\text{PAT}) \quad (9)$$

$$\text{if } \sigma_1 = 1$$

$$\sigma_{j>1} = \frac{\sum L_2(j \cdot n)}{\sum L_2(n)} \quad \left[ \begin{matrix} j=m \\ j=2m \end{matrix} \right] \quad (10)$$

Inversion

$$I = \frac{\Sigma L_2(2n)}{\Sigma L_2(n)} \quad (11)$$

Rotation-Reflection

$$S_2 = \frac{\Sigma L_2(2n)}{\Sigma L_2(n)} \quad (\sigma_1 \text{ and } \sigma_4) \quad (12)$$

Texture [6]

Texture is defined as the pattern of relationships between the gray levels of the defined image. The objective of texture morphology analysis is develop an analytical method whereby the image can be regenerated.

In order to do this the points of the image have to be incorporated into the analysis in the form of invariant descriptors. The interpretation of the textural morphology features depends upon the physics of the situation (for example, the gray level may be related to altitude or in another case to the chemical analysis from point to point. The interpretation also depends upon the mathematical relationships between the various morphological descriptors used. There are three major types of morphological texture descriptors. These are: statistical terms, symmetry operations, and invariant texture morphology descriptors (ITMD's).

$$\bar{G}_T = \sum_{i=1}^L i P_i \quad (13)$$

$$\sigma_T^2 = \sum_{i=1}^L (i - \bar{G}_T)^2 P_i \quad (14)$$

in which:

$\bar{G}_T$  is the mean gray level of the image

$\sigma_T^2$  is the standard deviation of the image gray level

$L$  is the maximum gray level

$P_i$  is the probability distribution at gray level  $i$ .

If the image is rotated by  $2\pi/n$  and the original configuration is reproduced, the image is said to possess an  $n$ -fold rotational symmetry.

The textural symmetry is

$$C_n = 1 - \frac{\iint [G(x,y) - TG(x',y')]^2 dx dy}{\iint G(x,y) dx dy} \quad (15)$$

(TDs)

in which:

$G(xy)$  is the gray level at  $(x,y)$

$x'y'$  are locations corresponding  $G(x,y)$

The invariant ITMD's have been developed using a combined Fourier-Bessel equation in which the Fourier terms account for the repetitive nature of the image described by a radius vector sweeping round on a central origin. The Bessel terms deal with the features of the image in the direction outwards along the radii from the origin. The general form of the descriptors will be reported at a later date.

#### Indications of Physical Meanings of Shape and Textural Descriptors

Particle Size. The equivalent radius  $R_0$  may also be reported out as the equivalent particle diameter  $2R_0$ . The size may be reported out as mean and standard deviation as shown in Table II or as a histogram as shown in Figure 1a,b. The size template in Figure 2 illustrates the principle underlying the  $R_0$  term.

Shape Classifier. It has long been known that different methods of particle production which involve different modes of particle formation will produce particles of different morphology. To demonstrate this fact, three samples of adipic acid powder were made by three methods: atomization, comminution and crystallization. The NR and SKE values were plotted against each other for the three particulate materials. The data shown in Figure 3a,b clearly shows that it is possible to classify the three products on the basis of their morphology. The method of data plotting used, stretches the points out in a diagonal fashion and this permits the classification lines to be drawn in as shown. The ATM, RED and ELECT data correspond to commercial iron powders made by atomization, reduction and electrolytic deposition, respectively. These commercial material data do not correspond to the adipic acid data because the commercial processes are comprised of many steps including: crushing and grinding, sintering, hammer milling, mixing and blending. For example, consider the atomized iron powder, each one of the these steps influences the particle morphology to such an extent that the data is shifted into the region corresponding to the comminuted adipic acid.

Not-Roundness. The size normalized radial standard deviation is illustrated in the NR template shown in Figure 4. Thus, no matter how the profile deviates from a circle the NR value will only indicate the statistical property of the radial distribution. There is no information in this term concerning the sequence of radial terms.

L2(2) Indicator. The effect of shape change on the size of the L2(2) term is illustrated in Figure 5.

Table II. Size Reported as Means and Standard Deviations for Spheroidal Carbides in Ferrite Matrix (left) and for Atomized and Sponge Iron Powders (right).

| $R_o$    |           | $R_o$       |           |
|----------|-----------|-------------|-----------|
| Mean     | Std. Dev. | Mean        | Std. Dev. |
| 0.432    | 0.036     | Atom (10)   | 0.076     |
| (CIF 40) |           | Sponge (10) | 0.031     |

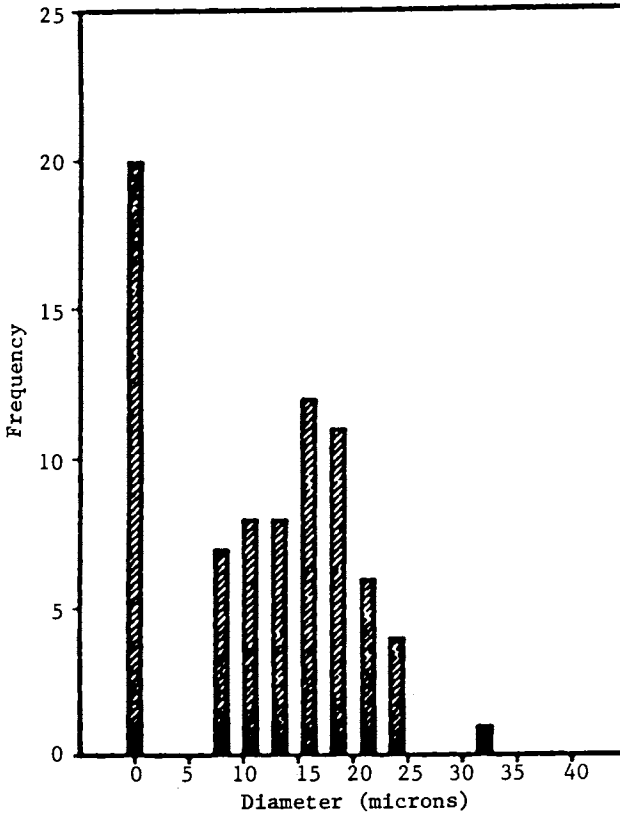


Figure 1a. Size distribution for Rey 511. Reproduced with permission from Ref. 8. Copyright 1985 Oxford & IBH Publishing.

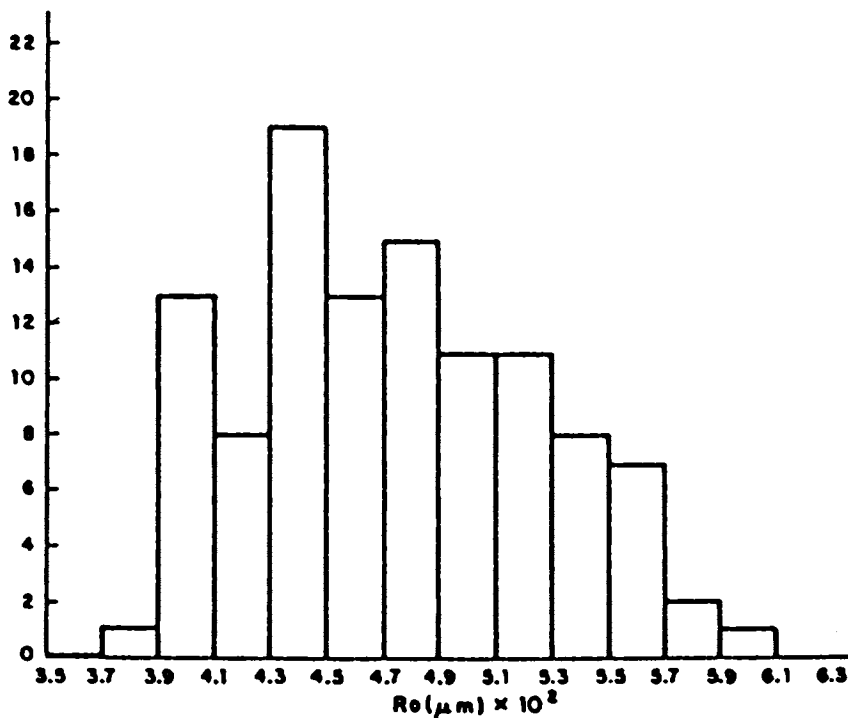


Figure 1b. Histogram representation of a particle size distribution. Reproduced with permission from Ref. 8. Copyright 1985 Oxford & IBH Publishing.



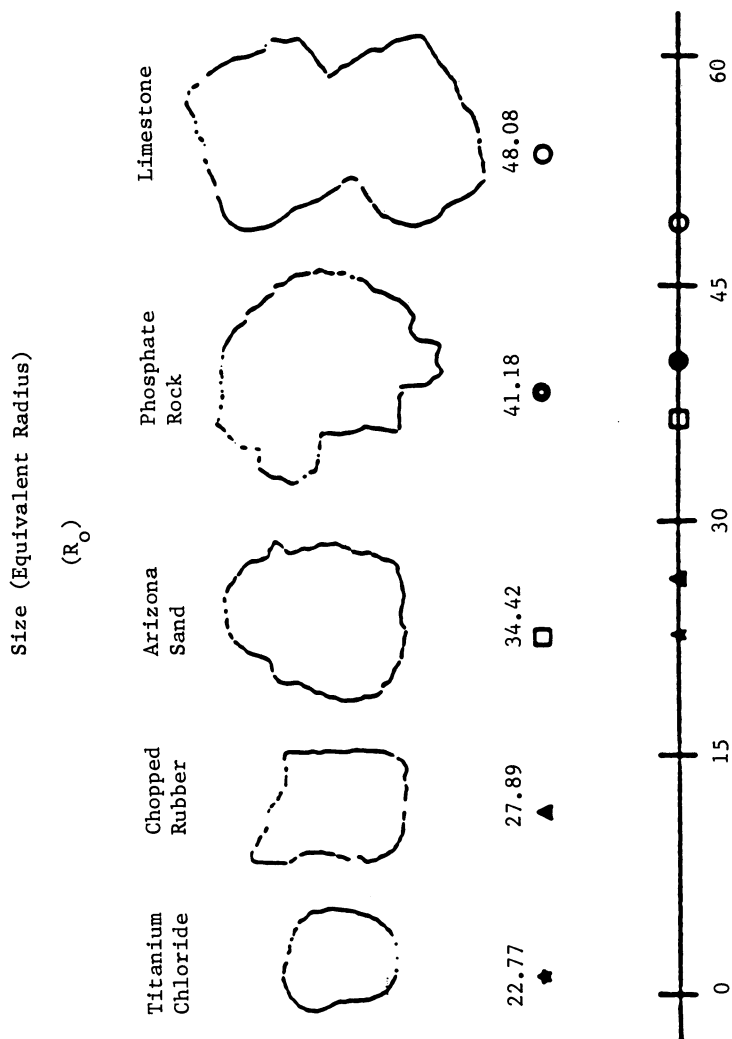


Figure 2. Size template illustrating the principle underlying the  $R_0$  term. The actual size depends on the magnification used. The area of the profile is  $\pi R_0^2$ .

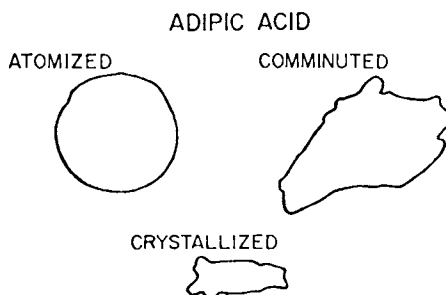


Figure 3a. Morphologies of adipic acid. Reproduced with permission from Ref. 2. Copyright 1984 CRC Press.

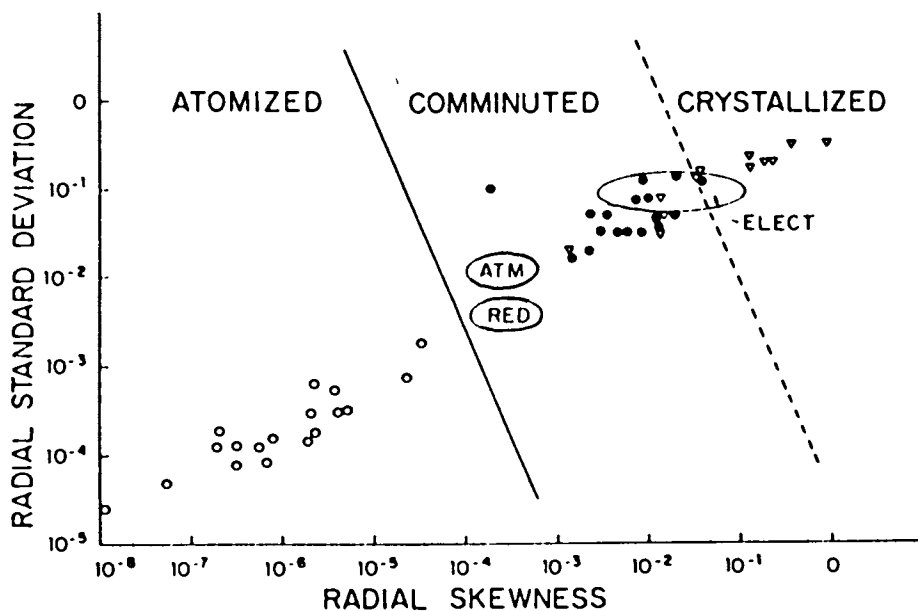


Figure 3b. Morphology plot for adipic acid; ATM - atomized iron, RED - reduced iron, ELECT - electrolytic iron. Reproduced with permission from Ref. 2. Copyright 1984 CRC Press.

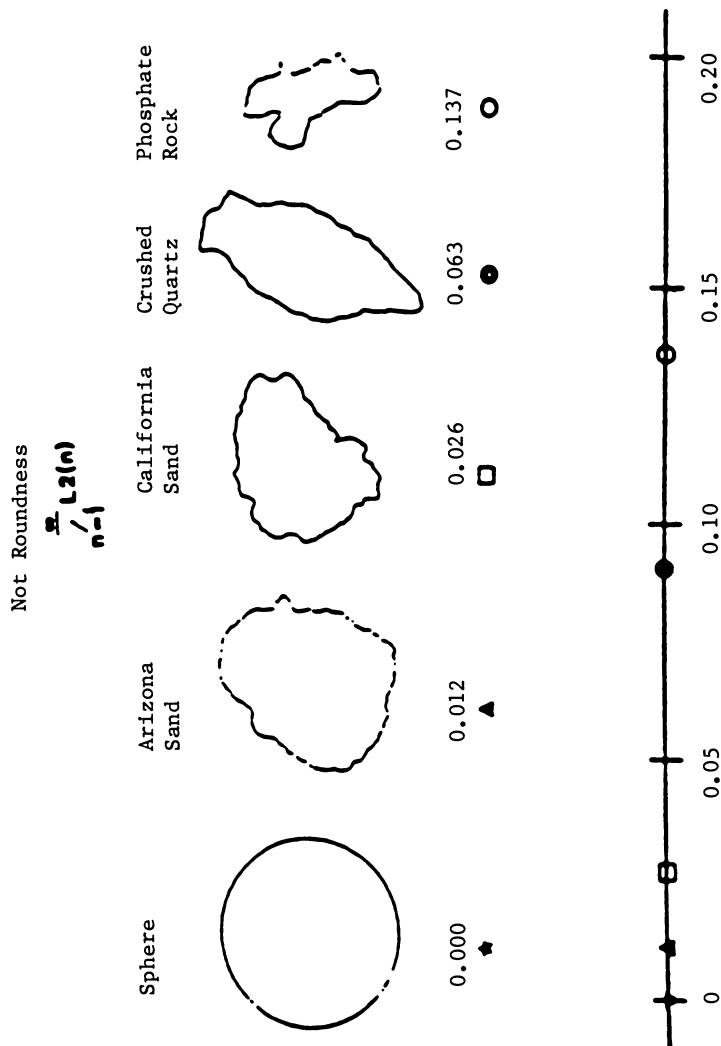


Figure 4. NR template illustrating the size normalized radial standard deviation. Reproduced with permission from Ref. 8. Copyright 1985 Oxford & IBH Publishing.

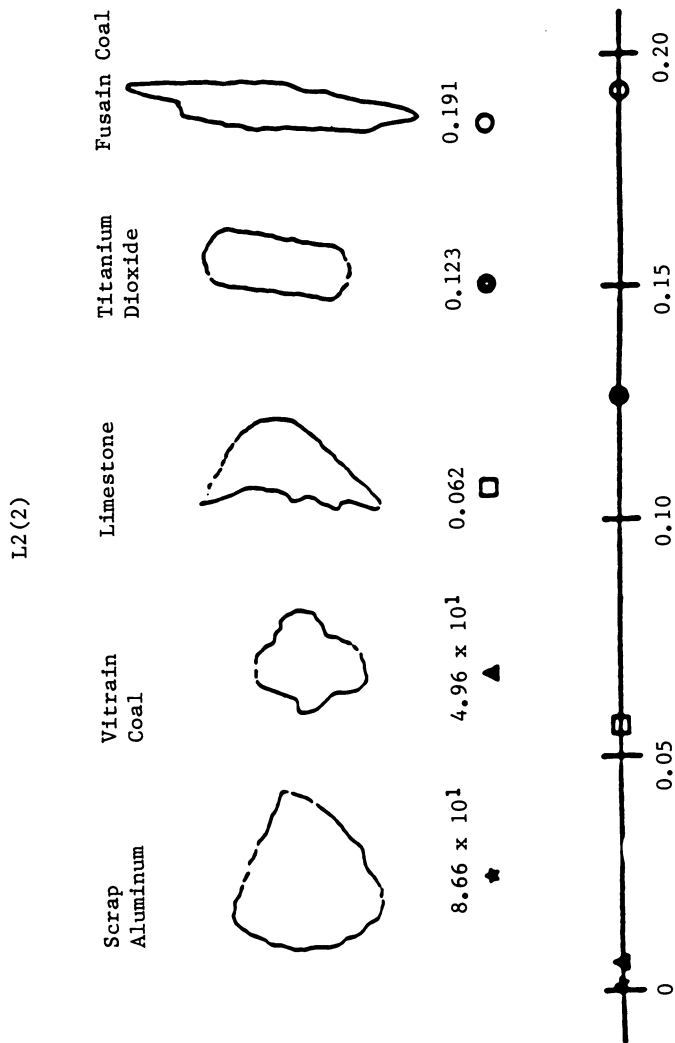


Figure 5. Effect of shape change on the size of the L2(2) term.

L2(3) Indicator. The effect of shape change on the value of the L2(3) terms is shown in Figure 6.

Roughness Indicator. This term is defined as the sum of the higher order L2(n) terms. It represents the minor deviations and irregularities in the particle profile and is illustrated in the template of Figure 7.

Shape Distribution. One often hears of "narrow size distribution" or "broad size distribution". It is also meaningful to consider a narrow shape distribution and a broad shape distribution. Examples of these are given in Figure 8. The narrow shape distribution shows a plot of not-roundness of crystals of NaCl. After milling, the broad shape distribution results.

Shape Composition. The NR is composed of the other terms described above. Specifically:

$$NR = L2(2) + L2(3) + L2(4) + \dots + L2(n)$$

An accounting of the proportion of NR for each component terms is called the Shape Composition. It is illustrated in Table 3 for the two samples of NaCl. The first column corresponds to the received crystals, the second column corresponds to the milled salt material.

Residual Porosity. This can be determined on an area basis by examination of suitably prepared microstructures. For example, as shown in Table IVa,b, there are substantial differences between the residual porosity in an atomized sintered iron compact and a similar sponge iron compact.

Shape Symmetry. The meaning of the rotational symmetry, for example, is demonstrated in Figure 9. In this figure the values of  $C_2$ ,  $C_3$  and  $C_4$  are compared between an equilateral triangle and an isosceles triangle. The precise definitions of the symmetries are given below.

Figure 10 shows an interesting application of particle shape symmetry in the case of seven types of instant coffee products. It will be seen that the symmetry analysis shows that coffee #3 is fundamentally different from each one of the other coffee products.

Texture analysis is illustrated in Figure 11 which shows the gray level distribution for a polished and etched sample of tungsten carbide material. From this distribution one can obtain the mean and standard deviation of the texture. In addition, the  $\eta^*$  value indicates the sharpness of the image.

Some applications of the mean gray level are shown in Figures 12a,b and 13. In the measurement of grain size it is necessary to utilize the services of a skilled human operator in order to interpret the size measurement. Using the mean textural indicator the decision might be made by the Shape Analyzer. Thus, in Figure 12, a correlation is depicted showing that gray level can correspond to grain size in carefully prepared samples.

Figure 13 shows four stages during the sintering of Fe-C compacts at successively higher temperatures. Again, the mean texture value can be used as an indicator of the sintering temperature used in the sample preparation.

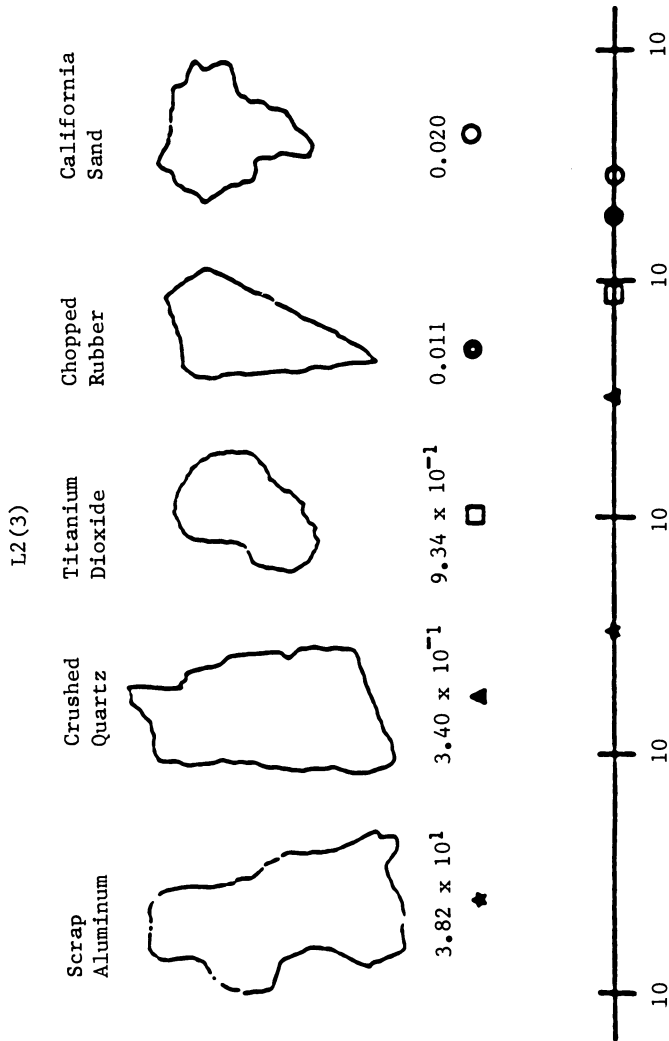


Figure 6. Effect of shape change on the value of the L2(3) terms.

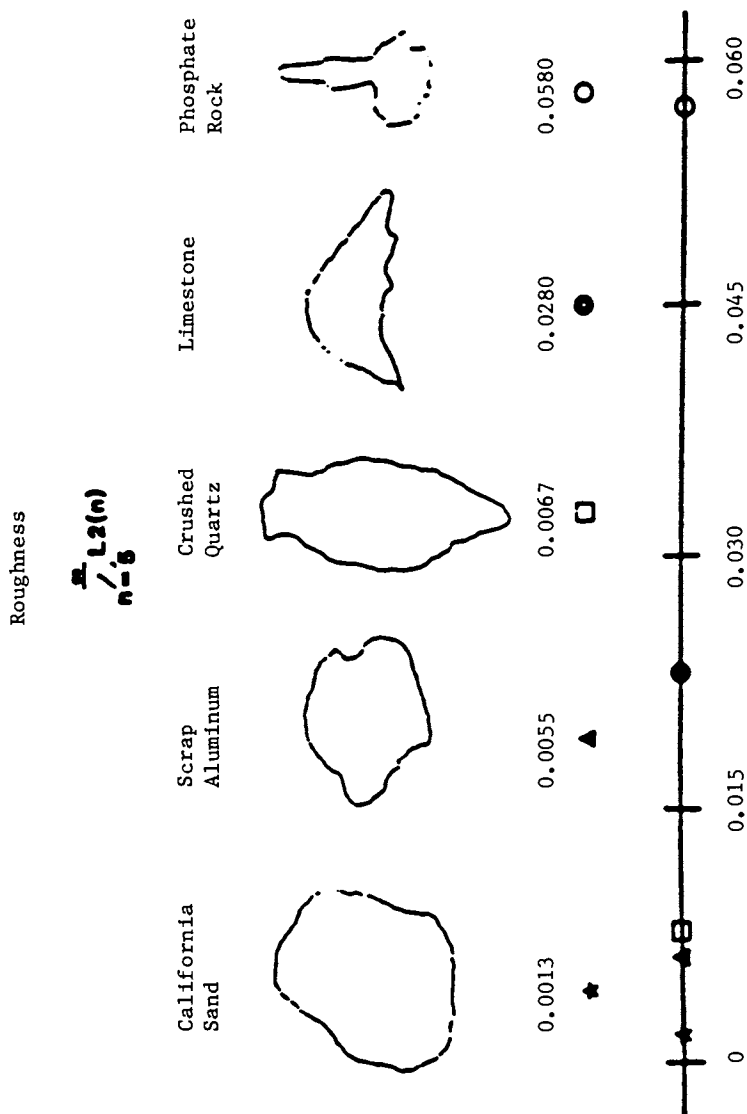


Figure 7. Template illustrating the roughness indicator. Reproduced with permission from Ref. 8. Copyright 1985 Oxford & IBH Publishing.

**material : sodium chloride  
two-step processing, BM**

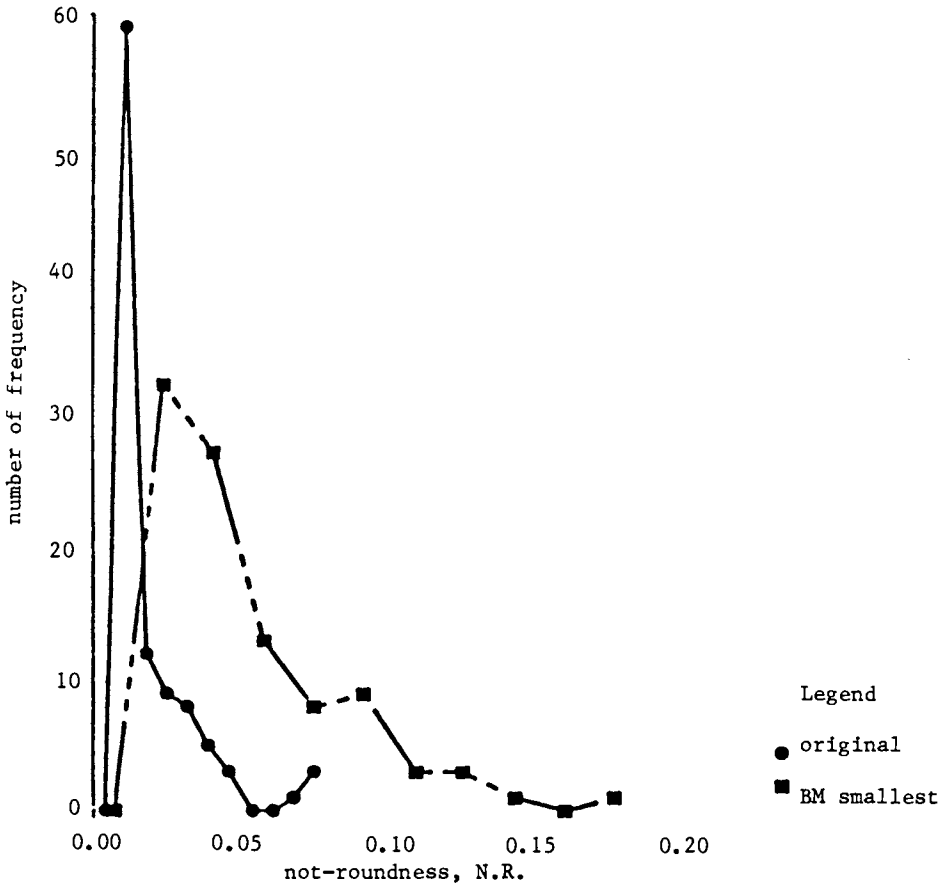


Figure 8. Broad and narrow shape distributions.



Table III. Shape Composition Changes for Sodium Chloride

| morphic descriptor | S <sup>a</sup> | BM <sup>b</sup> |
|--------------------|----------------|-----------------|
| L2(2)              | 49.80          | 65.94           |
| L2(3)              | 6.92           | 14.08           |
| L2(4)              | 31.53          | 8.16            |
| Ruff               | 11.75          | 11.82           |

<sup>a</sup>S indicates starting material.

<sup>b</sup>BM indicates ball-milling material.

Table IVa. Morphic Features of Residual Porosity in Iron Compacts

|               | Elongation |           | Not-Roundness |           |
|---------------|------------|-----------|---------------|-----------|
|               | Mean       | Std. Dev. | Mean          | Std. Dev. |
| Atomized Iron | 0.049      | 0.063     | 0.065         | 0.085     |
| Sponge Iron   | 0.008      | 0.042     | 0.119         | 0.057     |

Table IVb. Morphic Properties of Spheroidal Carbide Particles (n=40) in a Ferrite Matrix

| Elongation<br>(10 <sup>-2</sup> ) |           | Not-Roundness<br>(10 <sup>-2</sup> ) |           |
|-----------------------------------|-----------|--------------------------------------|-----------|
| Mean                              | Std. Dev. | Mean                                 | Std. Dev. |
| 3.3                               | 3.5       | 4.1                                  | 4.6       |

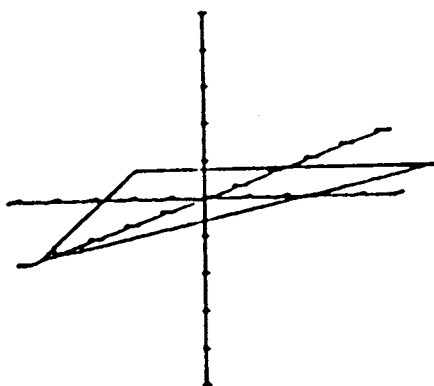
Includes rotation, reflection, inversion & rotation-reflection

$$C_m = \frac{\sum L_2(m-n)}{\sum L_2(n)} \quad (m = 1, 2, 3, \dots)$$

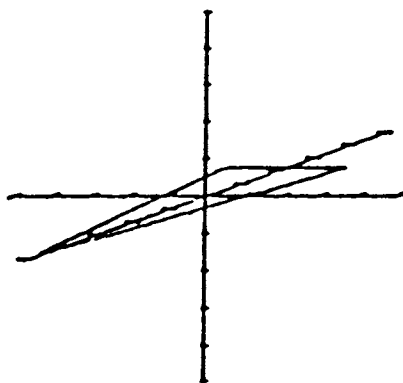
$C_2$  = 2-fold rotational symmetry  $0 \leq C_2 \leq 1$

$C_3$  = 3-fold rotational symmetry  $0 \leq C_3 \leq 1$

$C_4$  = 4-fold rotational symmetry  $0 \leq C_4 \leq 1$



REGULAR  
TRIANGLE



ELONGATED TRIANGLE

$C_2 = 0.13$

$C_3 = 0.99$

$C_4 = 0.01$

Inversion = 0.14

$C_2 = 0.55$

$C_3 = 0.24$

$C_4 = 0.24$

Inversion = 0.55

Figure 9. Demonstration of the meaning of the rotational symmetry.

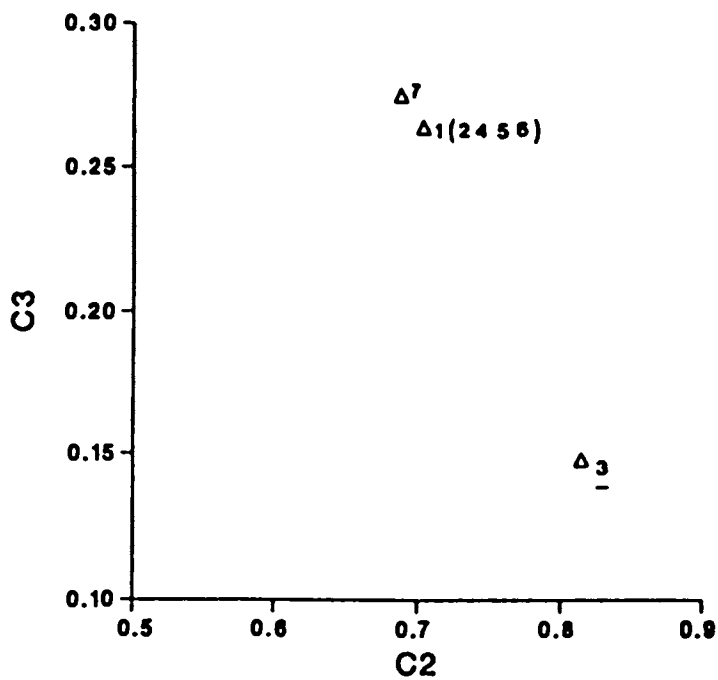


Figure 10. Symmetry C2 vs. symmetry C3. Illustration of the use of rotational shape symmetry in differentiating coffee samples.

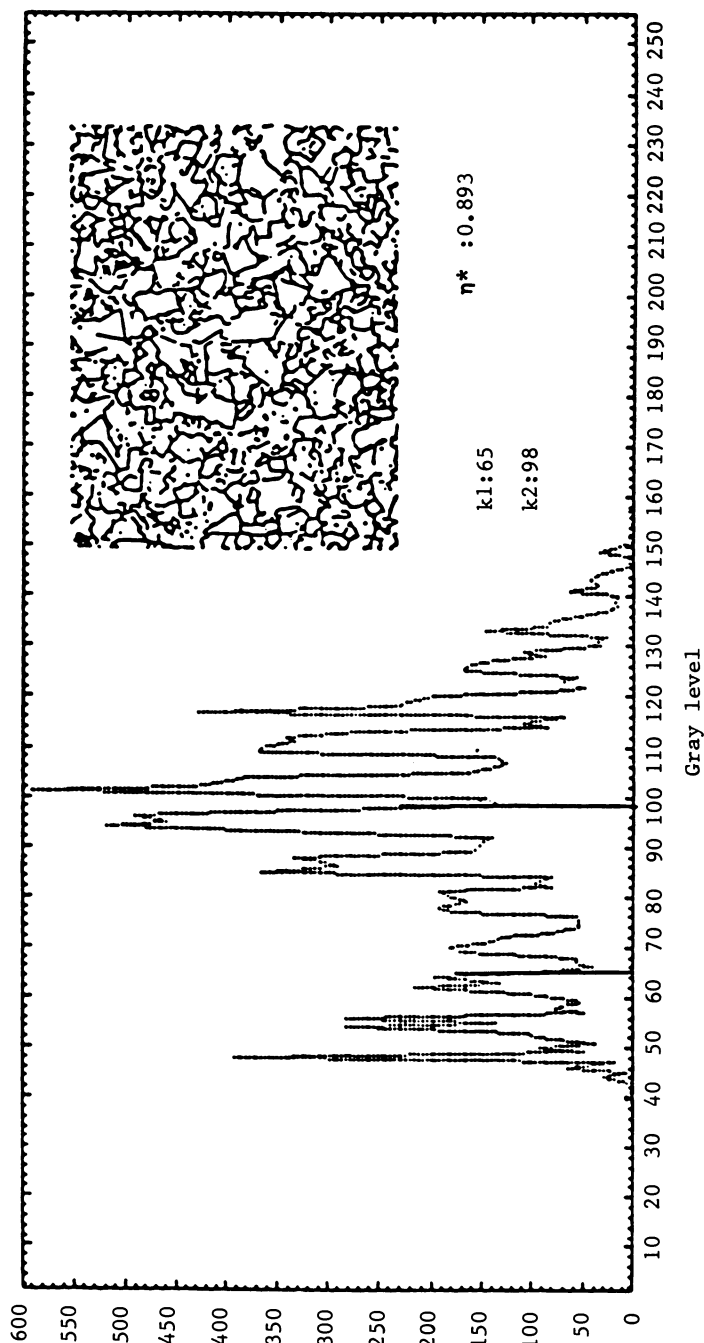


Figure 11. Tungsten carbide gray level distribution.  $\eta^*$  indicates the sharpness of the image;  $K1$  and  $K2$  are limits, two standard thresholds apart.

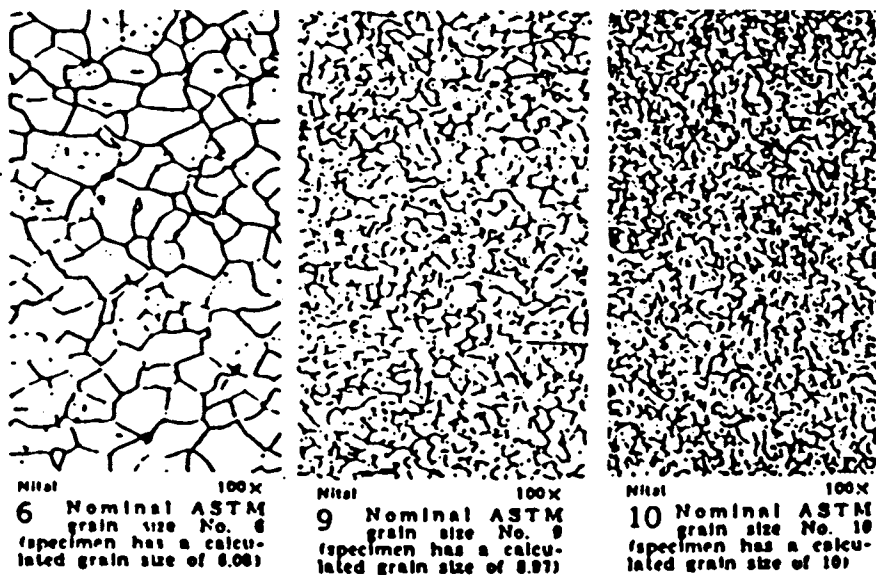


Figure 12a. Normal ASTM grain size microstructure. Reproduced with permission from Ref. 7. Copyright 1972 American Society for Metals.

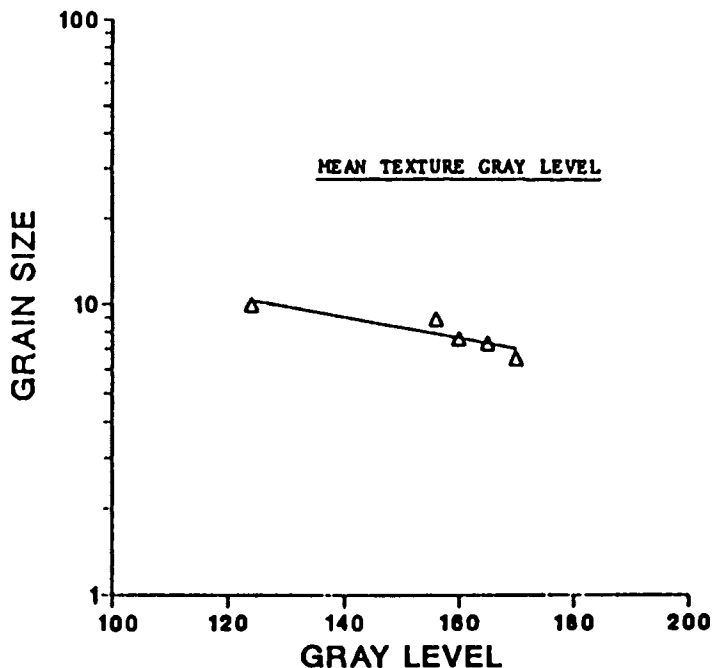
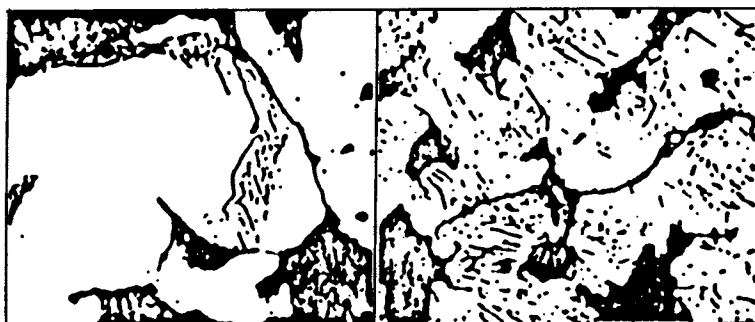
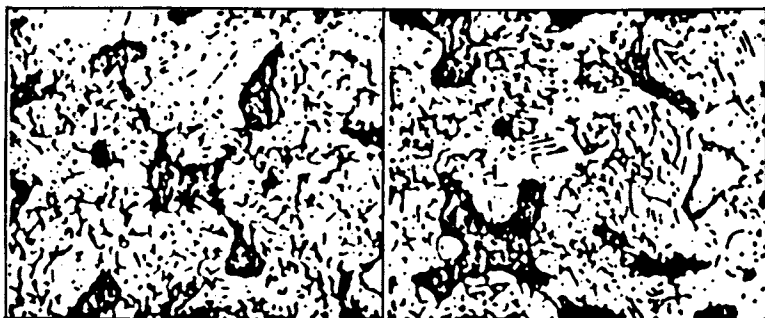


Figure 12b. Grain size vs. gray level for ASTM microstructure. Reproduced with permission from Ref. 7. Copyright 1972 American Society for Metals.



4% picral plus 0.5% HNO<sub>3</sub>, 800x  
**1660** Iron powder mixed with 1.35% graphite, pressed to 61 g per cu cm, sintered 30 min at 1850 F (1010 C). Slight pearlite formation (0.10% combined carbon), remaining carbon is graphite in pores (dark). Transverse-rupture strength is 20,000 psi (138 MPa).

4% picral plus 0.5% HNO<sub>3</sub>, 800x  
**1661** Same as 1660 except the sintering temperature was increased to 1900 F (1038 C), which resulted in combined carbon content of 0.75%, an essentially all-pearlite structure, and an increase in transverse-rupture strength to 31,000 psi (352 MPa).



4% picral plus 0.5% HNO<sub>3</sub>, 800x  
**1662** Same as 1660 and 1661 except sintering temperature was increased to 2050 F (1121 C), which resulted in increases in particle bonding and pore spheroidization, and a transverse-rupture strength of 30,000 psi (352 MPa). Combined carbon content, 0.75%.

4% picral plus 0.5% HNO<sub>3</sub>, 800x  
**1663** Same as 1660 to 1662 except sintering temperature was increased to 2150 F (1177 C). This further increased particle bonding, pore spheroidization; transverse-rupture strength increased to about 35,000 psi (353 MPa). Combined carbon, 0.75%.

Figure 13. Iron powder microstructure. Reproduced with permission from Ref. 7. Copyright 1972 American Society for Metals.

Continued on next page

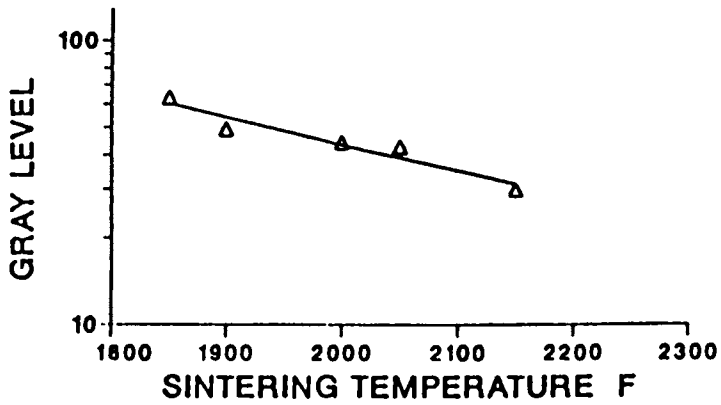


Figure 13. Continued. Sintering temperature vs. gray level for ASTM microstructure.

Mixture Analysis. It has always been difficult to analyze particulate material mixtures for a number of reasons including the large amount of data that has to be collected and analyzed and also including the proper choice of the many "degree of mixidness" parameters available in the literature. Figure 14 shows three stages in the mixing of a binary mixture at progressively increasing mixing times  $T_1$ ,  $T_2$ , and  $T_3$ . The progress of the mixing process is followed in Figure 15a,b, which shows a plot of rotational texture symmetry versus time.

Cancer and Normal Cells. Although a fairly simple analysis, the use of the mean and standard deviation of the morphological texture may have some significance. Figure 16 shows a normal cell and cancer cell patten of a human liver. The corresponding morphic texture values are shown in Table 5. It is clearly possible to use texture analysis to differentiate between healthy and unhealthy cells.

#### Acknowledgments

The authors are grateful to the National Science Foundation Particulate Morphology Processing Program, Dr. M. Ojalvo, Director for financial support under grant CPE 8023868.

#### Appendix

##### Shape Analyzer

##### I. Classical Measurements of Particles

###### A. Size

Equivalent radius: mean equivalent radius, standard deviation, distribution curve.

###### B. Classical Measures

Perimeter, Hausner shape factors, Martins diameter, Feret diameter, two dimensional sphericity, rugosity.

##### II. Morphological Analysis

###### A. Shape

Not-roundness, L2(2), L2(3), L2(4), roughness. Mean and standard deviation of these shape features, distribution curve. Shape composition. (R, $\theta$ ); ( $\phi$ ,1) and (R,S) methods of analysis.

###### B. Interior Measures

Porosity-total area, relative area, pore size distribution, mean and standard deviation of pore size. Pore shape: mean, standard deviation and distribution of shape feature selected.

###### C. Shape Symmetry Measures

Two-fold, 3-fold, 4-fold, rotational symmetry. Mirror symmetry and inversion.

###### D. Texture

Mean and standard deviation of gray level of image, texture symmetry, color analysis and mixture analysis.



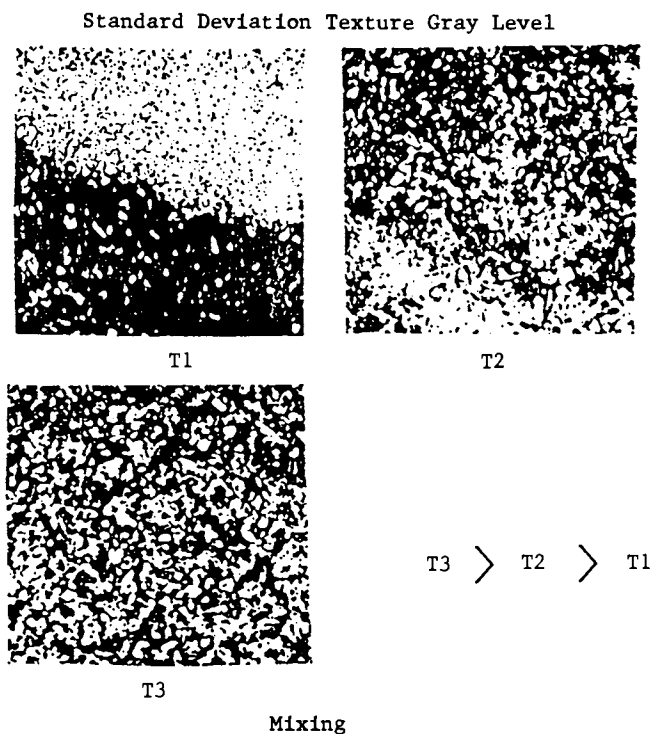


Figure 14. Mixture of equal parts of black and white particles after times  $T_1$ ,  $T_2$  &  $T_3$ .

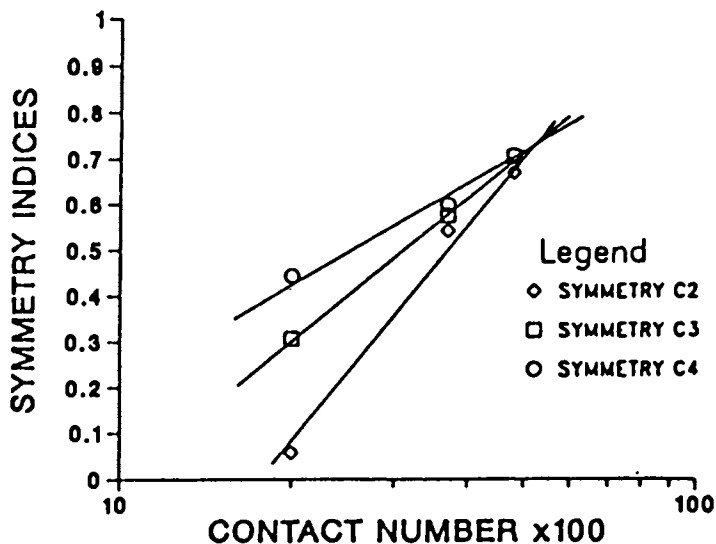


Figure 15a. The degree of mixing: symmetry indices vs. contact number. The convergence point indicates complete mixing. The contact number indicates the total number of black-white transitions in a scan of the field.

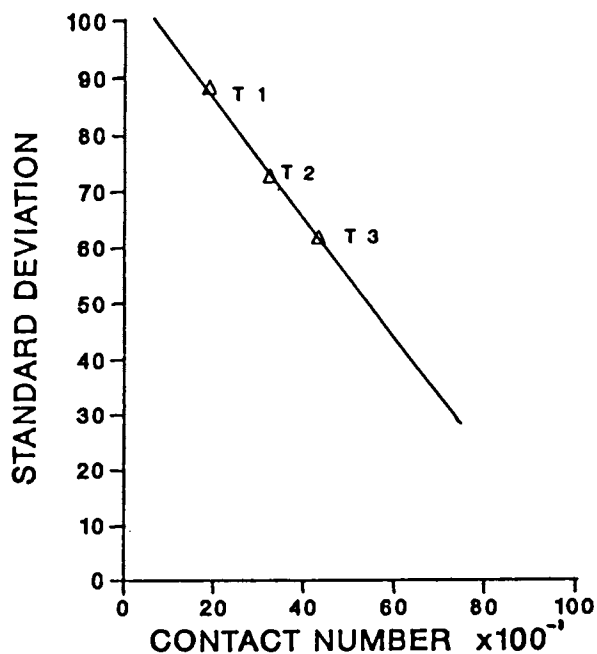
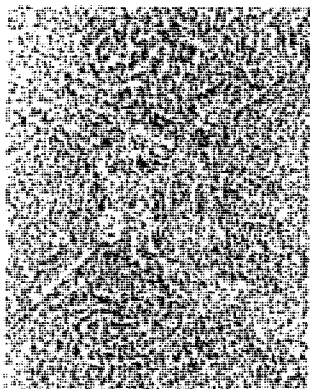
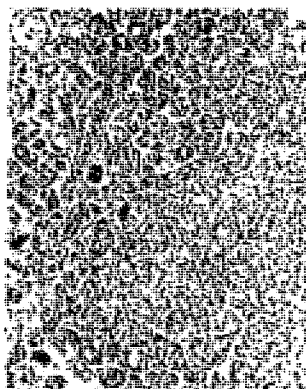


Figure 15b. Standard deviation vs. contact number.



Normal Cell Pattern



Tumor Cell Pattern

Figure 16. A normal cell and a cancer cell pattern of a human liver.

Table V. S.D. and M.G.L. for Different Cell Patterns

| Normal Cell  | Tumor Cell | Normal + Tumor Cell |
|--------------|------------|---------------------|
| S.D. 20.37   | 30.26      | 26.48               |
| M.G.L. 123.4 | 101.60     | 115.70              |

S.D. : Standard Deviation

M.G.L.: Mean Gray Level

III. Fractal Analysis

Measure of the fractal of particles selected.

References

1. Beddow, J.K., Particulate Science and Technology, Chemical Publishing Company, New York, 1980.
2. Beddow, J.K. (ed.), "Particle Characterization in Technology," CRC Press, Boca Raton, Florida, 1984.
3. Shape Technology Limited, "Shape Analyzer Handbook," March 1986.
4. Luerkens, D.W., Beddow, J.K. and Vetter, A.F., "Invariant Fourier Descriptors," Powder Technology, 31, 2, 217-220, 1982.
5. Luerkens, D.W., "Symmetry Operations in Morphological Analysis," be submitted to Particulate Science and Technology, an International Journal.
6. Hsyung, Nley-Bor, MS Thesis, " Particle Texture Analysis," University of Iowa, 1984.
7. American Society for Metals, "Metals Handbook," Vol.7, 1972.
8. Beddow, J.K. In Powder Metallurgy and Related High Temperature Materials; Ramakrishnan, Ed.; Oxford & IBH Publishing, New Delhi, India, 1985.

RECEIVED July 21, 1986

## Chapter 2

# Assessment of Particle Size Distribution and Spatial Dispersion of Rubbery Phase in a Toughened Plastic

B. Z. Jang and Y. S. Chang

Materials Science Program, Auburn University, AL 36849

A simplified statistical scheme for image analysis has been proposed to describe the spatial distribution of rubber particles in a plastic matrix. Based on this scheme, a software package compatible with a Hewlett-Packard personal computer has been developed which is capable of analyzing the particle size distribution and spatial dispersion of rubber particles in a toughened plastic. With slight modification this package may be adapted to other computer systems for studying the second-phase morphology of any multiphase composite.

The normalized dispersion index (NDI) calculated from the TEM micrographs by the image analysis method appears to be a very sensitive index for describing the spatial dispersion of rubber particles in high impact polystyrene (HIPS) samples. Materials with a small NDI (e.g.,  $NDI < 0.142$ ), signaling a good dispersion of rubber particles in the polystyrene matrix, appear to have the capability of quickly and uniformly developing thick crazes upon loading and thereby dissipating a great amount of strain energy. The morphological parameters obtained were correlated with the microscopic crazing behavior and the macroscopic mechanical properties. A stress field overlap concept was proposed to explain the effects of particle dispersion on the mechanical behavior of HIPS. A general rubber-toughening theory was also reviewed and discussed.

The technical and commercial success of high impact polystyrene (HIPS) and acrylonitrile-butadiene-styrene (ABS) has led to a widespread research program on the use of rubbers as toughening agents for plastics. There is now an impressive list of rubber-toughened polymers including both amorphous and

0097-6156/87/0332-0030\$06.00/0

© 1987 American Chemical Society

semicrystalline thermoplastics, and thermosetting resins. In all of these materials, the aim is to increase fracture resistance while at the same time preserving the desirable properties of the parent polymer (1).

The relationships between structure and properties of rubber-modified polymers are complex because of the large number of structural variables involved (1-4). The major structural parameters that are important in a polymer with a given chemical composition and molecular weight characteristics are (a) rubber content, (b) volume fraction of the dispersed phase, (c) rubber particle size distribution, (d) degree of crosslinking of the rubber, and (e) degree of interfacial adhesion between the dispersed and matrix phases. One potentially important factor that has been largely overlooked is the state of rubber particle dispersion. Particle dispersion will affect the stress distribution in the plastic matrix and therefore will determine the mechanical behavior of a toughened plastic. Crazing and shear yielding generally are believed to be the two primary sources of energy absorption when a toughened plastic is mechanically loaded (1,3-4). The initiation and growth of both crazes and shear bands are critically dependent upon the morphology of the dispersed rubbery phase. Therefore, the ability to adequately characterize the complex morphology of the rubbery phase is of great importance. The development of suitable techniques has in fact played an important part in the study of structure-property relationships, and hence in improving and extending the range of toughened products.

The principal methods available for tackling the phase morphology characterization problems are optical and electron microscopy, light scattering, and Coulter Counter (1). If the rubber particles are large enough to be resolved, optical microscopy is the simplest and cheapest method for studying morphology. However, the most successful method for studying morphology in rubber-toughened plastics has been the osmium-staining method developed by Kato (5-7); the method being applicable to polymers containing unsaturated rubbers. For those materials containing rubbers that cannot be stained successfully the technique of light scattering might be useful (8-10). For polymers that can be dissolved in an electrolyte, Coulter Counter may be used to measure particle sizes (in the range 0.5 to 400  $\mu\text{m}$ ) (11). The method is well suited to measuring the relatively large particles in HIPS. Smaller particles tend to escape the detection of Coulter Counter. Further, the spatial dispersion of rubber particles cannot be revealed by this method. However, this method has the advantages of readily permitting a large sampling space as well as indicating both particle size and dispersity of the distribution.

Presented in this paper are the results of an investigation concerning the link between structure and properties of rubber-toughened plastics. An attempt has been made to assess the importance of the spatial distribution of rubber particles in terms of their effectiveness in controlling craze initiation and growth. Also studied in particular were the effects of rubber particle size on the mechanical properties of HIPS materials. A

computerized image analysis and TEM techniques were utilized to characterize the rubbery phase morphology. A software package based on BASIC language has been developed that is capable of analyzing the average particle size, size distribution, volume fraction of particles, and the degree of particle dispersion in a matrix. Although specifically designed for the Hewlett Packard Model 9836 personal computer, this package may be readily modified to be used in other computer systems.

### Degree of Dispersion of Rubber Particles

Gurland (12) has developed a quantitative microscopy scheme for measuring the degree of dispersion of aggregates. The state of aggregation of a constituent of a heterogeneous multiphase material may be described as being dispersed, agglomerated, or continuous. Such terms refer to the degree of dispersion, which is quantitatively related to three measurable parameters - the interface of separation, the fineness, and the distribution of the particles within the matrix (12).

Surface of separation. Where volume fraction of the dispersed phase is high so that the area of contact between contiguous particles of the second phase is unnegligible the extent of the surface of separation between the second phase and the matrix has to be considered in measuring the degree of dispersion. For a two-phase composite the degree of separation  $dp$  is defined as:

$$dp = \frac{Sv(ab)}{Sv(aa) + Sv(ab)} = \frac{Sv(ab)}{Sv(total)} \quad (1)$$

where  $Sv(ab)$  is the area of the interface between particles of the particulate phase and the matrix, and  $Sv(aa)$  is the area of contact between contiguous particles of the particulate phase in a volume. The value of  $dp$  may be determined from intercepts of random lines and internal surfaces (12):

$$dp = \frac{NL(ab)}{NL(ab) + 2NL(aa)} \quad (2)$$

where  $NL(ab)$  = average number of intersection with particulate-matrix interface per unit length of a random test line, and  $NL(aa)$  = that with particle-particle interface. The determination of contiguity or degree of dispersion does not require any assumptions regarding volume fraction, particle size, or particle shape. However, due to the generally discrete nature of the rubbery phase in a typical toughened plastic such as HIPS there exists essentially no contiguity between rubber particles, i.e.,  $dp \sim 1$ .

Fineness. The area of the interface between a particulate phase and the matrix is a function of the particle size, since particle size and specific surface are inversely related. The ultimate

level of dispersion is determined by the fineness which is usually specified by the average particle size and the size distribution function. The data on fineness may, therefore, be obtained from Coulter Counter measurements or image analysis in the case of toughened plastics. The computer programs developed in our lab provide a convenient tool to analyze the particle fineness in terms of particle radius, area, and perimeter.

Spatial Distribution. As suggested by Gurland (2), a quantitative measure of the degree of homogeneity of particle placement in the matrix is the standard deviation of the distribution of particles in small volumes or areas of the mixture:

$$\delta_n = \sqrt{\frac{1}{n} \sum_{i=1}^n (N_{vi} - \bar{N}_v)^2} \quad (3)$$

Where  $N_{vi}$  is the observed number of particles per unit volume in the  $i$ th sample and  $\bar{N}_v$  is the arithmetic mean number of particles in  $n$  samples. (The index  $i$  refers to the  $i$ th sample in a set of  $n$  samples, and not to the particle size class). Maximum homogeneity is characterized by a minimum standard deviation  $\delta_n$ . If, on the other hand, special separating or agglomerating tendencies exist among the particles, the value of  $\delta_n$  will be large.

In practice, the standard deviation values are determined from the observed particle distribution in small areas of metallographically prepared random sections through the multiphase sample. In studying HIPS morphology, thin sections were ultramicrotomed from OsO<sub>4</sub>-stained samples at random locations and orientations. A minimum of 20 transmission electron micrographs were taken from each sample and analyzed. Because the understanding of the link between the particle dispersion state and crazing is important, the use of the rubber particle volume fraction  $V_{Fi}$  per unit volume of the  $i$ th sample, instead of  $N_{vi}$ , as an index seems to be more appropriate. Therefore, Equation 3 may be replaced by:

$$\delta_v = \sqrt{\frac{1}{n} \sum (V_{Fi} - \bar{V}_F)^2} \quad (4)$$

where  $\bar{V}_F$  is the arithmetic mean volume fraction of rubber particles in  $n$  samples. In two dimensions (such as in TEM photographs), a convenient dispersion index (DI) may be defined as:

$$\delta_{AF} = \sqrt{\frac{1}{n} \sum (A_{Fi} - \bar{A}_F)^2} \quad (5)$$

where  $A_{Fi}$  is the area fraction of rubber particles in the  $i$ th micrograph and  $\bar{A}_F$  is the average area fraction in  $n$  micrographs. A small value of  $\delta_{AF}$  will represent a uniform dispersion of rubber particles and is generally a preferred morphological feature. In order to allow for comparison between two materials that may have different average particle sizes and particle volume fractions, the experimental standard deviation  $\delta_{AF}$  may be compared with a theoretical standard deviation  $\delta^*$  of some randomly distributed



arrangement of the particles as, for instance, the binomial and Poisson's distribution. The ratio  $(\delta_{AF} - \delta^*)/\delta^*$  approaches zero as the mixture approaches a random distribution. Since  $\delta^*$  for each HIPS material is not readily available, a useful normalized dispersion index (NDI) may be used instead:

$$NDI = \delta_{AF}/AF \quad (6)$$

A smaller value of NDI would indicate a better spatial distribution of particles.

### Experimental Methods

Materials. The materials used in the present study include both commercial and experimental grades of HIPS. A large number of materials covering a wide range of rubbery phase morphologies were investigated.

Tensile Deformation. An ASTM standard tensile test was conducted to understand the general tensile behavior of each sample. The specimens were stretched up to fracture. The crazing pattern of each fractured specimen was studied following the standard procedure of OsO<sub>4</sub> staining, ultramicrotoming, and TEM investigation. All the samples were subjected to different degrees of plastic deformation because their elongations at break ( $\epsilon_b$ ) are not identical. Therefore, a sensible comparison may not be made between the crazing patterns of two different samples.

To overcome this difficulty, the strategy was varied slightly. The specimens were each pulled up to 15% strain and then allowed to stress relax at this fixed elongation in the Instron universal testing machine. This would permit a more mature crazing degree and reduce the extent of craze recovery upon release of the load. Since each specimen has been elongated to the same 15% strain, the difference in crazing pattern may be ascribed to a variation in structural parameter(s) rather than in testing conditions.

Quantitative Image Analysis. A software package compatible with a HP personal computer (Model 9836) has been developed to assess the morphology of rubber particles in HIPS. The package is capable of analyzing the following information:

1. Average particles area ( $\bar{A}$ ), its standard deviation ( $\delta A$ ), and particle area histogram (particle size distribution based on area);
2. Average particle radius ( $\bar{R}$ ), its standard deviation ( $\delta R$ ), and particle radius histogram; and
3. Average particle area fraction  $\bar{AF}$ , standard deviation ( $\delta AF$ ), and normalized dispersion index (NDI).

Information derived from (1) and (2) would indicate if the particle sizes are uniform or not. A small  $\delta A$  (or more accurately  $\delta A/\bar{A}$ ) and small  $\delta R$  (or  $\delta R/\bar{R}$ ) in general imply a narrower size distribution or more uniform particle sizes. The standard deviation  $\delta AF$  (or  $\delta AF/\bar{AF}$ ) is an index of the "goodness" of particle dispersion or the spatial distribution of particles.

The normalized dispersion index NDI was calculated from the data of the particle area fraction in each TEM micrograph (at least twenty photographs were taken from different sites in a sample). A smaller magnitude of  $(\delta AF/AF)$  implies a more homogeneous dispersion of rubber particles.

Ultramicrotomy and Transmission Electron Microscopy (TEM). Small specimens (5 mm x 3 mm x 3 mm for short ones and 8 mm x 3 mm x 3 mm for long ones) were cut from both tensile deformed and undeformed samples. Short specimens were cut with the length perpendicular and the microtoming direction parallel to the tensile testing direction. Since crazes grow laterally in a direction normal to the principal stress and the areal dimensions of crazes are relatively large, the microtomed layers should contain many craze cross-sections. Contrarily, very few crazes may be seen in the thin sections microtomed from the long specimens where the sectioning direction is parallel to the craze planes. This is because the craze thickness is too small ( $<1 \mu\text{m}$ ) for the knife to traverse through the craze if the craze planes are perfectly parallel to the movement direction of knife.

All the specimens were immersed in  $\text{OsO}_4$  solution (1 gram in 100 ml water) for at least one week to harden the rubber particles (to reduce the microtoming distortion) and to give the necessary electron contrast during TEM investigation. A Phillips EM-300 TEM was used throughout this study.

## Results

Rubbery Phase Morphology and Image Analysis. A typical rubbery phase morphology of HIPS is shown in Figure 1, where the dark membrane in the more or less spherical particles is the osmium-stained polybutadiene (PB) phase with the polystyrene (PS) occlusions being white color while the majority, continuous phase is the PS matrix. The rubbery phase morphology of HIPS has been studied extensively (1). The importance of rubber particle size in controlling the toughness of rubber-modified polymers has been recognized for some time (13-30). For each type of material, there appears to exist an optimum particle size for toughening. The preferred average particle size in HIPS was believed to be  $0.8 \mu\text{m}$  (1). However, our current data indicate that a number average particle diameter of  $1.05 \mu\text{m}$  and  $0.5 \mu\text{m}$  appear to be a preferred size for HIPS and rubber-toughened polypropylene (PP), respectively. The morphology of the rubbery phase in a toughened PP appears to be less complex, as evidenced in Figure 2 where the dark, also osmium-stained, phase is the styrene-butadiene rubber (SBR) particles. No PP occlusions were found in this material since it is a physical blend of SBR and PP.

A typical image analysis output is presented in Figure 3 which not only shows graphically the particle size histogram but also gives the numerical data of average particle dimensions in a photograph; Figure 3a indicating the information on particle radius while Figure 3b on area in two dimensions. Data from analyzing a large number of photographs may also be merged together that would lead to a more reliable statistical result.

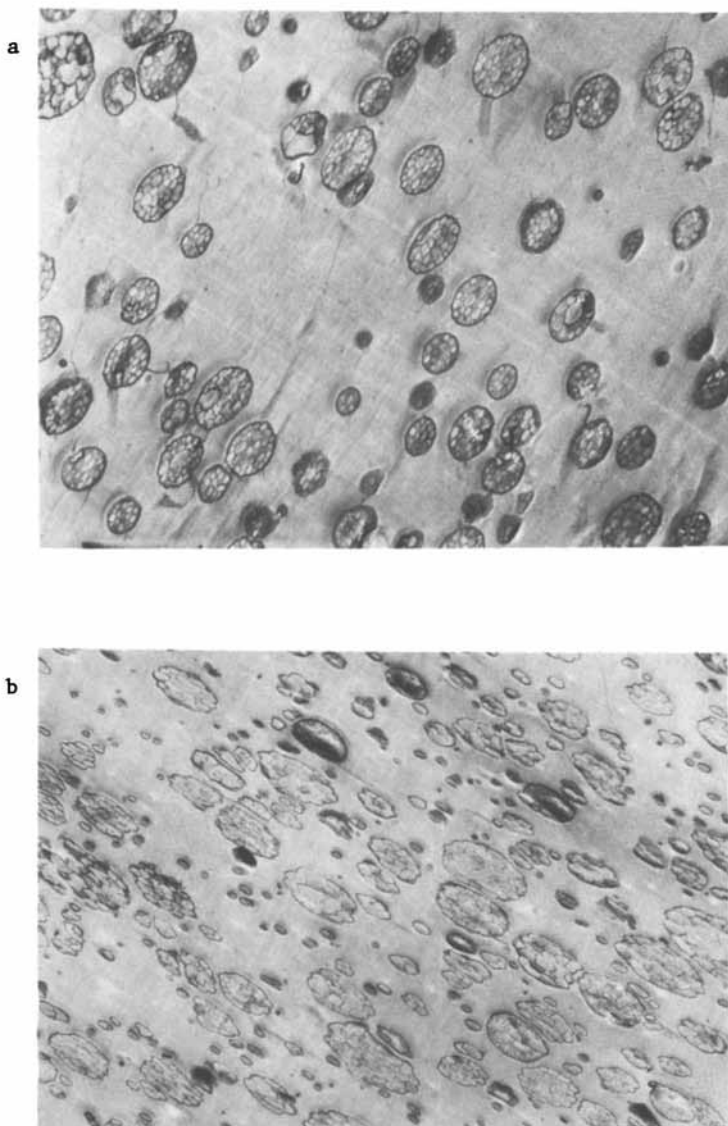


Figure 1. Typical morphology of high impact polystyrene.  
(a) HIPS-N, NDI=.161, poor dispersion. (b) HIPS-P, NDI=.079,  
better dispersion.

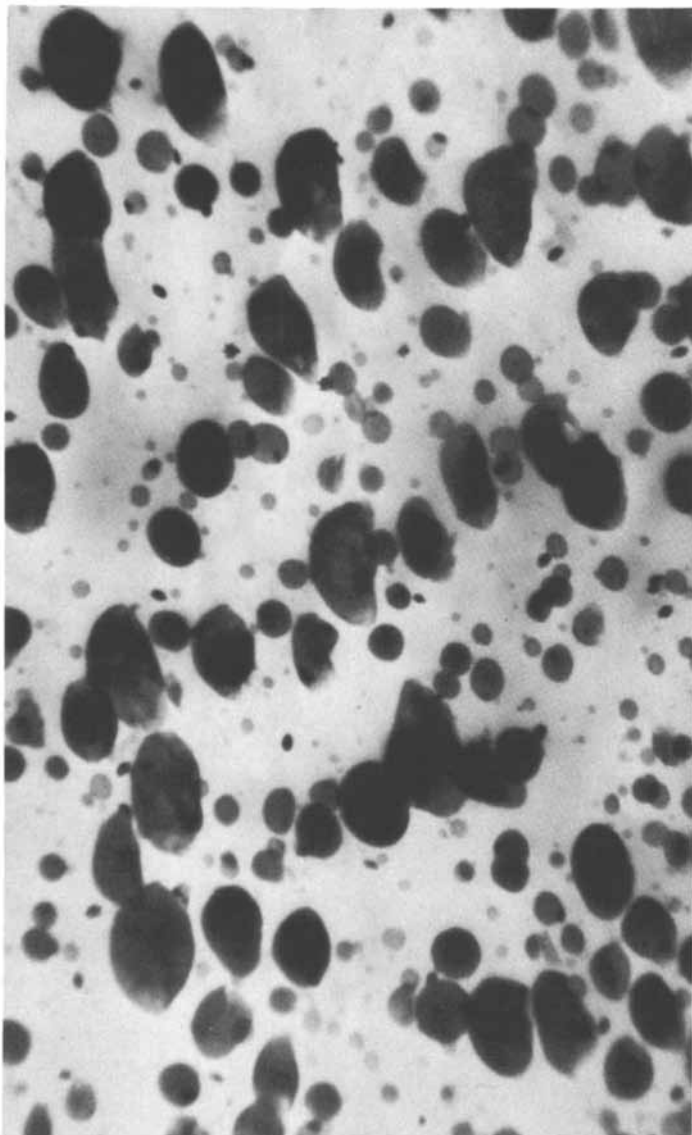


Figure 2. Rubbery phase morphology of a toughened polypropylene.

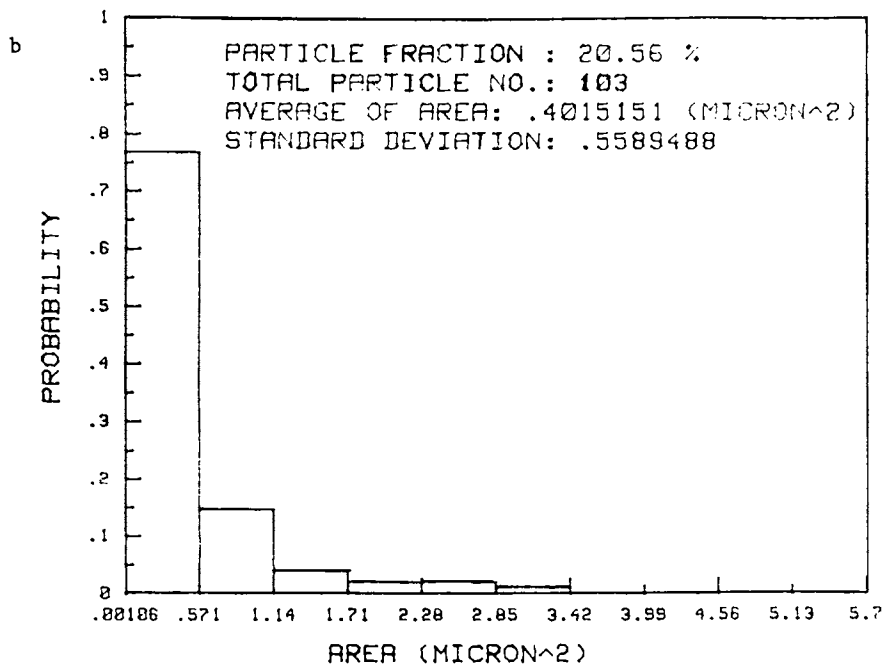
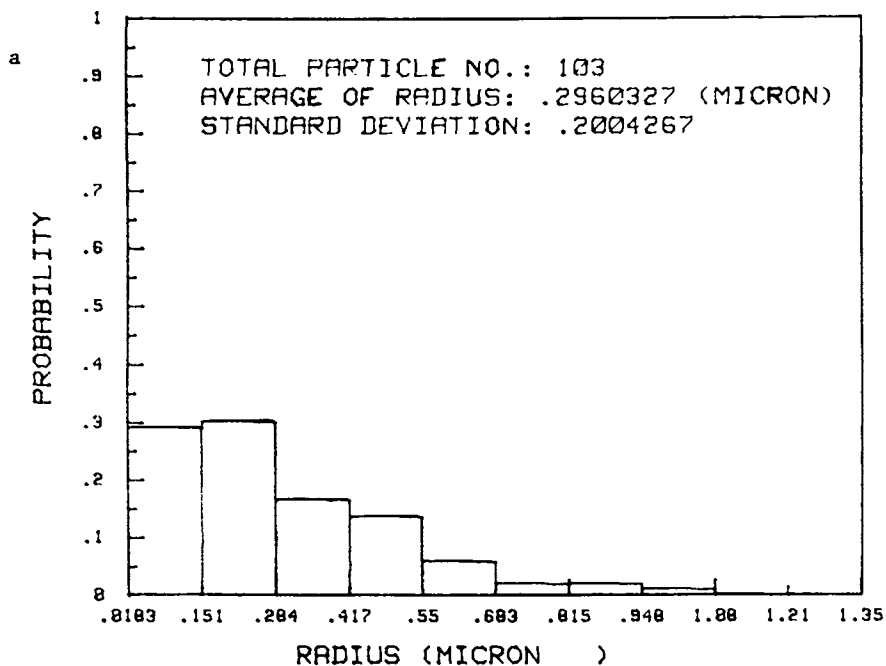


Figure 3. A typical image analysis output. (a) Particle radius distribution. (b) Particle area distribution.

The values of NDI presented are generally a cumulated result of 20 photographs (e.g., in Figure 4).

The total rubber particle area fraction in each randomly selected location can be measured (Figure 3b, e.g.). Physically, if the rubber particles are uniformly or randomly dispersed in a plastic matrix, then the measured particle area fraction would vary very little with the location selected. As a consequence, the dispersion index calculated would be relatively small. If, on the contrary, the particles tend to aggregate or cluster together, then the particle area fraction is expected to be large in the location containing clusters and small in the region containing only isolated particles. A high degree of location dependence of particle area fraction should lead to a relatively large dispersion index. As shown in Figure 1a for HIPS Sample-N, some zones are crowded with closely spaced particles while the others essentially free of particles; the normalized dispersion index (NDI) being 0.161. In contrast, the relatively uniform rubber morphology of Sample-P (Figure 1b) receives an index of 0.079. The sensitivity of the NDI technique has been fairly well demonstrated in several other samples as well. The image analysis data of 15 HIPS samples covering a wide variety of morphologies are summarized in Table 1.

Relationship Between Crazing and Rubbery Phase Morphology. Two distinct types of crazing behavior have been identified. The crazes in HIPS-A (Figure 5) are in general thicker than those in HIPS-B (Figure 6). In both materials the crazes are relatively thick near the craze-rubber interface. The thickness decreases very rapidly in HIPS-B as the craze grows laterally away from the particle surface. In HIPS-A, the craze thins down at a much slower rate. In both materials, crazes in certain areas are thicker than in others. When the interparticle spacings are short the crazes tend to develop to a more mature stage. Nucleation of crazes appears to start earlier in A than in B. Image analysis results (Table 1) indicate that A possesses a smaller average particle size and a better dispersion of particles than B. Despite having a larger Young's modulus, likely due to a smaller volume fraction of rubbery phase, HIPS-A is superior in impact resistance. The latter property seems to be due to a better rubbery phase morphology that is capable of rapidly developing a great number of thick crazes, thus dissipating a great deal of strain energy, before a catastrophic crack intervenes. An extensive morphological and crazing study indicated that a HIPS sample with an NDI greater than .142 seems to lose its ability to quickly accommodate a great crazed volume, resulting in an inferior impact resistance. These observations may be explained in light of the stress concentration requirements for craze initiation and the concept of stress field overlap between nearby particles. A poor dispersion of rubber particles may lead to plastic strain localization, unfavorable for uniform formation of crazes. Stress field overlap between two nearby small particles, which individually may not provide a sufficient volume of stress-enhanced zone (28), may form a favorable craze-initiation condition (13,14).

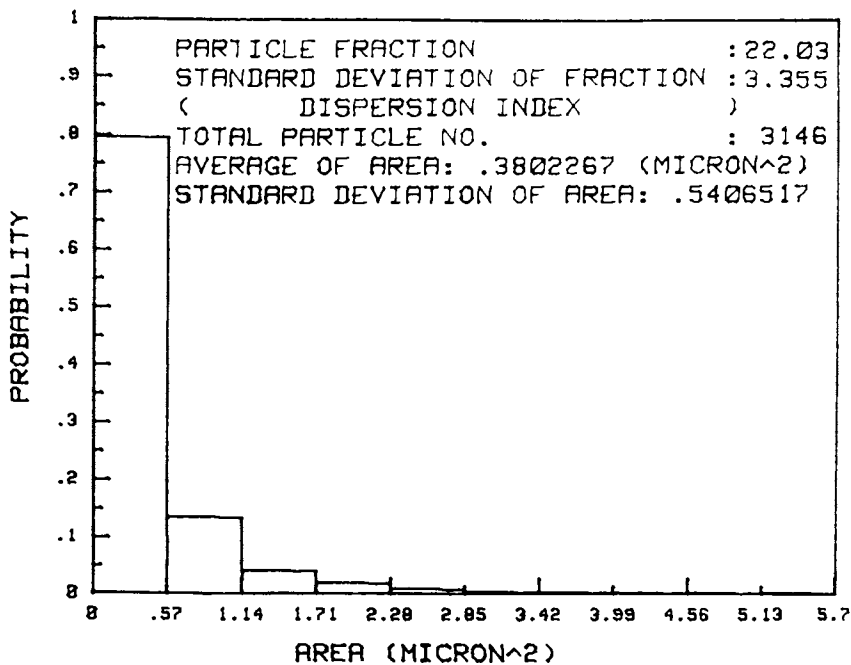
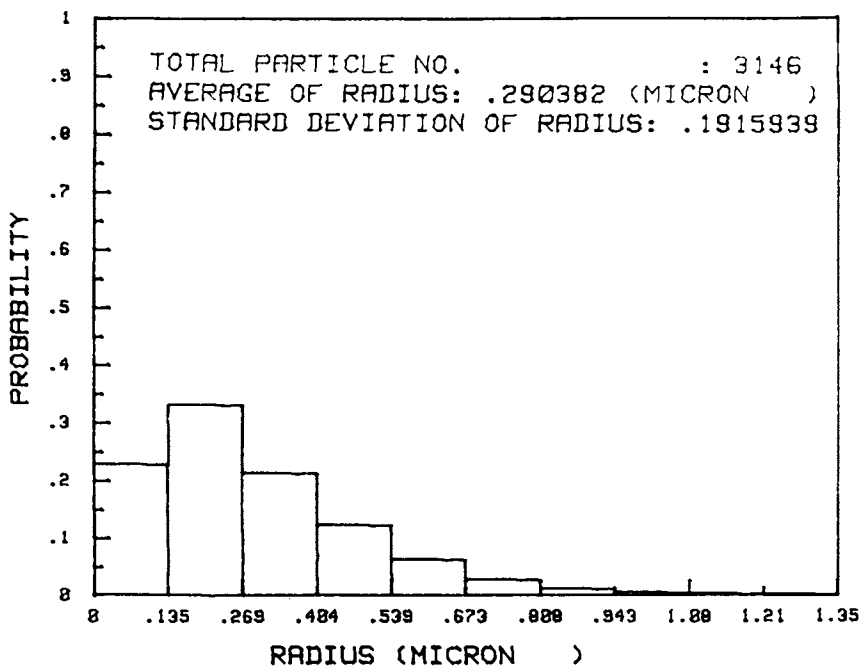


Figure 4. Cumulated image analysis results.

Table I. Partial list of image analysis data

| Sample | A,um <sup>2</sup> | A      | R,um  | R     | Af,%  | NDI  |
|--------|-------------------|--------|-------|-------|-------|------|
| A      | .4133             | .6127  | .3014 | .2018 | 24.46 | .139 |
| B      | .3802             | .5407  | .2904 | .1916 | 22.03 | .152 |
| C      | 1.5000            | 2.6592 | .5311 | .4420 | 35.39 | .195 |
| D      | .8342             | 1.4010 | .4010 | .3236 | 26.98 | .143 |
| E      | .4931             | .6436  | .3410 | .2017 | 23.54 | .151 |
| F      | .5510             | .7844  | .3510 | .2285 | 21.91 | .079 |
| G      | .3802             | .5407  | .2904 | .1916 | 22.03 | .152 |
| H      | .4296             | .6183  | .3118 | .1988 | 23.35 | .106 |
| I      | .5161             | .7217  | .3431 | .2158 | 23.02 | .117 |
| J      | .5304             | .7700  | .3466 | .2207 | 19.96 | .142 |
| K      | 1.1913            | 1.7645 | .4936 | .3683 | 31.34 | .110 |
| L      | .7277             | 1.1635 | .3946 | .2756 | 25.87 | .183 |
| M      | 1.0407            | 1.9200 | .4627 | .3423 | 29.80 | .205 |
| N      | 1.106             | .9534  | .5445 | .2357 | 22.70 | .161 |
| P      | .306              | .6010  | .236  | .2040 | 30.53 | .079 |

The previous observations were drawn on the basis of a large number of HIPS samples including small and large average particle size, narrow and broad particle distribution, and homogeneous and heterogeneous dispersion. One group of samples were simply diluted from the others by physically blending the parent polymers with PS homopolymers. The materials cover many different grades from various sources as well as a series of experimental grades prepared in the laboratory. Both impact loaded and tensile tested samples were investigated. They appear to give consistent results.

### Discussion

A combination of mechanical testing, electron microscopy, and the computer-aided image analysis has been shown to be a powerful tool for the study of structure-property relationships in toughened plastics. Examples were provided to highlight the importance of the spatial dispersion of rubber particles when considering the mechanical behavior of a toughened plastic. Also demonstrated was the feasibility of applying the image analysis technique to assess the state of particle dispersion in a multiphase composites.

The basic mechanism of rubber toughening in HIPS polymers may be summarized as follows. In the early stage of a tensile test the applied load is borne mainly by the matrix and is concentrated at the equators of the rubber particles. The rubber particles act as stress concentration sites and cause the initiation of a large number of crazes which leads to a yield point with the associated stress whitening. These crazes propagate into the matrix in a direction perpendicular to the applied stress, thereby engulfing a number of rubber particles or being retarded/terminated by



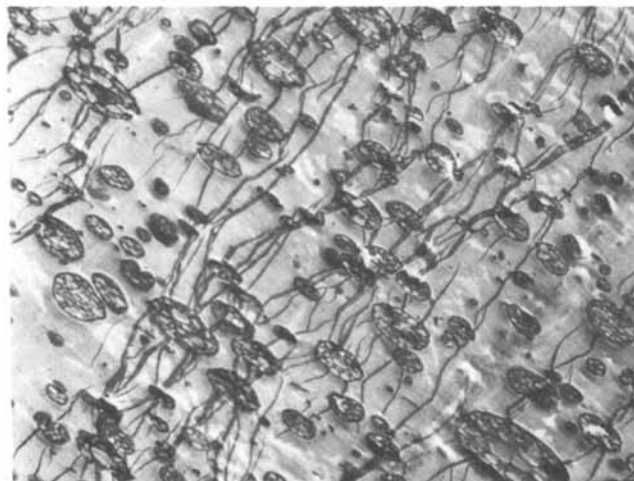


Figure 5. A uniform distribution of thick crazes nucleated from a good dispersion of rubber particles. Large number of crazes.

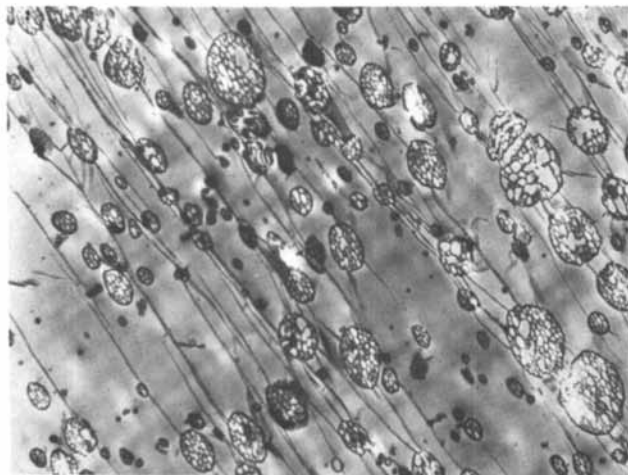


Figure 6. A nonhomogeneous distribution of thin crazes. Smaller number of crazes.

neighboring particles. During craze propagation, the rubber-matrix adhesion is of critical importance in sustaining triaxial tension and delaying the breakdown of crazes to produce cracks. Thus, the function of rubber particles is to initiate crazes and then to stabilize the growing craze which allows additional crazes to be initiated in the surrounding material. In order to toughen the brittle matrix material successfully, a uniform dispersion of tightly bonded rubber particles is required. This can be achieved in the polymerization process by making certain that the rubber phase is adequately grafted to the matrix material.

To ensure high impact resistance the rubber particles must be capable of quickly nucleating and controlling crazes to achieve a maximized crazed volume before a catastrophic crack propagates. This is because impact testing involves very high deformation rate. That HIPS materials like Sample-A tend to easily develop thicker crazes or the thickening process begins at an earlier stage in deformation than Sample-B makes type A capable of quickly accommodating a greater amount of crazed volume. The good dispersion of small rubber particles may be responsible for this efficient use of rubbery phase. Further, the interfacial adhesion seems to be adequate to help the rubber particles sustain the triaxial stress field.

In order to explain the particle dispersion dependence of the mechanical behavior of HIPS, one hypothesis is herein proposed which is based on the stress field overlap concept. Matsuo et al. (34) studied the crazing behavior of polystyrene samples containing two rubber balls of the same diameter with varying separation. The samples were subjected to simple tension, and their crazing behavior was observed. When the two balls were placed close together, the craze-initiation stress was considerably lower than that of single-ball samples. With an increase in the distance between two balls the craze-initiation stress increases at first almost linearly and levels off when  $l/d$  reaches about 1.45, where  $l$  and  $d$  are the center-to-center distance and the diameter of the balls, respectively. When  $l$  is sufficiently small, the crazes are seen to develop extensively at the inner surfaces of the balls and finally bridge with each other. The crazes bridged between the balls expand largely in the plane perpendicular to the applied load.

This study (34) implies that a right dispersion of rubber particles may permit optimum stress field overlap that affords lower craze-initiation stresses and therefore can rapidly dissipate the strain energy in the HIPS. A more homogeneous spatial distribution of rubber particles allow for a uniform development of crazes. Prevention of the strain localization phenomenon to avoid the detrimental situation, where crazes prefer to develop in certain areas and quickly lead to a catastrophic crack, could result in a larger total volume of crazed material. Further, Donald and Kramer (22) discovered no crazes nucleating from an isolated rubber particle with diameter smaller than 1  $\mu\text{m}$  because of an insufficient size of stress-enhanced zone. Since Sample-A has a small average particle size it should contain a large number of small rubber particles. Two small rubber

particles with a separation small enough to cause stress field superposition may be capable of initiating crazes. For instance, this advantageous arrangement may be destroyed due to the dilution effect of adding PS homopolymers to HIPS.

### Conclusions

The present study leads to the following conclusions:

- (1) A combination of electron microscopy, computerized image analysis, and mechanical testing provides a powerful tool for studying morphology-property relationships in toughened plastics.
- (2) A statistical framework has been established for describing the spatial dispersion of second phase particles in a continuous matrix. Based on this scheme a computerized image analysis method has been developed for characterizing the morphology of toughened plastics.
- (3) The proposed normalized dispersion index (NDI) has been shown to be a sensitive measure of the "goodness" of particle dispersion in space. An NDI value of .142 was shown to be a critical level of dispersion that demarcates two totally different types of crazing behavior in HIPS.
- (4) A good dispersion of rubber particles appears to favor the nucleation and growth of a large number of thick crazes uniformly distributed in the polystyrene matrix. This is believed to be an efficient source of energy absorption for the material under mechanical loading. The concepts of stress field overlap and critical volume of stress concentration zone for craze initiation were introduced to explain the observed mechanical behavior of HIPS.

### Acknowledgments

Financial support for this work is provided by the Plastics Div., American Hoechst Corp. We are grateful for this support.

### Literature Cited

1. Bucknall, C. B. "Toughened Plastics", Appl. Sci. Pub., London, 1977.
2. Newman, S. "Rubber Modification of Plastics", in "Polymer Blends". 1980 Ch. 13. Vol. 2; Paul, D. R., Ed.; Academic Press.
3. Kinlock, A. J. and Young, R. J. Fracture Behavior of Polymers, Appl. Sci. Pub., London, 1983.
4. Bucknall, C. B. in Polymer Blends, Vol. 2; Paul, D. R., et al, Ed.; Academic Press, 1978.
5. Kato, K. J. Electron Microsc. 1965, 14, 220.
6. Kato, K. Polym. Eng. Sci. 1967, 7, 38.
7. Kato, K. Koll. Z. Z. Polym. 1967, 220, 24.
8. Stein, R. S. in "New Methods of Polymer Characterization", Ke, B., Ed.; Interscience, New York, 1964, p. 155.
9. Moritani, M.; Inoue, T.; Motegi, M.; Kawai, H. and Kato, K. in "Colloidal and Morphological Behavior of Block and Graft

- Copolymers"; Molau, G. E., Ed.; Plenum Press, New York, 1971, p. 33.
10. Visconti, S. and Marchessault, R. H. Macromol. 1974, Vol. 7 p. 913.
  11. James, D. E. Polym. Eng. Sci. 1968, 8, 241.
  12. Gurland, J. In Quantitative Microscopy; DeHoff, R. T. and Rhines, F. N.; Eds.; McGraw-Hill, 1968, p. 279.
  13. Wang, T. T., Matsuo, M. and Kwei, T. K. Am. Chem. Soc., Div. Polym. Chem. Polym. Prepr. 12 (1971) 671.
  14. Wang, T. T., Matsuo, M. and Kwei, T. K. J. Appl. Phys., 1971, 42, 4188.
  15. Rosen, S. L. Polym. Eng. Sci., 1967, 7, 115.
  16. Bender, B. W., J. Appl. Polym. Sci., 1965, 9, 2887.
  17. Matsuo, M. Polymer, 1966, 7, 421.
  18. Bucknall, C. B., Clayton, D. and Keast, W. F. J. Mater. Sci. 1972, 7, 1443.
  19. Grancio, M. R. Polym. Eng. Sci., 1972, 12, 213.
  20. Dillon, M. and Bevis, M. Plast. Rubber Process. Applications, 1982, 2, 225.
  21. Dillon, M. and Bevis, M. J. Mater. Sci., 1982, 17, 1903.
  22. Donald, A. M. and Kramer, E. J. J. Appl. Polym. Sci., 1982, 27, 3729.
  23. Silberberg, J. and Han, C. D. J. Appl. Polym. Sci., 1978, 22, 599.
  24. Ricco, T., Pavan, A. and F. Danusso. Polym. Eng. Sci., 1978, 19, 774.
  25. Durst, R. R., Griffith, R. M., Urbanic, A. J. and van Essen, W. I. ACS Adv. Chem. Ser., 1976, 154, 239.
  26. Parsons, C. F. and Such, E. L. ACS Adv. Chem. Series, 1971, 99, 340.
  27. Purcell, T. O. Am. Chem. Soc. Div. Polym. Chem. Polym. Prepr., 1972, 13, 699.
  28. Donald, A. M. and Kramer, E. J. J. Mater. Sci., 1982, 13, 1765.
  29. Michler, G. H. Plaste Kaut. 1979, 12, 497 and 680.
  30. Jang, B. Z., Uhlmann, D. R. and Vander Sande, J. B. Polym. Eng. Sci., 1985, 25, 643.
  31. Bucknall, C. B. J. Materials, 1969, 4, 214.
  32. Goodier, J. N., Trans. ASME. 1933, 55, 39.
  33. Matsuo, M., Wang, T. T. and Kwei, T. K. J. Polym. Sci. A-2, 1972, 10, 1085.

RECEIVED July 9, 1986

## Chapter 3

# Uses and Abuses of Photon Correlation Spectroscopy in Particle Sizing

B. B. Weiner and W. W. Tscharnuter

Brookhaven Instruments Corporation, Ronkonkoma, NY 11779

Examples of particle sizing using photon correlation spectroscopy are presented to demonstrate the straight forward uses and difficulties with the technique. Examples include NBS SRM 1691, a crosslinked polystyrene-divinylbenzene, a fractionated sample of polyvinylchloride, "dusty" samples of reference latex, a bimodal mixture of reference latices, a bimodal mixture of rubber particles, and a 2:1 aggregate.

Correlator hardware and linearly-spaced sample time limitations are discussed. Data transformation from an intensity-weighted to a mass-weighted size distribution is demonstrated. The artificial width of broad distributions is discussed. The use of multi-angle measurements is considered, and the effect of baseline error is shown using computer simulated data.

During the past two decades the technique of quasi-elastic light scattering (QELS) has been used extensively to characterize colloidal-sized particles in the size range from a few nanometers to a few microns. In this range the particles exhibit significant random motion from collisions with the surrounding liquid medium. The random motion gives rise to fluctuations in the scattered light intensity which is usually analyzed with a digital correlator. As a result the name photon correlation spectroscopy (PCS) is often used.

Several monographs that describe the theory and experimental requirements for good measurements are available (1-5). Hundreds of literature citations are included in these sources. Every year conferences are devoted to the subject of QELS and PCS. Although the technique is relatively new to particle size analysts, most of the advantages and disadvantages are well-known.

Advantages include speed, accuracy, versatility, and a large potential size range. Disadvantages include limited shape information, intensity-weighted results, and difficult data analysis for broad distributions.

The purpose of this article is to demonstrate some of the advantages and disadvantages of PCS in particle sizing by presenting some typical examples of uses and abuses of the technique.

0097-6156/87/0332-0048\$06.00/0

© 1987 American Chemical Society

### Experimental

The measurements described here were made with either a Brookhaven Instruments model BI-90 particle sizer (90deg, fixed angle) or a model BI-200SM multiangle laser light scattering goniometer attached to a model BI-2030 digital correlator. Both instruments were operated in multiple sample time mode. In this mode the equivalent of several thousand linearly-spaced correlator channels is available, enabling the acquisition of a correlation function more fully representative of a broad size distribution. A 5mW, vertically polarized, HeNe laser was used in both instruments. Further details are given elsewhere (6-7).

Typical sample preparation consisted of diluting a few drops of concentrated dispersion in about 20cc of twice filtered (0.22 micron) diluent or until the diluted sample appeared slightly turbid to clear. Following sonication for about 1 minute, preliminary measurements were made to estimate the intensity of scattered light, average size, and polydispersity. For large average sizes or strong scatterers successive dilutions of about 30% were made until no concentration dependence was found in the final results.

All dilution bottles, pipette tips, and sample cells were rinsed repeatedly with twice filtered diluent prior to use.

Measurement time varied from under 1 minute for narrow distributions to several minutes for broad distributions. Data analysis times varied from seconds for narrow distributions to a few minutes for broad distributions. All measurements were analyzed using the technique of cumulants (8) and, for broad distributions, a modified version of exponential sampling theory (EST) (9).

### Results

Monodisperse Spheres. The most straight forward use of PCS is sizing monodisperse, rigid spheres in the submicron range. Monodisperse latex particles (SRM 1691, NBS, Gaithersburg, Maryland) were measured at 45, 90 and 135deg scattering angles. The NBS value is 269 +/- 7nm. The uncertainty includes random and all identifiable forms of systematic error. Our results are 273 +/- 5nm. The uncertainty includes random and systematic variations observed between different instruments and different days. Clearly the PCS results are very accurate and precise. No calibration was necessary. Additionally, sample preparation, measurement time, and data analysis were much faster and simpler than the analogous steps involved when using an electron microscope.

In 1972 Lee, Tscharnuter and Chu (10) showed that labelled 91nm latex (LS-1132-B, Dow Chemical) was 85 +/- 2nm using PCS and 2 different electron microscopes. Many of the so-called reference particles exhibit even greater discrepancies between labelled and measured values. Many are not even narrowly distributed as evidenced by polydispersities (defined in PCS as relative variances of the intensity-weighted diffusion coefficient distribution) significantly larger than the typical minimums (approx. 0.02) found on the few truly narrow standards. As a result, a properly designed and working PCS instrument gives results which are typically more accurate than those on the labels of many reference standards.

**Swollen Particles.** Another use for PCS is for sizing in situations where sample preparation, such as drying, would destroy the particle integrity. Table I shows the effect of sulfonation on particle size for 3 different formulations of monodisperse, polystyrene-divinylbenzene (PS-DVB) under consideration for use as packing in chromatography columns (11). Columns 2 & 3 show, respectively, the size before and after sulfonation. Upon dilution the same results were obtained indicating no interparticle effects were important at the concentrations used. PS-DVB is a rigid, hydrophobic particle. After sulfonation it is hydrophilic and would dissolve except for the DVB crosslinks. Instead it swells. Columns 4 & 5 show, respectively, the percent increase as measured and as predicted from analogous ion-exchange resins several microns in diameter. The values show clearly that extrapolation of results on swelling should be done with caution if at all. These results could not be obtained with an EM since sample preparation and measurement conditions would completely change the size of these swollen particles.

TABLE I: Swelling of Sulfonated PS-DVB using PCS

| Formulation | Size          |                 | Percent Increase |           |
|-------------|---------------|-----------------|------------------|-----------|
|             | Un sulfonated | Size Sulfonated | Measured         | Predicted |
| 6% DVB      | 74nm          | 185nm           | 150%             | 40%       |
| 10%         | 58            | 103             | 78               | 30        |
| 15%         | 73            | 124             | 70               | 20        |

PCS measurements yield the hydrodynamic size. This size includes any coating, solvation layer, surface attached molecules (surfactants), entrapped solvent (swelling), or any other matter which moves with the particle. This size may be quite different than the "dry" diameter.

**Fractionated Distributions.** It will become apparent that the unambiguous determination of broad size distributions, be they multimodal or unimodal, presents the most problems for PCS. Therefore, a combination of PCS and a technique which fractionates a broad distribution has the potential for yielding the most information with the least ambiguity. Sedimentation field-flow fractionation (SFFF) is one such technique (12).

In SFFF particles flowing in a narrow channel are subjected to a gravitational field perpendicular to the flow. The larger particles are pushed closer to the channel wall than the smaller ones. The velocity profile in a narrow channel is such that the larger particles flow more slowly than the smaller ones. Thus, small particles elute first.

In the complete theory the measured elution volume is shown to be a function of the product of the particle mass and density difference between particle and carrier liquid. The particle density must be accurately known before a mass and diameter can be calculated. The density of a colloidal-sized particle is not always well-known or conveniently measured. For example, significant adsorption of surfactant or entrapment of carrier within the particle can lead

to density differences between the bulk material and the suspended particles.

In contrast, a PCS measurement on a narrowly distributed sample yields a diffusion coefficient which does not depend on any particle property other than size. A combination of the techniques can, in principle, be used to fractionate a broad sample and determine both particle size and density.

Table II shows the results of combining SFFF and PCS measurements on a broad unimodal distribution of PVC in water. The manufacturer of the PVC (The BFGoodrich Company) reports the density as 1.4 g/cm<sup>3</sup>. The results reported here were obtained in Prof. K. D. Caldwell's laboratory at the University of Utah. Six fractions were collected near the peak of a broad fractogram obtained in the SFFF experiment. Each fraction was measured using the BI-90. Given the reported density, the average diameter of each fraction was calculated using SFFF theory. These values are given in column 2. Column 3 shows the average diameter of each fraction as measured by PCS, and column 4 shows the calculated density using the measured PCS diameter and the raw SFFF result for each fraction.

**TABLE II:** Size and Density Determination of a Polydisperse PVC Sample using PCS and SFFF

| Fraction | Ave. Dia.<br>SFFF | Ave. Dia.<br>PCS | Density<br>SFFF/PCS   |
|----------|-------------------|------------------|-----------------------|
| 1        | 212nm             | 216nm            | 1.38g/cm <sup>3</sup> |
| 2        | 225               | 225              | 1.40                  |
| 3        | 239               | 241              | 1.39                  |
| 4        | 250               | 257              | 1.37                  |
| 5        | 261               | 267              | 1.37                  |
| 6        | 271               | 276              | 1.38                  |

The results are in remarkable agreement. Both SFFF and PCS are first principle techniques, and neither needs calibration. The density of PVC is expected to be similar to the bulk value of 1.4 g/cm<sup>3</sup> since, under the conditions of the measurement, PVC remains a rigid sphere with negligible increase in size due to adsorbed surface molecules. The average density found by combining the SFFF and PCS measurements is 1.38 +/- 0.01 g/cm<sup>3</sup>.

The potential of combining these two techniques for analyzing samples with density as well as size distribution is quite clear.

**"Dusty" Samples.** Dust is a problem in light scattering, especially in a highly polar liquid like water. Dust is a name given to all unwanted scatterers. This includes any outliers in the size distribution which are not considered to be part of the main distribution. Filtering of liquids significantly reduces the problem; however, some dust usually remains unless extreme precautions are taken with the sample cell, transfer pipette or syringe, and any dilution bottles. Even then the sample itself may have dust. Such precautions begin to limit some of the advantages, like speed and simplicity, PCS has over other techniques. Finally, if PCS is ever to be used on-line,



then the problem of dust (including bubbles) will have to be overcome.

At the present time, in most PCS instruments, dust is handled in two ways: an experimentally measured, delayed baseline and/or a dust term in the calculation. The latter method usually assumes dust to be infinitely large with a zero diffusion coefficient. This leads to a constant, which is another way of saying a baseline. The problem with adjusting the baseline is that even a very small baseline uncertainty can lead to rather large errors in the distribution parameters as shown in the Appendix. A better procedure would be to reject dust before it contributed to the correlation function.

An electronic dust filter has been implemented in the BI-90 as follows. The total experiment duration is divided into cycles of approximately 100msec. An average and standard deviation of the count rate is established based upon many short measurements of the intensity prior to initiating the buildup of a correlation function. This is all automatic and takes only a few seconds. Then, during each cycle, the count rate is compared to the average. If it is larger than the average plus a user-selectable integer times the measured standard deviation, the data for that cycle are rejected. The fraction of rejected cycles is recorded.

If the integer is high (rejected cycles zero), all the scattered light contributes to the results. Any dust will increase the average diameter and broaden the distribution. As the integer is decreased (rejected cycles increased), a trend toward decreasing average diameter and narrower distributions should be observed. If real outliers exist, then a plateau should be apparent in plots of average size and distribution width versus fraction of cycles rejected. If a distribution is continuous, then no plateau is observed, and the possibility exists for distorting the results by clipping the upper tail

Figure 1 is a plot of the average PCS diameter versus percent rejected cycles for a labelled 87nm latex in once-filtered (0.22 micron) and unfiltered, local tap water. The average diameter continuously decreases with increasing rejection for the unfiltered case, and its deviation from the true value is quite significant. No plateau is observed. This suggests that the dust in this case is broadly and continuously distributed. A plateau is observed in the once-filtered case. The average diameter is 89nm from 1 to 7 percent rejection.

More dramatic evidence is shown in Figure 2 where the relative variance of the diffusion coefficient distribution is plotted against the percent rejected cycles. The unfiltered case starts out very broad and approaches the correct value after more than 40% of the cycles are rejected. However, no plateau is evident, and without the once-filtered results to guide the interpretation, it would not be clear where the correct answer occurs. The once-filtered case shows a dramatic decrease in the relative variance after approximately 3 percent of the cycles are rejected.

This example shows the potential for using PCS under less than ideal circumstances.

### **Broad Distributions**

Broad distributions present the greatest challenge. Among the several reasons for this are:

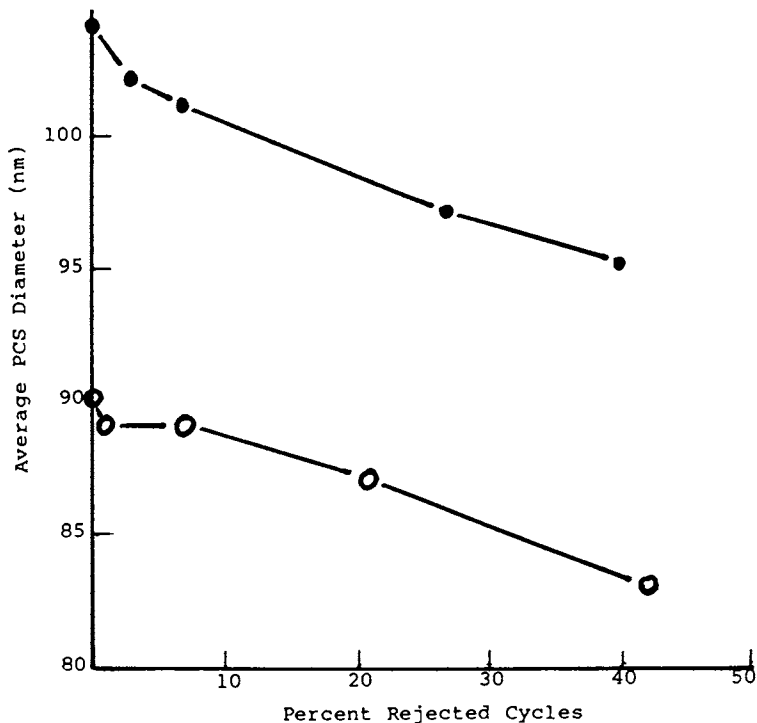


Figure 1. Average diameter versus percent rejected cycles due to dust. Nominal 87nm latex in unfiltered, local tap water (solid circles) and once-filtered (0.22 micron) water (open circles).

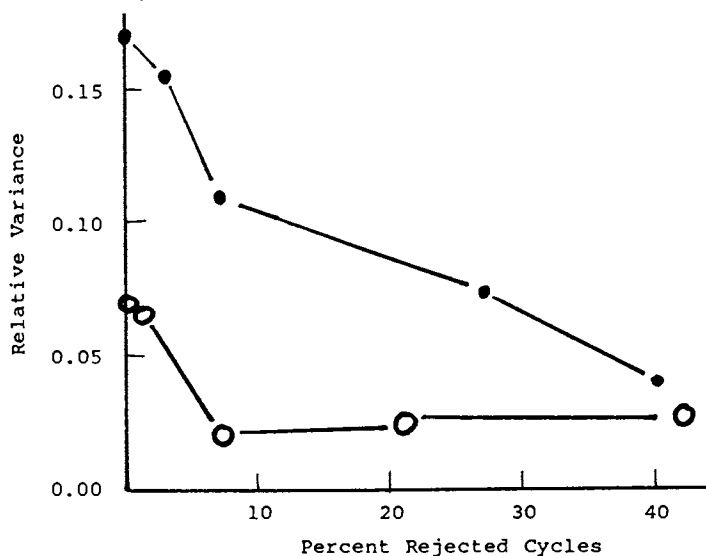


Figure 2. Relative variance versus percent rejected cycles due to dust. Nominal 87nm latex in unfiltered, local tap water (solid circles) and once-filtered (0.22 micron) water (open circles).

1. The scattered intensity is a strong function of size and, for larger particles, scattering angle. The measured signal may be dominated by the strong scatterers, and it may be difficult to detect the small particles in a distribution unless they are present in overwhelming concentration.
2. It is difficult to set a limited number of linearly-spaced correlator channels to cover the range of a broad distribution. Compromises often result in artifacts.
3. Very small errors in the baseline of a correlation function result in large anomalous behavior in the width of the distribution. (See the Appendix.)
4. With a broad range of sizes it is sometimes difficult for a 4-bit correlator to accommodate the range of photopulses per sample time encountered. Dilution or prescaling or reducing the laser's intensity only increases the experiment duration.
5. The deconvolution problem is exceptionally difficult.
6. Random noise on the correlation function broadens the calculated distribution, limiting resolution.

Nevertheless, PCS can yield valuable information on broad size distributions. Three examples are given which demonstrate the type of information available and the limitations.

Accuracy. Figure 3 shows the results obtained from a mixture of nominal 87nm (Duke Scientific) and 269nm (SRM 1691) latexes. Peaks occur at 84nm and 269nm. Prior to mixing the sizes were measured as 85nm and 275nm, respectively. Although peak positions are very accurate, the widths are artificially broad due to the noise on the correlation function.

These very accurate peaks were obtained in about 16 minutes. The uncertainty decreases with increasing experiment duration. Roughly, one can expect that the relative error decreases with the square root of the experiment duration. It takes several hours for the measured distribution widths to approach the correct values (13).

For strong scatterers an average diameter can be obtained within +/- 5% every 10 or 20 seconds. To get this precision with the polydispersity takes 2 or 3 minutes. To distinguish between a broad unimodal and a bimodal distribution may take several minutes. Finally, as already mentioned, it may take hours to obtain representative widths.

Figure 4 shows the results obtained from a rubber sample dispersed in 95:5 water/glycerin. The peaks occur at 270nm and 1010nm. Peaks of 300nm and 1150nm were obtained on a disc centrifuge, where the density of these particles, in suspension, affects the accuracy of these centrifuge results. Of interest here is the ability of PCS to obtain a good value near the high end of its size range in the presence of a second peak.

There are two aspects of this example which merit further discussion. One concerns correlator hardware, and the other concerns data transformation.

Correlator Hardware Limitation. The equivalent, average number of photopulses per sample time in this experiment was 16. The typical 4-bit circuitry found in many correlators would suffer overflow

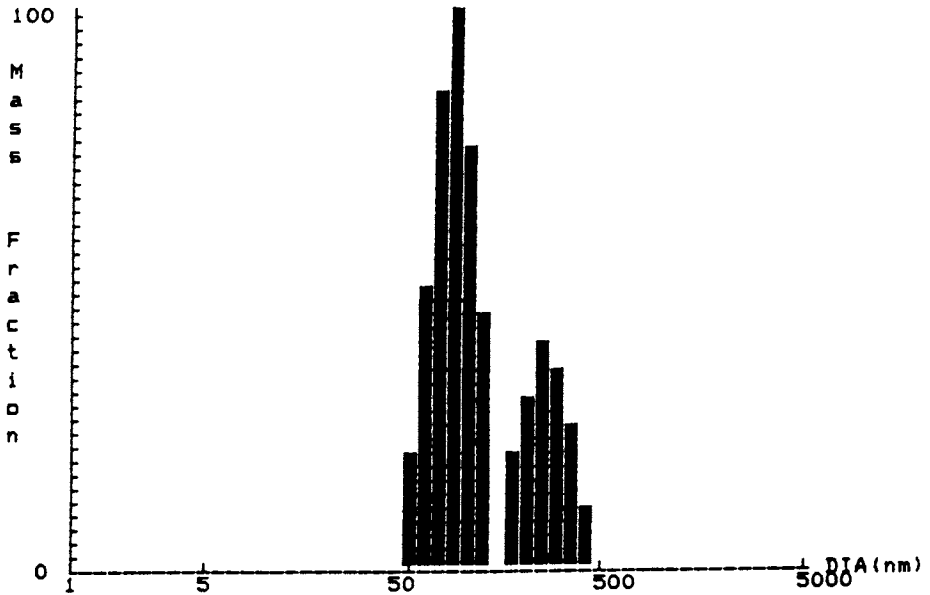


Figure 3. Mixture of 85nm and 275nm latexes. Peaks occur at 84nm and 269nm.

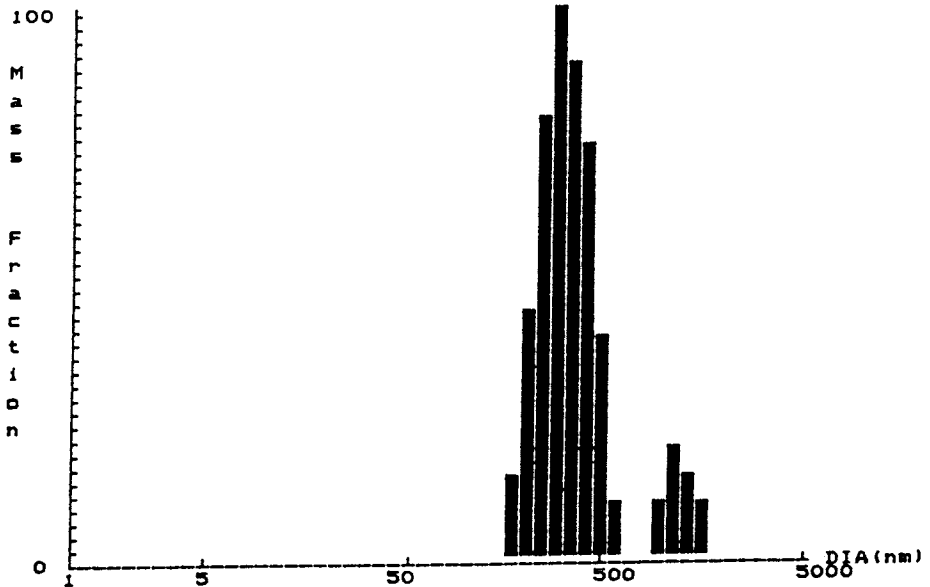


Figure 4. Size distribution of rubber blend. Peaks at 270nm and 1010nm agree with results from a disc centrifuge. After applying Mie scattering corrections the calculated mass ratio of the peaks agrees well with the blend as mixed by weight.

problems at this level. Prescaling would be necessary. However, this increases the data collection time. An 8-bit design (255 counts/sample time) could easily handle this case. However, at lower scattering angles, say 15 deg, where the sample time for a 1 micron particle using a 128 channel, linearly-spaced correlator is several milliseconds, the average number of photopulses per sample time can quickly exceed 255. The correlator in the BI-90 operates, entirely in hardware, up to the equivalent of 16bits per sample time, and would be especially suitable for use with low angle measurements.

Data Transformation. The raw size distribution obtained in PCS is intensity weighted. Most particle sizing results are either mass, area, or number weighted. Therefore, to compare results, the PCS measurements would have to be transformed. If the ratio of the concentrations in each peak is desired, then a transformation is also necessary. The intensity of light scattered by a sphere is given by

$$I = Kcd^3P$$

where K is an optical constant, c is the mass concentration, d is the diameter, and P is the scattering form factor calculated from either Mie theory or an approximation like Rayleigh-Gans-Debye theory (14).

Mass-weighted data are obtained by dividing the intensity-weighted results by  $d^3P$ , and number-weighted data are obtained by dividing the mass-weighted results by  $d^3$ .

P approaches 1 as particle size or scattering angle decreases. For sizes below about 300nm, P can be estimated reasonably well using RGD theory. The refractive index of the particle is not required in RGD theory. For larger particles P must be calculated from Mie theory, and it is an oscillating function of size and angle. Furthermore, in this size range it depends on the ratio of the refractive index of the particle and the suspension medium. The magnitude of P varies, in typical cases, over 4 orders of magnitude. This great variation combined with the d-cubed variation makes the transformed data subject to great error. It is not uncommon for an artifact at the low size end of the intensity-weighted distribution to become much more significant in the mass- or number-weighted distribution because of the division by  $d^3$  or  $d^6$ , respectively. Likewise, a spurious size in the intensity-weighted distribution, which happens to fall at a minimum in P, will be blown up into a significant contribution in the mass- and number-weighted distributions.

The results in Figure 4 yield a 50:50 ratio by mass when a smoothed approximation of P is used where the smoothing is performed in an attempt to remove particle refractive index as a necessary parameter. However, a better calculation, using the correct refractive index (1.545) of this particular rubber and the full Mie theory for spheres, yields a mass concentration ratio of 69:31 for the 1010nm:270nm sizes which is quite close to the 70:30 ratio of this blended sample.

Not all results agree this well. Before corrections are applied it is important to verify that peak positions and intensity-weighted ratios are repeatable. Also note that a particle property, index of refraction, was needed to transform an intensity-weighted size distribution into a mass- or number-weighted one. For monodisperse and narrow distributions this is not the case. For distributions where

the significant features are below about 300nm or for measurements at small angles, this is not the case either. But for broad distributions, where significant features are above about 300nm, and where the highest accuracy is sought, then the particle index of refraction must be known.

Figure 5 shows the results obtained from a nominal 65nm latex dispersion (Polyscience). Four separate samples were run, each showing bimodality with peaks at 45 +/- 1nm and 93 +/- 5nm, suggesting the formation of doublets. The discrepancy between the nominal and measured values, as well as the lack of monodispersity, is quite common for several other samples and sizes from the same source.

The "doublet" peak contributes about 33% by intensity, 6% by weight, and only 0.7% by number. Here RGD theory was used to transform the intensity-weighted results. Only a fraction of a percent formed aggregates, yet these were quite easily detected by light scattering. The opposite case, where a small number of smaller particles is in the presence of larger particles, is all but impossible.

### Summary

Abuses of PCS usually occur from attempts to ignore, either experimentally or theoretically, what has been learned in the past 20 years. A few of the more important considerations are reviewed here with respect to their impact on broad size distributions.

Deconvolution Algorithms. The correlation function for broad distributions is a sum of single exponentials. This ill-conditioned mathematical problem is not subject to the usual criteria for goodness-of-fit. Size resolution is ultimately limited by the noise on the measured correlation function, and measurements for several hours (13) are required to obtain accurate widths. Peaks closer than about 2:1 are unlikely to be resolved unless a-priori assumptions are invoked to constrain the possible solutions. Such constraints should be stated explicitly; otherwise, the results are misleading. Constraints that work well with one type of distribution and one set of data often fail with others. Thus, artifacts including nonexistent bi-, tri-, and quadramodals abound. Many particle size distributions are inherently nonsmooth, and attempts to smooth the data prior to deconvolution have not been particularly successful.

Given the difficulties one should view with suspicion any deconvolution features that are not repeatable, that are functions of a particular constraint, and those that occur at the extremes of the range. Often these are artifacts. A physical explanation for multiple peaks should be sought. Initial aggregation should lead to doublets (Figure 5) and triplets, and fusion should lead to a continuum. Invoking aggregation to explain widely spaced peaks is not sufficient.

Several deconvolution algorithms are now available including EST, NNLS, and CONTIN (3).

Number of Correlator Channels. Proper use of the above algorithms requires a correlation function which spans the time range over which large and small particles contribute. Sample time is usually set such that the last data channels (largest size) are within a few

tenths of a percent of the baseline. With linearly-spaced correlator channels the same sample time must also be used for all other particle sizes. This constraint leads to the following estimate of the required number,  $M$ , of linearly-spaced correlator channels,

$$M = 7mR$$

where  $R$  is the ratio of the largest to the smallest size,  $m$  is the channel number ( $m = 1, 2, 3, \dots, M$ ) at which the exponential corresponding to the smallest size decays to  $1/e$ , and the number 7 assumes the last data channel is within 0.1% of the baseline.

For broad distributions this equation predicts that at least several hundred linearly-spaced channels are required. Nonlinear sample time spacing is superior. Both the fixed-angle instrument and the correlator used in this work operate with up to the equivalent of several thousand linearly-spaced data channels.

Multiangle Measurements. More information is potentially available from multiangle measurements. Zero-angle extrapolated data are more amenable to proper data transformation. Separation of translational and rotational motion of highly acicular particles is possible. Verification of peaks at more than one angle lends credence to their existence. Simultaneous deconvolution of angular data may provide a useful constraint.

Angular measurements, however, are more difficult and may give rise to their own special types of artifacts. Alignment is critical, and periodic verification is necessary. Scattering by dust is particularly severe at low angles. As little as 0.5% flare can artificially broaden distributions significantly, and a few percent can lead to artificial bimodals (15). Back reflections may yield peaks corresponding to scattering at  $180^\circ$ .

Multiangle instruments are checked by verifying that  $I \sin \theta$  for a pure liquid is constant. Figure 6 shows deviations of  $I \sin \theta$  using toluene in the multiangle instrument used in this work. All the errors are less than a half percent.

Data Transformations. The deconvolution of correlation functions yields the intensity-weighted diffusion coefficient distribution. Transformation to a size distribution requires division by the diameter raised to a high power and by an angular dependent function which oscillates over several orders of magnitude for particles larger than a half a micron. Given the artifacts from the primary deconvolution, extreme caution is advised when transforming data.

### Conclusions

PCS is a valuable technique for particle sizing in the submicron range. Results are least ambiguous for narrow distributions. It may be used with broad distributions provided its limitations are understood. Compared to other techniques in this size range it is often very useful even with broad distributions.

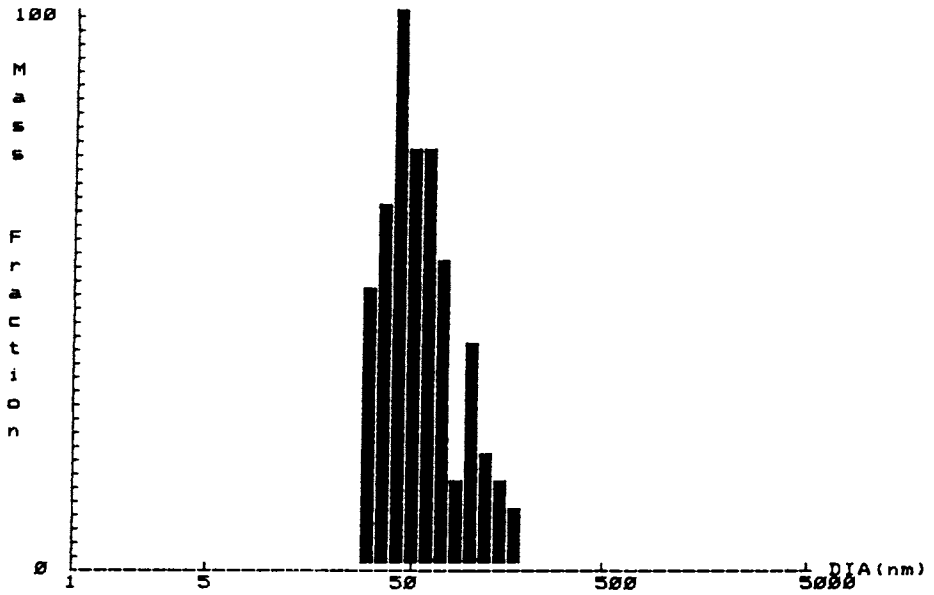


Figure 5. Size distribution of aggregated latex sample. The 2:1 size ratio suggests the formation of doublets.

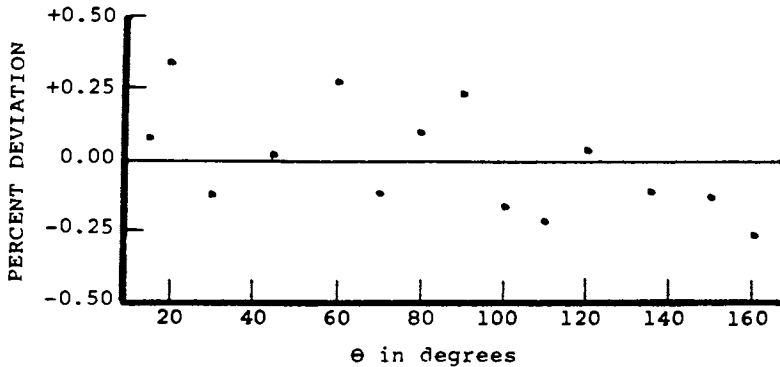


Figure 6. Deviations of  $I \sin \theta$  from 15 to 160 deg scattering angle using toluene in the multiangle system.



### Appendix

The measured autocorrelation function must be normalized before useful parameters can be extracted from it. The normalization consists of establishing a baseline. Normally this is done experimentally by measuring a delayed and/or infinite-time baseline. Occasionally, this is done by fitting a baseline as one of the parameters. In any of these cases the baseline must be correctly established within at least 0.1% or surprisingly large errors occur in any parameter which describes the width of the distribution.

To demonstrate the effect, simulated data with no noise added was used. The autocorrelation function for a monodisperse sample,

$$C(t) = B[1 + A \exp(-2\Gamma t)]$$

was used to generate exact data, where B is the baseline, A is a pre-exponential factor, and  $\Gamma$ , the linewidth is given by,

$$\Gamma = D_T q^2$$

$D_T$  is the translational diffusion coefficient, which, for spheres, is given by,

$$D_T = k_B T / 3\pi\eta d$$

where  $k_B$  is Boltzmann's constant, T is temperature in Kelvin, and  $\eta$  is the viscosity of the medium in which particles of diameter d are moving. The magnitude of the wave vector q is given by,

$$q = (4\pi n / \lambda_0) \sin(\theta/2)$$

where n is the index of refraction of the solution,  $\lambda_0$  is the wavelength in vacuum, and  $\theta$  is the scattering angle.

These exact data were then fit using a weighted, least squares algorithm. The first moments of the distribution, the cumulants (8), were obtained as a function of BLINE, where BLINE is the baseline which was stepped through in 0.1% increments. The results are shown in Table III.

**TABLE III: Effect of Baseline Errors on Distribution Parameters**

| BLINE | AVE. DIA. | POLY  | PEXP  |
|-------|-----------|-------|-------|
| 1.000 | 272.0     | 0.000 | 0.500 |
| 0.999 | 271.2     | 0.020 | 0.502 |
| 0.998 | 270.4     | 0.038 | 0.506 |
| 0.997 | 269.7     | 0.056 | 0.512 |
| 0.996 | 269.1     | 0.072 | 0.520 |
| 0.995 | 268.6     | 0.087 | 0.531 |
| 0.994 | 268.1     | 0.100 | 0.543 |
| 0.993 | 267.7     | 0.112 | 0.557 |
| 0.992 | 267.4     | 0.123 | 0.574 |
| 0.991 | 267.1     | 0.132 | 0.593 |
| 0.990 | 266.8     | 0.140 | 0.613 |

The first row shows the results using the exact baseline: an average diameter of 272nm; an infinitely narrow distribution with a relative variance in the diffusion coefficient distribution, POLY, of zero; and a typical pre-exponential factor of 0.5. These were the values used to generate the data.

For experiment durations of a few minutes with strong scatterers a random error of 0.1% in the baseline is typical, and the second row shows the effects of this. The average diameter is hardly changed, and the relative variance is 0.02. This is a fairly typical value found for narrow standards. However, an error of as little as 0.3% in the baseline results in a relative variance of 0.056. This is equivalent to a relative standard deviation of 0.24, or 24%. An error of 1% in the baseline results in an error of only 1.9% in the average diameter, but yields a distribution with a relative standard deviation of 37.4%. Thus, very small errors in the baseline result in large errors in the calculated width of the distribution.

If correlation data with a small, yet erroneous, baseline is used with one of the size distribution algorithms, then spurious peaks are generated. Worse yet, allowing the baseline to be fit with one of these algorithms may result in the same type of spurious peak. It is preferable to measure the baseline properly rather than use it as a fitting parameter.

### Literature Cited

1. Chu, B. "Laser Light Scattering"; Academic Press: New York, 1974.
2. Berne, B.J.; Pecora, R. "Dynamic Light Scattering with Applications to Chemistry, Biology and Physics"; Wiley-Interscience: New York, 1976.
3. Dahneke, B.E.; Ed. "Measurement of Suspended Particles by Quasi-Elastic Light Scattering"; Wiley-Interscience: New York, 1983.
4. Chen, S-H; Chu, B; Nossal, R.; Eds. "Scattering Techniques Applied to Supramolecular and Nonequilibrium Systems"; Plenum Press: New York, 1981.
5. Pecora, R.; Ed. "Dynamic Light Scattering, Applications of Photon Correlation Spectroscopy"; Plenum Press: New York, 1985.
6. Weiner, B.B. In "Modern Methods of Particle Sizing"; Barth, H., Ed.; Wiley-Interscience: New York, 1984; Chap. 3.
7. Weiner, B.B.; Thomas, J.C. "Introduction to Particle Sizing Using Photon Correlation Spectroscopy"; Brookhaven Instruments: Ronkonkoma, New York, 1984.
8. Koppel, D. E. *J. Chem. Phys.* 1972, 57, 4814.
9. Ostrowsky, N.; et. al. *Opt. Acta* 1981, 28, 1059.
10. Lee, S.P.; Tscharnuter, W.W.; Chu, B. *J. Polym. Sci.: Phys.* 1972, 10, 2453.
11. Papanu, S., Dionex Corp., Sunnyvale, California, private communication.
12. Caldwell, K.D. In "Modern Methods of Particle Size Analysis"; Barth, H., Ed.; Wiley-Interscience: New York, 1984; Chap. 7.
13. Morrison, I.D.; Grabowski, E.F.; Herb, C.A. "Improved Techniques for Particle Size Determination by QELS", accepted for publication in *Langmuir*.
14. Kerker, M. "The Scattering of Light and Other Electromagnetic Radiation", Academic Press: New York, 1969.
15. Chu, B.; Gulari, E.; Gulari, E. *Physica Scripta* 1979, 19, 476.

RECEIVED September 30, 1986

## Chapter 4

# A Comparison of Methods for Determining Macromolecular Polydispersity from Dynamic Laser Light Scattering Data

R. A. Vaidya, M. J. Mettillie, and R. D. Hester

Department of Polymer Science, University of Southern Mississippi,  
Hattiesburg, MS 39406

Several different methods for extracting macromolecular polydispersity information from normalized intensity correlation functions obtained from dynamic light scattering have been proposed. However, detailed comparisons of these methods are lacking. We have proposed a new analysis method involving the GEX function in conjunction with function fitting. Computer simulated data, convoluted with noise, was used to compare our method with Constrained Regularization and the Subdistribution technique. In general our method yielded results at least as good as those from constrained regularization and is more operator independent. The subdistribution method yielded the poorest results.

Particle size distribution and polymer molecular weight distribution (MWD) measurements by dynamic light scattering (DLS) have recently become an active area of research. Dynamic light scattering (also known as photon correlation spectroscopy, quasielastic light scattering (QLS), intensity correlation spectroscopy, and self beat spectroscopy) is dependent upon the molecular diffusion rate. The light scattered by various diffusing polymer molecules in solution is of different phase. It can be shown that if the response time of the detector is sufficiently fast, the intensity should fluctuate between zero and twice its average value. The timescale on which this intensity domain fluctuation takes place is approximately equal to the time required by two molecules to diffuse far enough relative to each other that the phase difference between the two is changed from zero to  $\pi$  radians. The intensity domain output can be transformed into a time domain function by autocorrelation (1).

The autocorrelation (AC) function as measured by the correlator is related to the first order autocorrelation function by Equation 1.

0097-6156/87/0332-0062\$06.00/0  
© 1987 American Chemical Society

$$G(\tau) = A(1+B(g(\tau))^2) \quad (1)$$

Where:  $G(\tau)$  = Measured autocorrelation function  
 $g(\tau)$  = First order autocorrelation function  
 $A$  = Baseline value  
 $B$  = Machine constant  
 $\tau$  = Delay time

The normalized correlation function can be related to the distribution of decay constants as shown by Equation 2.

$$g(\tau) = \int_0^{\infty} F(\Gamma) \exp(-\Gamma\tau) d\Gamma \quad (2)$$

Where:  $\Gamma$  = Decay constant  
 $F(\Gamma)$  = Decay constant distribution function

The relationship can also be cast in terms of distributions of molecular weights for polymer systems. This transformation is achieved by relating the decay constant to its corresponding diffusion coefficient 'D' which in turn is related to molecular weight through a Mark-Houwink like relationship. Equation 3 shows the fundamental relationship between the autocorrelation function and polymer molecular weight distributions.

$$g(\tau) = \frac{\int_0^{\infty} F(M)M^2 \exp(-\alpha q^2 M^\beta \tau) dM}{\int_0^{\infty} F(M)M^2 dM} \quad (3)$$

Where:  $F(M)$  = molecular weight distribution  
 $q$  = scattering vector  
 $\alpha, \beta$  = parameters relating diffusion coefficient to  $M$  through  $D = \alpha M^\beta$

The above relationship assumes that intramolecular motions are not measured and that the polarizability per unit scattering mass is independent of the total scattering mass. The quantities 'q', ' $\alpha$ ' and ' $\beta$ ' are constants and a DLS experiment measures  $g(\tau)$  at several values of  $\tau$ . Thus the problem of calculating a MWD from DLS data reduces to calculating  $F(M)$  by inverting Equation 3. Mathematically, Equation 3 is a Fredholm integral equation. Such equations are ill-conditioned and cannot be solved analytically. Numerical solution is difficult because the existence or uniqueness of a computed solution is not guaranteed and convergence to a solution is nonuniform.

Any proposed method for determining MWDs from the Fredholm equation must converge to the correct solution and must do so rapidly. Convergence to the correct solution is difficult because several local solutions can exist apart from the global solution and numerical methods often converge to a local solution. This problem is most serious with broad unimodal or multimodal MWDs.

#### Past Methods Used To Solve The Fredholm Integral Equation

There have been many methods proposed and used to extract MWDs from QLS data. Some have had a reasonable amount of success. One of the first used a simple Fourier transform of the AC data (2). Although this method is analytically correct, it places such stringent

precision requirements upon the data that it is, in practical terms, unsuited for use with any but the most simple (unimodal monodisperse) systems.

Another method that has enjoyed a great deal of success is the method of cumulants. In 1972 Koppel (3) showed that the logarithm of the first order AC function was identical to the cumulant generating function for the distribution of decay constants. The coefficients of the cumulant expansion can be related to the moments of the distribution. From the complete set of moments it is theoretically possible to regenerate the exact distribution function. In practice however, even small amounts of noise in the AC data can cause large amounts of error in all but the first two or three moments. For narrow unimodal distributions the first two moments basically define the distribution. However, for multimodal, highly skewed, or very broad distributions, the cumulant expansion is inadequate.

A third method that has been widely used is the histogram method (4). This method approximates the Fredholm equation with a discrete form containing a finite sum of exponentials. There is no practical method known to directly regress this type of equation; therefore, a set of approximate decay constants is assumed. This converts the equation from a finite sum of exponentials to a multilinear equation which can be easily regressed. The method rejects physically meaningless solutions by constraining both the distribution coefficients and the decay constants to be non-negative. The major flaw with the histogram method is that it has great difficulty in discriminating between unimodal and multimodal distributions unless the peaks are sufficiently separated.

#### Recent Methods To solve the Fredholm Integral Equation

Although the methods previously discussed have shown some promise in solving the Fredholm equation, two recent methods were chosen for intensive study and comparison with our GEX function fit method. These methods were the constrained regularization method, and the polynomial subdistribution method.

Constrained Regularization Method. The constrained regularization technique has been developed into a computer package (CONTIN) by Provencher (5) and has been used for a variety of purposes of which molecular weight distribution determination is only one. This method finds the simplest best fit solution to the MWD by minimizing the least squares error between experimental and fitted values of  $g(\tau)$  while concurrently minimizing the third derivative of the distribution of molecular sizes. The requirement of a minimum third derivative is incorporated into the algorithm by using a penalty function consisting of a user specified constant times the value of the third derivative. Setting this constant too large can lead to over-smoothing the solution. In addition to minimizing the irregularity of the solution, CONTIN constrains the distribution to be non-negative.

Polynomial Subdistribution Method. The polynomial subdistribution method as described by Cha and Min (6) assumes that the distribution can be represented by a sum of subdistributions as shown by the equation:

$$F(\Gamma) = \sum_{n=0}^N C_n' F_n(\Gamma) \quad (4)$$

where  $C_n'$  is a weighting factor and  $F_n(\Gamma)$  is the normalized subdistribution. In order to show what form of distribution  $F_n(\Gamma)$  takes, it is necessary to perform a Laguerre polynomial expansion of the decay constant distribution.

Assuming,

$$F(\Gamma) = \frac{\exp(-\psi\Gamma)(\Gamma)^\theta(\psi)^{\theta+1}}{\Gamma(\theta+1)} \sum_{n=0}^N C_n' L_n^\theta(\psi\Gamma) \quad (5)$$

$$\text{Where: } L_n^\theta(\psi\Gamma) = \sum_{j=0}^n (-1)^j \binom{n+\theta}{n-j} \frac{(\psi\Gamma)^j}{j!}$$

$N, \theta, \psi = \text{constants}$

the orthogonality of Laguerre polynomials can be used to rewrite Equation 5 as:

$$F(\Gamma) = \sum_{n=0}^N C_n' \frac{\exp(-\psi\Gamma)(\psi\Gamma)^\theta + n_\psi}{\Gamma(\theta + n + 1)} = \sum_{n=0}^N C_n' F_n(\Gamma) \quad (6)$$

Therefore,

$$F_n(\Gamma) = \frac{\exp(-\psi\Gamma)(\psi\Gamma)^\theta + n_\psi}{\Gamma(\theta + n + 1)} \quad (7)$$

From this it is immediately obvious that  $F_n(\Gamma)$  is a gamma distribution. Each subdistribution has a mean of  $\theta+n+1/\psi$  and a variance of  $\theta+n+1/\psi^2$ . Although in the above equation the variable  $\Gamma$  can take on any values from zero to infinity, gamma is constrained to be within three standard deviations of the subdistribution mean for simplicity. Also the baseline between these limits is subtracted in order to provide a distribution with zero frequency at its limits, and we can write the AC function as:

$$g^2(\Gamma) = \left( \int_0^\infty \left[ \sum_{n=0}^N C_n' F_n(\Gamma) \right] \exp(-\tau\Gamma) d\Gamma \right)^2 \quad (8)$$

The coefficients  $C_n'$ , and the constants  $\theta$  and  $\psi$  are the unknown parameters to be solved for in the regression. The number of subdistributions 'N+1' usually range from 5 to 9 for unimodal distributions and up to 13 for multimodal distributions. The subdistribution method is essentially a continuous version of the histogram method in that it uses overlapping gamma distributions instead of the non-overlapping square distributions used in the histogram method.

### The GEX function fit method.

An alternative approach to determine polymer MWDs from DLS data is to assume that the molecular weight distribution can be represented by a mathematical function and then regressing Equation 3 to obtain the best fit values for the parameters involved in the chosen model. This assumption becomes limiting if the function chosen cannot fit the sample molecular weight distribution. In general methods using this strategy are called function fit methods.

In this paper we propose the use of the generalized exponential ('GEX') function as a peak model in the function fit method. The GEX function for a single peak is shown in Figure 1. Each peak has five parameters three of which ( $h$ ,  $X_0$ , and  $X_m$ ) have direct physical meaning (Figure 1). 'A' and 'B' are shape parameters that determine the skew and kurtosis of the peak. We have previously shown that the GEX function fits polymer molecular weight distributions well and is very versatile in that it can fit a very wide variety of peak shapes (7) (Figure 2). The versatility of the GEX function makes the peak shape assumption inherent in the GEX method very non-limiting.

The GEX function can be integrated analytically (8) and thus the denominator in Equation 3 can be calculated in a closed form. The numerator cannot be integrated and therefore has to be calculated numerically. In Equation 3, ' $\alpha$ ', ' $\beta$ ' and ' $q$ ' are known constants and hence for a given set of GEX parameters at a given value of ' $\tau$ ' the right hand side of the equation can be completely calculated. The data from a dynamic light scattering experiment is in the form of ( $\tau$ ,  $g(\tau)$ ) data points. For every value of ' $\tau$ ', Equation 3 can be used to calculate a fitted value of  $g(\tau)$  and the sum of the square of the difference between the calculated and experimental values of  $g(\tau)$  is the least squares error. The problem of finding a MWD thus reduces to finding the best values for the GEX parameters to fit the experimental AC function.

### Experimental

In order to compare the results of an analysis technique with the 'true' solution it is essential that the MWD be known before the analysis is started. Consequently, computer simulated data generated by assuming a molecular weight distribution and subsequently using Equation 3 to generate  $g(\tau)$  for a series of ' $\tau$ ' values, was used for analysis. Five different MWDs were used, four of which were generated using GEX functions as models (two GEX functions for bimodal peaks), and Table I shows the GEX parameters used for each of these MWDs.

$$h = h_m L^{B-1} \exp\{(1 - L^A)(B-1)/A\}$$

$$\text{with: } L = (X - X_0)/(X_m - X_0)$$

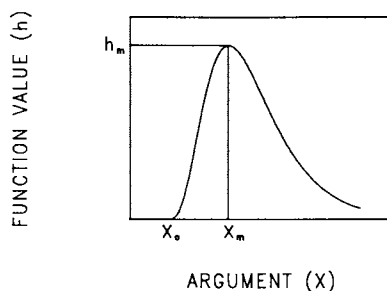


Figure 1 : The GEX function for a unimodal distribution.

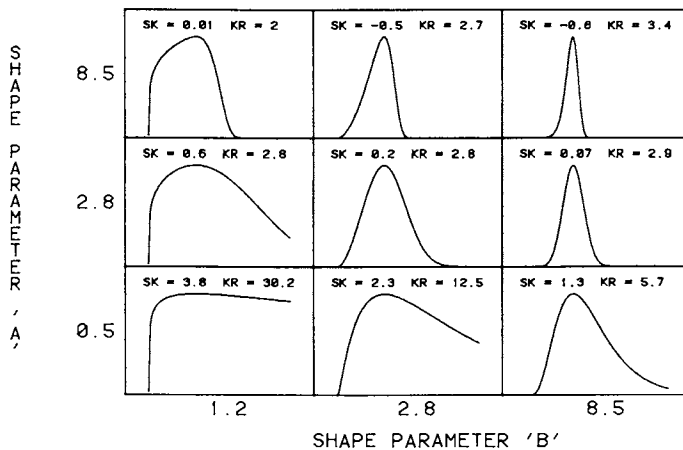


Figure 2 : Variation in the shape of the GEX distribution as a function of the shape parameters 'A' and 'B'.



Table I. Molecular Weight Distribution Specifications

| Distribution                                   | Peak 1 |     |                  |                  | Peak 2 |     |                  |                  | $\Delta\tau \times 10^6$<br>sec |
|--|--------|-----|------------------|------------------|--------|-----|------------------|------------------|---------------------------------|
|  | A      | B   | $X_0$            | $X_m$            | A      | B   | $X_0$            | $X_m$            |                                 |
|  |        |     | $\times 10^{-4}$ | $\times 10^{-4}$ |        |     | $\times 10^{-4}$ | $\times 10^{-4}$ |                                 |
| Normal   | 2.8    | 2.8 | 1                | 10               | ---    | --- | ---              | ---              | 5                               |
| Skewed   | 1.1    | 1.6 | 1                | 5                | ---    | --- | ---              | ---              | 5                               |
| Bimodal I<br>(Skewed:Normal = 3:1 mass ratio)  | 1.1    | 1.6 | 1                | 5                | 2.8    | 2.8 | 25               | 34               | 5                               |
| Bimodal II<br>(Skewed:Normal = 1:3 mass ratio) | 1.1    | 1.6 | 1                | 5                | 2.8    | 2.8 | 25               | 34               | 10                              |

$q=1.87 \times 10^5 \text{ cm}^{-1}$ ,  $\alpha = 8 \times 10^{-5} \text{ cm}^2/\text{sec}$ ,  $\beta = -0.5$

Each of the bimodal cases represented a mix of a skewed low molecular weight peak and a higher molecular weight normal peak. The two cases have a three-to-one and a one-to-three ratio of peak areas respectively. The fifth distribution corresponds to a classical free radical polymerization with a number average molecular weight of 50,000 (9).

Data for the normal, skewed, and free radical distributions was generated with 50 linearly spaced delay times (channels), while 100 channels were used for the bimodal cases. To realistically model experimental data approximately 1% random noise was added to the AC data. Each of the AC data sets, with 0 and 1% noise levels, were then analyzed for a MWD using constrained regularization, subdistribution, and GEX fit techniques.

For both the subdistribution and the GEX fit methods a Marquardt algorithm for constrained non-linear regression was used to minimize the sum of squares error (10). The FORTRAN program CONTIN was used for the constrained regularization method. All computations were performed on a Harris H-800 super mini computer.

## Results

Comparisons between generated MWDs and the distribution computed by the three methods for both normal and skewed distributions with no noise are shown in Figure 3. Figure 4 shows the results for these cases with 1% added noise. In these and subsequent figures, the thinner line represents the computed molecular weight distribution. Table II shows a comparison between the moments of the distributions computed by the constrained regularization and GEX fit methods and the corresponding values for the true solution. The results for the bimodal MWDs are shown in Figure 5 and those for the free radical case in Figure 6.

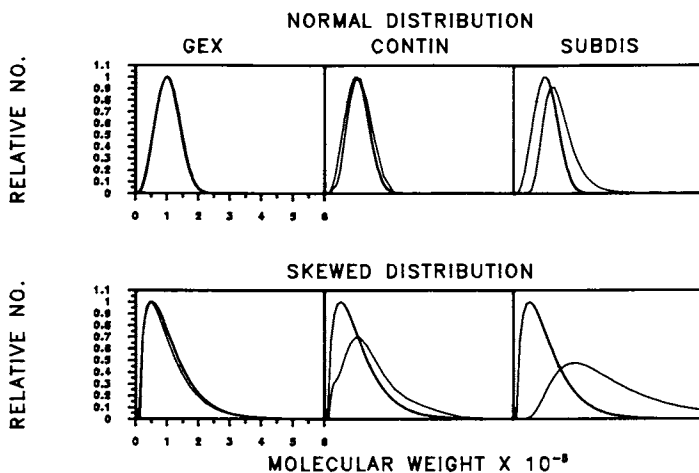


Figure 3 : Results of the analyses for normal and skewed unimodal distributions without noise in the AC function.

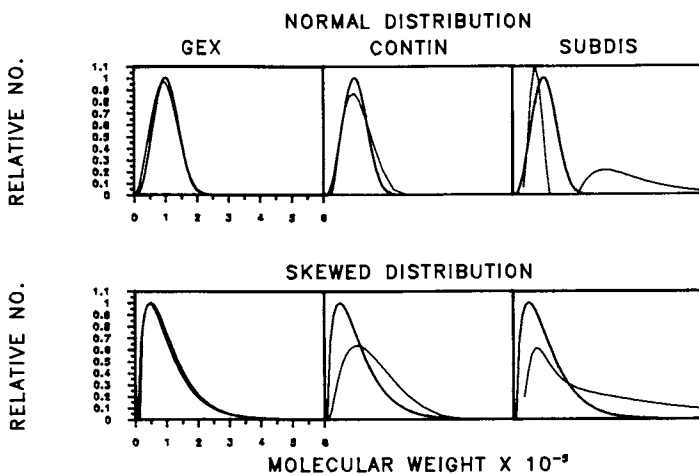


Figure 4 : Results of the analyses for normal and skewed unimodal distributions with 1% noise in the AC function.

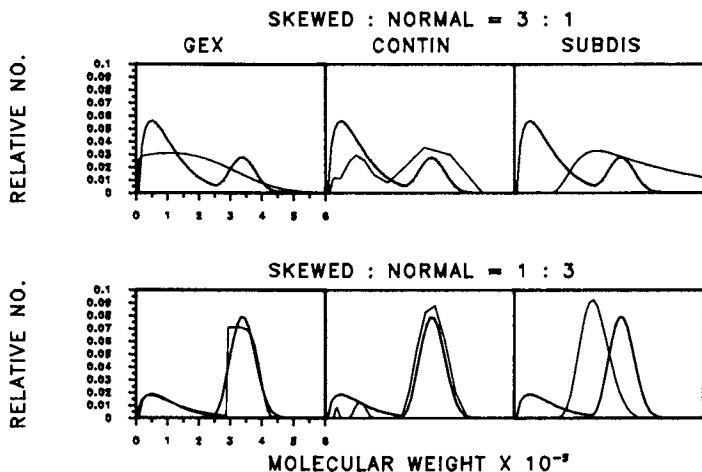


Figure 5 : Results of the analyses for the bimodal distributions without noise in the AC function.

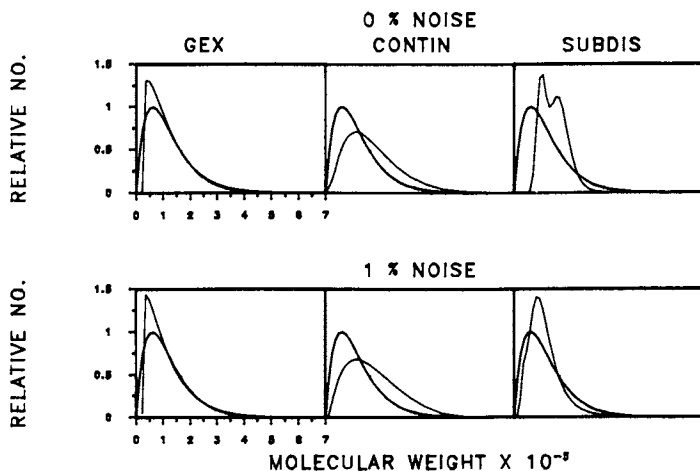


Figure 6 : Results of the analyses for the classical free radical distribution with 0 and 1% noise in the AC function.

Table II. Comparison of Methods

| Method                     | Noise Level | $M_n \times 10^{-3}$ | $M_w \times 10^{-3}$ | $Var \times 10^{-11}$ | Skew | Kurtosis |
|----------------------------|-------------|----------------------|----------------------|-----------------------|------|----------|
| <u>Normal Distribution</u> |             |                      |                      |                       |      |          |
|                            | True Values | 104                  | 116                  | 1.3                   | 0.24 | 2.7      |
| GEX Fit                    | 0%          | 104                  | 116                  | 1.3                   | 0.22 | 2.7      |
|                            | 1%          | 100                  | 116                  | 1.5                   | 0.28 | 2.7      |
| CONTIN                     | 0%          | 103                  | 115                  | 1.3                   | 0.11 | 2.6      |
|                            | 1%          | 97                   | 113                  | 1.6                   | 0.35 | 3.1      |
| <u>Skewed Distribution</u> |             |                      |                      |                       |      |          |
|                            | True Values | 105                  | 154                  | 5.2                   | 1.44 | 6.0      |
| GEX Fit                    | 0%          | 105                  | 154                  | 5.2                   | 1.45 | 6.0      |
|                            | 1%          | 105                  | 155                  | 5.2                   | 1.61 | 6.9      |
| CONTIN                     | 0%          | 104                  | 152                  | 5.0                   | 0.68 | 5.2      |
|                            | 1%          | 123                  | 160                  | 4.6                   | 0.48 | 3.6      |

### Discussion

There are two broad criteria by which the three methods can be compared. They are: the correctness of the computed solution; and, the degree of operator independence.

Correctness of the solution. As can be seen from Figures 3 and 4 the subdistribution method yields inferior solutions as compared to the other two methods for the unimodal case. Consequently, the results from this method are not included in Table II. In the absence of noise CONTIN fits the normal case well but shows an artificial shoulder on the skewed MWD. The GEX fit method reproduces the input distributions with great accuracy. The subdistribution method had great difficulty in handling the cases with added noise. CONTIN and the GEX fit method were not significantly affected by noisy data. However, CONTIN showed broadening of the MWD instead of the artificial shoulder in the skewed case. The values in Table II attest to the quality of the fits obtained with the GEX fit and CONTIN methods. The GEX method gives slightly better numbers but this is to be expected since the input distributions were GEX functions.

For bimodal MWDs none of the methods successfully resolved the two peaks for the case where a majority of the molecules were of low molecular weight (Figure 5). However, CONTIN provided the closest solution. For the case where the skewed low molecular weight peak consisted of only one quarter of the total mass, the GEX fit method gave good results. CONTIN showed three peaks, but the agreement can still be considered fair because of the difficulty in discerning two widely separated peaks of this type. As in the unimodal cases, the subdistribution method showed the poorest fits.

The GEX fitting technique worked well to find MWDs from AC data that have been generated by a GEX function. Determining if it would work on other types of distributions was the next logical step. As can be seen from Figure 6, it apparently can. The GEX fit method shows good agreement between the input MWD and the computed distribution in the classical free radical case. CONTIN shows fair agreement, but the subdistribution gave a bimodal peak when there was no noise in the AC function.

Operator independence. The GEX method is virtually operator independent. The only inputs required before fitting are parameters concerning the precision of the numerical integration and exit criteria for the Marquardt algorithm. The same set of inputs was used for all five MWDs. Currently the method also requires upper and lower limits on the GEX parameters but a simple modification of the code can eliminate this need. The CONTIN algorithm has several operator and case dependent parameters that have to be chosen before analysis. However, it is fairly stable with respect to bad choices for some of these inputs. The GEX fit method cannot fit multimodal MWDs without prior knowledge of the number of peaks in the distribution. While CONTIN does not impose this limitation it is recommended that the number of peaks be specified before analysis. In our experience with CONTIN if this condition is not met the algorithm tends to compute unimodal solutions for multimodal MWDs and sometimes visa versa.

The subdistribution method requires the operator to specify the number of distributions to be used in an analysis. The method is extremely sensitive to this input and a bad choice can lead to false answers or no convergence. This choice is particularly critical in the case of broad unimodal or multimodal MWDs.

### Conclusions

The subdistribution method is extremely sensitive to operator input and consistently yielded the poorest results of the three methods compared. In general CONTIN yields good results but tends to shift MWDs to higher molecular weights and sometimes produces artifact peaks or shoulders for broad unimodal or multimodal distributions. Of the three methods, the proposed GEX fitting technique seems to provide results that are most consistent with the input distributions and is the most operator independent. CONTIN and GEX fitting are not significantly affected by noisy data.

### Acknowledgments

We wish to thank the Department of Energy and the Department of Commerce for their support of this project.

### Literature Cited

1. Ford, N. C. In Dynamic Light Scattering: Applications of Photon Correlation Spectroscopy; Pecora, R., Ed.; Plenum Press: New York, 1985; pp. 12-15
2. McWhirter, J. G.; Pike, E. R. J. Phys. A: Math. Gen. 1978, 11, 1729-45.
3. Koppel, D. E. J. Chem. Phys. 1972, 57, 4814-20.
4. Gulari, E.; Gulari, E.; Tsunashima, Y; Chu, B. J. Chem. Phys. 1979, 70, 3965-72.
5. Provencher, S. W. Makromol. Chem. 1979, 180, 201-209.
6. Cha, C. Y.; Min K. W. J. Poly. Sci. Poly. Phys. Ed. 1983, 21, 807-20.
7. Vaidya, R. A.; Hester, R. D. J. Chromatogr. 1984, 287, 231-44.

8. Vaidya, R. A.; Hester, R. D. J. Chromatogr. 1985, 333, 152-55.
9. Tanford, C. "Physical Chemistry of Macromolecules"; John Wiley and Sons:New York, 1961; pp 603-6.
10. Kuester, J. L.; Mize, J. H. "Optimization Techniques with Fortran"; McGraw-Hill Book Company:New York, 1973; pp 240-50.

RECEIVED June 27, 1986

## Chapter 5

# Submicrometer Particle Sizing by Photon Correlation Spectroscopy: Use of Multiple-Angle Detection

S. E. Bott

Coulter Electronics, Inc., 29 Cottage Street, Amherst, MA 01002

Photon correlation spectroscopy (PCS) has become a method of choice for sizing particles in the 3-3000nm range. Advances in the analysis of PCS data permit extraction of the particle size distribution as well as the mean diameter.

An important problem in PCS involves converting intensity averaged distributions, which are measured by PCS but have little direct meaning, to physically meaningful weight (volume) averaged distributions. For spherical particles the intensity to weight conversion at each scattering angle is given by the 'Mie' equations. However, the 'Mie' conversion is often an oscillatory function in which particles of certain sizes contribute virtually no scattered light. It is shown here that weight distributions from single angle PCS measurements can have huge errors. Complementary information obtained by measurement at an additional angle allow a good measure of the weight averaged size distribution.

As new techniques to produce material are developed and older processes are refined, there has been a general trend toward the use of component materials of smaller and smaller size. Using smaller size components often results in bulk materials of greater strength or uniformity or possessing other advantageous qualities. Some examples of this trend can be found in coatings, ceramics and latices<sup>1,2</sup>. Concomitant with the trend has been a requirement for measuring size distributions of smaller particles in order to control or to characterize the industrial process.

For particles smaller than around .5 to 1 micron, measuring methods based on single particle detection generally break down because the signals (e.g. scattered light, electrical conductivity through a pore, etc.) obtainable from individual particles below this size are simply too small to detect. A few years ago, a commercial instrument, based on a new principle, photon correlation spectroscopy (PCS)<sup>3</sup>, became available for measurement of mean particle sizes in the submicron range. PCS (also known as dynamic light scattering (DLS) or quasi-elastic

0097-6156/87/0332-0074\$06.00/0  
© 1987 American Chemical Society

light scattering (QELS)) offers several outstanding advantages over other measurement methods: 1> the measurement is absolute, i.e. it requires no calibration standards, 2> the measurement is noninvasive - the sample can be recovered unchanged after the measurement and 3> the measurement is quick, usually requiring only a few minutes. PCS circumvents the problem of inadequate signal level for individual particles by simultaneously detecting of the order of thousands to many millions of particles. In the last few years, PCS has become a widely used particle sizing tool for mean particle sizes in the submicron range.

The positive attributes of particle sizing by PCS are opposed by two negative ones: the method, because it is based on light scattering, measures angle dependent (scattered light) intensity weighted rather than the more useful volume weighted particle distributions; and, the particle sizing has relatively low resolution. The angle dependent intensity weighted averages must usually be converted to volume averages for interpretation and comparison with other particle sizing methods. The relatively low resolution of PCS combined with the severity of the conversion of intensity averages to weight averages and the heavy dependence of intensity averaged distributions on the scattering angle at which the measurement is performed, means that single PCS measurements made at one scattering angle will often give misleading results. This article presents data which show that by making multiple measurements at several scattering angles, much more reliable results can be obtained.

#### PHOTON CORRELATION SPECTROSCOPY

Figure 1 shows the geometry of a PCS measurement. Laser light is incident on a sample of particles suspended or dissolved in a transparent liquid. The particles, undergoing Brownian motion, diffuse throughout the solution. At any given instant, the light intensity sensed at the detector is proportional to the square of the electric field at the detector. The phase of the light scattered from each particle and measured at the fixed detector, will depend on the position of the particle in the beam and on the distance between the particle and the detector. Thus the composite light scattered from the group of particles in the scattering volume will form an interference pattern at the detector. Figure 2 shows an interference pattern resulting from the light scattering from two particles. The two sets of concentric circles represent the wave fronts of the scattered light. The dark 'rays' formed when two sets of concentric circles are superimposed, as in the figure, are regions where the light scattered from the two particles constructively interferes. If the detector is located in one of these dark rays, a high light intensity will be sensed.

As the particles randomly diffuse through the solution, the location of the dark rays of constructive interference will change; therefore the intensity sensed by the fixed detector will vary, i.e. the interference pattern produced by the scattering particles will be modulated by the particle motions. The intensity fluctuations at the detector, though random, will be more rapid for small, rapidly moving particles than for



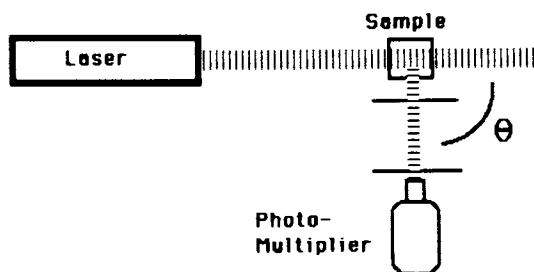


Figure 1. Geometry of a PCS measurement. The scattering angle,  $\theta$ , can vary between 0 degrees and 180 degrees.

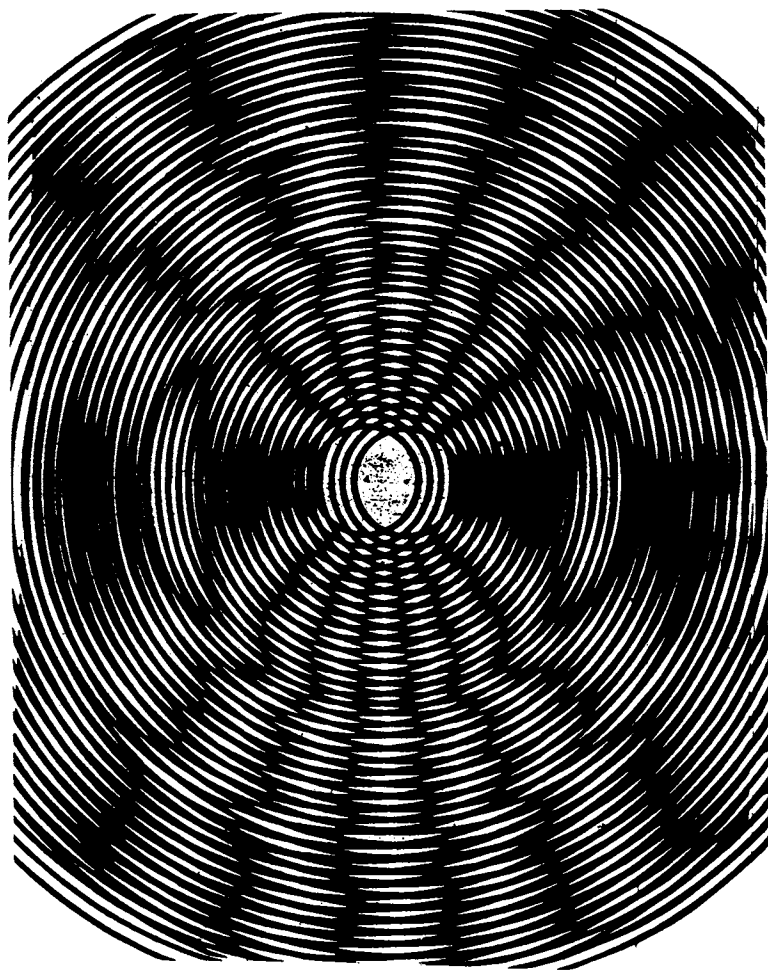


Figure 2. An interference pattern resulting from the scattering from two particles.

larger more slowly diffusing particles. The 'noise' signal produced by the light scattered from diffusing particles can be characterized by its autocorrelation function,  $g(t)$ , defined by

$$(1) \quad g(t) = \langle I(\tau) I(\tau+t) \rangle$$

where  $I(\tau)$  is the intensity at the detector at time  $\tau$ , and where the angular brackets represent a time average over  $\tau$ . The autocorrelation function measures the similarity, or correlation between the configuration of particles contributing to an intensity  $I$  at  $\tau$  to that a time  $t$  later. For system of Brownian particles of uniform size and shape, the autocorrelation function will be a decaying exponential:

$$(2) \quad g(\tau) = A e^{-2\Gamma\tau} + B$$

where  $\Gamma$  is a decay constant characteristic of particles of that size and  $A$  and  $B$  are constants dependent on the sample, experimental geometry and counting efficiency of the optics and electronics.  $1/\Gamma$  is the decay time of the Brownian motion; roughly speaking, it is the time required for any particular configuration of particle positions within the scattering volume to 'relax'. After several decay times, the particles will have diffused such that their new positions will be statistically uncorrelated with their former positions.

The decay constant is related to the diffusion constant of the particles and to the geometry of the experiment through the equation,

$$(3) \quad \Gamma = q^2 D ; \quad q = 4 \pi n \sin(\theta/2) / \lambda$$

where  $n$  is the refractive index of the solvent,  $\theta$  is the scattering angle,  $D$  is the diffusion constant of the particles,  $\lambda$  is the wavelength of the laser in vacuum and  $q$  is the magnitude of the so called 'scattering vector'. In turn, for spherical particles, the diffusion constant is related to the particle diameter through the Stokes-Einstein equation:

$$(4) \quad D = k T / 3 \pi \eta d$$

where  $k$  is Boltzmann's constant,  $T$  is the absolute temperature,  $\eta$  is the viscosity of the solution and  $d$  is the particle diameter. Using (3) and (4), the measured decay constant  $\Gamma$  can be directly related to the particle diameter.

When the sample contains particles of different sizes, the autocorrelation function will be a sum of decaying exponentials weighted by the intensity of light scattered from particles of each characteristic size. This can be described in general by the equation:

$$(5) \quad g(\tau) = \int_a^b \chi(s) e^{-\Gamma(s)\tau} ds$$

where the index,  $s$ , labels the size of the particles and  $X(s)$  is the particle size distribution, which gives the relative proportion of the scattering from particles of size  $s$ . The constants  $a$  and  $b$  are the lower and upper limits of particle size. This integral equation must be numerically inverted to extract the size distribution,  $X(s)$ , from the measured autocorrelation function. The inversion procedure is non-trivial. Although various algorithms have been developed for the inversion, by far the most widely used analysis program for this type of data analysis is a FORTRAN program called CONTIN, details of which are available in the open literature<sup>4,5</sup>.

It might be imagined that with a reasonable measurement of the autocorrelation function and an appropriate inversion algorithm, that a very accurate size distribution measurement could be made with PCS. However, in fact, the autocorrelation function itself has useful, but limited information about the distribution of particle sizes<sup>6</sup>. To get an idea about the precision of PCS measurements on bimodal samples, bimodal mixtures of polystyrene latex spheres (PSL) were prepared to give equal scattering intensities from each population at a 90 degree scattering angle. Twenty measurements were made with each mixture. The coefficient of variation (c.v. = standard deviation/mean) of percentage of scattering intensity from each peak over the twenty runs was computed. The results are given below.

| PSL #1 (nm) | PSL #2 (nm) | Run Time (sec) | c.v. of #1 | c.v. of #2 |
|-------------|-------------|----------------|------------|------------|
| 90          | 310         | 120            | 12%        | 15%        |
| 90          | 822         | 600            | 5%         | 8%         |
| 170         | 1100        | 600            | 6%         | 6%         |
| 310         | 1300        | 120            | 16%        | 32%        |

As can be seen, the c.v.s vary from sample to sample but are of the order of 10%. As measurement times increase, the c.v.s of the measurements will, naturally, decrease.

#### INTENSITY, WEIGHT AND NUMBER AVERAGES

The particle size distribution,  $X(s)$ , above is, unfortunately, not in a form which is useful for most applications. This is because it is a scattered intensity weighted distribution (for brevity, 'intensity distribution') rather than a size distribution based on the volume (weight) or number of particles. The difference between distributions weighted in different ways can be most easily explained by relating the various distributions to a number distribution.

A number distribution gives the relative number,  $N$ , of particles of size  $s$ . A volume or weight distribution  $V(s)$  is related to a number distribution by

$$(6) \quad V(s) = N(s) C_V(s)$$

where  $C_V$  is a factor to convert number to volume;  $C_V(s)$  is equal to the volume of a particle of size  $s$ . Similarly, an intensity distribution is related to a number distribution by

$$(7) \quad X(s, \theta) = N(s) C_I(s, \theta)$$

$C_I(s, \theta)$  is the conversion factor of number to intensity, i.e. the amount of scattering from a particle of size  $s$ . Notice the explicit dependence of  $X$  and  $C_I$  on  $\theta$ . This dependence is included to emphasize that the intensity distribution measured by PCS at one scattering angle will be different than that at another scattering angle. Weight and number distributions are, of course, independent of scattering angle.

The implication of equation (7) as it relates to PCS, is that larger particles scatter considerably more light per particle than smaller particles. Thus the intensity distributions measured by PCS heavily emphasize the presence of larger particles. If the intensity distributions measured with PCS were extremely accurate, the fact that PCS measures intensity rather than volume or number distributions would be of little consequence, provided that the proper conversion factor,  $C_I(s, \theta)$  were known. As will be seen in the next section, fairly good conversions are in fact, available. However, as was pointed out in the previous section, PCS is a low resolution sizing method; this implies that the intensity distribution,  $X(s, \theta)$ , is measured with low precision and accuracy. Typically, the intensities in the two peaks in a bimodal sample, for example, will be measured to 10% of the total scattering intensity. Peaks which comprise less than 10% of the total scattering intensity, therefore, can be artifacts. For small real peaks, small errors in the measurement of the scattering intensity from a population of small particles will often lead to huge errors in volume distributions derived from the measured intensity distribution because the conversion involves a high amplification factor on the small particles to compensate for their low scattering intensities compared to larger particles.

#### RAYLEIGH AND RAYLEIGH DEBYE REGIMES

When particles are small compared to the magnitude of the scattering vector ( $q = 4\pi n \sin(\theta/2) / \lambda$ ),  $C_I(s, \theta) = s^6$ ; i.e. the

conversion of intensity to number distributions is angle independent and scales as the square of the volume of the particle. In this regime, called the Rayleigh regime, the scattering intensity is independent of particle shape. For particles of a size of the order of the magnitude of the inverse of the scattering vector  $q$ ,  $C_I$  can be found by conceptually dividing the particle into many small subsegments, and summing the scattered light contribution of each subsegment, taking into account the relative positions of each subsegment and the distance of each from the detector (and including, if necessary, non-isotropic polarizabilities of the subsegments and polarization of incident and detected light). The result of this process for spherical, isotropic particles is

$$C_I = \{ [3/(qr)^3] [\sin qr - qr \cos qr] \}^2 r^6$$

where  $r=s/2$ . The angle dependence of  $C_I$  comes through the angle dependence of  $q$ . This is the Rayleigh Debye approximation for isotropic spheres. It is commonly used because of its simplicity. In this approximation,  $C_I$  comprises two factors: the volume squared ( $r^6$ ) factor and an attenuating factor,  $\{3/(qr)^3 [ \sin qr - qr \cos qr ] \}^2 r^6$ , which is always between 0 and 1, and which quantifies the degree of intraparticle destructive interference in the scattered light from such a spherical particle. As will be seen below, the range of applicability of the Rayleigh Debye approximation is limited. Rayleigh Debye approximations can be found for non-spherical particles, e.g. ellipses of revolution, rigid rods and Gaussian coils<sup>3</sup>.

#### MIE EQUATION

For isotropic spherical particles of given refractive index in a medium of known refractive index, the exact form of  $C$  can be found by matching the incident, internal and scattered electromagnetic waves at the particle surface, subject to certain boundary conditions<sup>7</sup>. The solution comes in the form of an infinite series:

$$C_I(s, \theta) = \sum_{n=1}^{\infty} \{ [(2n+1)/(n(n+1))] \{ a_n \pi_n(\cos \theta) + b_n \tau_n(\cos \theta) \} (-1)^{n+1} \}$$

where

$$\pi_n(\cos \theta) = P_n^{(1)}(\cos \theta) / \sin \theta$$

$$\tau_n(\cos \theta) = d/d\theta (P_n^{(1)}(\cos \theta))$$

$$a_n = \{ \psi_n(\alpha) \psi_n'(\beta) - m \psi_n(\beta) \psi_n'(\alpha) \} / \{ \zeta_n(\alpha) \psi_n'(\beta) - m \psi_n(\beta) \zeta_n'(\alpha) \}$$

$$b_n = \{ m \psi_n(\alpha) \psi_n'(\beta) - \psi_n(\beta) \psi_n'(\alpha) \} / \{ m \zeta_n(\alpha) \psi_n'(\beta) - \psi_n(\beta) \zeta_n'(\alpha) \}$$

$$\alpha = 2\pi s / \lambda ; \quad \beta = m\alpha ;$$

$\psi$  : Ricatti-Bessel functions ;  $\zeta$  : Hankel functions.

$\Pi_\eta$  and  $\Gamma_\eta$  are related to Legendre polynomials and  $a_n$  and  $b_n$  are coefficients dependent on the particle size  $s$  and the relative refractive index of the particles to the medium in which they are suspended. As before,  $\theta$  is the scattering angle.

A complete understanding of the equation is not important for purposes here; the important points are that the amount of light scattered by a particle of a certain size depends on the scattering angle and the refractive index of the particle compared to that of the medium in which it is suspended. In the previous approximations,  $C_I$  was independent of the refractive index of the particle. It might be noted that the expression for  $C_I$  is rather complicated; it is for this reason that the Rayleigh Debye (or sometimes other) approximations are substituted for the exact Mie expression. Figure 3 shows  $C_I$  for an isotropic spherical particle of refractive index 1.6 in a medium of refractive index 1.33 at a scattering angle of 90 degrees, with an incident laser wavelength of 632.8 nm. The solid line shows the exact Mie conversion; the dotted line shows the Rayleigh Debye approximation. Although the lines are fairly close for small particles, beyond about 400 nm, the two intensity conversions go 'out of phase'; huge errors could result from using the Rayleigh Debye approximation beyond its limited range of applicability. Figure 4 shows a bimodal volume distribution (chained line) and the corresponding intensity distributions according to the Mie (solid line) and Rayleigh Debye (dotted line) expressions. Notice the difference between the relative sizes of the two peaks in the volume versus in the two intensity graphs. Also note the relative height of the smaller sized peak and the shifting of the larger size peak in the Mie versus Rayleigh Debye graphs.

Figure 5 shows the angular dependence of the scattering intensity for the same sample as in figure 3. The oscillations of scattering intensity per particle over a range of particle sizes is characteristic of  $C_I(s, \theta)$  for dielectric (transparent) particles. The positions and amplitudes of the peaks and valleys in the plots are dependent on the relative refractive indices. For the lower scattering angle, there are fewer oscillations in the graph. This is a general trend. As the scattering angle is lowered, the number of oscillations in  $C_I(s, \theta)$  decreases. For small sized particles, the lines corresponding to the 30 and 90 degree scattering angles overlap. This is the region in which  $C_I$  follows the  $s^6$  dependence; in this region the conversion of relative intensity to number distributions is independent of the refractive index of the particle.

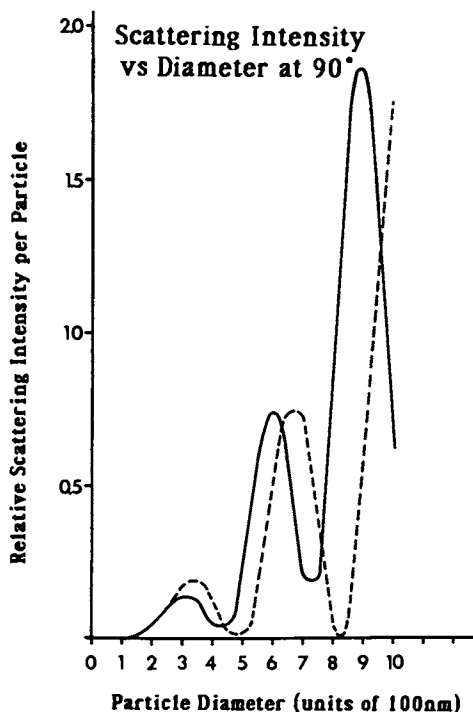


Figure 3. The scattering intensity,  $C_I$ , per particle as a function of particle diameter according to the exact Mie theory (solid line) and the Rayleigh Debye approximation (dotted line).

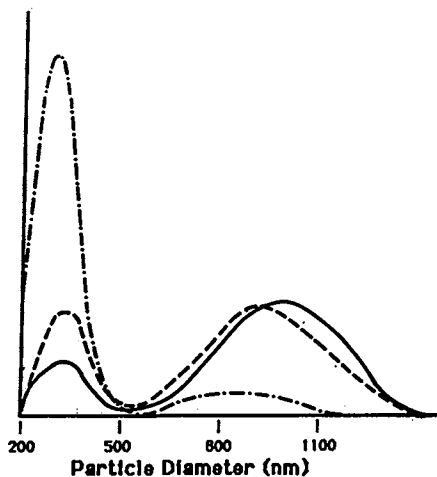


Figure 4. A bimodal volume weighted distribution (chained line) and the corresponding intensity distributions according to the Mie theory (solid line) and the Rayleigh Debye approximation (dotted line).

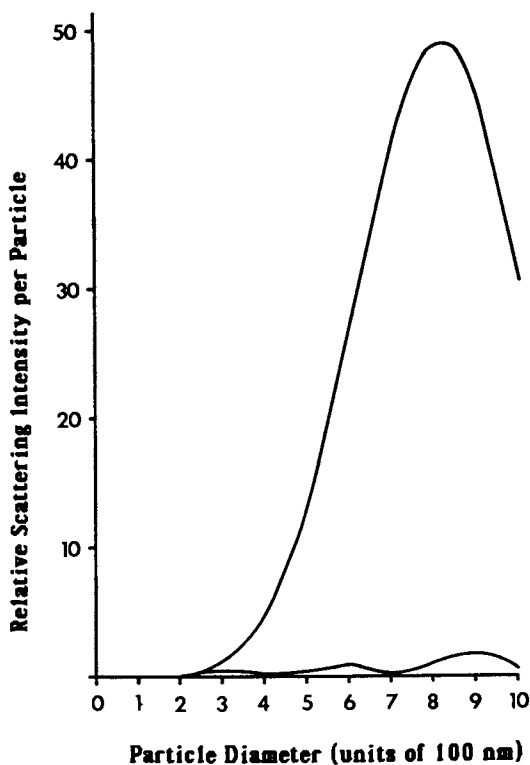


Figure 5. Scattering intensity per particle as a function of particle diameter according to the Mie theory. Upper line corresponds to a 30 degree angle, lower line to a 90 degree scattering angle.



In the parts of the  $C_I(s, 90^\circ)$  and  $C_I(s, 30^\circ)$  that do not overlap, the extremely different form of the intensity conversion at the two angles means that the scattered light intensities at the two angles will weight particles extremely differently. Because of this, the information gleaned from measurements at different angles is, to a certain extent, independent. Thus the low resolution inherent in PCS measurements can be enhanced by making measurements at several angles. To look at it in another way, a peak containing less than 10% of the scattering intensity at one angle might contain a substantially greater portion of the scattering intensity at another angle and therefore be easier to detect. Because of the low precision of PCS measurements, routine sizing measurements at several angles can help to separate real peaks from artifacts, and, as will be shown below, to identify populations of particles which do not scatter enough light to be detected at 90 degrees (or any other single fixed angle).

The second important piece of information given by figure 5 is that the scattering intensity per particle of large particles is much greater at the lower angle. This is, again, a general observation. PCS measurements at lower angles emphasize the presence of larger particles.

The Mie equation also holds for absorbing or reflecting particles, which have complex refractive indices. The graphs of  $C_I(s, \theta)$  for such particles are similar to those for dielectric particles except that the amplitudes of the oscillations are generally smaller.

#### MATERIALS AND METHODS

The polystyrene latex (PSL) spheres were obtained from Seragen Diagnostics. The nominal sizes of these standards were from electron microscopy measurements. The samples were prepared by diluting the 10% solids in filtered, doubly distilled water, adding a small amount of SDS to help disperse the samples and sonicating with Branson 60 watt bath sonicator for 30 seconds to disperse any aggregates. The relative volumes (weights) of the two sizes of PSL in the mixed sample were estimated to be accurate to about 5-10%.

The light scattering measurements were made with a Coulter model N4MD particle sizer, which measures particles sizes at six laboratory fixed scattering angles (90, 63, 30, 22, 15 and 11 degrees). The instrument uses an internal computer running a version of CONTIN to perform the inversion of equation (5). It converts intensity to volume distributions using exact Mie expression (equation 8). The results of the multiple runs

through the six scattering angles were stored to floppy disk using a Coulter N4 Accucomp data handling system which also automatically computes the averages over the multiple runs over all angles and over the multiple runs at each separate scattering angle.

#### EXPERIMENTAL RESULTS AND DISCUSSION

The ramifications of the conversion of intensity to weight distributions are illustrated by the following examples. Figure 6a shows a particle size histogram of a sample of polystyrene latex (PLS) spheres taken at a scattering angle of 90 degrees. Only one peak is detected at this angle. Figures 6b and 6c show the same sample measured at scattering angles of 30 and 11 degrees respectively. Both show the presence of two peaks; the relative proportions of the two peaks are, however quite different. The difference between the size distributions taken at the three angles graphically illustrates the dependence of intensity distributions on angle.

The PSL in the actual sample was composed of 91% by weight of 170 nm PSL and 9% by weight of 822 nm PSL. (These weight amounts PSL were accurate to not better than 5%, i.e.  $91\% \pm 4.55\%$  of the 170 nm PSL and  $9\% \pm .45\%$  of the 822 nm PSL.) Using the Mie equation, these weight proportions convert to intensity distributions of 96% 170 nm PSL and 4% 822 nm PSL at 90 degrees scattering angle, 50% of each at 30 degrees and 13% of the 170 nm to 87% of the 822 nm PSL at 11 degrees. Note that the relative proportions of the two populations of PSL, as measured by intensity distributions, are almost reversed for the 90 degree measurements compared to the 11 degree measurement.

Since the run times used for the measurement were such that the threshold for detection of a peak was around 5% of the total scattering intensity, the 822 nm PSL was not even detected at the 90 degree scattering angle. Actual measured intensities for the two peaks compared well to the values expected by the Mie conversion.

|                 |        | Actual | Measured |
|-----------------|--------|--------|----------|
| Intensity at 90 | Peak 1 | 96%    | 100%     |
| Intensity at 90 | Peak 2 | 4%     | 0%       |
| Intensity at 30 | Peak 1 | 50%    | 48%      |
| Intensity at 30 | Peak 2 | 50%    | 52%      |
| Intensity at 11 | Peak 1 | 13%    | 21%      |
| Intensity at 11 | Peak 2 | 87%    | 79%      |

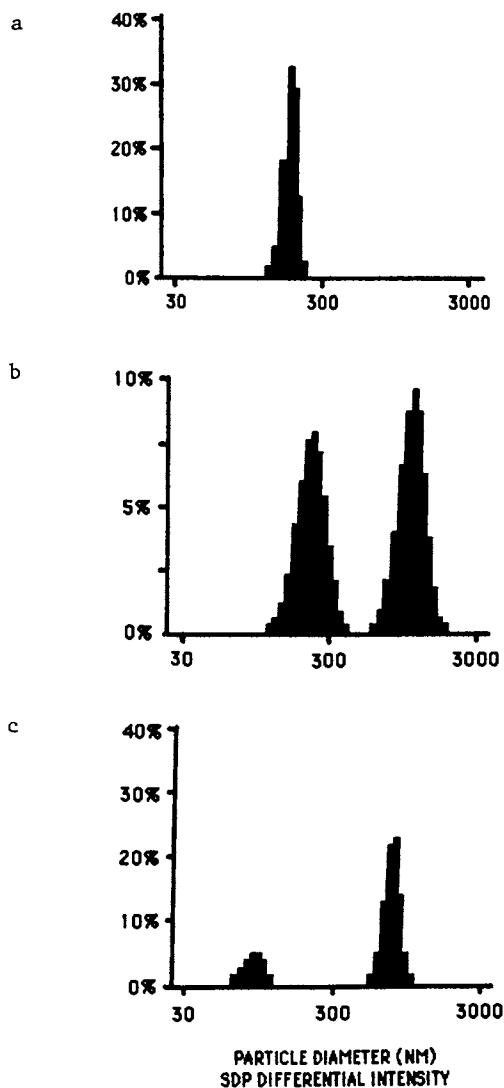


Figure 6a,b, and c. Measured intensity weighted particle size distribution of a bimodal distribution (91% by weight 170 nm PSL and 9% by weight 822 nm PSL). a, b, and c correspond to measurements made at 90 degree, 30 degree, and 11 degree scattering angles, respectively.

Notice that if a measurement had been made at 90 degrees alone, the presence of the 822 nm PSL would have been missed.

While intensity distributions are dependent on the angle at which they are measured, and therefore cannot be compared unless measured at the same angle, volume distributions are, of course, angle independent. As was mentioned earlier, PCS measurements made at different angles, because of the different weightings at the different angles, contain a fair degree of independent information. To integrate this information, is, however, difficult. The simplest approach toward integration is to simply average the volume distributions made over several angles to get a composite picture of the sample.

The PCS instrument used could automatically collect data from any six angles, store the results of individual runs to disk and average the runs afterwards. The instrument was set to make five 300 second runs at each of three scattering angles: 15, 30 and 90 degrees on the same bimodal sample (170/822nm PSL) as above. The individual angle and composite results of the five runs at each of the three angles are given below.

| Angle | Peak 1(nm) | Peak 2(nm) | Peak 1(% int,%vol) | Peak 2(%int,%vol) |
|-------|------------|------------|--------------------|-------------------|
| 15    | 162        | 1085       | 20, 89             | 80, 11            |
| 30    | 183        | 977        | 42, 78             | 58, 22            |
| 90    | 198        | --         | 100, 100           | 100, 0            |
| all   | 181        | 1031       | 89                 | 11                |

It should be mentioned that 300 second runs are rather short for resolving bimodals, especially at the lower angles. The signal to noise ratio in the autocorrelation function increases as the inverse of the scattering vector magnitude. Thus the signal to noise ratio at 15 degrees and 30 degrees increase, respectively, around 5.4 times and 2.7 times slower than 90 degrees. The 300 second run at 30 degrees is roughly equivalent to a 100 second run at 90 degree.

The multi angle averaging allows identification of both peaks; with a 90 degree measurement alone, the peak at larger size would have been missed. In addition, the sizes and volume percents of the two peaks are reasonably well characterized. In the table above, notice the difference in the % intensities in the two peaks at the different angles. To repeat, these differences in intensities with different scattering angles mean that independent information is obtained at different angles.

This independent information at different angles will occur whenever the particle size distribution in a sample is broad enough (whethethe distribution be mono, bi or multimodal) and the particle sizes large enough that the scattered light intensities at different scattering angles are different.

## CONCLUSIONS

The discussion and results above show the danger of relying heavily on size distribution information based on PCS measurements taken at a single scattering angle, especially on unknown samples. The relation between intensity and weight distributions, stipulated by the Mie equations, is such that in many cases two populations of particles may each comprise a substantial proportion of a sample when measured by weight proportion but be vastly different when compared by the intensity distributions measured by PCS. In these cases, the presence of a population of particles may be overlooked or poorly sized. By routinely making measurements at two or more scattering angles, especially on previously uncharacterized samples, there is a better chance of obtaining accurate size information. For many samples, results obtained with PCS measurements at only one scattering angle must be treated with caution.

Acknowledgment

The author gratefully acknowledges Karin Evans of Langley Ford instruments for her expert assistance in preparing and running the polystyrene samples.

## REFERENCES

1. B. Flegley and E.A. Barringer, Materials Research Soc. Symposium, 32, 187 (1984).
2. R.L. Martin and M.R. Niesman, Chem. Phys. Lipids, 34, 245 (1984).
3. B.J. Berne and R. Pecora, "Dynamic Light Scattering," John Wiley and Sons, N.Y., 1976.
4. S.W. Provencher, Makromol. Chem., 180, 201 (1979)
5. S.W. Provencher, Computer Physics Communications, 27, 229 (1982).
6. J.G. McWhirter and E.R. Pike, J. Phys. A: Math. Gen., 11, 1729 (1978).
7. M. Kerker. "The Scattering of Light and Other Electromagnetic Radiation," Academic Press N.Y., 1969.

RECEIVED July 17, 1986

## Chapter 6

# Using Quasi-Elastic Light Scattering To Study Particle Size Distributions in Submicrometer Emulsion Systems

C. A. Herb<sup>1</sup>, E. J. Berger<sup>1</sup>, K. Chang<sup>1</sup>, I. D. Morrison<sup>2</sup>, and E. F. Grabowski<sup>2</sup>

<sup>1</sup>Technical Center, Owens-Corning Fiberglas Corporation, Granville, OH 43023

<sup>2</sup>Webster Research Center, Xerox Corporation, Webster, NY 14580

Quasi-elastic light scattering is an excellent technique for studying the formation and stability of sub-micrometer emulsions. Improvements in the methods of quasi-elastic light scattering data acquisition and analysis that enable full particle-size distribution studies of sub-micrometer emulsion systems are discussed. Using several oil/water emulsion systems as examples, we demonstrate the ability of these techniques to determine the effect of emulsifier concentration on the particle-size distribution produced by an inversion method of emulsification. Some of the benefits of obtaining the full distribution are also discussed.

In addition to affecting its own stability and rheology, an emulsion's particle-size distribution often influences the quality of the products in which the emulsion is incorporated. The full particle-size distribution is, therefore, of some concern to the researcher trying to improve or modify the product properties. Once the link between the properties and the particle-size distribution is known, the goal of creating an acceptable distribution through control of processing variables during the emulsification can be addressed. The mean diameter, the width of the distribution, or even the distribution shape may be affected by altering variables such as the surfactant concentration, agitation intensity, and temperature.<sup>(1)</sup> Thus, the ability to monitor the full distribution, rather than just a mean diameter, allows better control of product quality and provides valuable additional information for product improvement and more fundamental emulsion studies.

When the particle sizes in question are below about 1 micrometer, the techniques available for determining the distribution become limited. The use of quasi-elastic light scattering (QELS) for the measurement of these sub-micrometer particles is becoming increasingly popular with the availability of several commercial instruments capable of both gathering and analyzing data.<sup>(2)</sup> One of the major advantages of using QELS for emulsion studies is the

0097-6156/87/0332-0089\$06.00/0

© 1987 American Chemical Society

ability to work in any medium. Thus, both water/oil and oil/water emulsions are easily studied. In addition, concentrated samples can be diluted with the original continuous phase, thus maintaining the proper environment for the droplets. Likewise, one can systematically alter the environment to study the effects of such changes on the stability of the system. In addition, the preparation of the scattering samples is fast and simple.

The aim of this paper is to describe the experimental and numerical techniques that, when combined, provide a procedure that enables full particle-size distribution studies of sub-micrometer emulsion systems. We then present distribution results for several oil/water emulsions to demonstrate the ability of these techniques to monitor the effect of processing variables (such as surfactant concentration) on the final emulsion. Finally, we discuss some of the problems of converting the intensity weighted distribution to a mass weighted distribution and suggest methods for minimizing or eliminating some of these problems.

### Background

Many excellent introductions to quasi-elastic light scattering can be found in the literature describing the theory and experimental technique (e.g. 3-6). The use of QELS to determine particle size is based on the measurement, via the autocorrelation of the time dependence of the scattered light, of the diffusion coefficients of suspended particles undergoing Brownian motion. The measured autocorrelation function,  $G^{(2)}(\tau)$ , is given by

$$G^{(2)}(\tau) = A \left[ 1 + \beta |g^{(1)}(\tau)|^2 \right] \quad (1)$$

A is the base line, which is obtained either from the long-time asymptote of the measured autocorrelation function or from the square of the average photon flux.  $\beta$  is an equipment-related constant, and  $g^{(1)}(\tau)$  is the normalized first-order autocorrelation function, which is easily obtained from the measured function,  $G^{(2)}(\tau)$ . For monodisperse systems  $g^{(1)}(\tau)$  is a simple exponential decay with the desired information being contained in the decay constant,  $\Gamma$ , which is equal to  $q^2 D$ , where  $q$  is the magnitude of the scattering vector ( $q = (4\pi n/\lambda) \sin(\theta/2)$ ) and  $D$  is the translational diffusion coefficient. If the sample is dilute enough that the motion of a particle is not affected by the presence of the other particles in the sample, or if  $\Gamma$  is obtained as a function of concentration and extrapolated to zero concentration, one obtains the single-particle diffusion coefficient. If the medium is a Newtonian fluid and one further assumes that the particles are spherical (an excellent assumption for emulsions), the Stokes-Einstein relation between the single-particle diffusion coefficient and the hydrodynamic diameter of a particle can be used (i.e.  $D = kT/(3\pi\eta d)$ ), or:

$$\Gamma = (16\pi k T n^2 \sin^2 \frac{\theta}{2}) / (3\eta \lambda^2 d) \quad (2)$$

where  $k$  is the Boltzmann constant,  $T$  is temperature,  $n$  is the refractive index of the fluid,  $\theta$  is the scattering angle,  $\eta$  is the viscosity,  $\lambda$  is the wavelength of the light, and  $d$  is the particle diameter.

For polydisperse samples,  $g^{(1)}(\tau)$  is a function not only of the delay time  $\tau$ , but also of the distribution of decay constants as shown in Equation 3 in integral form and in Equation 4 in algebraic form.

$$g^{(1)}(\tau) = \int_0^{\infty} F(\Gamma) \exp(-\Gamma\tau) d\Gamma \quad (3)$$

$$g^{(1)}(\tau) = \sum_{i=1}^M a_i \exp(-\Gamma_i\tau) \quad (4)$$

Thus, given  $g^{(1)}(\tau)$ , we need to determine the particle size distribution. For narrow size distributions, the autocorrelation function is satisfactorily analyzed by the method of cumulants to give the moments of the particle size distribution.<sup>(7)</sup> However, the analysis of QELS data for samples with polydisperse or multimodal distributions remains an area of active research.<sup>(8)</sup>

In order to obtain the particle-size distribution, one must invert Equation 3 or 4 numerically. When the data are analyzed via Equation 4, one obtains a histogram described by a probability for each decay constant, expressed by the vector set  $(a_i, \Gamma_i)$ . A particle diameter distribution can then be obtained from this via Equation 2. On first glance, it would seem that one could simply choose a large number of particle sizes, calculate the corresponding decay constants, and find the best set of  $a_i$ 's by a least squares fit of the  $g^{(1)}(\tau)$  data to Equation 4 for the assumed particle sizes. The expectation is that only those sizes that are actually in the dispersion will appear in the final distribution. Unfortunately, the inversion of Equation 4 is known to be ill-conditioned for the standard least squares technique. That is, small changes in the measured data lead to large variations in the calculated distributions.<sup>(9)</sup> A more detailed discussion of the problem has been given by Pike<sup>(10)</sup>, in which he suggests that the ill-conditioned nature of the inversion will be reduced by limiting the range of the solution space via a priori information about the distribution, and by increasing the range of delay times over which the autocorrelation function is obtained. The increase in the range of delay times has been successfully addressed by the manufacturers of digital autocorrelators by providing non-linear spacing of the correlator channels. The use of reasonable a priori information to limit the range of the solution space will be discussed in the next section.

### The Inversion Algorithm

Requirements. A successful and yet practical numerical procedure for obtaining particle-size distributions from QELS data must: 1) be stable against random experimental error, 2) clearly differentiate multimodal distributions from broad unimodal ones without a priori knowledge of the shape of the distribution, 3) require only minimal operator input, and 4) apply to both narrow and broad particle size distributions. An additional desideratum is that the computer requirements be kept to a reasonable level.



Proposal. We have recently described a procedure that we believe meets the requirements listed above.(11) More specifically, we have shown that the particle size distribution can be extracted from the QELS data by a combination of a) a convergent numerical algorithm that makes use of the fact that the distribution of sizes must be non-negative (12), b) analysis of each data set with multiple but equivalent basis sets of particle sizes (13), and c) the averaging of distributions obtained from repeated, independent measurements for each sample analyzed.(11) Only a brief discussion of the procedure will be given here. More complete discussions are given elsewhere.(11,12)

The Non-Negative Constraint. As discussed above, the inversion of Equation 4 is ill-conditioned. This manifests itself most clearly by providing distributions with negative components when ordinary least squares algorithms are used. The tendency to produce these physically impossible solutions can be reduced by limiting the number of assumed particle sizes used in the inversion. This decreases the range of the solution space, thus reducing the ill-conditioned nature of the problem as discussed in the last section. Unfortunately, it has been found that the number of sizes that can be used successfully is so few (5 or 6 at best) that the size resolution is poor. Another way to significantly decrease the range of the solution space is to disallow all solutions that contain negative components. The use of this non-negative constraint during the calculations substantially reduces the ill-conditioned nature of the inversion. The increase in the stability of the inversion allows a larger number of unknowns to be used, thus increasing the potential resolution. To implement the method of non-negatively constrained least squares, we choose the method of Lawson and Hanson (14) called NNLS (for non-negative least squares). The use of this a priori information has not limited the general nature of the distribution in any way. The details of using NNLS for the QELS problem have been presented elsewhere.(12)

Multiple Pass Analysis. Pike and coworkers (13) have provided a method to increase the resolution of the ordinary least squares algorithm somewhat. It was noted that any reasonable set of assumed particle sizes constitutes a basis set for the inversion (within experimental error). Thus, the data can be analyzed a number of times with a different basis set each time, and the results combined. A statistically more-probable solution results from an average of the several equally-likely solutions. Although this "multiple pass analysis" helps locate the peaks of the distribution with better resolution and provides a smoother presentation of the result, it can still only provide limited resolution without the use of a non-negatively constrained least squares technique. We have shown, however, that the combination of both the non-negatively constrained calculation and the multiple pass analysis gives the advantages of both.

We implement multiple pass analysis for an arbitrary spacing of assumed sizes as follows. Let there be M assumed particle sizes submitted to the NNLS inversion routine for each of P passes. Thus, the final histogram will contain MP different particle sizes spaced in some fashion (e.g. logarithmically, quadratically, or linearly)

over the appropriate range. The upper and lower limits of the range can be chosen by the operator if reasonable values are known, or they can be chosen by the program from the shape of the first auto-correlation function. Once the range is selected, all MP sizes are calculated according to the chosen spacing scheme.

We actually submit  $M+1$  sizes to NNLS on each pass, the extra size corresponding to a "dust" signal (i.e. infinite particle size or a zero decay constant). Thus, on the first pass, we find the best fit to the correlation function using only the  $M+1$  particle sizes:

$$d_1, d_{P+1}, d_{2P+1}, \dots, d_{MP-P+1}, \text{ and } d_{\text{dust}}$$

In general, on the  $j$ th pass, we use the  $M+1$  particle sizes:

$$d_j, d_{P+j}, d_{2P+j}, \dots, d_{MP-P+j}, \text{ and } d_{\text{dust}}$$

The analysis from the  $P$  passes are combined to give an overall multiple pass analysis of the data. The result is an MP bin histogram and a measure of the amount of the signal that is due to "dust".

Distribution Averaging. Although the resolution is significantly improved by the use of a non-negatively constrained least squares algorithm, it has two shortcomings: 1) Correlated experimental error is often interpreted as small spurious peaks; and 2) Broad unimodal distributions tend to be represented by a set of separated peaks. Although multiple pass analysis improves the presentation of multimodal distributions and unimodal distributions that are not too wide, it fails to correct these two shortcomings.

We have found that both these shortcomings can be reduced or eliminated by taking multiple data sets on the same sample, analyzing each data set independently, and averaging all of the resulting size distributions. The correct peaks are reinforced while spurious peaks are diminished. A gap will remain between the peaks of a true bimodal sample. If, however, the sample actually has a wide unimodal distribution, the positions of the separated peaks will vary from one data set to another, thus filling in to a smooth unimodal peak. Once again, a statistically more-probable solution results from an average of the several equally-likely solutions. (The number of independent data sets used should be greater than twice the number of particle sizes in the broadest peak divided by  $P$ , the number of passes.)

What is particularly significant is that the QELS analysis is enhanced by the combination of the three techniques presented here without introducing any new assumptions or requiring any unreasonable a priori information, not even that the distribution must be smooth.

Peak Broadening. The peaks obtained by the procedure outlined above can be broadened beyond the true distribution by two things. First, the use of too few assumed particle sizes for the inversion will obviously cause the reported distribution to be broader than it should be. This problem is resolved by choosing a larger number of assumed sizes. (We typically choose twenty particle diameters for each inversion.) The second problem is that the reported distribution will be artificially broadened by excessive noise in the auto-

correlation functions obtained. This can only be solved by increasing the quality of the data collected, which implies longer data collection times or an increase in the photon count rate, if possible. We have previously demonstrated this noise related broadening with a mixture of latex standards (11,15). Practically, we have found that this broadening is not a serious problem if the total photon count for each autocorrelation function is kept above 15 or 20 million (e.g. 10 million samples with a count rate of 1.5 to 2 photons per sample time).

### Emulsion Studies

As discussed earlier, it is known that the surfactant concentration present during emulsification can affect the particle size of an emulsion. It has also been shown that the stability of an emulsion can be affected in rather unexpected ways by changing the concentration of the surfactant (16). The techniques presented in the last section allow the researcher to follow the full particle-size distribution of the emulsion system rather than just an average diameter. Using several oil/water emulsion systems as examples, we demonstrate the ability of these techniques to determine the effect of emulsifier concentration on the particle-size distribution produced by an inversion method of emulsification. Some of the benefits of obtaining the full distribution will also be discussed.

Experimental. Particle-size distribution results were obtained for three emulsion systems, referred to as systems A, B, and C. The oil phase of emulsion systems A and C consists of 70% by weight of a thermoset resin in an organic solvent. The oil phase of emulsion system B is a different thermoset resin with no solvent present. A different nonionic emulsifier was used for each of the three emulsion systems. The emulsions were prepared by slowly adding water to the mixture of oil phase and surfactant in a high shear mixer. Following inversion from the water/oil to oil/water emulsion, additional water was added to bring the final internal phase to 50% by weight. The light scattering samples were prepared by diluting a small portion of the emulsion to 20 mg/L oil phase with a dust free, 10 mg/L solution of the emulsifier. The sample was then filtered through a 5 micrometer membrane filter directly into the scattering cell.

Equipment. All scattering experiments were done on a BI240 light scattering goniometer from Brookhaven Instruments Corporation. This includes all the necessary optics, sample cell assembly, photomultiplier tube, amplifier/discriminator, and the goniometer base itself. The temperature of the sample cell and index matching liquid surrounding the cell was held at 25°C with a Neslab RTE-5DD circulating bath. The light source is a Spectra-Physics, Model 124B, 15 mW, linearly polarized, HeNe laser. The laser and optical components are mounted on a Newport Research Corporation vibration isolation table.

A BI2020 digital correlator, also from Brookhaven Instruments, receives the signal from the amplifier/discriminator. The correlator has 136 channels followed by 4 baseline channels starting at 1024 sample times. In our laboratory, the correlator is controlled

by a Hewlett-Packard 236 microcomputer (formerly designated the HP9836), which also performs the distribution analysis. The program controls the BI2020 correlator while calculating the distribution from the latest autocorrelation function. In this way data can be collected while the individual distributions are being calculated and averaged. The system requires no operator input once the run has been started. The final distributions are converted from light intensities to mass fractions using the Mie correction factors as is discussed in a later section.

**Results.** Figure 1 shows the distributions for emulsion system A for total emulsifier concentrations ranging from 3.5 to 20 g/100g oil phase. It can be seen that both the mean diameter and the width of the distribution decrease with increasing surfactant level. The same trend was seen for system B over the range of 8 to 21 g/100g oil phase. System B could not be emulsified by the inversion technique below this range. Figure 2 shows the mean diameter and standard deviations of both systems as a function of emulsifier concentration. (It is interesting, but only a coincidence, that both systems give the same results over the 8 to 20 g/100g range.) Thus, for these systems one can now predict the mean diameter and the width of the distribution once the surfactant concentration is known. Conversely, if the distribution of a sample were measured for quality control purposes and the diameter and width were too high, an incorrect surfactant concentration during emulsification would be indicated as a possible cause.

A more interesting way to look at the data is to plot the specific surface area of the emulsion droplets as a function of the surfactant concentration as shown in Figure 3. (The surface area was calculated from the full distribution rather than from a mean diameter.) Thus, it can be seen that, over the range studied, an increase in the amount of surfactant present causes a proportional increase in the surface area created.

Because all of these distributions are unimodal and have relative standard deviations less than 35%, the method of cumulants could have been used to obtain the data of Figure 2. However, the distribution technique used here can distinguish between bimodal and broad unimodal distributions with no operator intervention or a priori knowledge about the sample. The importance of this ability is demonstrated by the distribution of emulsion system C shown in Figure 4. This system was prepared in an identical fashion to systems A and B, but with a low concentration of a different nonionic emulsifier. The resulting bimodal distribution was certainly not an expected result. Note that the broad unimodal of Figure 1a and the bimodal of Figure 4 have similar mean diameters and standard deviations. The ability to distinguish between the two can be of significant assistance in the investigation of emulsion systems. Indeed, the distribution shown in Figure 4 is indicative of non-uniform shear conditions during the emulsification rather than a surfactant concentration problem.

**Flocculation versus Coalescence.** The breaking of an emulsion is a two step process requiring the coalescence of the droplets after they are in contact.<sup>(17)</sup> If the system flocculates but is resistant to coalescence, the system will not phase separate. Over a period

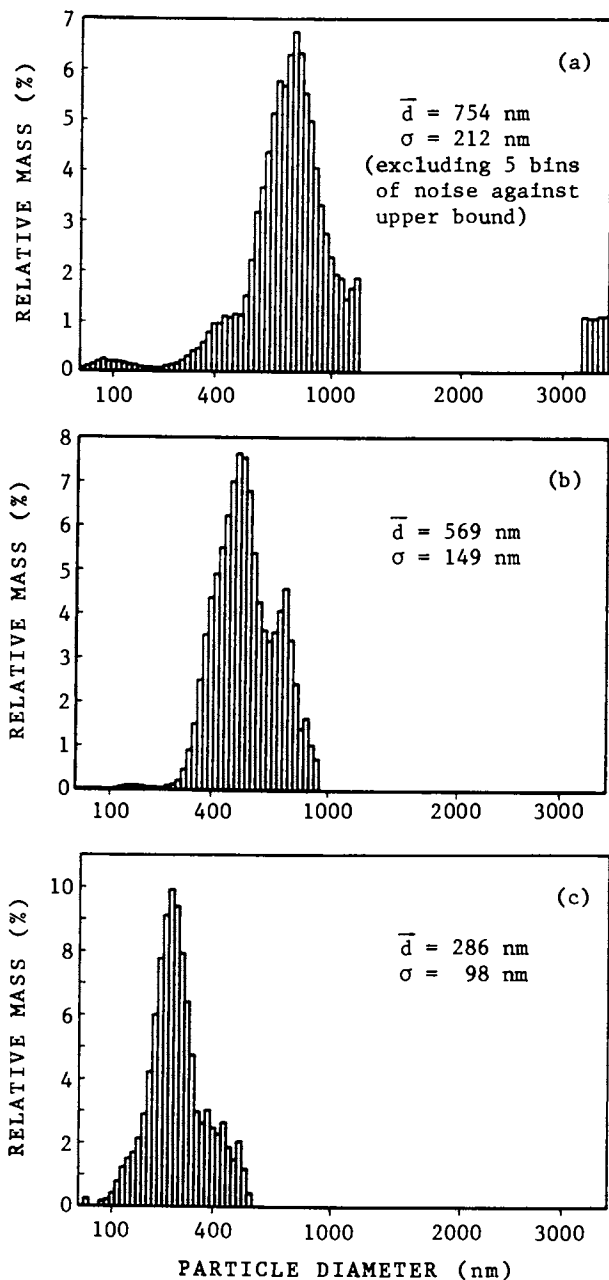


Figure 1. Particle size distributions for emulsion system A with various emulsifier concentrations (in g/100g oil phase): (a) 3.5, (b) 5, (c) 10. Each figure is an average of 15 distributions, each of which was obtained using quadratic spacing with 20 particle sizes per pass and 5 passes.

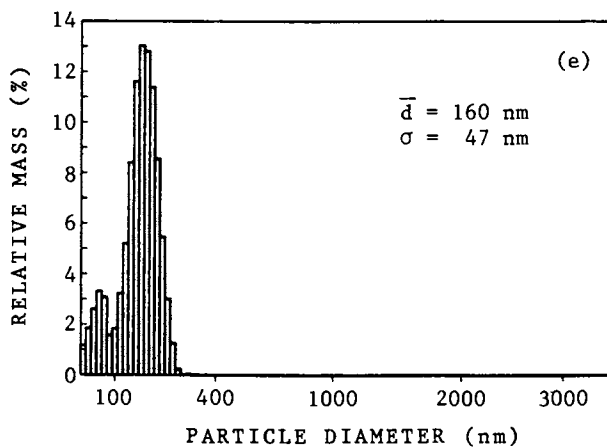
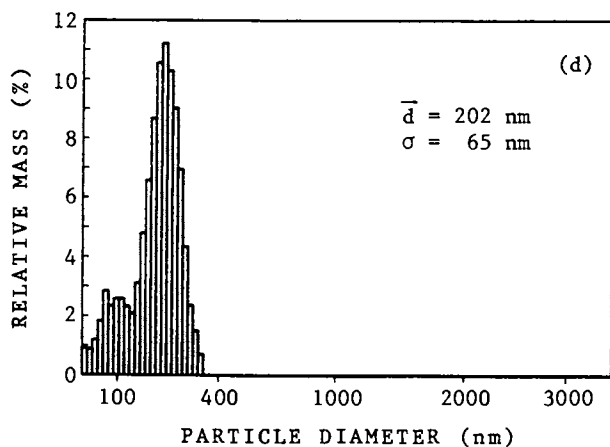


Figure 1. Continued. Particle size distributions for emulsion system A with various emulsifier concentrations (in g/100g oil phase): (d) 15, (e) 20. Each figure is an average of 15 distributions, each of which was obtained using quadratic spacing with 20 particle sizes per pass and 5 passes.

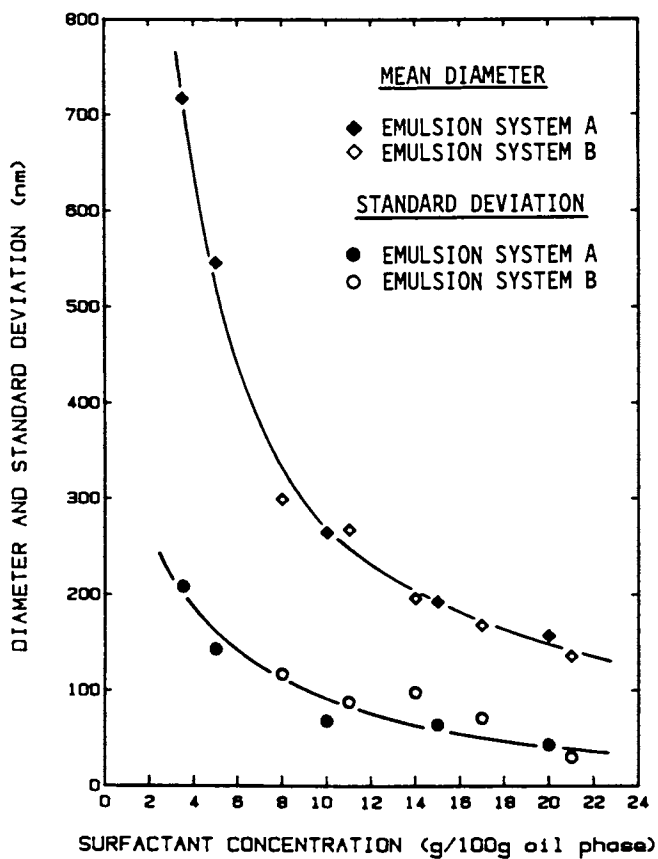


Figure 2. Mean diameter and standard deviation versus surfactant concentration for emulsion systems A and B.

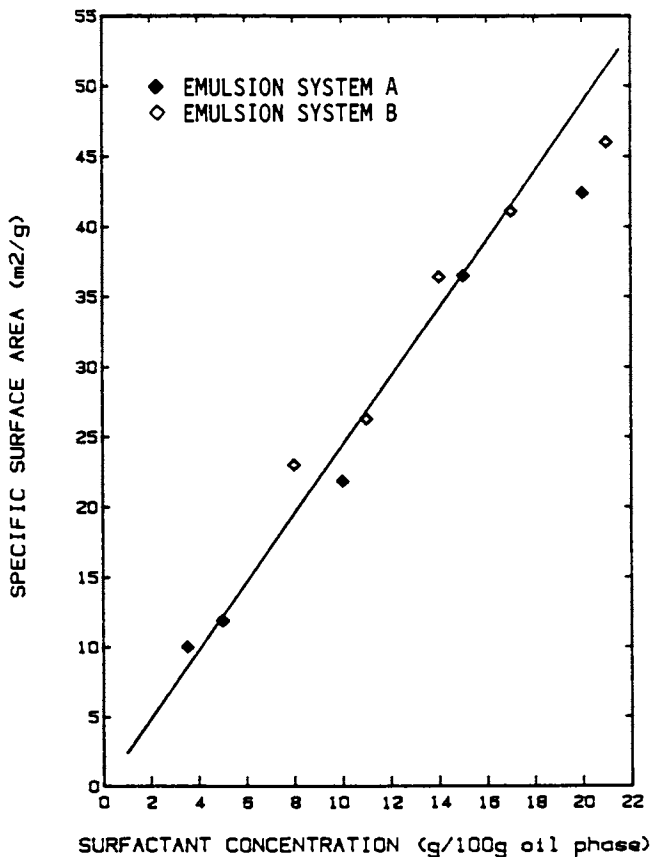


Figure 3. Specific surface area of internal phase versus surfactant concentration for emulsion systems A and B, as calculated from the full distributions.

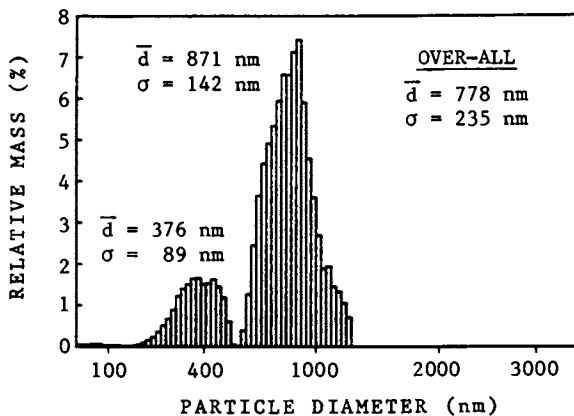


Figure 4. Particle-size distribution of emulsion system C with emulsifier concentration of 7 g/100g oil phase. The figure is an average of 10 distributions, each of which was obtained using quadratic spacing with 20 particle sizes per pass and 5 passes.

In Particle Size Distribution; Prover, T.;



of time, some of our samples flocculated and settled. It was of interest to determine whether there was any coalescence of the particles under these conditions. After several months, these samples were re-examined to determine their particle size distributions. No change in the distributions was found, indicating that the samples were, indeed, resistant to coalescence. An example of the ability of the QELS techniques presented here to follow slowly flocculating emulsion samples can be found in reference 15.

### Light Scattering Corrections

The distribution obtained from the inversion of Equation 4 is an intensity weighted distribution. That is, it displays the percentage of light scattered from each particle size in the population. What is desired is the amount of mass at each particle size (mass distribution), or the number of particles at each particle size (number or frequency distribution). In principle, once any distribution is known, the others can be calculated. Because of finite detection limits and noise in actual experimental data, however, it is not that straightforward.

What is required is a knowledge of the relative amount of light scattered from particles of different diameters in the sample. In general this depends not only on the particle size, but also on the refractive indices of the particles and the medium, the scattering angle, the wavelength of the incident light, and the shape of the particles. (18,19) The range of particle sizes accessible to the QELS technique extends up to about 5 micrometers, thus exceeding the limits of both the Rayleigh approximation and (for any reasonable refractive index ratio) the Rayleigh-Debye-Gans approximation. Because emulsion particles are spherical, the exact solution of the absorption and scattering problem for spheres, commonly referred to as the Mie theory, can be applied. Until recently, a large main-frame computer was required to carry out the necessary calculations involved. Tables of Mie coefficients have been published by various people, allowing table look up methods to be used. We originally used the 90 degree scattering tables of Pangonis, et al. (20) for the correction of our QELS data. With the advent of 16 bit micro-processor based desk top computers, however, there is little reason not to calculate the exact Mie coefficients needed for the distribution being corrected. We now use a modified form of the subroutine BHMIE of Bohren and Huffman (19) to calculate the required coefficients. This allows us to work easily at any angle and with particles of any refractive index (including complex refractive indices).

Having obtained the relative scattering intensity per unit mass for each particle size from the Mie theory, the mass weighted distribution should be obtained by dividing the histogram magnitude for each particle size by this scattering factor. For very narrow distributions (such as monodisperse latex standards) or bimodal distributions composed of two narrow distributions, this will work very well. If the sample has a broad unimodal distribution and includes diameters approaching or larger than the wavelength of the incident light, small errors in the intensity weighted distribution can lead to large errors in the calculated mass weighted result. In addition, the presence of certain particle diameters may go undetected in the

presence of more highly scattering particles for any given angle. These problems are due to the oscillations in the scattering intensity as a function of particle size at a given angle. Figure 5 shows the scattering intensity per unit mass of particles as a function of diameter for a system in which the particles have a refractive index of 1.59 (e.g. polystyrene), the medium has a refractive index of 1.33 (e.g. water), and the light source has a wavelength of 632.8 nm (i.e. a HeNe laser). Note that the first three minima are at approximately 450 nm, 760 nm, and 1080 nm. It can be seen that if the sample had a bimodal distribution with narrow distributions at 250 nm (the first maximum) and 760 nm, it would be difficult to detect the 760 nm peak unless it contained a large percentage of the mass. Likewise, if a broad unimodal distribution that extended from 200 nm to 1200 nm was measured at 90 degrees and corrected using Figure 5, small amounts of error at the minima would lead to large errors in the final mass weighted result.

We currently attempt to minimize this problem by averaging the Mie scattering factor over several particle sizes before applying the correction. On each pass of the multiple pass analysis, the inversion algorithm chooses the two particle sizes that bracket the actual diameter. Thus, there is some "spilling over" into adjacent diameters. We assume that for "good" data (i.e. low noise in the autocorrelation functions), this will go no farther than one diameter to either side. Thus, the light scattering factor may also need to be averaged over the three diameters. If there are P passes, this becomes an average over 3P diameters in the final distribution. This procedure tends to "soften" the effect of the sharp maxima and minima in the function shown in Figure 5. Although this provides reasonable histograms, it is not a completely satisfactory solution because of the arbitrary choice of 3P diameters for the averaging.

Because the light scattering versus particle size relationship depends on angle, it is reasonable to assume that a solution to the problem lies in the judicious use of multiangle data. We suggest that a possible solution would be to obtain autocorrelation functions at more than one angle and to fit all angles simultaneously with the Mie factors included in the inversion. Such a calculation would require no more computer memory than single angle data and should, if the angles are chosen properly, help reduce the problems discussed above.

### Conclusions

We have shown that the particle-size distributions of sub-micrometer emulsions can be successfully obtained from QELS data by: 1) using a least-squares technique that utilizes the non-negativity constraint as part of the iterative calculation, 2) analyzing each data run with several sets of assumed particle sizes and combining the resulting distributions, and 3) taking several sets of data on the same sample, analyzing each set independently, and averaging the final distributions. The combination of these techniques provides increased resolution while minimizing the tendency to confuse bimodal and broad unimodal distributions. In addition, the technique requires very little input from the operator, no a priori information about the shape of the distribution, and can be run on a desk top computer.

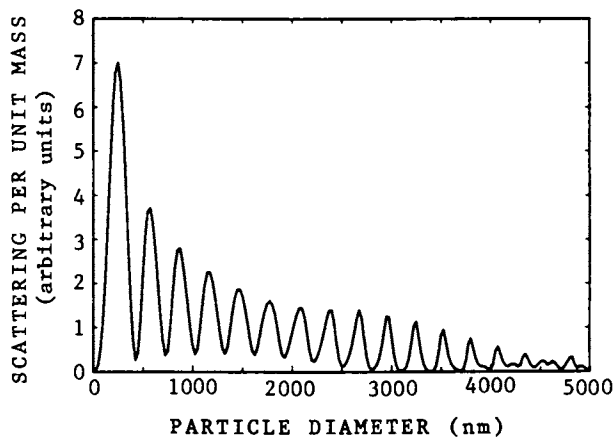


Figure 5. Scattering intensity per unit mass of particles as a function of particle diameter for a system in which the wavelength of the incident light is 632.8 nm, the scattering angle is  $90^\circ$ , the particle refractive index is 1.59, and the medium refractive index is 1.33 (for example polystyrene spheres in water).

We presented distribution results for several oil/water emulsions to demonstrate the ability of these techniques to monitor the effect of processing variables (such as surfactant concentration) on the final emulsion. The benefits of knowing the full distribution rather than a mean diameter only were discussed. Finally, we discussed some of the problems of converting the intensity weighted distribution to a mass weighted distribution and suggested methods for minimizing these problems.

A FORTRAN implementation of this technique is available from the authors.

#### Literature Cited

1. Walstra, P. In "Encyclopedia of Emulsion Technology"; Becher, P., Ed.; Dekker: New York, 1983; Vol. 1, Chap. 2.
2. Brookhaven Instruments Corp., Ronkonkoma, NY.  
Coulter Electronics, Hialeah, FA.  
Hiac/Royco (Nicom instrument), Menlo Park, CA.  
Malvern Instruments Ltd., Malvern, Worcestershire, UK.
3. Pecora, R. In "Measurement of Suspended Particles by Quasi-Elastic Light Scattering"; Dahneke, B. E., Ed.; Wiley: New York, 1983; Chap. 1.
4. Ford, N. C. In "Measurement of Suspended Particles by Quasi-Elastic Light Scattering"; Dahneke, B. E., Ed.; Wiley: New York, 1983; Chap. 2.
5. Berne, B. J.; Pecora, R. "Dynamic Light Scattering with Applications to Chemistry, Biology and Physics"; Wiley-Interscience: New York, 1976.
6. Chu, B. "Laser Light Scattering"; Academic Press: New York, 1974.
7. Koppel, D. E. J. Chem. Phys. 1972, 57, 4814.
8. Dahneke, B. E., Ed. "Measurement of Suspended Particles by Quasi-Elastic Light Scattering"; Wiley: New York, 1983.
9. Tikhonov, A. N.; Arsenin, V. Y. "Solutions of Ill-Posed Problems"; John, F., Translator; Wiley: New York, 1977.
10. Pike, E. R. In "Scattering Techniques Applied to Supramolecular and Nonequilibrium Systems"; Chen, S.; Chu, B.; Nossal, R., Eds.; NATO Advanced Study Institutes Series, Vol. B73, Plenum: New York, 1981; pp. 179-200.
11. Morrison, I. D.; Grabowski, E. F.; Herb, C. A. Langmuir 1985, 1, 496-501.
12. Grabowski, E. F.; Morrison, I. D. In "Measurement of Suspended Particles by Quasi-Elastic Light Scattering"; Dahneke, B. E., Ed.; Wiley: New York, 1983; Chap. 7.
13. McWhirter, J. G.; Pike, E. R. J. Phys. A. Math. Gen. 1978, 11, 1729.
14. Lawson, C. L.; Hanson, R. J. "Solving Least Squares Problems"; Prentice-Hall: Englewood Cliffs, NJ, 1974. A FORTRAN program and subroutines called NNLS.
15. Herb, C. A.; Morrison, I. D.; Grabowski, E. F. In "Magnetic Resonance and Scattering in Surfactant Systems"; Magid, L., Ed.; Plenum: New York, (in press).
16. Fairhurst, D.; Aronson, M. P.; Gum, M. L.; Goddard, E. D. Colloids and Surfaces 1983, 7, 153-159.

17. Tadros, T. F.; Vincent, B. In "Encyclopedia of Emulsion Technology"; Becher, P., Ed.; Dekker: New York, 1983; Vol. 1, Chap. 3.
18. Kerker, M. "The Scattering of Light and Other Electromagnetic Radiation"; Academic Press: New York, 1969.
19. Bohren, C. F.; Huffman, D. R. "Absorption and Scattering of Light by Small Particles"; Wiley: New York, 1983.
20. Pangonis, W. J.; Heller, W.; Economou, M. A. J. Chem. Phys. 1961, 34, 960-970.

RECEIVED June 27, 1986

## Chapter 7

# Measuring Particle Size Distribution of Latex Particles Using Dynamic Light Scattering

Ruth S. Stock<sup>1</sup> and W. Harmon Ray

Chemical Engineering Department, University of Wisconsin, Madison, WI 53706

In a light-scattering experiment, particles that have diameters on the order of the wavelength of incident light and a large refractive index relative to that of the medium, e.g. polymer latex in water, scatter light according to Mie theory. The intensity of the scattered light varies by an order of magnitude in an oscillatory fashion with respect to particle size. It was possible to incorporate the mathematical description of Mie theory into Provencher's constrained regularization method to find the distribution by weight. Alternatively, a simple linear least squares algorithm is used to find the particle size distribution by intensity; this is then transformed to a distribution by weight using Mie theory. Measurements are made at multiple scattering angles and the particle size distributions are compared. A composite distribution formed by averaging the weight distributions found at various angles is considered. These methods are demonstrated on multimodal and broad distributions.

Dynamic light scattering may be used to determine the particle size distribution or molecular weight distribution in a wide variety of applications. See ref. (1) for discussion of this literature. There are special problems that occur when the particle diameter is large relative to the wavelength of incident light. This is of interest since many latex systems have particles with diameters of 300 to 1000 nm and a large ratio of particle to fluid refractive index (1.2 for polystyrene latex). The most common wavelengths for lasers used in light scattering are on the order of 500 nm.

Light entering a particle at two different points will experience different path lengths. The refractive index difference between the particle and the medium will also cause a phase shift in the scattered light leaving the particle (see Figure 1). Due to these effects, the intensity of light scattered by suspended spherical particles depends on the particle diameter relative to the wavelength of incident light, the scattering angle and the refractive index ratio. Plots of intensity as a function of angle for a polystyrene/water system with 514.5 nm incident laser wavelength are shown in Figure 2.

<sup>1</sup>Current address: General Motors Research Laboratories, Warren, MI 48090-9055

0097-6156/87/0332-0105\$06.00/0

© 1987 American Chemical Society

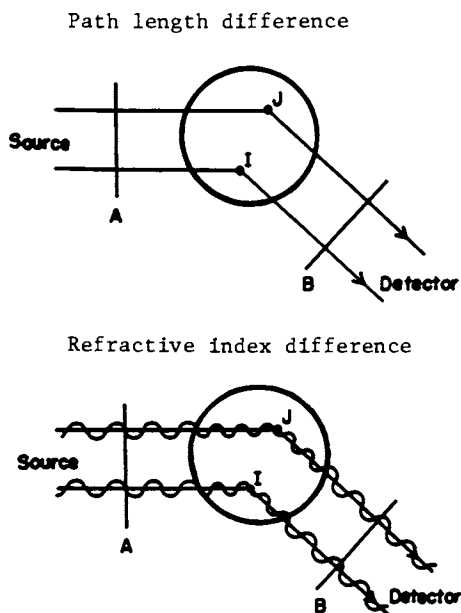


Figure 1. Schematic diagram of effects which give rise to Mie scattering.

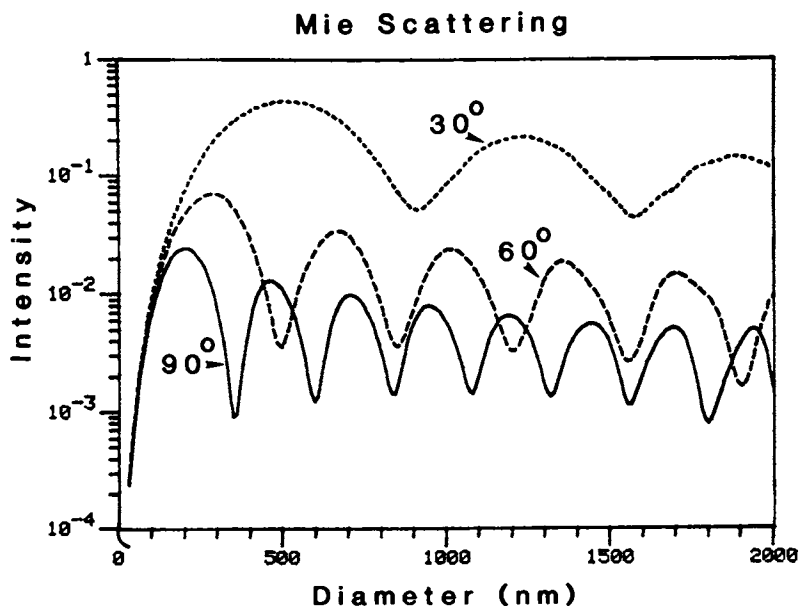


Figure 2. Predictions of intensity per unit particle volume as a function of particle diameter for three scattering angles given incident wavelength 514.5 nm and refractive index ratio polystyrene/water of 1.2.

In order to account for these effects, one may use Mie theory to obtain the volume or mass (in the case of a homogeneous density system) distribution of latex particles instead of the intensity distribution initially obtained from quasielastic light scattering data. Bedwell et. al. (2) have obtained the mass distribution of large particles by incorporating Mie theory into the histogram method. Here we propose two methods of data analysis. First, Provencher's method of constrained regularization has been modified to include the Mie scattering factor in the kernel of the integral to be inverted. This method is similar to that developed independently by S. Bott (3). Second we consider using a simple non-negatively constrained linear least squares fit and combining information obtained from data taken at several scattering angles.

### Data Analysis

Both Provencher's method and the non-negative least squares (NNLS) method first obtain the best fit in the least squares sense. In fact Provencher's program uses the NNLS program as part of the analysis procedure. Provencher's method departs from the NNLS solution by regularizing so that the smoothest particle size distribution consistent with the data is obtained. This regularization is accomplished by including a term in the objective function which is related to the second derivative of the particle size distribution. As the particle size distribution becomes smoother this term becomes smaller resulting in the minimum value of the objective function. In both methods the least squares parameters consisted of 40 histogram step heights spread over a two decade particle size range. The maximum number of parameters allowed in Provencher's program is 50.

The intensity distribution of particle size,  $G(a)$ , is related to the experimentally observed electric field autocorrelation function,  $g^{(1)}(\tau)$  as follows

$$g^{(1)}(\tau) = \int_{a_{\min}}^{a_{\max}} G(a) \exp(-k_B T k^2 \tau / 3\pi \eta a) da \quad (1)$$

Here  $G(a)$  is the intensity scattered by the particles with diameters between  $a$  and  $a+da$ ,  $k_B$  is Boltzmann's constant,  $T$  the temperature,  $k$  the scattering vector ( $k$  dependent on scattering angle and wavelength),  $\tau$  the correlation time and  $\eta$  the viscosity. To find the mass fraction distribution,  $F(a)$ , we use

$$g^{(1)}(\tau) = \int_{a_{\min}}^{a_{\max}} F(a) (i_1(a) / \alpha^3) \exp(-k_B T k^2 \tau / 3\pi \eta a) da \quad (2)$$

where  $i_1(a)$  is the scattered intensity per particle (6) and  $\alpha$  is the dimensionless particle size

$$\alpha = \pi a n / \lambda \quad (3)$$



Here  $n$  is the refractive index of the medium and  $\lambda$  is the wavelength of incident light in a vacuum. We modified Provencher's program to call a subroutine which would supply values of  $(i_1(a)/\alpha^3)$  for the kernel of the integral. The initial solution is that with little or no regularization. A chosen solution where the increase in the objective function over the initial solution could about 50% of the time be due to experimental noise and about 50% of the time be due to oversmoothing, is selected by a statistical criterion (4,5).

A second analysis procedure involves using the results from many scattering angles to extract the mass fraction distribution of particle size from the data. Since it would be hard to find an optimum scattering angle (that which has a relatively high intensity for the particle size(s) of interest) without already knowing the particle size distribution, one possibility is to average information from several scattering angles. We use the non-negatively constrained least squares method (6), without further regularization, to obtain the particle size distribution. Then, the Mie factors (7) are computed for each particle size. These scattering factors are used to convert the intensity distribution at each angle to a mass distribution of particle sizes. Finally, the 10 mass distributions (one for each angle) are averaged together to form a composite distribution. Other investigators (8,9,10) have used a similar method in which intensity distributions from NNLS are converted to mass distributions using Mie factors; however, they obtain data for longer time periods at a single scattering angle.

### Experimental

Four separate latex samples were analysed. A bimodal mixture was composed by mixing equal parts of solutions with 0.003% solids of Dow latex monodisperse standards with nominal diameters 109- and 497-nm having standard deviations of 2.7 and 5.9 nm respectively. The mixture was sonicated to eliminate aggregates. A polystyrene latex with a broad distribution was obtained from Kodak. This distribution had been characterized previously by electron microscopy, ultra centrifuge and Coulter counter. A monodisperse, surfactant free, sulfated, polystyrene standard and a mixture of 10 such monodisperse standards were purchased from Interfacial Dynamics Corporation. A polyvinyl chloride latex with a broad distribution was donated by B. F. Goodrich. This sample had been characterized by Joyce Loebel disc centrifuge. These samples were diluted to 0.01% solids and sonicated to eliminate aggregates.

The correlation function was measured using a Malvern K7025 correlator. The wavelength of the incident light (argon ion laser, Lexel Model 95) was 514.5 nm. The temperature of the water bath surrounding the sample cell was 307.6 K. The same equipment was used in a previous publication (1). However, the data collection program was modified to discriminate against dust (11). In this FORTRAN program total photon count from several short (5 or 10 second) runs were used to establish photon count average and standard deviation. After each short experiment the data was accepted only if its photon count was less than the mean photon count plus three standard deviations. Each short experiment was normalized to its own base line. A series of 60 five second experiments were

averaged to yield one autocorrelation function. Three correlation sample times were used at each angle. The maximum and minimum were computed using Raczek's formula (12) for the 497- and 109-nm particles respectively. For the Kodak distribution the expected upper and lower bounds of the distribution were used.

For the broad distributions analysed by the NNLS method, data was taken at 10 scattering angles: 20°, 30°, 40°, 50°, 60°, 70°, 80°, 90°, 100° and 110°. At each angle three sample times were used. These sample times were computed using Raczek's formula with different values for the bandwidth of the autocorrelation function:  $v=2, 4$  and 8. For each set of conditions a series of 30 ten second experiments were averaged to yield a single autocorrelation function.

### Results

We now demonstrate these methods on experimental data. First we consider Provencher's method as modified using the examples of a bimodal distribution and broad distribution. The NNLS method is demonstrated on a monodisperse distribution, a mixture of 10 monodisperse standards and a broad distribution.

For Provencher's method as modified, the statistics for the intensity and mass fraction distributions found for the bimodal mixture are shown in Table I. We select the sample times which give the intensity distributions having the peak area ratio of the 109 nm peak to the 497 nm peak closest to unity. The final mass distributions show overall means which are quite accurate, see Table I. From Figure 3 one observes that the relative peak areas and peak locations are quite accurate. Figure 3 also shows that the final mass fraction distribution is the same at three different scattering angles although the intensity distribution for a scattering angle of 30° was very different. Table II shows data obtained from a broad polystyrene latex sample donated by Kodak. The mass average and standard deviation compare well with the statistics from the mass distribution found by electron microscopy. The solutions for scattering angles of 30° and 90° represent the major features of the distribution fairly well but they are too smooth. Note that the distribution found at 60° has the highest dust level of all these solutions; it is likely that the low mean is due to overcompensation of the dust term. Thus Provencher's method as modified yields satisfying results for both the bimodal and broad distribution examples except when the dust term is large.

Table I. Bimodal Distribution Results

| Angle                | Sample Time | Average Diameter(nm) |      | Relative Standard Deviation |      |      |
|----------------------|-------------|----------------------|------|-----------------------------|------|------|
|                      |             | Intensity            | Mass | Intensity                   | Mass |      |
| Actual               | (microsec)  |                      | 303  |                             | 0.64 |      |
| Chosen <sup>a</sup>  | 30          | 140                  | 478  | 281                         | 0.23 | 0.74 |
| Initial <sup>b</sup> | 30          | 140                  | 472  | 281                         | 0.15 | 0.66 |
| Chosen <sup>a</sup>  | 60          | 8                    | 337  | 243                         | 0.80 | 0.89 |
| Initial <sup>b</sup> | 60          | 8                    | 313  | 328                         | 0.68 | 0.62 |
| Chosen <sup>a</sup>  | 90          | 9                    | 347  | 353                         | 0.56 | 0.56 |
| Initial <sup>b</sup> | 90          | 9                    | 346  | 348                         | 0.55 | 0.57 |

<sup>a</sup> The chosen solution has the optimal amount of regularization.

<sup>b</sup> The initial solution has little or no regularization.

Table II. Kodak Distribution Results

| Angle               | Sample Time | Average Diameter(nm) |      | Relative Standard Deviation |      | Dust (%) |    |
|---------------------|-------------|----------------------|------|-----------------------------|------|----------|----|
|                     |             | Intensity            | Mass | Intensity                   | Mass |          |    |
| Actual              | (micro-sec) |                      | 1050 |                             | 0.30 |          |    |
| Chosen <sup>a</sup> | 90          | 14                   | 1000 | 1044                        | 0.21 | 0.24     | 11 |
| Chosen <sup>a</sup> | 60          | 98                   | 906  | 892                         | 0.08 | 0.09     | 15 |
| Chosen <sup>a</sup> | 30          | 28                   | 1112 | 1075                        | 0.13 | 0.16     | 0  |

<sup>a</sup> The chosen solution has the optimal amount of regularization.

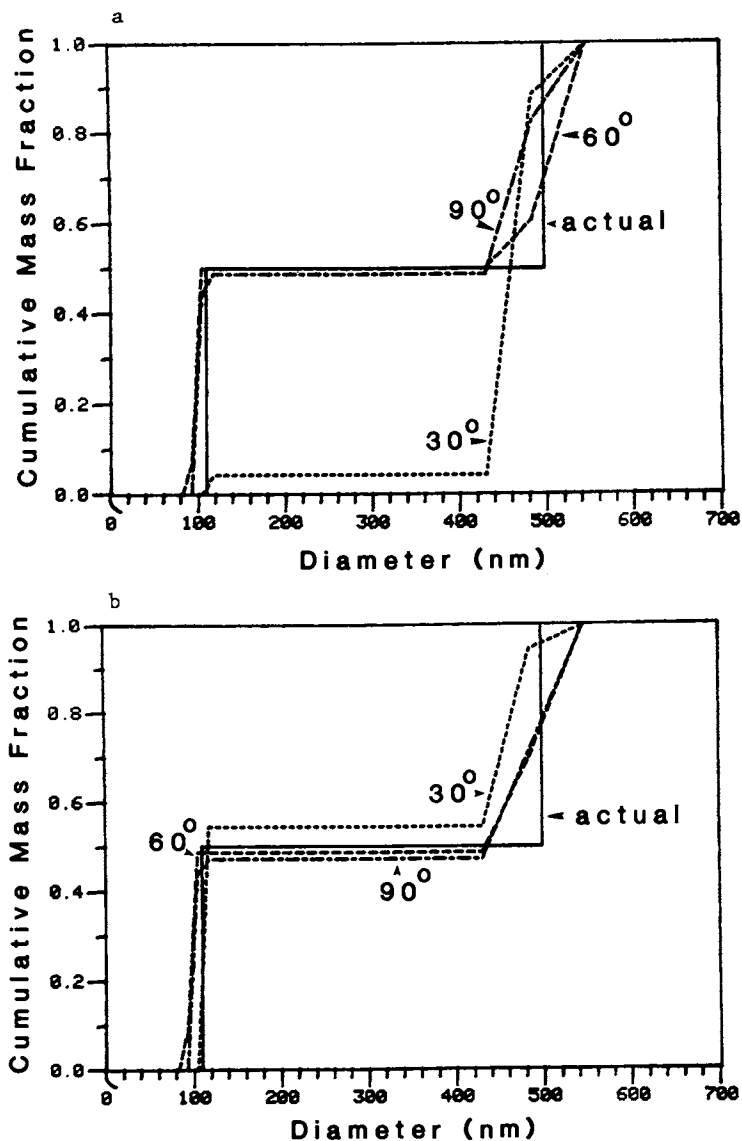


Figure 3. Constrained regularization solutions for the bimodal distribution for three scattering angles shown.

(a) No correction with Mie factor.

(b) Including correction with Mie factor.

For the second method, composite distribution results from the non-negatively constrained least squares method using several angles are shown in Table III. The composite mass distribution slightly underestimates the mean of the broad distributions shown. However, the estimate of the mean never displays a greater error than 5%. The standard deviation of the composite mass distribution overestimates that of all distributions. In Table III and in Figure 4 we consider the results from the B. F. Goodrich sample. Both Figures 4a and 4b are the average of 10 particle size distributions each from an autocorrelation function collected for 15 minutes. In Figure 4a each autocorrelation function was from scattering at a different scattering angle while in Figure 4b all the autocorrelation functions were from scattering at 90°. Note that somewhat better results are obtained by combining data from scattering at several angles.

Table III. Modified NNLS Method Results; Composite Distributions from All Angles

|                      | Average diameter(nm) |      |        | Relative Standard Deviation |       |        |
|----------------------|----------------------|------|--------|-----------------------------|-------|--------|
|                      | Intensity            | Mass | Actual | Intensity                   | Mass  | Actual |
| 412-nm PS Standard   | 451                  | 428  | 412    | 0.181                       | 0.077 | 0.02   |
| Mixture of Standards | 564                  | 612  | 648    | 0.66                        | 0.54  | 0.40   |
| BFG PVC1 Composite   | 618                  | 641  | 658    | 0.44                        | 0.50  | 0.41   |
| BFG PVC1 90 only     | 571                  | 617  | 658    | 0.46                        | 0.39  | 0.41   |

### Conclusion

By incorporating theoretical predictions of the intensity as a function of particle size for each scattering angle given the incident wavelength and approximate refractive index ratio into the data analysis (via constrained regularization and NNLS), it is possible to obtain the mass fraction distribution of particle size from the photon autocorrelation function of Mie scatterers without separate measurements of intensity scattering as a function of angle and without extrapolation to zero angle. The Mie scattering factor was included in the kernel of the integral analysed by constrained regularization. For the NNLS method, the intensity distribution determined by analysis of the autocorrelation function was converted to a mass distribution by multiplying each histogram step area by the appropriate scattering factor (average over the particle size represented by the step). We have shown that the composite mass distribution averaged over several scattering angles is sometimes more accurate than the composite mass distribution averaged over the same total time from a single scattering angle. The modification of the NNLS method involves simpler and faster computation than the modification of the constrained regularization method.

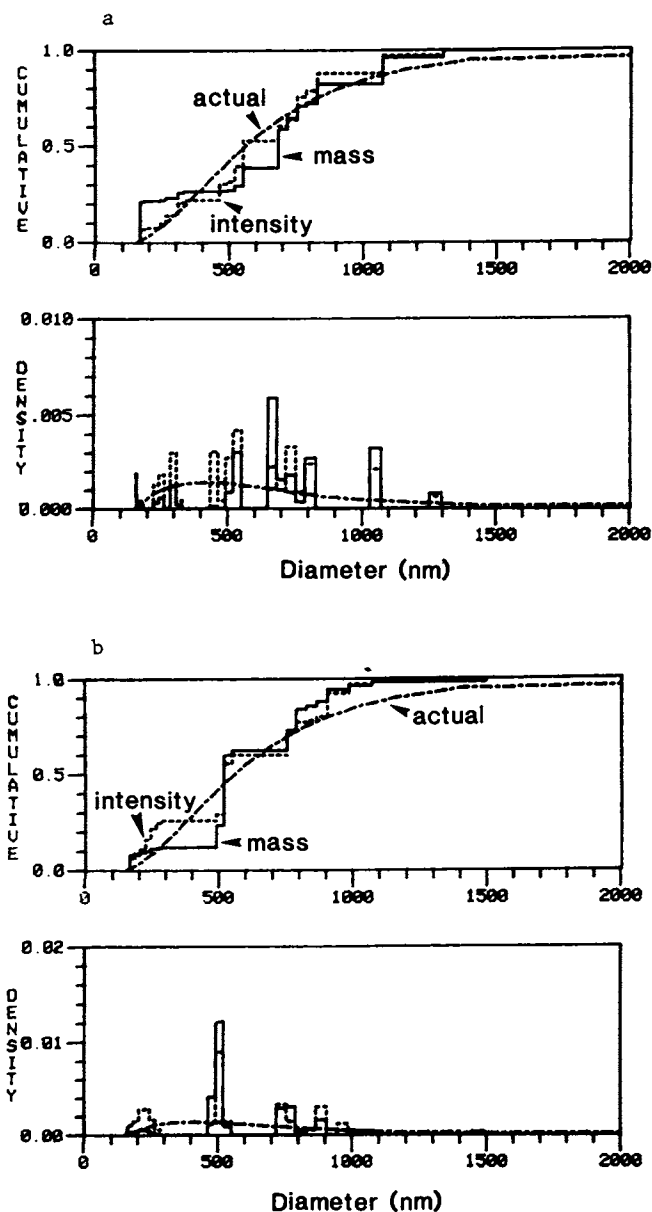


Figure 4. NNLS solutions for the B. F. Goodrich sample. Both solutions including the Mie factor (mass) and without correction (intensity) are shown.

(a) Average of results from correlation functions taken at ten scattering angles.

(b) Average of results from ten correlation functions taken at 90°

Literature Cited

1. R. S. Stock and W. H. Ray, J. Polym. Sci. Polym. Phys. Ed., 23, 1393, (1985).
2. B. Bedwell, Erd. Gulari and D. Melnik in "Measurement of Suspended Particles by Quasielastic Light Scattering", B. E. Dahneke Ed., Wiley, New York, p. 237, 1983.
3. S. Bott, in this volume.
4. S. W. Provencher, J. Hendrix, L. DeMaeyer and N. Paulussen, J. Chem. Phys., 69, 4273 (1978).
5. S. W. Provencher, Comput. Phys. Commun., 27, 213 and 219, (1982).
6. E. F. Grabowski and I. D. Morrison in "Measurement of Suspended Particles by Quasielastic Light Scattering", B. E. Dahneke Ed., Wiley, New York, p. 199, 1983.
7. H. H. Denman, W. Heller and W. J. Pangonis, "Angular Scattering Functions for Spheres", Wayne State University Press, Detroit, 1966.
8. C. A. Herb, I. D. Morrison and E. F. Grabowski, in this volume.
9. C. A. Herb, I. D. Morrison and E. F. Grabowski, in "Magnetic Resonance and Scattering in Surfactant Systems", L. Magid, ed., Plenum Press, to be published.
10. I. D. Morrison, E. F. Grabowski and C. A. Herb, Langmuir, 1, 496, (1985).
11. Erd. Gulari, Es. Gulari, S. Tsunashima and B. Chu, Polymer, 20, 347, (1979).
12. J. Raczek, Eur. Polym. J., 18, 863 (1982).

RECEIVED August 7, 1986

## Chapter 8

# Photon Correlation Spectroscopy, Transient Electric Birefringence, and Characterization of Particle Size Distributions in Colloidal Suspensions

Renliang Xu, James R. Ford, and Benjamin Chu

Department of Chemistry, State University of New York at Stony Brook,  
Long Island, NY 11794-3400

By using a combination of static and dynamic laser light scattering (LLS) and transient electric birefringence (TEB) we have been able to determine structural characteristics and size distributions of polydisperse disk-shaped particles (bentonite) in suspensions. In the limit of low concentration and scattering angle we obtained the weight-average molecular weight  $M_w$ , the z-average radius of gyration  $\langle R_g^2 \rangle^{1/2}$  and the second virial coefficient  $A_2$  from static light scattering measurements; at higher scattering angles we were able to estimate an average particle thickness. Photon correlation function measurements of both the polarized and the depolarized components of scattered light give us the average diffusion coefficients  $\bar{D}_T$  (translational) and  $\bar{D}_R$  (rotational) which can in turn be converted to average particle dimensions. Detailed analysis of characteristic linewidth distributions yield particle size distributions consistent with direct observations using electron microscopy. The TEB experiment provides us with the average optical polarizability difference  $\Delta\alpha^0$ , the ratio of permanent dipolar moment to electric polarizability difference, and the average rotational diffusion coefficient  $\bar{D}_R$  (TEB). Profile analysis of the decay curve yields a distribution of particle sizes consistent with the results from LLS.

Laser light scattering (LLS), which takes advantage of both static (intensity) and dynamic (intensity correlation/linewidth) measurements, has been used successfully in determining the molecular weight distribution (MWD) of polymers in solution. The essential steps are: 1. to use static light scattering to measure the weight-average molecular weight  $M_w$  which calibrates the MWD, 2. to use dynamic light scattering to measure the intensity-intensity

0097-6156/87/0332-0115\$06.00/0

© 1987 American Chemical Society



time correlation function  $G^{(2)}(\tau)$ , and 3. to perform a Laplace inversion of the  $G^{(2)}(\tau)$  in order to obtain an approximation to the characteristic linewidth distribution function  $G(\tau)$  which is related to the MWD by means of an empirical scaling relation.

In colloidal suspensions of anisotropic particles, the static structure factor plays a prominent role in particle size analysis. We have used transient electric birefringence (TEB) and electron microscopy, in addition to laser light scattering, to correlate our analysis of particle size distributions of bentonite suspensions. The complementary nature of TEB and photon correlation spectroscopy (PCS) in particle size analysis will be discussed.

### Theory

TEB. Transient electric birefringence (TEB) with single, reversed or sinusoidal electric pulses has become a useful tool for studying the structure of large anisotropic particles in solution (or suspension) since it was first proposed by O'Konski and Zimm (1). By applying linearly polarized light to a system of anisotropic particles aligned by an external electric field and by observing the depolarized intensity  $I$  of the transmitted light as the system relaxes after removal of the external field, we can observe the change in the refractive index difference of two orthogonal directions with respect to time and thereby determine the rotational diffusion coefficient and obtain information on the optical polarizability difference and the ratio of permanent dipole moment to electric polarizability difference.

The relationship between the depolarized time-dependent transmitted intensity  $I(t)$  and the refractive index difference in two orthogonal directions  $x$  and  $y$ , in which one is in the direction of the applied electric field and both are perpendicular to the direction of propagation of the incident light, is given by (2)

$$I(t) - I_b = k I_p \sin^2\left(\alpha + \frac{\delta(t)}{2}\right) \quad (1)$$

where  $I_b$  is the instrument stray light intensity;  $I_p$ , the polarized incident light intensity;  $k$ , a light reflection and absorption loss factor;  $\alpha$ , the angle between the slow axis of the quarter wave plate (Q) and the axis of the third polarizer ( $B_3$ ) (see figure 1); and  $\delta(t)$ , the optical retardation defined by

$$\delta(t) = \frac{2\pi s}{\lambda_0} (n_x(t) - n_y(t)) = \frac{2\pi s}{\lambda_0} \Delta n(t) \quad (2)$$

with  $n_x$  and  $n_y$  being the refractive indices of the solution in  $x$  and  $y$  directions;  $s$ , the effective length of the electrodes; and  $\lambda_0$ , the wavelength of light in vacuo.

For thin disks, the rise and decay curves of optical retardation  $\delta(t)$  are related to the particle rotational motion by (3)

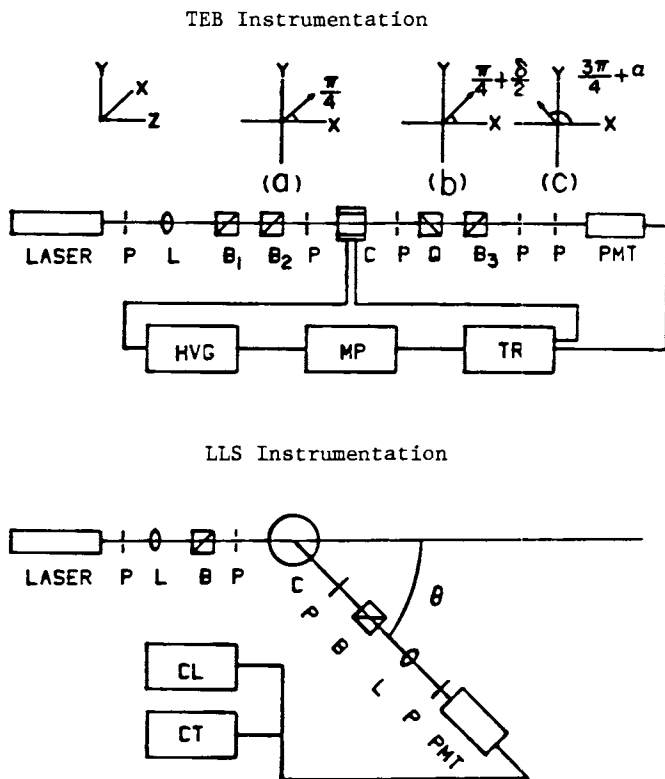


Figure 1. Schematic diagrams of TEB and LLS instrumentation. P, pinholes; L, lenses; B, polarizers; C, cell; Q, quarter wave plate; PMT, photomultiplier tube; HVG, high voltage generator; MP, microprocessor; TR, transient recorder; CL, correlator; CT, counter;  $\theta$ , scattering angle. For the TEB setup polarizers  $B_1$ ,  $B_2$  have polarization axis oriented at  $\pi/4$  with respect to the x-axis, as shown in (a). After the light beam passed through the cell with electric field in the x-direction containing a suspension of anisotropic particles and the quarter wave plate with its fast axis oriented at  $\pi/4$  with respect to the x-axis, the transmitted light beam is polarized in the direction of  $\pi/4 + \delta/2$ , as shown in (b). Analyzer  $B_3$  has polarization axis oriented at  $3\pi/4 + \alpha$  as shown in (c).

$$\text{rise: } \delta(t) = \sum \delta_{oi} \left[ 1 - \frac{3B_i}{2(B_i+1)} e^{-2D_{Ri}t} + \frac{(B_i-2)}{2(B_i+1)} e^{-6D_{Ri}t} \right] \quad (3)$$

$$\text{decay: } \delta(t) = \sum \delta_{oi} e^{-6D_{Ri}t} \quad (4)$$

where  $\delta_{oi}$  and  $D_{Ri}$  are the steady state value of  $\delta_i(t)$  and the rotational diffusion coefficient for the  $i$ th fraction of polydisperse particles, respectively.  $B$  is the ratio of the orientational polarizability  $P$  (which is related to the permanent dipole moment  $u_1$  along the symmetric axis) to the electrical polarizability difference  $Q$  and has the form

$$B \approx P/Q = \frac{(u_1/k_B T)^2}{(\alpha_1^e - \alpha_3^e)/k_B T} \quad (5)$$

where  $\alpha_3^e$  and  $\alpha_1^e$  are the electrical polarizabilities along the major and the minor particle axis, respectively;  $k_B$  is the Boltzmann constant and  $T$ , the absolute temperature. We have taken the permanent dipole moment along the major axis to be relatively small when compared with the induced dipole moment difference  $Q$  (16).

The steady state refractive index difference of each fraction,  $\Delta n_{oi}$ , depends upon the external field strength due to the differing degrees of orientation of each particle fraction. At low field strengths,

$$\Delta n_{oi} = \frac{\Delta n_{si}}{15} (P_i + Q_i) E^2 \quad (6)$$

When the external field is sufficiently strong to fully align all particle fractions,  $\Delta n_{oi}$  reaches its saturation value  $\Delta n_{si}$

$$\Delta n_{si} = \frac{2\pi\phi_i}{n} (g_3 - g_1) \quad (7)$$

where  $\phi_i$  is the volume fraction of the  $i$ th particle fraction and  $g_3$  and  $g_1$  are the major and the minor particle axis optical anisotropy factors given by

$$g_j = \frac{\alpha_j^o}{4\pi\epsilon_0 v} \quad (8)$$

with  $\alpha_j^o$  being the optical polarizability in the  $j$ th direction;  $\epsilon_0$ , the permittivity in vacuo;  $v$ , the volume of a single particle; and  $n$ , the refractive index of the solution.

Static Light Scattering. For a solution of polydisperse non-absorbing particles, the Rayleigh ratio  $R_{vv}(\theta)$  is the excess absolute scattered intensity of the solution over that of the pure

solvent at scattering angle  $\theta$ , where the subscript vv indicates vertically polarized incident and scattered light, and has the form

$$\frac{R_{vv}(\theta)}{H} = \sum C_i [M_i P(KL_i) - 2A_2 C_i (M_i P(KL_i))^2] \quad (9)$$

where  $C_i$  and  $P(KL_i)$  are the concentration and the particle scattering factor of species  $i$  having molecular weight  $M_i$ ,  $K$  is the magnitude of the momentum transfer vector given by  $K = (4\pi/\lambda)\sin(\theta/2)$ ,  $L_i$  is the equivalent diameter of the  $i$ th particle fraction,  $A_2$  is the second virial coefficient, and the optical constant  $H$  is given by

$$H = \frac{4\pi^2 n^2 (\partial n / \partial C)^2}{N_A \lambda_o^4}$$

with  $N_A$  and  $(\partial n / \partial C)$  being Avogadro's number and the refractive index increment, respectively. For sufficiently small values of  $\theta$ , equation (9) can be written as (4)

$$\frac{HC}{R_{vv}(\theta)} = \frac{1}{M_w P(KL)} + 2A_2 C = \frac{1}{M_w} \left[ 1 + \frac{\langle R_g^2(C) \rangle_z K^2}{3} + 2A_2 M_w C \right] \quad (10)$$

where  $M_w$  is the weight-average molecular weight;  $C$ , the total concentration of particles;  $P(KL)$ , the  $z$ -average particle scattering factor; and  $\langle R_g^2(C) \rangle_z$ , the mean square "radius of gyration" at finite concentration  $C$ , which can be corrected for concentration by

$$\langle R_g^2(0) \rangle_z = \langle R_g^2(C) \rangle_z [1 + 2A_2 M_w C] \quad (11)$$

with  $\langle R_g^2(0) \rangle_z^{1/2}$  being the radius of gyration. For disk-like particles, such as the bentonite particles, eqs. (9), (10) and (11) are only approximate because of optical anisotropy. In fact, polarized light scattering (vv-component) yields only apparent values for the molecular weight, the radius of gyration and the second virial coefficient. The correct values can be computed if we know the depolarization ratio and the particle shape. For bentonite particles, the depolarization ratio is very small ( $\sim 0.02$ ). Thus, the correction factor is of the order of a few percent which we shall ignore in the present study.

Dynamic Light Scattering. The measured single clipped photoelectron count autocorrelation function for the self-beating experiment has the form (5)

$$G^{(2)}(\tau, k) = N_s \langle n_k \rangle \langle n \rangle [1 + b |g^{(1)}(\tau, k)|^2] \quad (12)$$

where  $\tau$  is the delay time;  $k$ , the clipping level;  $N_s$ , the total number of samples;  $\langle n_k \rangle$  and  $\langle n \rangle$  the mean clipped and unclipped

counts, respectively;  $b$  is a spatial coherence factor generally taken as an unknown parameter in the fitting procedure; and  $g^{(1)}(\tau, K)$  is the normalized first order electric field autocorrelation function. Equation (12) is valid for Gaussian signals (6).

For monodisperse systems the normalized polarized and depolarized time correlation functions can be expressed as (7)

$$g_{vv}^{(1)}(\tau, K) = \sum_{m=0, \text{even}} P_m(KL) \exp[(-D_T K^2 - m(m+1)D_R)\tau] \quad (13)$$

$$g_{vh}^{(1)}(\tau, K) = \exp[(-D_T K^2 - 6D_R)\tau] \quad (14)$$

where  $D_T$  and  $D_R$  are the translational and rotational diffusion coefficients and the particle scattering intensity factors  $P_m(KL)$  can be calculated theoretically for particles of different shapes (7,8). Eq. (14) is valid only for small  $KL$ . Scattering factors for disk-like particles have been published elsewhere (8) and we recapitulate them in Figure 2. At sufficiently small scattering angles we can use equations (13) and (14) to determine the values of  $D_T$  and  $D_R$  from the measured polarized and depolarized intensity-intensity autocorrelation functions  $G_{vv}^{(2)}(\tau, K)$  and  $G_{vh}^{(2)}(\tau, K)$ . It should be noted that the model (7,8) assumed isotropic translational diffusive motion, while in reality, we must take into account anisotropy in translational diffusion (9). However, in extrapolation to infinite dilution and zero scattering angle, we can retrieve the correct translational diffusion coefficient experimentally, regardless of model.

For polydisperse particles, we can write

$$|g^{(1)}(\tau, K)| = \int G(\Gamma, K) e^{-\Gamma\tau} d\Gamma \quad (15)$$

where  $G(\Gamma, K)$  is the normalized distribution of characteristic line width  $\Gamma$  at a given value of  $K$ . Inversion of equation (15) in the presence of experimental noise to obtain the characteristic linewidth distribution  $G(\Gamma, K)$  is an ill-conditioned problem which has received much attention in the recent literature (6,10,11). For the sake of clarity we have omitted the polarization subscripts ( $vv$  or  $vh$ ) in this section.

The method of cumulants (12) expands  $g^{(1)}(\tau)$  in terms of the moments of the characteristic linewidth distribution

$$|g^{(1)}(\tau, K)| = A \exp[-\bar{\Gamma}(K)\tau + \frac{\mu_2(K)\tau^2}{2} - \frac{\mu_3(K)\tau^3}{6} + \dots] \quad (16)$$

where  $\bar{\Gamma}$  is the average linewidth and  $\mu_i = \langle(\Gamma - \bar{\Gamma})^i\rangle$ . A modified Marquadt-Levenberg nonlinear least squares routine was used to determine the best values of  $\bar{\Gamma}$  and  $\mu_i$ . Another straightforward approach involved approximating  $G(\Gamma, K)$  as the weighted sum of two characteristic decay times  $\Gamma_1^{-1}$  and  $\Gamma_2^{-1}$

$$G(\Gamma, K) = w_1 e^{-\Gamma_1 \tau} + w_2 e^{-\Gamma_2 \tau} \quad (17)$$

The same nonlinear fitting routine could determine the best values for  $w_i$  and  $\Gamma_i$  which might not necessarily have physical meaning but could be used to compute  $\Gamma$  and  $\mu_2$ . We used a regularized inversion of equation (15) that incorporates a positivity constraint on  $G(\Gamma, K)$  in order to obtain more detailed information on the characteristic linewidth profile. A discussion of this approach may be pursued in reference (10).

### Experimental Methods

Sample Preparation. The bentonite powder obtained from Fisher Scientific Company was dissolved in doubly distilled and filtered water to make a stock solution with  $C = 3.65 \times 10^{-4}$  g/g. This stock solution was further diluted to the concentrations listed in Table I. All measurements were made within 10 days of sample preparation in order to avoid possible aging problems.

TEB. Our TEB apparatus consists of a 15 mW He-Ne laser with  $\lambda_0 = 632.8$  nm., three Glan-Thomson polarizers and a quarter wave plate arranged as shown in figure 1. The sample was contained in a Beckman 1 cm<sup>2</sup> quartz cell with two platinum electrodes, held at 25.00±0.05°C. The transmitted light intensity was measured by a photomultiplier tube (IP-28) and the output sent to a Biomation 8100 transient recorder. The external electric field was provided by a Cober 605P high voltage pulse generator. The entire experiment was under the control of a microcomputer.

High voltage square pulses from 0.5 to 3.3 KV/cm with pulse widths of around 2 msec were applied to the five bentonite suspensions. The pulse traces and the signal from the photomultiplier tube were simultaneously recorded at a resolution of 1024 points each in the transient recorder using a sample time increment of 40 μsec and displayed on an oscilloscope. After 10 passes the data were transferred to the microcomputer and saved on floppy disk for subsequent analysis. The entire measurement sequence for one sample took a few minutes.

Light Scattering. The light scattering table consists of an argon ion laser, suitable lenses and pinholes to condition the incident beam, a sample cell in a brass thermostat (25.00±0.05°C) and a rotatable detector arm on which are mounted optical parts to define the scattering geometry and the photomultiplier tube as shown in figure 1. The signal from the photomultiplier tube is channeled through a preamplifier/discriminator to either a pulse counter for intensity measurements or a Malvern 7027 single-clipping correlator for the time correlation measurements.

Intensity measurements of the five suspensions were performed using the laser at an incident wavelength  $\lambda_0 = 514.5$  nm over an angular range of 15 to 36 degrees. Dynamic measurements were done using incident wavelengths of  $\lambda_0 = 514.5$  and 488.0 nm over angular ranges of 15 to 54 degrees and of 35 to 80 degrees, respectively.

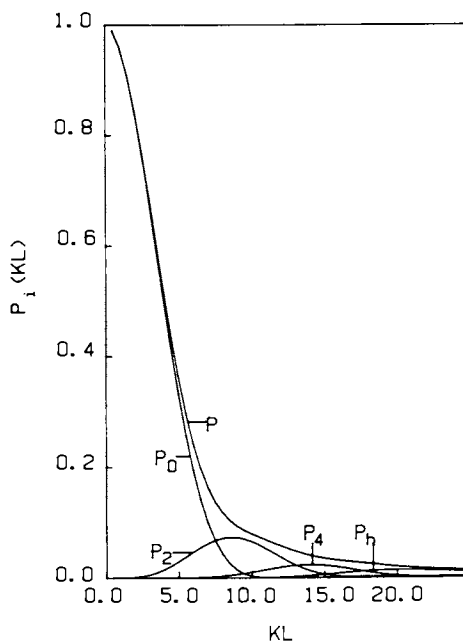


Figure 2. Scattering factor of disk-like particles where  $K = 4\pi \sin(\theta/2)/\lambda$ , and  $L$ , the particle diameter.  $P_h$  represents the remaining higher order terms.

Table I. Sample Concentrations

| Sample Number | Concentration ( $10^{-5}$ g/g water) |      |
|---------------|--------------------------------------|------|
| TEB           | 1                                    | 2.14 |
|               | 2                                    | 1.18 |
|               | 3                                    | 0.83 |
|               | 4                                    | 2.93 |
|               | 5                                    | 6.43 |
| LLS           | 1                                    | 1.02 |
|               | 2                                    | 0.67 |
|               | 3                                    | 0.38 |
|               | 4                                    | 0.21 |
|               | 5                                    | 0.13 |

$(\partial n/\partial C)$ . The refractive index increment  $(\partial n/\partial C)$  of the bentonite suspension was determined using a Brice Phoenix differential refractometer at wavelengths 436 and 546 nm. By interpolation, we estimated  $(\partial n/\partial C)$  to be 0.086 at 514.5 nm, and 0.082 at 488 nm, in reasonable agreement with those values reported by other authors (13,14,15).

### Results and Discussion

Static Light Scattering Measurements. A Zimm plot for the bentonite suspensions is shown in figure 3. Here we have plotted  $HC/R_{VV}(\theta)$  against  $CK'+\sin^2(\theta/2)$  where  $K'$  is an arbitrary constant, and determined  $M_w = 3.57 \times 10^9$  g/mole,  $A_2 = 2.93 \times 10^{-5}$  mole-g/g<sup>2</sup>, and  $\langle R_g^2(0) \rangle_z = 1.51 \times 10^{-9}$  cm<sup>2</sup> from

$$\lim_{C \rightarrow 0} \frac{HC}{R_{VV}(\theta)} = \frac{1}{M_w} \left[ 1 + \frac{K^2 \langle R_g^2(0) \rangle_z}{3} \right] \quad (18)$$

$$\lim_{\theta \rightarrow 0} \frac{HC}{R_{VV}(\theta)} = \frac{1}{M_w} + 2A_2C \quad (19)$$

and

$$\lim_{\substack{C \rightarrow 0 \\ \theta \rightarrow 0}} \frac{HC}{R_{VV}(\theta)} = \frac{1}{M_w} \quad (20)$$

We have also been able to estimate the average thickness of bentonite disks from the slope of the Zimm plot at zero concentration and high scattering angles. If we take

$$P(KL_1) = \frac{8}{(KL_1)^2} \left[ 1 - \frac{2J_1(KL_1)}{KL_1} \right] \quad (21)$$

as the particle scattering factor for a disk shaped particle (8), where  $J_1(KL_1)$  is the first order Bessel function. For  $KL > 3.5$ , equation (21) becomes

$$P(KL_1) = 8/(KL_1)^2 \quad (22)$$

with an error of less than 13%. Therefore, equation (9) becomes

$$\frac{R_{VV}(\theta)}{HC} \cong \frac{1}{CK^2} \Sigma \frac{8C_1 M_1}{L_1^2} \quad (23)$$

By assuming that all the bentonite particles have the same thickness  $d$  and density  $\rho$ , and using the relation

$$\frac{L_1^2}{M_1} = \frac{4}{\rho \pi d N_A} \quad (24)$$



we obtain an equation from which the thickness  $d$  of the bentonite disks can be determined:

$$\frac{HC}{R_{VV}(\theta)} = \frac{8\pi n^2}{\lambda_o^2 d \rho N_A} \sin^2\left(\frac{\theta}{2}\right) \quad (25)$$

If we take a value of 2.0 g/ml for the  $\rho$  density of the bentonite disks, we obtain an estimate of 30 Å for the thickness of a bentonite disk from the slope of the Zimm plot in figure 3 at zero concentration and high scattering angles.

Dynamic Light Scattering Measurements. At sufficiently low scattering angles where only the first term of the static structure factor  $P_0(KL)$  in equation (13) is important, we can express the linewidth obtained from polarized dynamic light scattering measurements as (17)

$$\Gamma_{VV}(L,K) = D_T(L)K^2 (1 + f \langle R_g^2(C) \rangle_z K^2) \quad (26)$$

where

$$D_T(L) = D_T^0(L) (1 + k_d C) \quad (27)$$

with  $D_T^0(L)$  being the translational diffusion coefficient of particles with main dimension  $L$  extrapolated to infinite dilution.  $k_d$  is a system specific second virial coefficient which combines hydrodynamic and thermodynamic factors, and  $f$  is a dimensionless number dependent upon the particle structure, polydispersity and solvent.

By using the method of cumulants, we determined  $\bar{\Gamma}_{VV}$ . With values of  $\langle R_g^2(0) \rangle_z$ ,  $A_2$  and  $M_w$  obtained from static light scattering measurements, we obtained  $\bar{D}_T$  and  $f$  from the slope of a plot of  $\bar{\Gamma}_{VV}/K^2$  versus  $K^2$  at different concentrations. By plotting  $\bar{D}_T$  against concentration, we estimated  $\bar{D}_T^0 = 9.70 \times 10^{-9}$  cm<sup>2</sup>/sec and  $k_d = -5.10 \times 10^4$  g/g. The concentration dependence of the  $f$  values suggests that for large particles, internal motions have a measurable effect on translational motions. Thus, we expect that  $D_R$  has a concentration dependence.

We were also able to obtain a continuous linewidth distribution curve  $G(\Gamma_{VV}, K)$  from the regularization approach by inversion of equation (15). The result obtained from the Laplace inversion procedure is a set of delta functions  $G(\Gamma_i, K)$  which approximate the continuous  $G(\Gamma_{VV}, K)$  curve sampled at equal intervals. The subscript  $vv$  shall henceforth be omitted in the interest of clarity in notation. In order to obtain a size distribution from  $G(\Gamma_i, K)$  we need to convert both the ordinate and the abscissa ( $\Gamma_i$ ) in the following way.

From equations (26) and (27) we obtain

$$\Gamma = \frac{k_d C}{6\eta L} K^2 (1 + k_d C) (1 + \bar{f} \langle R_g^2(C) \rangle_z K^2) \quad (28)$$

where  $\eta_0$  is the solvent viscosity and we have used the relation (5)

$$D_T^0 = \frac{k_B T}{6\eta_0 L} \quad (29)$$

With values for  $k_d$ ,  $\bar{f}$  and  $\langle R_g^2(0) \rangle_z$ , we could convert the abscissa from  $\Gamma$  space to  $L$  space. After having determined the range in  $L$  space required to adequately cover the size distribution, we chose equally spaced values of  $L_i$  and calculated the corresponding  $\Gamma_i$  values. The amplitudes  $G(\Gamma_i, K)$  for this new set of  $\Gamma_i$  were determined by interpolation from the original continuous distribution curve. By taking into account both the Jacobian of the transformation and the form factors calculated from theoretical principles (8), we could convert the ordinate by setting

$$F(L_i) = \frac{\Gamma_i^2}{P(KL_i)} G(\Gamma_i, K) \quad (30)$$

The normalized results for one bentonite suspension measured at two different scattering angles are shown to be self-consistent in figure 4.

By fitting the depolarized time correlation function data with a double exponential model, we obtained  $D_R$  values inconsistent with the other results we obtained. However, by plotting the values obtained for the faster component of the double exponential fit against  $K^2$ , and by plotting the resulting intercepts and slopes against concentration, we obtained  $D_T^0 = 10.9 \times 10^{-9} \text{ cm}^2/\text{sec}$  and  $D_R^0 = 8.24 \text{ sec}^{-1}$ . The results are consistent with those obtained from other methods. Thus, there may be a low-frequency component of the depolarized time correlation function arising possibly from dust.

Parameters from TEB Measurements. By equations (6) and (7) a typical retardation curve ( $\delta_0$  vs  $E^2$ ) should be linear at low field strength and reach a plateau when the field strength is sufficient to fully align all the particles along the electric field vector. We found the plateau at field strengths higher than 2.0 KV/cm. A plot of  $\delta_{90}$  versus  $C$  at a field strength of 3.3 KV/cm yielded a straight line. From the slope of  $\delta_{90} = 5.57 \times 10^2 C - 7.50 \times 10^{-4}$ , we estimated the optical polarizabilities in the following way.

From equations (2) and (7) we have

$$\delta_{90} = \frac{4\pi^2 S}{n\lambda_0} \Sigma \phi_i (g_3 - g_1) \quad (31)$$

As the particle anisotropy factors  $g_j$  have a value per unit volume, it is reasonable to assume that these quantities are the same for all particles. By changing to concentration units and by accounting for the fact that the short axis of the particles can be aligned in any direction perpendicular to the field we have

$$\delta_{90} = \frac{4\pi^2 S}{n\lambda_0} C \frac{\rho_{H_2O}}{\rho_{bento}} \left( g_3 - \frac{g_3 + g_1}{2} \right) \quad (32)$$

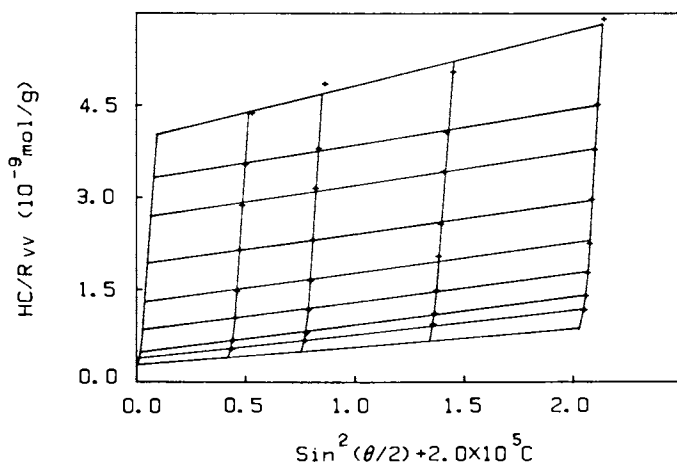


Figure 3. Zimm plot of bentonite suspensions using  $\lambda_0 = 514.5$  nm. The numbers denote concentrations as shown in Table I (LLS).

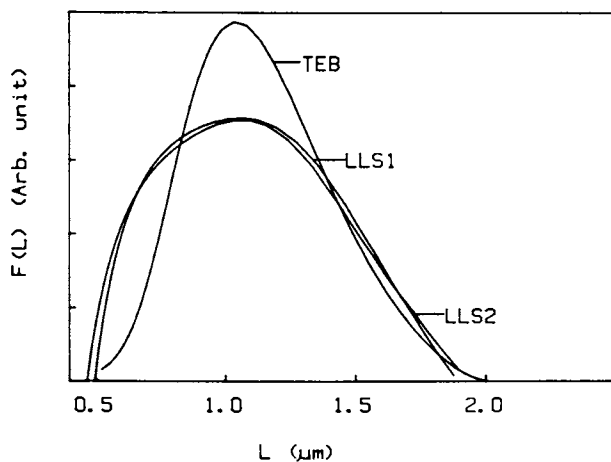


Figure 4. Size distributions from LLS sample 3 at  $\theta = 21^\circ$  (LLS1) and at  $\theta = 24^\circ$  (LLS2) and from TEB sample 4. It should be noted that the scattered intensity from LLS is proportional to  $N_i M_i^2$  while the transmitted intensity from TEB is proportional to  $N_i M_i$ . In this comparison, we have converted the TEB size distribution to the same weighting factor as LLS.

whereby we used an average value of  $g_3$  and  $g_1$  instead of simply  $g_1$ . Recalling that from eq. (8)

$$g_j = \frac{\alpha_j^0 N A^{\rho} \text{bento}}{4\pi\epsilon_0 M_n} \quad (33)$$

we calculated  $\Delta g (=g_3-g_1) = 5.26 \times 10^{-3}$  and  $\Delta\alpha^0 = \alpha_3^0 - \alpha_1^0 = 1.24 \times 10^{-33} \text{ Fm}^2$  where we used  $M_w \approx 3.57 \times 10^9 \text{ g/mole}$  and  $m_w/M_n \sim 1.4$ .

The ratio of orientational to electric polarizability can be estimated from the ratio of two integrations (see equations (3) and (4))

$$\frac{\int_0^{\infty} (\Delta n_0 - \Delta n(t)) dt}{\int_0^{\infty} \Delta n(t) dt} = \frac{6D_R(B+1)}{\frac{\Delta n_0}{6D_R}} = \frac{4B+1}{B+1} \quad (34)$$

We find that B is a constant independent of concentration and has a value of -0.248, the negative sign indicating the direction of orientation of the particles, i.e., the electric field (x-direction) is perpendicular to the symmetric axis of the particle.

Analysis of the TEB decay curves was carried out using both the cumulants and the regularization procedures. From the cumulants results, we plotted  $D_R$  against C and obtained  $\bar{D}_R^0 = 7.4 \text{ sec}^{-1}$ , as shown in figure 5.

From the regularization approach we obtained the characteristic linewidth distribution. We converted the ordinate according to

$$F(L_i) = \Gamma_i^{4/3} G(\Gamma_i) \quad (35)$$

and the abscissa according to

$$L_i = \left[ \frac{3k_B T \cdot 6(1+k_d C)}{4\eta_0 \Gamma_i} \right]^{1/3} \quad (36)$$

With  $k_d = 1.35 \times 10^5$  (and  $[C] \equiv \text{g/g}$ ) obtained from the cumulants fit, the resulting size distribution is shown in figure 4, which has been converted further to a z-average for comparison with the distribution from LLS.

Comparison of LLS and TEB Results. By means of equation (29) and

$$D_R^0 = \frac{3k_B T}{4\eta_0 L^3} \quad (37)$$

we can compute an average particle diameter  $\langle L \rangle$  from either  $\bar{D}_R^0$  or  $\bar{D}_\eta^0$  and therefore compare directly the different results described above. However, we should be careful to account for the z-average

nature of the distribution curve from LLS measurements. Values of  $\langle L \rangle$  so determined are shown in Table II. We note that different techniques are quite consistent, the only exception being the average values computed from  $\overline{D}_T^0$  and  $D_T^0$ . The discrepancy is probably because we have neglected to correct for additional contributions at finite scattering angles due to the particle scattering factors when computing averages from  $D_T^0$  (or  $\overline{D}_T^0$ ). An average disk thickness  $\langle d \rangle$  can be computed from

$$\langle d \rangle = \frac{4M_w \langle L^2 \rangle}{\pi N_A^0 \text{bento} \langle L^4 \rangle} \quad (38)$$

With the  $M_w$  value obtained from static light scattering measurements,  $\langle d \rangle = 35 \text{ \AA}$ , in reasonable agreement with  $d \approx 30 \text{ \AA}$  estimated from static light scattering measurements alone. Ratios of  $M_n:M_w:M_z$  can be calculated from the TEB or light scattering particle size distributions (PSD) if we assume that the density and thickness are the same for all bentonite particles (see Table II). It is also interesting to use the particle size distribution obtained from TEB to generate a light scattering time correlation function and to compare the theoretically generated curve with the measured data. Figure 6 shows such a comparison.

From the values of  $\overline{D}_T^0$  and  $\overline{D}_R^0$  we can calculate the average linewidth using the expression (7)

$$\overline{\Gamma}_{VV}(K) = \frac{1}{P(KL)} \{ P_0(KL)DK^2 + P_2(KL)[DK^2 + 6D_R] + P_4(KL)[DK^2 + 20D_R] + \dots \} \quad (39)$$

and check the values against the measured ones over a wide angular range as shown in figure 7. The agreement suggests that particle absorption effects are negligible, and that although bentonite particles are already on the edge of the validity of the Rayleigh-Debye scattering theory reasonable results can still be obtained if experiments are done at small enough scattering angles.

Finally, we have examined the bentonite particles directly by electron microscopy under a magnification of about 24,000X. The particles actually appear to be ellipsoidal ones with an approximate axial ratio of 1.3 rather than perfectly round disks. We counted 266 particles using pictures at higher magnifications and obtained  $\langle L \rangle = 0.97 \text{ \mu m}$ . The distribution ( $F'(L)$ ) is close to the TEB result which is converted to number distribution from the result using the regularization approach, as shown in figure 8.

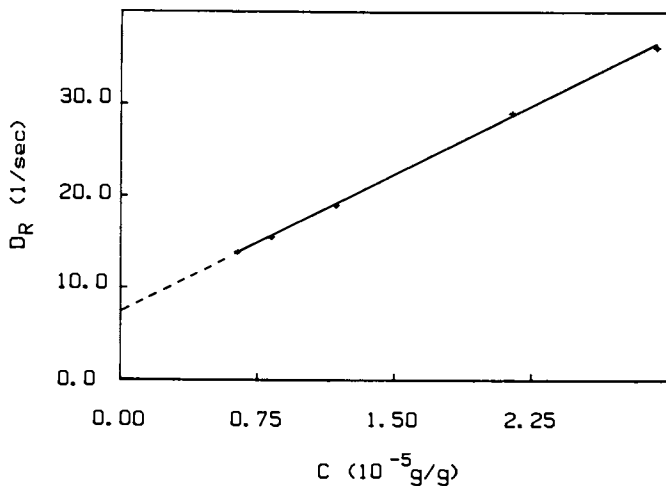


Figure 5.  $\bar{D}_R$  versus  $C$  from TEB measurements.  $\bar{D}_R = D_R^0(1+1.35 \times 10^5 C) \text{ sec}^{-1}$  with  $\bar{D}_R^0 = 7.4 \text{ sec}^{-1}$  and  $C$  expressed in Table I.

Table II. Average Length Values Computed From Different Techniques and Methods of Analysis

| Data Source                            | $\langle L^{-1} \rangle_z^{-1}$ | $\langle L^2 \rangle_z^{1/2}$ | $\langle L^{-3} \rangle_z^{-1/3}$ |
|--|---------------------------------|-------------------------------|-----------------------------------|
| LLS PSD                                | 0.96                            | 1.14                          | 0.76                              |
| TEB PSD                                | 1.04                            | 1.18                          | 0.78                              |
| $\bar{D}_T^0$ from $\bar{\Gamma}_{vv}$ | 0.79                            | -                             | -                                 |
| $D_T^0$ from $\Gamma_{vh}$             | 0.70                            | -                             | -                                 |
| $\bar{D}_R^0$ from TEB                 | -                               | -                             | 0.78                              |
| $\langle R_g^2 \rangle_z$ from LLS     | -                               | 1.10                          | -                                 |
|  | *                               | *                             | *                                 |

| Data Source | $\underline{M}_n$ | $\underline{M}_w$ | $\underline{M}_z$ |
|-------------|-------------------|-------------------|-------------------|
| LLS PSD     | 1.00              | 1.47              | 2.10              |
| TEB PSD     | 1.00              | 1.33              | 1.82              |
| EM PSD      | 1.00              | 1.47              | 1.86              |

PSD denotes particle size distribution; length in units of  $\mu\text{m}$ .

In Particle Size Distribution; Provdor, T.;

ACS Symposium Series; American Chemical Society: Washington, DC, 1987.

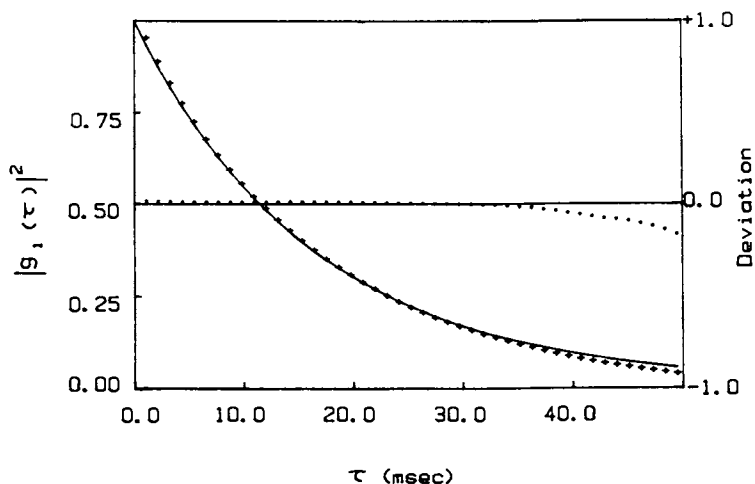


Figure 6. Autocorrelation function data at  $\theta = 24^\circ$  (+) for LLS sample 3. Generated time correlation function (continuous curve) from the size distribution curve of TEB as shown in figure 4 with relative deviation between the two curves. Deviation =  $1.0 - (g_1(\tau)_{\text{generated}} / g_1(\tau)_{\text{measured}})^2$ .

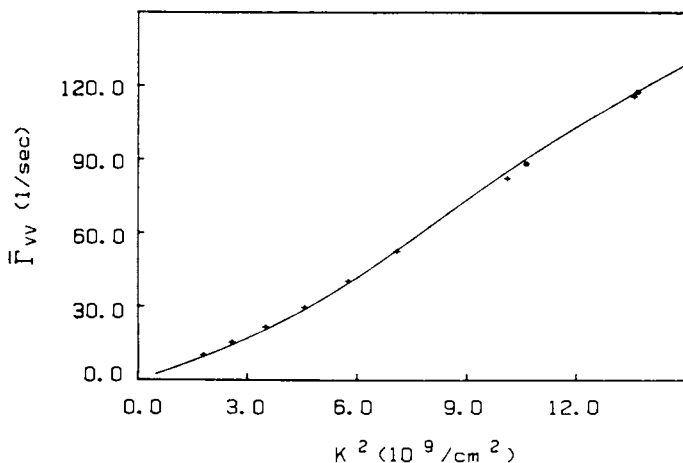


Figure 7. A comparison of  $\bar{\Gamma}_{vv}$  between the LLS experimental data of sample 1 at  $C = 1.02 \times 10^{-5}$  g/g (+: at  $\lambda_0 = 514.5$  nm, and \*: at  $\lambda_0 = 488.0$  nm) and a best fit curve from theory (Eq. 40), which was constructed by using  $D_T = 4.8 \times 10^{-9}$  cm<sup>2</sup>/sec [=  $9.7 \times 10^{-9}(1 - 5 \times 10^4 C)$  cm<sup>2</sup>/sec],  $D_R = 6.98$ /sec [=  $8.24(1 - 1.5 \times 10^4 C)$ /sec],  $L = 8.5 \times 10^{-5}$  cm.

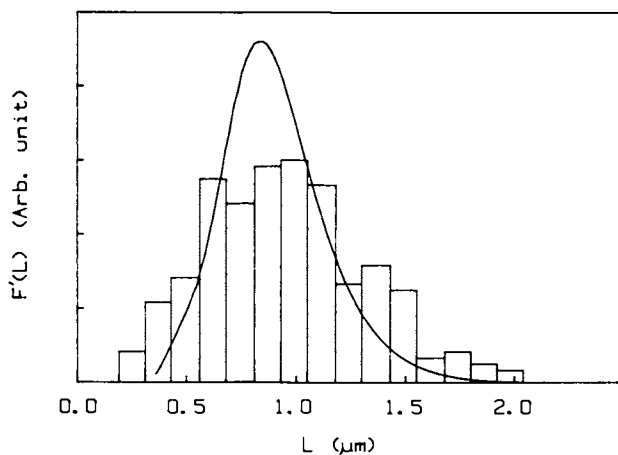


Figure 8.  $F'(L)$  number size distribution from EM and TEB measurements.  $M_z:M_w:M_n$  ratios are listed in Table II.

#### Acknowledgments

We gratefully acknowledge support of this project by the National Science Foundation, Polymers Program (DMR 8314193), and the U.S. Army Research Office, Durham.



Literature Cited

1. O'Konski, C. T.; Zimm, B. H. Science 1950, 111, 113.
2. Fredericq, E.; Houssier, C. "Electric Dichroism and Electric Birefringence"; Clarendon Press: Oxford, 1973; p.92.
3. Tinoco, I., Jr.; Yamaoka, K. J. Phys. Chem. 1959, 63, 423.
4. Huglin, M. B. Topics in Current Chemistry 1978, 77, 143.
5. Chu, B. "Laser Light Scattering"; Academic Press: New York, 1974.
6. Chu, B. Proceedings of the NATO ASI on the Application of Laser Light Scattering to the Study of Biological Motions, J.C. Earnshaw and M.W. Steer, Ed.; Plenum Press: 1983 pp.53-76.
7. Berne, B. J.; Pecora, R. "Dynamic Light Scattering"; John Wiley & Sons, Inc., 1976.
8. Aragon, S. R.; Pecora, R. J. Chem. Phys. 1977, 66, 2506.
9. Maeda, T.; Fujime, S. Macromolecules 1984, 17, 1153; Kubota, K.; Fujime, S. Macromolecules, in press.
10. Chu, B.; Ford, J. R.; Dhadwal, H. In "Methods of Enzymology"; S. P. Colowick and N. O. Kaplan, Eds.; Academic Press: New York, 1985; Vol. 104, pp. 256-297; Ford, J. R.; Chu, B. Proceedings of the 5th International Conference on Photon Correlation Techniques in Fluid Mechanics, E. O. Schulz-DuBois, Ed.; Springer-Verlag: 1983, pp. 303-314.
11. Pike, E. P. In "Scattering Techniques Applied to Supramolecular and Non-Equilibrium Systems"; S. H. Chen; B. Chu; R. Nossal, Ed.; 1981, pp. 179-200.
12. Koppel, D. E. J. Chem. Phys. 1972, 57, 4814.
13. Jennings, B. R.; Brown, B. L.; Plummer, H. J. Coll. and Inter. Sci. 1970, 32, 606.
14. Schweitzer, J.; Jennings, B. R. J. Coll. and Interface Sci. 1971, 37, 443.
15. Suong, Thai Thanh; Stoylov, S. Izv. Khim. Bulg. Akad. Nauk.(Bulgaria) 1982, 15, 542.
16. Shah, M. J.; Thompson, D. C.; Hart, C. M. J. Phys. Chem. 1963, 67, 1170.
17. Stockmayer, W. H.; Schmidt, M. Pure & Appl. Chem. 1982, 54, 407.

RECEIVED July 17, 1986

## Chapter 9

# Determination of Particle Size Distributions Using Light-Scattering Techniques

Erdogan Gulari<sup>1</sup>, A. Annapragada<sup>1</sup>, Esin Gulari<sup>2</sup>, and B. Jawad<sup>2</sup>

<sup>1</sup>Department of Chemical Engineering, University of Michigan, Ann Arbor, MI 48109

<sup>2</sup>Department of Chemical and Metallurgical Engineering, Wayne State University,  
Detroit, MI 48202

A comparison of the advantages and disadvantages of the three light scattering based particle sizing techniques: photon correlation spectroscopy (PCS), multiwavelength turbidity spectra (TS) and Fraunhofer diffraction pattern analysis (FDPA) in the overlap region of 0.5  $\mu\text{m}$  to 5  $\mu\text{m}$  was made. Using monodisperse latex spheres, we observed that in terms of the mean size the resolution of PCS and TS were very good. Despite the manufacturer's claims of a 1  $\mu\text{m}$  lower limit, we found that commercial FDPA instruments cannot accurately measure the sizes below 2  $\mu\text{m}$ . Due to the finite width and the fixed spacing of detector diodes, the resolution was comparable to the mean size measured. In terms of quantitative measurements of the relative mass fractions in a bimodal mixture, both TS and FDPA gave fairly accurate results with FDPA being closer to the actual mass fractions. PCS results were not at all quantitative. In terms of the ease of usage, FDPA was the easiest followed by TS. PCS was the most difficult one, both in sample preparation and data analysis.

Light scattering based particle sizing techniques have the advantage of nonintrusively measuring sizes of emulsions and dispersions. Depending on the parameters involved, there are several techniques which can be used and a choice of the most convenient method can be made. Parameters governing the applicability of a given method are the relative refractive index  $m = n_2/n_1$ , and the relative size  $\alpha = \pi D/\lambda$ , where  $\lambda$  is the wavelength of the light in the surrounding medium,  $n_2$  is the refractive index of the particle and  $n_1$  is the refractive index of the medium. When the particles are small compared to the wavelength of the incident light or  $\alpha < 0.4$  one can use either Photon Correlation Spectroscopy (PCS) (1,2) to measure particle size distributions or angular intensity measurements to obtain the radius of gyration (3). When the particles are large, 5  $\mu\text{m}$  <

0097-6156/87/0332-0133\$06.00/0

© 1987 American Chemical Society

$D < 500 \mu\text{m}$ , Fraunhofer Diffraction Pattern Analysis (FDPA) can be employed in measuring particle size distributions (4,5). For the particles in the intermediate range,  $0.7 \mu\text{m} < D < 10 \mu\text{m}$ , Mie theory of scattering holds and Turbidity Spectra (TS) can furnish information about particle sizes (6).

Our objective in this paper is to compare all three methods in the overlap region of  $0.5 \mu\text{m}$  to  $5 \mu\text{m}$ . We are particularly interested in accuracy, noise tolerance, ease of usage, and ability to deal with multimodal distributions.

### Theory

Photon Correlation. Particles suspended in a fluid undergo Brownian motion due to collisions with the liquid molecules. This random motion results in scattering and Doppler broadening of the frequency of the scattered light. Experimentally, it is more accurate to measure the autocorrelation function in the time domain than measuring the power spectrum in the frequency domain. The normalized electric field autocorrelation function  $g(t)$  for a suspension of monodisperse particles or droplets is given by:

$$g(t) = \exp(-Dq^2t) \quad (1)$$

$D$  = the diffusion coefficient of the particles in the medium

$q$  = scattering vector =  $(4\pi n_1/\lambda) \sin(\theta/2)$  where  $\theta$  is the scattering angle

$t$  = time.

For a polydisperse system equation (1) must be integrated over the size distribution with the appropriate weighting. For spherical particles the result is (7):

$$g(t) = \int f(r)r^6 \exp(-Dq^2t)P(q,r)dr \quad (2)$$

where  $f(r)$  is the size distribution function,  $P(q,r)$  is the form factor. The sixth power of the particle radius appears because the scattered electric field is proportional to the square of the polarizability which in turn is proportional to the volume of the particle. Equation (2) forms the basis for obtaining particle size distributions by PCS.

Turbidity. The attenuation of a light beam traversing a scattering medium containing  $N$  particles per unit volume is equal to the total scattered radiation; i.e.,

$$-dI/I = NR dx \quad (3)$$

where  $R$  is the scattering cross section of one particle. For an optical path length of  $x$  and incident intensity  $I_0$ ,

$$\ln(I_0/I) = NRx \quad (4)$$

For a monodisperse system of nonabsorbing spheres in the absence of multiple scattering, the turbidity is given by (8)

$$\tau = N R(r,\lambda,m) \quad (5)$$

$R(r, \lambda, m)$  is the total energy scattered by one sphere when incident wave is of unit intensity and is given by

$$R = \frac{\lambda^2}{2\pi} \sum_1^{\infty} \frac{|a_n|^2 + |b_n|^2}{2n + 1} \quad (6)$$

where  $a_n$  and  $b_n$  are complex coefficients, computation of which are discussed in detail by Heller and coworkers (8,9).

For a polydisperse system the total turbidity  $\tau$  at a specific wavelength  $\lambda$  can be written as an integral

$$\tau_{\lambda} = N \int f(r_i) \tau_{i, \lambda} dr \quad (7)$$

where  $\tau_{i, \lambda}$  is the turbidity of particles of size  $r_i$  at wavelength  $\lambda$ . To extract an average particle size from the wavelength dependence of turbidity has been around for a reasonably long time. Different methods such as the maximum turbidity method (10), turbidity quotient method (11) and turbidity at two different wavelengths (12) have been used for particle size measurement. Recently, inverting turbidity spectra by assuming a log-normal distribution has been proposed (13). With the development of automated spectrophotometers and scanning diode arrays as detectors, turbidity measurements of very high precision at wavelength steps of 0.5 nm apart can be made in the ultraviolet and visible range. Thus, more detailed information is available and equation (7) can be inverted to obtain multimodal particle size distributions.

**Fraunhofer Diffraction.** For spherical particles with diameter greater than the wavelength of the illuminating radiation, the diameter of the diffraction pattern is inversely proportional to the particle diameter. The light energy within any ring on the focal plane bounded by radii  $s_1, s_2$  due to a particle of radius  $r$  is given by:

$$L_{s_1, s_2} = E \{ J_0^2(krs_1/f) + J_1^2(krs_1/f) - J_0^2(krs_2/f) - J_1^2(krs_2/f) \} \quad (8)$$

where  $f$  is the focal length,  $E$  is the energy falling on the particle and is proportional to the cross sectional area of the particle.

$$E = CN\pi r^2 \quad (9)$$

where  $C$  is a proportionality constant. For a collection of particles of different sizes the total energy is a sum over all the sizes and is given by:

$$L_{s_1, s_2} = C' \sum_i^M N_i \{ (J_0^2 + J_1^2)_{s_1} - (J_0^2 + J_1^2)_{s_2} \} \quad (10)$$

For a detector which measures the light energy falling onto many rings we have a matrix equation

$$L(j) = N(i) T(j, i) \quad (11)$$

This equation can be solved assuming a distribution containing  $M$  fractions of sizes and then iteratively adjusting the parameters of the distribution until the deviation between the observed and calculated energy curves is a minimum.

### Experimental

Latex sphere suspensions were prepared using latex spheres of uniform size purchased from Duke Scientific and distilled-deionized water. Measurements were made immediately after rigorous shaking and sonicating to prevent settling.

Autocorrelation functions were measured with a Brookhaven Instruments 128 channel multi-time full correlator. Other details of the spectrometer have been described previously (7).

Turbidity measurements were made with an HP 8451A diode array UV-VIS spectrometer. Since styrene has an absorbance peak of 250 nm, only the data in the region of 300-800 nm was used.

Fraunhofer diffraction data were obtained with a Malvern model 2600 HSD particle sizer. This unit has 32 semicircular detector units. The detector ring spacing is related to the most intense peak of the diffraction pattern of particles with size  $r_i$  by  $2\pi r_i s_i / \lambda f = 1.375$ . Thus for a given detector the histogram spacing is fixed by the focal length of the lens and the incident wavelength of radiation.

### Results and Discussion

Monodisperse Suspensions. The absolute accuracy of the instruments were tested with a set of monodisperse solutions. Table I shows the results of this comparative study.

Table I. Particle Size Measurements of Monodisperse Systems Using Different Techniques

#### I. Photon Correlation Spectroscopy

| Nominal Diameter ( $\mu\text{m}$ ) | Size Band ( $\mu\text{m}$ ) | % wt. in Band |
|------------------------------------|-----------------------------|---------------|
| 0.261                              | 0.15 - 0.17                 | 7.1           |
|                                    | 0.17 - 0.19                 | 7.4           |
|                                    | 0.19 - 0.21                 | 9.9           |
|                                    | 0.21 - 0.23                 | 20.8          |
|                                    | 0.23 - 0.25                 | 50.8          |
|                                    | 0.25 - 0.27                 | 4.1           |
| 2.02                               | 1.92 - 1.96                 | 9.1           |
|                                    | 1.96 - 2.00                 | 9.8           |
|                                    | 2.00 - 2.04                 | 43.8          |
|                                    | 2.04 - 2.08                 | 18.1          |
|                                    | 2.08 - 2.12                 | 3.3           |
|                                    | 2.12 - 2.16                 | 3.4           |
|                                    | 2.16 - 2.20                 | 11.6          |
|                                    | 2.20 - 2.24                 | 0.8           |

Table I (continued)

## II. Turbidity Spectra

| Nominal Diameter ( $\mu\text{m}$ ) | Size of Peak ( $\mu\text{m}$ ) | % wt. of Peak |
|------------------------------------|--------------------------------|---------------|
| 1.09                               | 0.885                          | 36.9          |
|                                    | 1.150                          | 63.0          |
| 2.02                               | 1.85                           | 23.2          |
|                                    | 2.00                           | 37.0          |
|                                    | 2.15                           | 39.8          |

## III. Fraunhofer Diffraction Pattern Analysis

| Nominal Diameter ( $\mu\text{m}$ ) | Size Band ( $\mu\text{m}$ ) | % Wt. in Band |
|------------------------------------|-----------------------------|---------------|
| 1.09                               | 1.2 - 1.5                   | 9.2           |
|                                    | 1.5 - 1.9                   | 46.9          |
|                                    | 1.9 - 2.4                   | 42.2          |
| 2.99                               | 1.9 - 2.4                   | 2.6           |
|                                    | 2.4 - 3.0                   | 12.7          |
|                                    | 3.0 - 3.8                   | 46.2          |
|                                    | 3.8 - 4.8                   | 37.5          |
|                                    | 4.8 - 6.2                   | 0.3           |
| 5.0                                | 3.8 - 4.8                   | 1.6           |
|                                    | 4.8 - 6.2                   | 67.8          |
|                                    | 6.2 - 7.9                   | 30.5          |

We found out that PCS is reliable up to 7  $\mu\text{m}$  provided that dispersions of particles above one micron are dilute enough to minimize aggregation and multiple scattering. The lower size limit for PCS can go as low as 0.001  $\mu\text{m}$  depending on signal-to-noise ratios. Two experimental details one needs to be aware of in using PCS are the low counts needed not to saturate the counters of the correlator and long data collection times necessitated by longer sample times for the larger particles.

Assuming the suspended particles do not absorb in the wavelength range, 250-850 nm, the lowest size that can be measured using TS is 0.5  $\mu\text{m}$ . This is determined by measurable deviations from  $\lambda$  dependence of turbidity, i.e., the particle must be a Mie-scatterer. The upper limit of approximately 7  $\mu\text{m}$  is imposed by the numerical problems associated with calculating Bessel functions of large arguments. We have also tested the accuracy and noise tolerance of TS inversion by using simulated data (14). We found that particle size determination was not appreciably affected with noise levels as high as ~10%.

Despite claims of 1  $\mu\text{m}$  by the equipment manufacturer, the smallest size that can be sampled by FDPA reliably is 2  $\mu\text{m}$ . FDPA results for 1.09  $\mu\text{m}$  spheres listed in Table I illustrates this fact.

It is due to low resolution imposed by the fixed spacing and width of 32 detector elements designed to sample a very wide range of particle sizes, 2-1800  $\mu\text{m}$ .

Polydisperse Suspensions. Polydisperse suspensions were approximated by mixtures of monodisperse suspensions. In order not to introduce any bias in the analysis, all the data from three different instruments were analyzed using the same program. The distribution functions were assumed to be a sum of equally spaced histograms for PCS, delta functions for TS and logarithmically spaced histograms for FDPA. The height and position of each parameter was optimized using a nonlinear least squares minimization process (15).

It is important to take into consideration the limitations imposed by the size dependence of the signal in using any one of the three techniques to detect polydispersity. For example, in PCS, when the sizes are in the Rayleigh-Ganz range, the size dependence of the scattered intensity is  $r^2$  in homodyne detection. Thus, a difference of two in diameter reflects a ratio of 1:4096 in relative weighting. For particles in the Mie-scattering range, the relative weighting is not as severe but becomes strongly angle-dependent. For turbidity measurements, the weighting factors with respect to size vary from  $r^6$  at the small end to  $r^2$  for the larger particles. For the case of Fraunhofer Diffraction, the weighting factor is approximately proportional to the geometric cross section of the particle or  $r^2$ . Based on these considerations, PCS can easily detect large particles at very low concentrations whereas TS and FDPA are relatively more sensitive to smaller particles in the presence of larger ones.

We have applied each technique to several bimodal systems in the overlap region. The nominal and measured diameters and the input and measured mass fractions determined by using the different techniques are listed in Table II.

Table II. Bimodal Distribution Measurements Using Different Techniques

| Nominal Diameter<br>( $\mu\text{m}$ ) | Measured Diameter<br>( $\mu\text{m}$ ) | Input Mass<br>Fraction | Measured Mass<br>Fraction |
|---------------------------------------|--|------------------------|---------------------------|
| I. Photon Correlation Spectroscopy    |  |                        |                           |
| 1.09                                  | 1.04                                   | 0.59                   | 0.76                      |
| 5.0                                   | 5.25                                   | 0.41                   | 0.24                      |
| 1.09                                  | 0.96                                   | 0.33                   | 0.98                      |
| 2.99                                  | 2.95                                   | 0.67                   | 0.02                      |
| 1.09                                  | 0.95                                   | 0.44                   | 0.66                      |
| 2.02                                  | 2.16                                   | 0.56                   | 0.34                      |

Table II (continued)

| Nominal Diameter<br>( $\mu\text{m}$ )        | Measured Diameter<br>( $\mu\text{m}$ ) | Input Mass<br>Fraction | Measured Mass<br>Fraction |
|--|--|------------------------|---------------------------|
| II. Turbidity Spectra                        |  |                        |                           |
| 1.09   | 0.89                                   | 0.33                   | 0.36                      |
| 2.99   | 2.95                                   | 0.67                   | 0.64                      |
| 1.09   | 0.96                                   | 0.44                   | 0.52                      |
| 2.02   | 2.04                                   | 0.56                   | 0.48                      |
| III. Franhofer Diffraction Pattern Analysis* |  |                        |                           |
| 1.09   | 2.1                                    | 0.24                   | 0.19                      |
| 5.0  | 5.7                                    | 0.76                   | 0.80                      |
| 2.02   | 2.62                                   | 0.42                   | 0.49                      |
| 5.0  | 6.22                                   | 0.58                   | 0.51                      |

\*63 mm focal length lens was used.

Figure 1 shows the PCS results for three mixtures of 1.09 and 5.0, 1.09 and 2.99, and 1.09 and 2.02  $\mu\text{m}$  diameter spheres. We see that the two fractions are resolved in all cases and the means are accurately determined. The use of multiple sample times corresponding to the optimum time scales of individual peaks always improves the agreement between PCS size measurements and nominal size information. The mass fractions determined by PCS are not in quantitative agreement with the actual mass fractions which is a result of very uneven weighting of the relative contributions of the two fractions to the scattered intensity. Figure 2 is a plot of the distributions determined by using TS of two mixtures containing 1.09 and 2.99 and 1.09 and 2.02  $\mu\text{m}$  diameter spheres. The two close peaks are resolved and are at their nominal radii. In both cases the measured mass fractions of the smaller and the larger size spheres compare favorably with the input values. The bimodal distributions from FDPA for mixtures of 1.09 and 5.0, 2.02 and 2.99, and 2.02 and 5.0  $\mu\text{m}$  diameter spheres are shown in Fig. 3. The spacing and the width of the detector elements are such that the spread of a given peak is roughly equal to its mean. Therefore, 2.02 and 2.99  $\mu\text{m}$  spheres cannot be resolved. In both the monodisperse and bimodal systems, FDPA measurements of 1.09  $\mu\text{m}$  spheres yield  $\sim 2.0 \mu\text{m}$ . This is a limitation of the technique and the geometry of the detector. The input and measured mass fractions by FDPA are in quantitative agreement. Figure 4 is a comparison of the three different techniques for a mixture of 1.09 and 2.99  $\mu\text{m}$  spheres. Again 1.09  $\mu\text{m}$  is not detected by FDPA.

We also analyzed trimodal systems to test further the three methods. The results from PCS, TS and FDPA are shown in Figs. 5, 6 and 7, respectively. PCS detects the presence of three fractions. Means sizes are in good agreement with nominal sizes but there is again poor agreement of input and calculated mass fractions. This is not surprising when one considers the fact that there is an order of magnitude difference in the sizes which results in very uneven



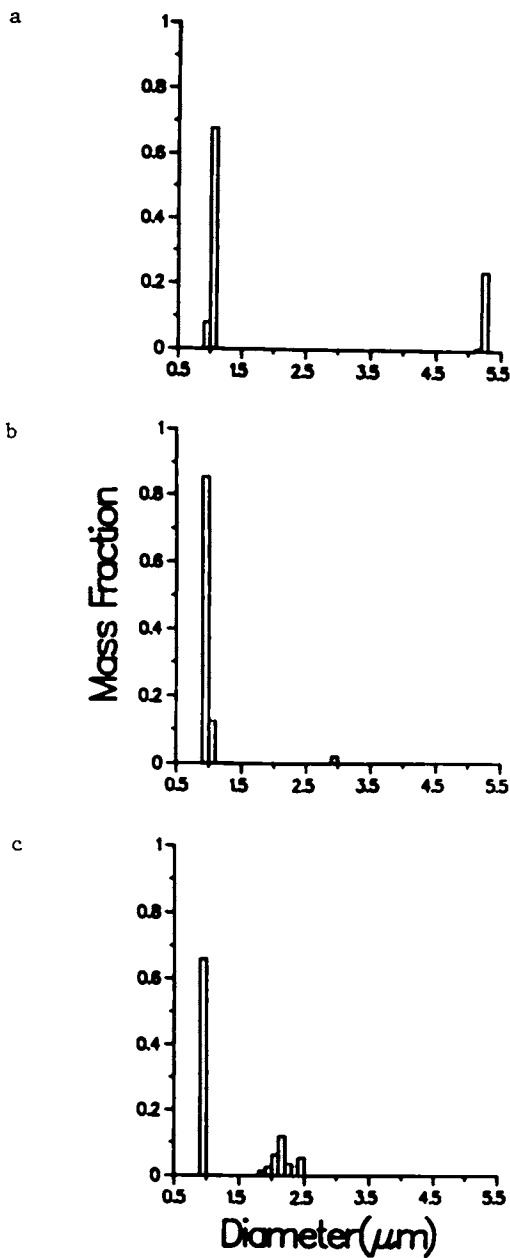


Figure 1. Bimodal distributions of suspensions containing mixtures of a) 1.09 and 5.0  $\mu\text{m}$ , b) 1.09 and 2.99  $\mu\text{m}$ , c) 1.09 and 2.02  $\mu\text{m}$  latex spheres measured by PCS.

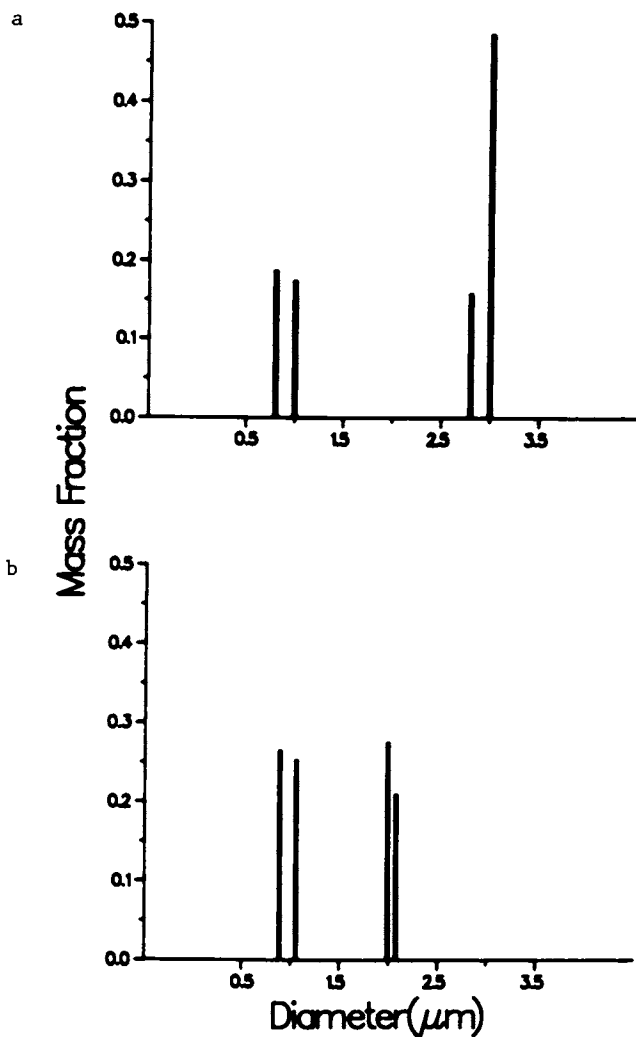


Figure 2. Bimodal distributions of suspensions containing mixtures of a) 1.09 and 2.99  $\mu\text{m}$ , b) 1.09 and 2.02  $\mu\text{m}$  latex spheres measured by TS.

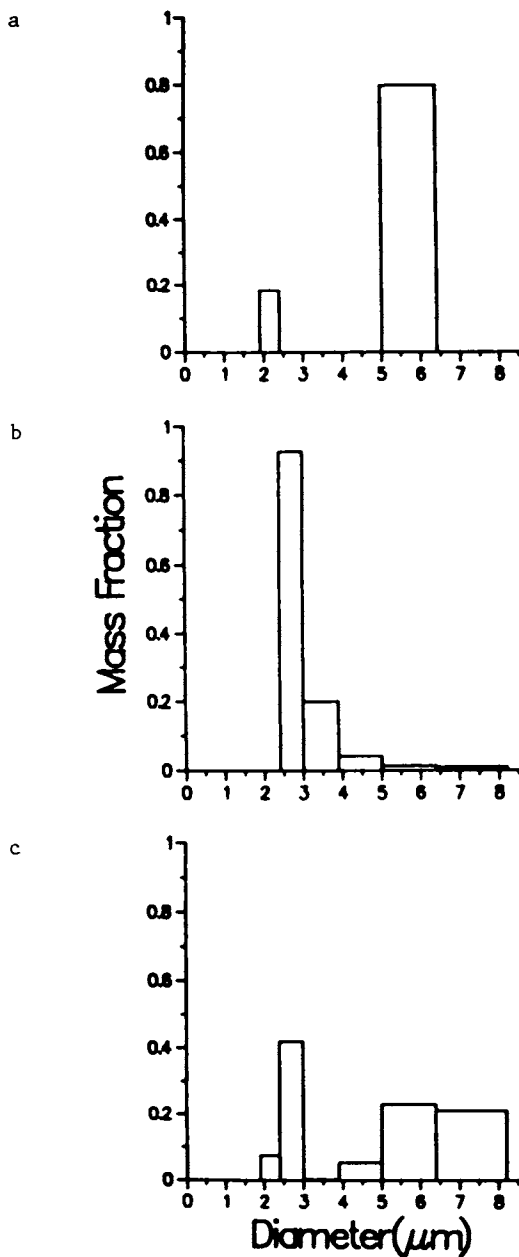


Figure 3. Bimodal distributions of suspensions containing mixtures of a) 1.09 and 5.0  $\mu\text{m}$ , b) 2.02 and 2.99  $\mu\text{m}$ , c) 2.02 and 5.0  $\mu\text{m}$  latex spheres measured by FDPA.

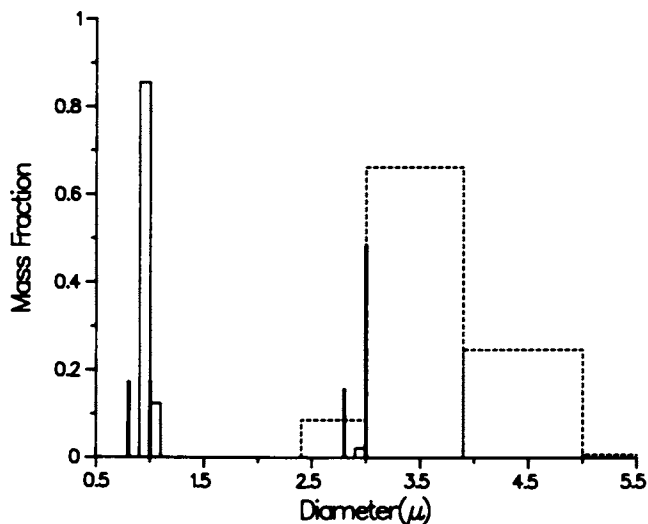


Figure 4. Comparison of the measured distributions by PCS (solid histogram), TS (delta functions), and FDPA (dashed histogram) for a mixture of 1.09 and 2.99  $\mu\text{m}$  spheres.

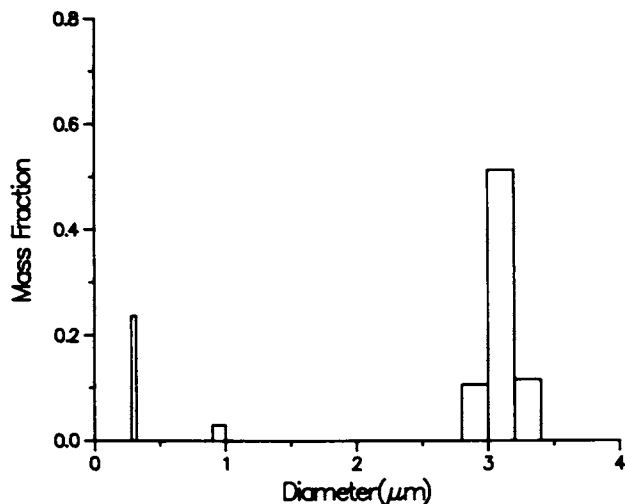


Figure 5. Trimodal distribution of a suspension containing 0.261, 1.09 and 2.99  $\mu\text{m}$  latex spheres measured by PCS. For each nominal size, the input and measured mass fractions were as follows: For 0.261  $\mu\text{m}$ , input = 0.07, measured = 0.24; for 1.09  $\mu\text{m}$ , input = 0.74, measured = 0.03; for 2.99  $\mu\text{m}$ , input = 0.19, measured = 0.73.

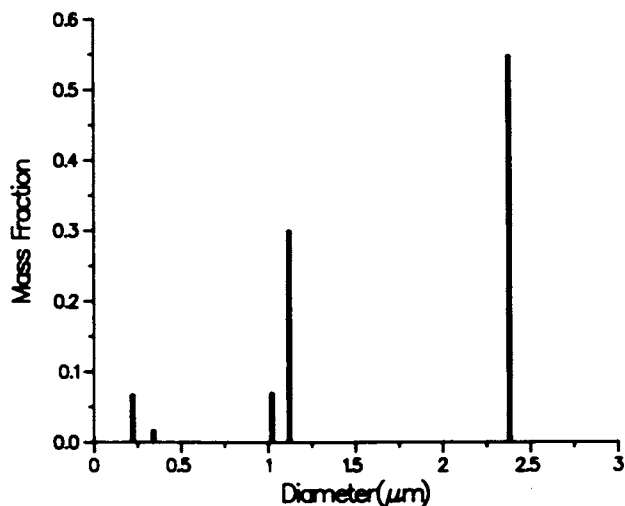


Figure 6. Trimodal distribution of a suspension containing 0.261, 1.09 and 2.02  $\mu\text{m}$  latex spheres measured by TS. For each nominal size, the input and measured mass fractions were as follows: For 0.261  $\mu\text{m}$ , input = 0.086, measured = 0.083; for 1.09  $\mu\text{m}$ , input = 0.34, measured = 0.37; for 2.02  $\mu\text{m}$ , input = 0.57, measured = 0.55.

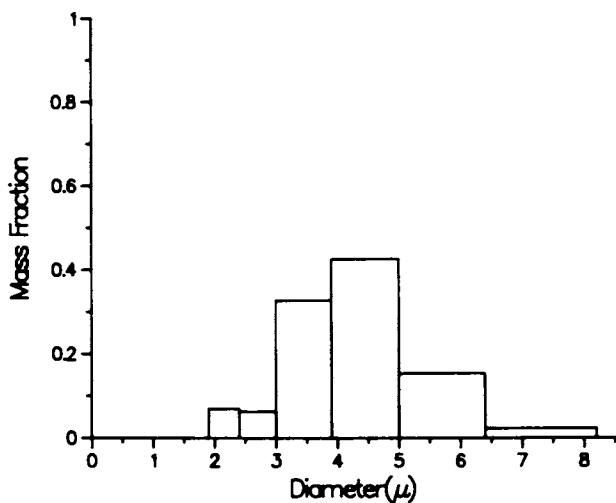


Figure 7. Size distribution of a suspension containing 2.02, 2.99 and 5.0  $\mu\text{m}$  latex spheres measured by FDPA.

contributions of each fraction to the total signal. Turbidity clearly separates 0.261, 1.09 and 2.02  $\mu\text{m}$  fractions even though the individual sizes of the peaks are about 10 percent higher than their normal sizes. As expected from the results of FDPA discussed before, 2.02, 2.99 and 5  $\mu\text{m}$  fractions of the trimodal system are not resolved and instead a broad peak extending from 2 to 8  $\mu\text{m}$  is detected.

### Conclusions

It is clear that PCS and FDPA are complementary particle sizing techniques with a dividing size limit of about 5  $\mu\text{m}$ . TS overlaps with both PCS and FDPA in the region of 0.5 to 5  $\mu\text{m}$ . PCS and TS have comparable resolution in the overlap region while the resolution for FDPA is lower. PCS needs the most care in sample preparation and data acquisition. TS and FDPA can be used with higher concentrations of particles. In using FDPA, there is a trade-off between lower resolution and ease of usage and speed. For both FDPA and TS, the signals are deterministic in nature and the times required to obtain data is trivial compared to the analysis times. For PCS, data acquisition could take longer than data analysis because of the needed statistical accuracy.

### Acknowledgments

We gratefully acknowledge the financial support of this work by NSF and U.S. Army.

### Literature Cited

1. Gulari, Es; Gulari, Er.; Tsunashima, Y.; Chu, B. J. Chem. Phys., 1979, 70, 3965.
2. McWhirter, J.G.; Pike, E.R. J. Phys. A, 1978, 11, 1729.
3. Kerker, M. "The Scattering of Light and Other Electromagnetic Radiation"; Academic: New York, 1969.
4. Swithenbank, J.; Beer, J.M.; Taylor, D.S.; McCreath, G.C. Progress in Astronautics and Aeronautics, 1977, 53, 421.
5. Burkholz, A.; Polke, R. Particle Characterization, 1984, 1, 153.
6. Wallach, M.L.; Heller, W.; Stevenson, A.F. J. Chem. Phys., 1961, 34, 1796.
7. Bedwell, B.; Gulari, Er.; Melik, D.H. "Measurement of Suspended Particles by Quasi-Elastic Light Scattering"; Dahneke, B.E., Ed.; Wiley: New York, 1983; p. 237.
8. Heller, W.; Pangonis, W.J. J. Chem. Phys., 1957, 26, 498.
9. Denman, H.H.; Heller, W.; Pangonis, W.J. "Angular Scattering Functions for Spheres"; Wayne State Univ. Press: Detroit, 1966.
10. Inn, E.C.Y. J. Colloid. Sci., 1951, 6, 368.
11. Dezelic, G.; Dezelic, N; Tezak, B. J. Colloid. Sci., 1963, 18, 888.
12. Melik, D.H.; Fogler, H.S. J. Colloid. Interface Sci., 1983, 92, 161.
13. Zollars, R.L. J. Colloid. Interface Sci., 1980, 74, 163.
14. Gulari, Es.; Bazzi, G.; Gulari, Er.; Annapragada, A. Particle Characterization, 1986.
15. Chu, B.; Gulari, Es.; Gulari, Er. Physica Scripta, 1979, 19, 476.

## Chapter 10

# Particle Size Determination Using Angular Light Scattering

Harold N. Frock

Leeds & Northrup Instruments, 3000 Old Roosevelt Boulevard,  
St. Petersburg, FL 33702

The size of particles can be determined by observing the patterns of light scattered at various angles. Angular light scattering (described by Fraunhofer Diffraction Theory) can be applied to particles with dimensions large compared to the wavelength of light producing the scatter. The more complex Mie Theory (1) must be invoked to analyze particles with dimensions near the wavelength of light. Fraunhofer theory is an interference phenomenon, and is described in various optics text books (2,3). It is adequate for most particle sizing applications and will be discussed in detail. Mie Theory requires a knowledge of the refractive index of the material. A unique use of polarized side scatter at several wavelengths is employed to obtain particle size channels in the submicron region.

### Fraunhofer Light Scattering

The diffraction phenomenon, on which most light scattering instruments are based, is well known. This section provides a summary of the mathematical background. Considering the light which is scattered from a single illuminating beam, one finds that the information regarding the particle dimension is found in the angular distribution of scattered light flux, and that information relating to the cross sectional area of the particle is contained in a measure of the total scattered flux. However, it is desirable to have a measure of some quantity directly related to the mass of the particle, namely the volume of the particle. The approach that has been taken is to extract volume information from the scattered flux signal by forming the Fraunhofer diffraction pattern in the focal plane of a positive lens. An optical filter is placed in the plane of the Fraunhofer diffraction pattern, which is shaped so as to pass a fraction of the collected flux proportional to the cube of the diameter of the particle which produces the scattering.

A convenient description of light scatter, or diffraction as it relates to particle size measurement (4,5), is shown in Figure 1. In the simplest case, one can visualize two particles--one large

0097-6156/87/0332-0146\$06.00/0  
© 1987 American Chemical Society

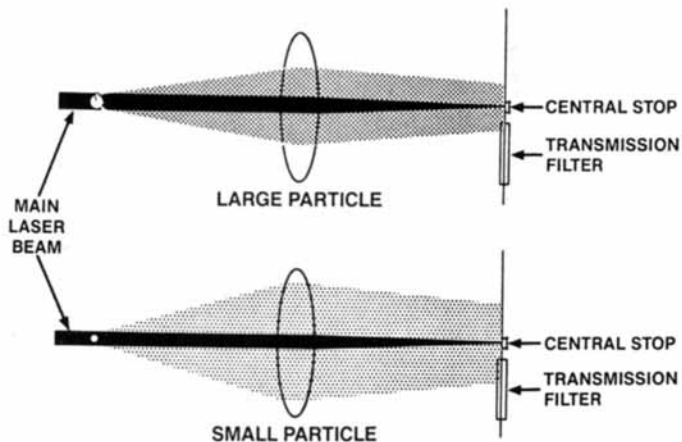


Figure 1. Comparison of scattered light flux angle and intensity for large and small particles. Reproduced with permission from Ref. 9. Copyright 1980 American Ceramic Society.

American Chemical Society  
Library

1155 16th St., N.W.

In Particle Size Distribution: Procyer, T.;  
ACS Symposium Series; American Chemical Society: Washington, DC, 1987.

Washington, D.C. 20036



and one small--illuminated by a collimated light source. The angle through which light is scattered by particles is inversely proportional to the diameters of the particles. The small particle scatters light through wider angles than the large particle. Measurement of scattered intensities at various angles will produce a profile which can be used to precisely determine the dimensions of the scattering particle. The collimated light beam itself must be prevented from reaching the detection area, because of its very high intensity relative to the scattered light. This is accomplished by focusing the main beam to a very small image and blocking it in the plane of the optical filter. Only the light scattered at angles that transcend the extent of the main beam is transmitted through the optical filter to the detection area. The unique shape of the optical filter transmits light, the intensities of which are proportional to the volume of particulate material. The net result of this optomechanical arrangement is a multi-channel histogram of the particle size distribution in a size range from approximately one micrometer to 300 micrometers. For a particle whose radius is sufficiently large compared with the wavelength, the intensity distribution of the Fraunhofer diffraction pattern is given by the familiar Airy formula: (6)

$$I(w) = Ek^2 a^4 \left[ \frac{J_1(kaw)}{kaw} \right]^2 \quad \text{Equation 1}$$

where E is the flux per unit area of the incident beam,  $k = 2\pi/\lambda$ , a is the particle radius,  $W = \sin \theta$  with  $\theta$  the angle relative to the direction of the incident beam, and  $J_1$  is the first order Bessel function of the first kind.

It is well known that if the total diffracted flux is collected and measured, a signal will be generated that is proportional to the square of the particle radius, permitting a direct measurement of the cross-sectional or surface area of the sphere.

$$\begin{aligned} F_2(a) &= \int_0^1 I(w) 2\pi w \, dw \\ &= 2\pi E k^2 a^4 \int_0^1 \left[ \frac{J_1(kaw)}{kaw} \right]^2 w \, dw \\ &= 2\pi E a^2 \int_0^{ka} \frac{J_1^2(x)}{x} \, dx \end{aligned}$$

and since for values of the particle radius for which Equation (1) is valid, the integrand is negligibly small beyond the upper limit, this may be written

$$\begin{aligned}
 F_2(a) &= 2\pi E a^2 \int_0^{\infty} \frac{J_1^2(x)}{x} dx \\
 &= \pi E a^2
 \end{aligned}
 \tag{Equation 2}$$

Many industrial processes, however, require measurement of the total mass or volume of particulates. Selective attenuation and collection of the diffracted flux can produce a signal proportional to the cube of the particle radius, and hence a measure of the volume, or mass, if the specific gravity is known. A Fraunhofer plane mask which passes flux proportional to the radius cubed is desirable. Attenuation of this kind can be accomplished by a fixed spatial filter whose properties to a first approximation do not depend on  $a$ . The reason is that, as shown by Equation (1), the radial variation of diffracted flux depends only on the product  $aw$ , so that attenuating the flux is proportional to  $1/a$ . Thus, after passage through a filter having transmission  $T(w) = C/w$ , where  $C$  is constant, the integrated flux, using Equation (1),

$$\begin{aligned}
 F_3(a) &= \int_0^1 I(w) T(w) 2\pi w dw \\
 &= 2\pi E k^2 C a^4 \int_0^1 \left[ \frac{J_1(kaw)}{kaw} \right]^2 dw \\
 &= 2\pi E k C a^3 \int_0^{ka} \left[ \frac{J_1(x)}{x} \right]^2 dx
 \end{aligned}$$

and, assuming as before that  $a$  is large enough for the upper limit of the integral to be taken as infinity, this gives

$$F_3(a) = \frac{8}{3} E k C a^3
 \tag{Equation 4}$$

Actual measurements deviate from theory at the large particle end because the angle of the diffracted flux is not sufficient to be distinguishable from the unscattered beam for very large particles. Deviation at the small particle end occurs as the particle size approaches the wavelength of the light source. These limitations

define a working range of particle size from about 2 to 300 micrometers for a standard "midrange" instrument design.

### Mie Scattering

Submicron particle size analysis employs a scatter theory not completely described by Fraunhofer diffraction. The small particle range down to about 0.1 micrometer in diameter utilizes a combination of Fraunhofer diffraction and Mie theory for the forward scattered light and 90-degree Mie scatter at three (3) wavelengths and two (2) polarizations of each wavelength. Because of its need for a technology more involved than diffraction theory, submicron measurements are influenced by the index of refraction of the material making up the particulates to be sized.

The index of refraction of a material is a measure of the change in the velocity and wavelength of the light, and of the change in amplitude as light penetrates the material. Refractive index ( $N$ ) is defined mathematically by an equation containing two components; the real index ( $n$ ), and the complex component ( $n'$ ):

$$N = n - in'$$

where:  $n$  = the real component, which is the ratio of the velocity of light in the material

$n'$  = the extinction coefficient of the material

$$i = \sqrt{-1}$$

For particulate materials with high real indices, the reported size depends less on the complex component (7). Also, as the size of particles increases, the total scattering phenomenon simplifies to Fraunhofer diffraction, and becomes a very weak function of refractive index.

Forward scatter, Fraunhofer and Mie, is utilized for measurement throughout most of the particle size range. As particles become very small, however, it is difficult to collect the light scattered at those extremely wide angles with practical optical systems. For this reason, the 3 channels at the lower end of the size range are produced using light scattered at 90-degrees. The Mie constants discussed in the previous sections are evaluated for and applied only to the forward scattered light. Size determinations made by the light scattered at a right angle (90-degree scatter) are computed separately by using orthogonal polarization at difference wavelengths (8). To illustrate the operation of the 90-degree scatter, Figures 2 and 3 are plots of the logarithms of intensity of scattered light vs. angle of scatter from 0 to 180 degrees. Figure 2 shows intensity values ( $i_1$ ) in one plane of polarization, and Figure 3 shows intensity values ( $i_2$ ) from the orthogonal plane (i.e., the planes of polarization are mutually perpendicular).

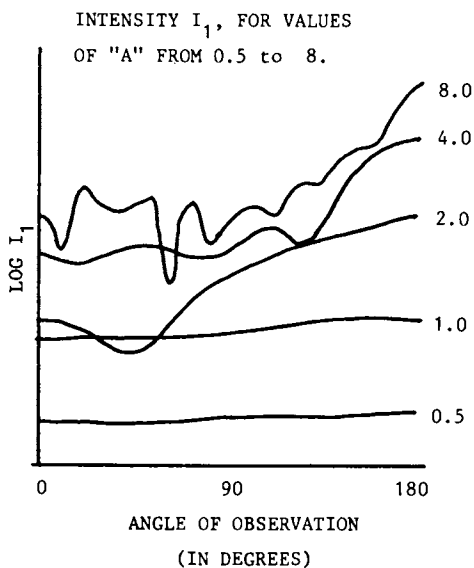


Figure 2. Right-angle scatter in  $I_1$  plane of polarization.

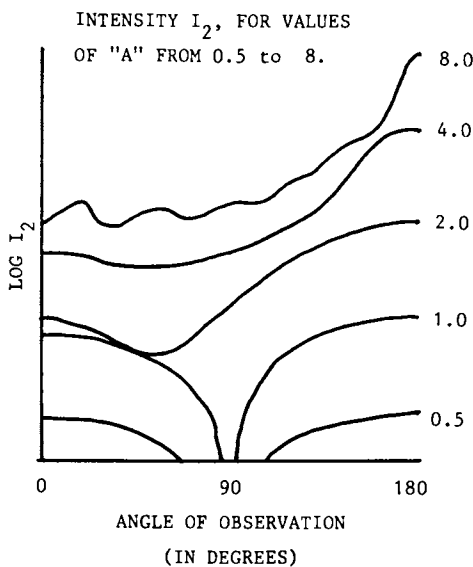


Figure 3. Right-angle in  $I_2$  plane of polarization.

In this example, water droplets are used. The curves themselves are plots of the size parameter, "A", where:

$$A = \pi D / \lambda$$

with  $D$  = particle diameter  
and  $\lambda$  = wavelength of light

One of the more stable characteristics of the patterns in the two figures is the null at 90-degrees for small values of "A" with  $i_2$ , one of the planes of polarization (Figure 3). For small "A" values, the difference between Figures 2 and 3 are greatest at 90-degrees, making this useful for measurement purposes.

This particular execution of particle size measurement, in its utilization of Fraunhofer diffraction and Mie Theory, measures the volume of particulate material. It is, therefore, appropriate to introduce this volume concept by determining the flux difference per unit volume. This is straightforward because the intensity of 90-degree scatter for any size parameter is directly proportional to the number of particles of that size. When the flux difference per particle,  $i_1 - i_2$  is divided by the volume of one particle, and plotted against the log of "A", a well defined peak occurs. Figure 4 shows this curve, computed for spheres of index 1.33 (water). The curve in Figure 4 has a mean value slightly greater than 1. Using wavelengths generated by a wide-band white light source, three (3) channels are formed as shown in Figure 5. It is evident from the figure, and also from Equation 5, that channel values scale directly with wavelength. These numbers are computed for an index of 1.33 (water). Other indices produce curves that are similar. For example, computations for glass spheres produce a size parameter that is about the same, indicating a minimal dependence of side scatter on refractive index, in contrast to much larger effects on small particles measured by forward scatter.

The two sets of computations - forward scatter and side scatter - are made separately. In order to determine the complete size distribution, the forward and side scatter determinations must be combined. This is accomplished by adjusting the gain on the side scatter computations until those channels blend together with the distribution--incorporating both forward and side scatter distributions--is then renormalized and printed out as a 16-channel particle size distribution from 0.12 to 42.2 microns. Any Mie constant adjustment is made to the forward scatter computations alone because the side scatter channels are relatively insensitive to variations in the refractive index.

Extensive applications experience has shown that most particulate materials can be analyzed without any consideration of the refractive index. This is generally true because most practical materials have a high index, or are somewhat absorbing. In the exceptional case in which refractive index corrections must be applied, the values of the real and complex indices must be determined carefully. Arbitrary use of index corrections to arbitrarily alter instrument calibration may produce highly erroneous results. Table I serves as a guide to the effects of the refractive index on small particle measurements.

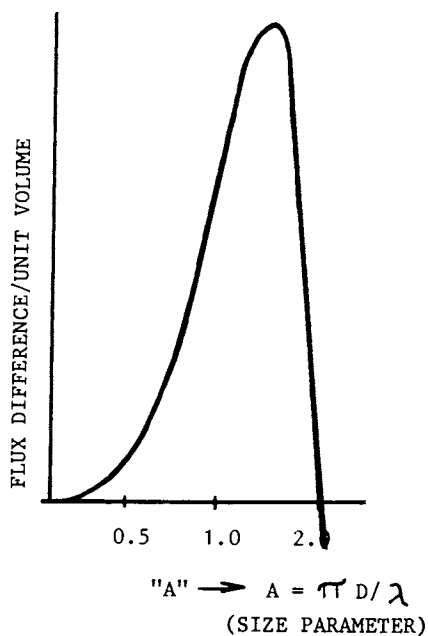


Figure 4. Flux difference per particle per unit volume. Reproduced with permission from Ref. 10. Copyright 1980 Hemisphere Publishing.

|                              |            |            |            |
|------------------------------|------------|------------|------------|
| <b>WAVELENGTH</b>            | <b>.45</b> | <b>.60</b> | <b>.90</b> |
| <b>PARTICLE<br/>DIAMETER</b> | <b>.15</b> | <b>.2</b>  | <b>.3</b>  |

**All units in micrometers**

Figure 5. Wavelength/Channel center relation for three lowest channels.

Table I.

## INDEX OF REFRACTION

| <u>Real Component</u> | <u>Complex Component</u>    |
|-----------------------|-----------------------------|
| High                  | High (Absorbing Materials)  |
| High                  | Low (Transparent Materials) |
| Low                   | High (Absorbing Materials)  |
| *Low                  | Low (Transparent Materials) |

( \* MIE CORRECTIONS BECOME SIGNIFICANT)

Systems For Light Scattering Measurements

Implementation of Fraunhofer and Mie scattering is accomplished through the use of various optical and electronic designs. Schematic diagrams of a combined system are shown in Figure 6. In one configuration--the forward scatter mode--a helium-neon laser illuminates particles flowing through a sample cell. The diffraction patterns generated are directed through an optical filter and sensed by a silicon photodetector. Measurement of the very small particles is carried out by detecting the light scattered at 90deg.--the side scatter mode in the figure.

Detection of the optically-filtered scattered light is followed by digital processing of the signals to compute the particle size distribution. The Z-80 microprocessor accepts digitized signals from the ADC (Analog-to-Digital converter), stores them in RAM (Random-Access Memory) until the end of the data collection cycle, and then performs the computation of the size distribution (see Figure 7). A multi-channel histogram of the size distribution is displayed on a digital printer, and also presented to an RS-232 port for computer interfacing.

The measurement does not require particles to pass through the laser beam one at a time. In fact, there are normally large numbers of particles in the beam at any point in time. Each particle forms its own diffraction pattern, and the system sums the results from these patterns over the total measurement period. It is important that the particulate concentration be low enough so that multiple scattering does not occur. This happens when light which is scattered from one particle strikes another particle and is scattered further before it is collected. This phenomenon is easily detected, and the loading range is usually quite broad.

Particle sizers employing light scattering do not require field calibration. The measurement of particle size is determined by focal lengths of lenses and the angular extent of the optical filters and detectors. This feature is an important one for production and quality control situations in which calibration could be easily set incorrectly or disturbed in some way during operation. It is prudent, however, to periodically check the operation of the instrument using a well-known diagnostic material, and to perform recommended periodic maintenance.

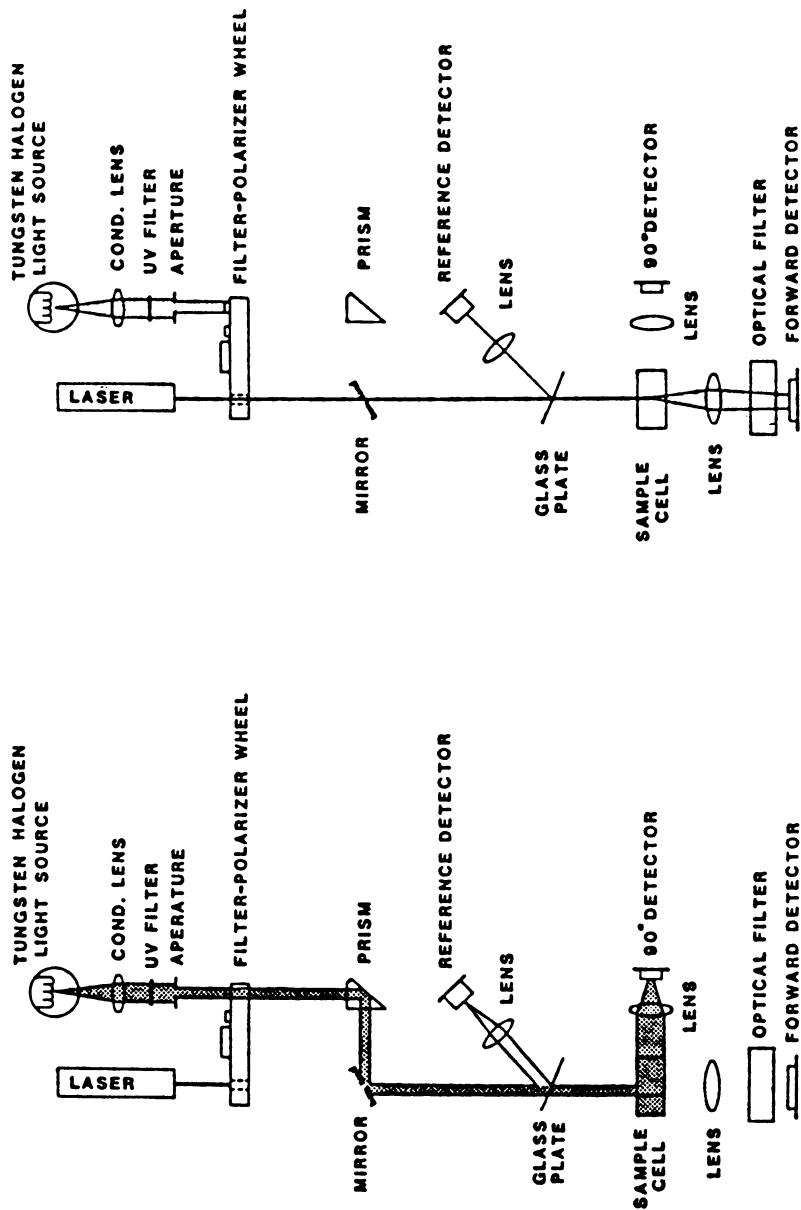


Figure 6. Optics for light scattering. Reproduced with permission from Ref. 10. Copyright 1980 Hemisphere Publishing.



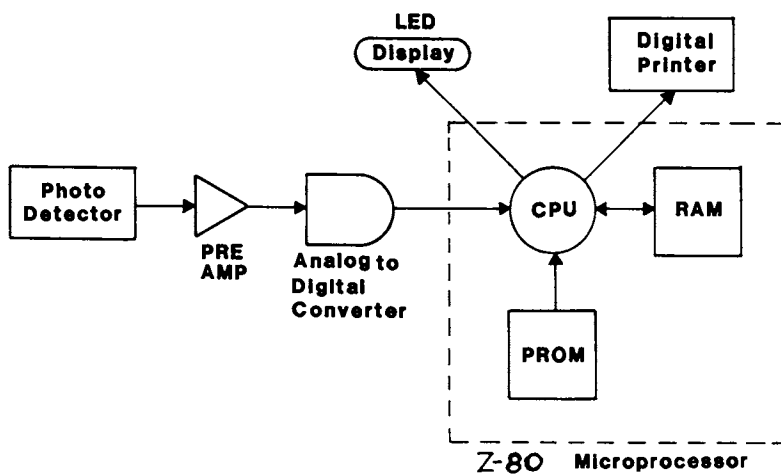


Figure 7. Block diagram of electronics.

### Data Correlation

The theory and design of all particle size measurement devices are based on the assumption that particles are spherical. Most materials submitted for size analysis are not spherical. When these materials are analyzed by instruments employing different physical principles, the results are different. Figure 8 illustrates this point by comparing the cumulative (percent passing) distribution of three identical samples analyzed on three different instruments, each employing a different measurement technique. The absolute values of the distributions are different, but their shapes are quite similar. Because these results usually exhibit differences which are consistent, a correlation can be determined between one or more parameters of the distribution.

A correlation can be determined by carrying out analysis on a number of different samples on the instruments to be correlated. The samples should be chosen to cover as wide a range as practical so that a good curve-fit may be computed. An example of a correlation curve for a set of alumina samples is shown in Figure 9. A sedimentation instrument was correlated with a light scattering instrument. Each individual point on the graph is the result of one parameter (the median in this case) of the distribution as reported by each of the two instruments for one sample. The 7 data points, representing the medians of 7 different samples, were plotted to determine the correlation between the two instruments for that type of sample material. A best-fit linear regression produced the straight line on the graph as well as the equation shown.

### Applications

Light scattering has been applied to the measurement of particle in just about every field. These include ceramics, minerals, metal powders, food, energy, environmental, pharmaceuticals, and the very important field of chemicals. Some examples of applications in the chemical industry are:

|                   |                   |            |
|-------------------|-------------------|------------|
| catalysts         | propellants       | explosives |
| pigments          | toners            | coatings   |
| polymers          | titanium dioxide  | emulsions  |
| adhesives         | manganese dioxide | phosphates |
| coal-oil mixtures |                   |            |

### Conclusions

Particle size and distributions can be determined by a number of different methods. The technique described here is light scattering. Different measurement methods produce different results which can be correlated experimentally. The absence of distribution standards for light scattering particle sizing instruments precludes any determination of size accuracy. This is further complicated by particles of non-spherical shape which makes the concept of size very difficult to define. However, for particulate materials encountered in most industrial processes, the assumption that particles are spheres produces quite useful results that are repeatable and relate to important parameters of many processes.

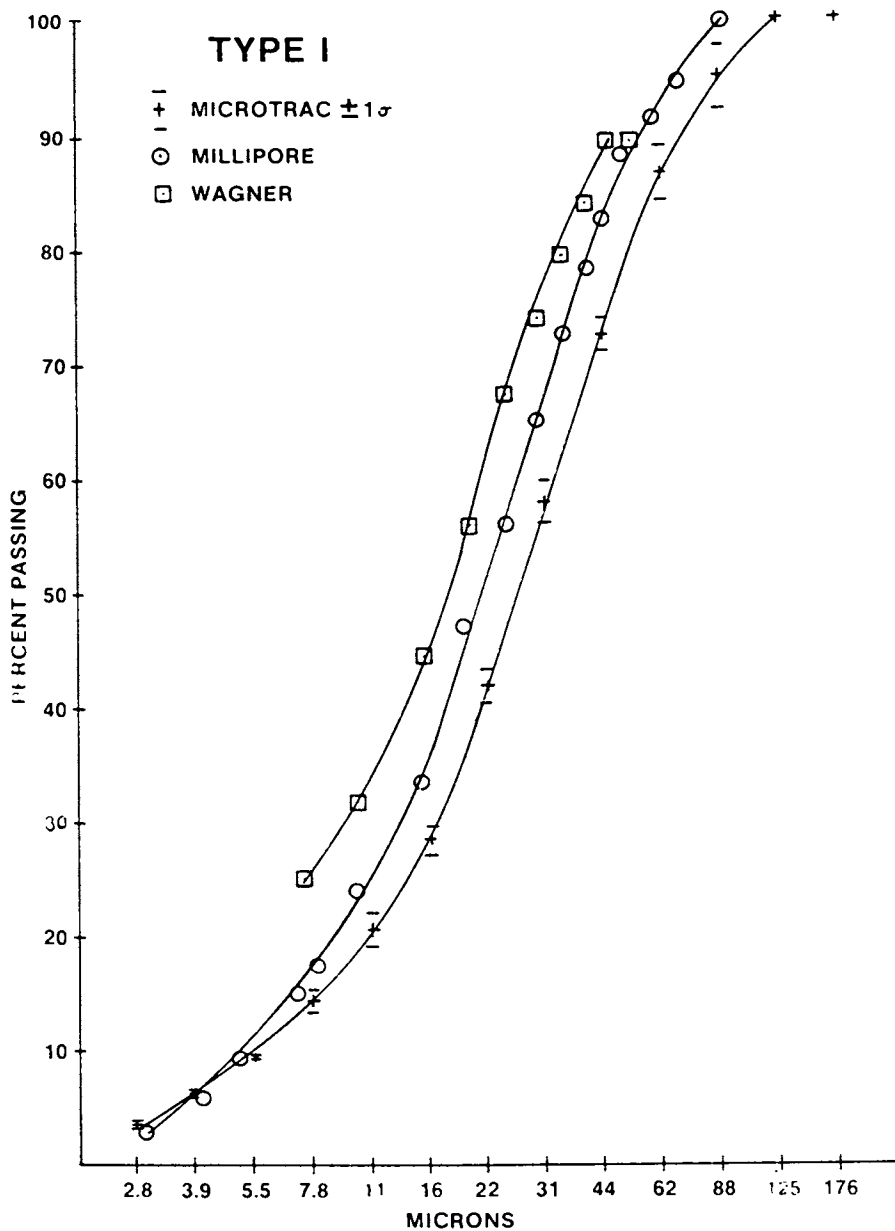


Figure 8. Comparison of three identical samples.

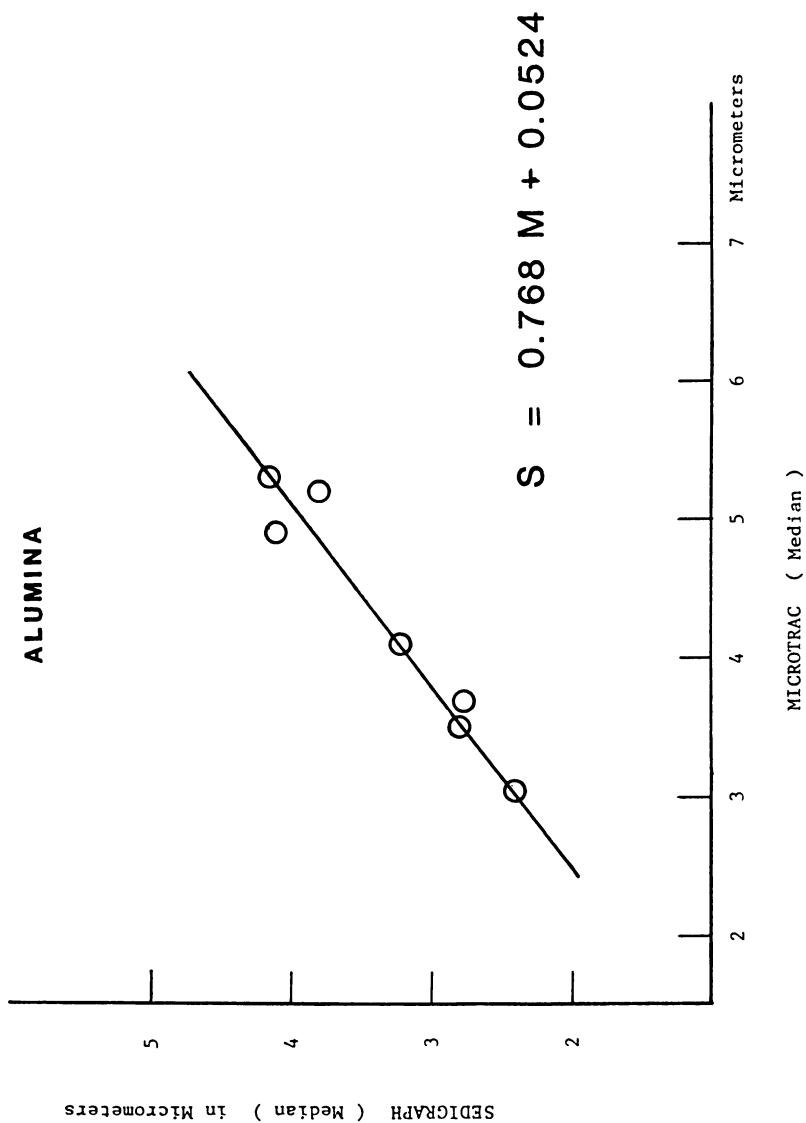


Figure 9. Correlation: Sedimentation (S) vs. light scattering (M).

References

1. Mie, Gustave, Annalen der Physik, Vol. 25, No. 3, (1908) p.377.
2. Jenkins & White, "Fundamentals of Optics"; McGraw-Hill, Second Ed.
3. Born, M. and Wolf, E., "Principles of Optics"; (4th Ed.), Pergamon Press, Oxford, 1970.
4. Muly, E. C. and H. N. Frock, Opt. Eng., Vol.19, No.6, Nov/Dec 1980, p. 861.
5. Plantz, P.E., "Modern Methods of Particle Size Analysis"; Chap. 6. p. 173, Edited by Howard G. Barth, copyright 1984 by John Wiley & Sons, Inc.
6. Wertheimer, A. L. and W. L. Wilcock, Appl. Opt., Vol. 15, June 1976, p. 1616.
7. "International Critical Tables"; McGraw-Hill, 1929.
8. Wertheimer, A. L. , et.al., "Optical Measurements of Particulate Size in Stationary Source Emissions"; presented at the U.S.E.P.A., Research Triangle Park, N.C., May 15-17, 1978.
9. Frock, H. N. and Walton, R. L., Am. Ceramic Soc. Bull., Vol. 59, No. 6, June 1980, pp. 650-651.
10. Muly, E. C. and Frock, H. N. "Submicron Particle Size Analysis Using Light Scattering" presented at the Fine Particle Society Conference at the University of Maryland, Sept. 16, 1980.

RECEIVED July 25, 1986

## Chapter 11

# Averages from Turbidity Measurements

L. H. Garcia-Rubio

Department of Chemical Engineering, College of Engineering, University of South  
Florida, Tampa, FL 33620

The information content of turbidity measurements from polydisperse particulate systems has been analysed on the basis of Mie theory and reported approximations to Mie theory. The results from the analysis suggest two alternative interpretations of turbidity data for the small and intermediate particle size regimes: an interpretation in terms of moments of the particle size distribution and an equivalent interpretation in terms of the volume to surface average particle diameter. It is also shown that in the intermediate particle size regime, the effective average diameter that satisfies the mean surface average extinction efficiency does not correspond to a particular average of the particle size distribution. The value of the effective particle diameter depends on both the wavelength and the spread of the particle size distribution. It is possible, however, to interpret turbidity data in terms of an effective average diameter and the volume to surface particle diameter. The results obtained explain some of the discrepancies existing in the literature regarding the interpretation of the average particle diameters obtained from scattering measurements. The theoretical and practical implications of the results are presented and discussed.

0097-6156/87/0332-0161\$06.00/0  
© 1987 American Chemical Society

The analysis of particulate systems using light scattering measurements is of great scientific and industrial importance and as such it has been treated extensively in the literature (1-5). For monodisperse particulate systems, the theory and the practice of light scattering have been quite successful and are well established. However, this is not the case for polydisperse systems, where the turbidity at a given wavelength is related to the particle size distribution (equations 1-9). Mie Theory relates the measured turbidity ( $\tau$ ), to the number, size and optical constants of suspended isotropic spherical particles through the following equations (1-5):

$$\tau(\lambda) = N \ell \int_0^{\infty} \frac{\pi}{4} D^2 Q(\alpha, m) f(D) dD \quad (1)$$

or

$$\tau(\lambda) = \frac{3 C \ell}{2 \rho} \frac{\int_0^{\infty} D^2 Q(\alpha, m) f(D) dD}{\int_0^{\infty} D^3 f(D) dD} \quad (2)$$

$$\alpha = \frac{\pi D}{\lambda}$$

Where,  $\tau(\lambda)$  is the turbidity at the wavelength  $\lambda$ ,  $N$  the number of particles/ml,  $C$  the concentration in g/ml,  $D$  the particle diameter,  $f(D)$  the frequency distribution of particle sizes,  $\rho$  the density of the particles,  $m$  is the complex refractive index ratio and  $Q(\alpha, m)$  is the Mie overall extinction efficiency. The extinction efficiency is given by

$$Q(\alpha, m) = (2/\alpha^2) \sum_{n=1}^{\infty} (2n+1) \operatorname{Re}(a_n + b_n) \quad (3)$$

If the particles are non-absorbing, equation 3 becomes

$$Q_{\text{scat}} = (2/\alpha^2) \sum_{n=1}^{\infty} (2n+1) [ |a_n|^2 + |b_n|^2 ] \quad (4)$$

$$a_n = \frac{\psi_n(\alpha) \psi'_n(\alpha m) - m \psi_n(\alpha m) \psi'_n(\alpha)}{\zeta_n(\alpha) \psi'_n(\alpha m) - m \psi_n(\alpha m) \zeta'_n(\alpha)} \quad (5)$$

$$b_n = \frac{m \psi_n(\alpha) \psi'_n(\alpha m) - \psi_n(\alpha m) \psi'_n(\alpha)}{m \psi_n(\alpha) \psi'_n(\alpha m) - \psi_n(\alpha m) \zeta'_n(\alpha)} \quad (6)$$

$$\zeta_n(\alpha) = \psi_n(\alpha) + i \chi_n(\alpha) \quad (7)$$

$$\psi_n(\alpha) = (\pi \alpha/2)^{1/2} J_{n+1/2}(\alpha) \quad (8)$$

$$\chi_n(\alpha) = -(\pi \alpha/2)^{1/2} N_{n+1/2}(\alpha) \quad (9)$$

Where,  $m = (n + ik)/n_0$  and  $n_0$  is the refractive index of the suspending medium.  $J(\alpha)$  and  $N(\alpha)$  are half order integral Bessel and Neuman functions.

The solution to the integral equations 1 or 2-9 is rather difficult, the scattering coefficients ( $a_n + b_n$ ) have to be calculated at every measured wavelength and every particle diameter for a given form of the particle diameter distribution, where the form of the distribution is generally unknown. The problem of solving equations 1 or 2 for the particle size distribution is known as the "Inverse Scattering Problem" and although this problem has been treated extensively, no general solutions have been reported (3, 6, 7,). Alternative approaches to the solution of the integral equations include the assumption of the shape of the particle size distribution (3, 8-12) and the estimation of "Effective Particle Diameters" (3, 13-15).

If the form of the particle size distribution is known or it can be assumed then, the main problem in the solution of equations 1 or 2 stems from the complex calculations required to evaluate the integral

$$\int_0^{\infty} D^2 Q(\alpha, m) f(D) dD \quad (10)$$

A number of distribution functions have been identified experimentally for a variety of systems (3) and, in particular, the Log-Normal distribution is extensively used for the calculation of the integral and for the evaluation of the moments of the particle size distribution (8-12). The problem with this approach is that, in general, the shape of the particle size distribution is unknown and thus, the average particle diameters obtained are conditional upon



the validity of the assumption regarding the form of the distribution.

Direct application of the scattering equations for monodisperse systems to particulate systems that are polydisperse, will clearly result in the estimation of average or effective particle diameters. The interpretation of these average diameters is not straightforward. Quoting Kerker (3), "there is no simple method of comparing the size determined by the electron microscope with the average size obtained from light scattering. Indeed, not only will different light scattering methods give different averages, but each particular distribution of sizes will have its own characteristic average." Maron, Pierce and Ulevitch (13) experimentally investigated this problem and reported good agreement between the particle diameters obtained from specific turbidity measurements taken at several wavelengths, and the turbidity average particle diameters calculated from electron microscopy measurements of the size distribution. Dobbins and Jizmagian (14), on the other hand, noted that for a wide variety of monomodal distribution functions with radii comparable to and larger to the wavelength, the specific turbidity can be adequately represented in terms of the volume surface mean diameter and the mean surface scattering efficiency.

$$\tau(\lambda) = \frac{3 C \ell}{2 \rho} \frac{Q(\alpha, m)}{D_{3,2}} \quad (11)$$

where the mean surface scattering efficiency is given by

$$\overline{Q(\alpha, m)} = \int_0^{\infty} D^2 Q(\alpha, m) f(d) dD / \int_0^{\infty} D^2 f(D) dD$$

Since the ratio  $\overline{Q(\alpha, m)} / D_{3,2}$  was shown, numerically, to be independent of the shape of the distribution, Dobbins and Jizmagian computed tables of the mean surface scattering efficiency as a function of the volume surface mean diameter for the evaluation of  $D_{3,2}$  directly from transmission measurements. More recently, Bagchi and Vold, analysed latex particles considerably larger than the wavelength of the incident radiation where the extinction coefficient is approximately independent of the particle size. Their results suggest that, in the particle range investigated, the specific turbidity can be directly related to the first three moments of the particle size distribution and to the volume to surface average particle diameter. Unfortunately, the polydispersities of the latices investigated were relatively small preventing any definitive statement as to the average that best correlates the data.

Ideally, it is desirable to solve equations 1 or 2 for the complete size distribution whenever polydisperse systems are being analysed. However, from the computational point of view, the direct application of the equations for monodisperse systems is more

appealing. It is therefore necessary to establish both, the physical meaning of the "effective" average diameters as well as the information content of the turbidity data in terms of the moments of the particle size distribution.

#### Problem Formulation And Analysis

By first considering the Rayleigh regime and expanding the complex scattering coefficients in power series of  $\alpha$ , it can be shown that the extinction can be approximated by (1, 3, 17)

$$Q(\alpha, m) = \Gamma_1' \alpha + \Gamma_3' \alpha^3 + \Gamma_4' \alpha^4 + \Gamma_5' \alpha^5 + \dots \quad (12)$$

or

$$Q(\alpha, m) = \Gamma_1 D + \Gamma_3 D^3 + \Gamma_4 D^4 + \Gamma_5 D^5 + \dots \quad (13)$$

Where the coefficients  $\Gamma$  and  $\Gamma$ 's are implicit functions of the optical constants and thus of the wavelength (see Appendix I).

For monodisperse systems, replacement of equation 13 into equation 2, yields an approximation to the turbidity in terms of powers of the particle diameter

$$\tau(\lambda) = \frac{3 C \ell}{2\rho} [ \Gamma_1 + \Gamma_3 D^2 + \Gamma_4 D^3 + \Gamma_5 D^4 + \dots ] \quad (14)$$

For polydisperse systems, replacement of equation 13 into equation 2 for every particle diameter, yields an approximation to the turbidity in terms of ratios of moments of the particle size distribution without having to make assumptions regarding the shape of the distribution:

$$\tau(\lambda) = \frac{3 C \ell}{2\rho \bar{D}_3} [ \Gamma_1 \bar{D}_3 + \Gamma_3 \bar{D}_5 + \Gamma_4 \bar{D}_6 + \Gamma_5 \bar{D}_7 + \dots ] \quad (15)$$

Where  $\bar{D}_n$  represents the nth moment of the particle diameter.

For monodisperse systems in the large particle size regime, where the extinction efficiency can be assumed constant and approximately equal to 2, equation 2 becomes

$$\tau(\lambda) = 3 C \ell / (\rho D) \quad (16)$$

For polydisperse systems in the large particle size regime equation 2 becomes

$$\tau(\lambda) = 3 C \ell / (\rho D_{3,2}) \quad (17)$$

Where  $D_{3,2}$  is the volume to surface average particle diameter.

Equations 15 and 17 point to some of the difficulties in the interpretation of the turbidity data in terms of averages or moments of the particle size distribution. From equation 15 it is clear that the interpretation of the diameter depends on the level of approximation used to evaluate the extinction efficiency. Furthermore, it suggests that, in principle, a significant number of moments and therefore the shape of the particle size distribution can be evaluated directly from turbidity experiments. The only limitation being the signal to noise ratio of the measurements. On the other hand, in the large particle size regime (equation 17), only one average, the volume to surface average is available. If the particle size distribution is known, only two moments (the second and the third) can be obtained directly from turbidity experiments.

The problem of deciding on a particular average diameter (or diameters) to be used in the calculation of the extinction efficiency can be formulated as finding average particle diameters,  $D_{av}$ , such that

$$Q(\alpha_{av}, m) \int_0^{\infty} D^2 f(D) dD = \int_0^{\infty} D^2 Q(\alpha, m) f(D) dD \quad (18)$$

where  $\alpha_{av} = \pi D_{av} / \lambda$

subject to the following constraints:

1. The average diameter(s), as representative of the population behavior, should satisfy the analytic behavior of the scattering equations (ie: the resulting equations should have the same functional form as equations 14 and 16).
2. The equations obtained for the average particle diameter(s) should reduce to the equations developed for monodisperse systems (ie: the resulting equations should reduce to equations 14 and 16 for monodisperse systems).

Note that the formulation stated by equation 18 is different from that of Dobbins et al (Equation 11) in that we are seeking a solution to the integral equation 18 in terms of one or several of the moments of the particle size distribution and in that, simultaneously, we are inquiring as to the information content of the scattering function with regards to the particle size distribution.

There are two regions in the diameter space where the behavior of the average diameter(s) can easily be investigated: the region where the diameter is small compared to the wavelength of the incident radiation (ie: the Rayleigh regime) and the region where the diameter is much larger than the wavelength (ie: the large particle size regime). In the large particle size regime, it is clear from equation 17 that the only average obtained from turbidity measurements is the volume to surface average diameter. It is also evident that equation 17 has the same functional form as equation 16 and that in fact reduces to equation 16 for monodisperse systems. Thus satisfying the constraints imposed for the selection of the average diameters. Note that although ratios of successive moments will satisfy the constraints imposed, only  $D_{3,2}$  results directly from equation 2.

For the analysis in the small particle size regime, rather than approximating the scattering efficiency with a power series as it was done to obtain equation 15, equation 18 will be replaced first into equation 2 to obtain

$$\tau(\lambda) = \frac{3 C \ell}{2 \rho} \frac{Q(\alpha_{av,m})}{D_{3,2}} \quad (19)$$

Then on the basis of the first constraint, the extinction efficiency is expanded in power series of  $\alpha_{av}$  to yield

$$\tau(\lambda) = \frac{3 C \ell}{2 \rho D_{3,2}} [\Gamma_1 Dav + \Gamma_3 Dav^3 + \Gamma_4 Dav^4 + \Gamma_5 Dav^5 + \dots] \quad (20)$$

note that by following this approach the errors in the approximation of  $Q(\alpha,m)$  are not integrated.

There are many averages that when substituted into equation 20 will reduce it to equation 14 for monodisperse distributions. However, only the  $D_{3,2}$  average yields the same functional form as equation 14 for polydisperse and monodisperse particle size distributions. Therefore, it follows that the volume to surface average diameter satisfies the constraints imposed at both, the small and the large particle size regimes. Equations 15 and 20 provide two equivalent interpretations for the turbidity data in the small particle size regime. Equation 20 is particularly attractive because a single average could be used for the interpretation of turbidity data in both the small and large particle size regimes. However, it remains to demonstrate if this is also true for the intermediate size regime (ie:  $D \sim \lambda$ ).

To search for the average diameter(s) that would satisfy equation 18 in the intermediate particle size regime, a numerical approach was taken. The obvious approach is to calculate the right hand side of equation 18 for a variety of distributions and a

sufficiently broad range of their parameter values and then, search for a diameter that when substituted into the expression for the extinction efficiency (ie: equation 3), satisfies equation 18. A comparison between  $D_{av}$  and the moments or ratios of moments of the distribution in question will indicate which average diameter satisfies equation 18. A major difficulty with the above approach stems from the diameter being a multivalued function of the extinction efficiency (1-3). In other words, there is not a unique value for the diameter as a function of the extinction efficiency. An alternative approach that circumvents the uniqueness problem is to substitute the moments and the ratios of moments of the distribution into the extinction efficiency and then select those that best approximate the condition stated by equation 18.

The effect of the shape of the distribution can be taken into consideration, without loss of generality, if it is assumed that the shape of the distribution in question can be approximated with a weighted sum of gaussian density functions (16)

$$f(D) = \sum_{j=1}^J v(j) N(D, \mu(j), \sigma(j)) \quad (21)$$

$$\text{subject to } \sum_{j=1}^J v(j) = 1$$

and where  $\mu(j)$  and  $\sigma(j)$  are the parameters for the  $j$ th approximation function.

Replacement of equation 21 into 18 yields

$$Q(\alpha_{av}, m) = \sum_{j=1}^J v(j) Q(\alpha_{av}(j), m) / \sum_{j=1}^J v(j) \bar{D}_2(j) \quad (22)$$

Equation 22 indicates that the surface average scattering efficiency can be expressed as a linear combination of the average efficiency for each of the approximation functions. Therefore, it is only necessary to find which averages satisfy equation 8 for a gaussian distribution. Extensive computations with a variety of parameter values indicates that  $D_{av}$  does not correspond to any particular average or ratio of moments of the particle size distribution. This can be seen in figures 1-4. Where the fractional errors, between the surface average extinction efficiency and the extinction calculated with trial averages of the particle size distribution ( $\epsilon = 1 - Q(\alpha_{av}, m)/Q(\alpha, m)$ ), are shown as function of the size parameter  $\alpha$ . Clearly, it appears that different particle averages will be more effective at different size parameter values. In general, averages including higher moments appear to perform better overall. The reason for the observed performance can be better understood with

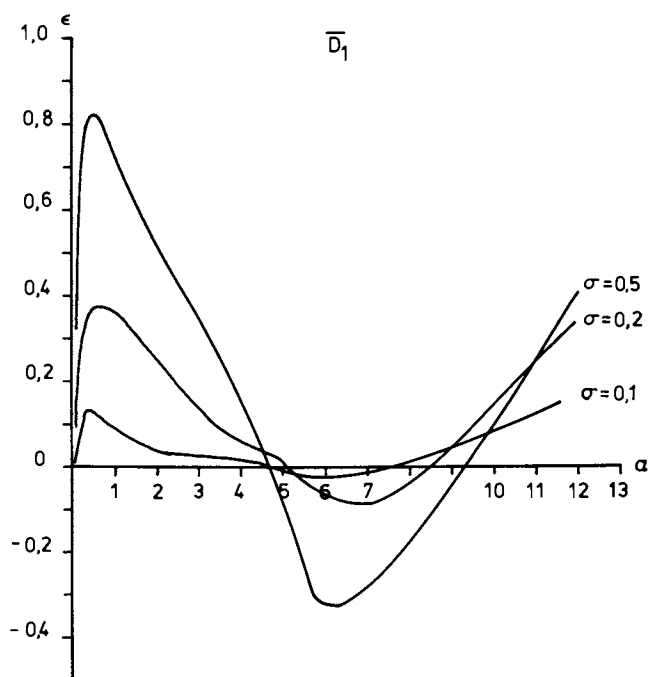


Fig. 1. Approximate behavior of the fractional error as a function of the mean size parameter  $\alpha_1 = \pi D_1/\lambda$  and the fractional standard deviation  $\sigma$ . Where  $D_1$  is the mean particle diameter.

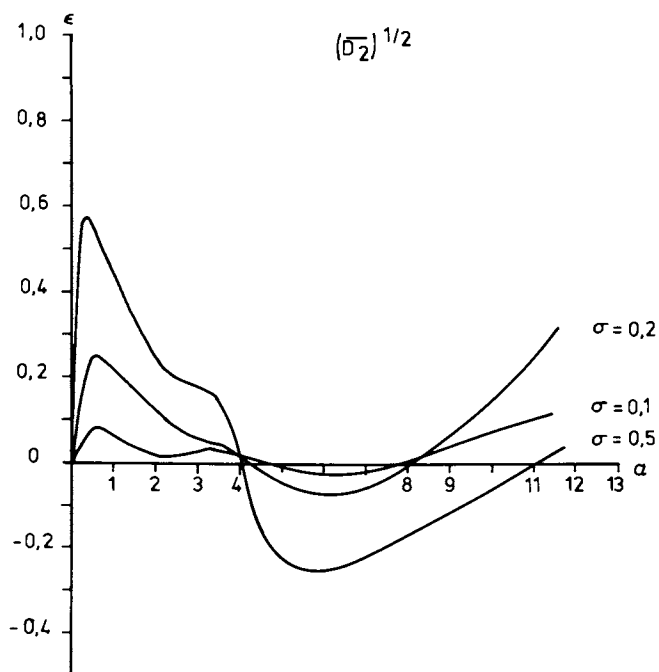


Fig. 2. Approximate behavior of the fractional error as a function of the mean size parameter  $\alpha_2 = \pi D_2/\lambda$  and the fractional standard deviation  $\sigma$ . Where  $D_2$  is the surface average particle diameter.

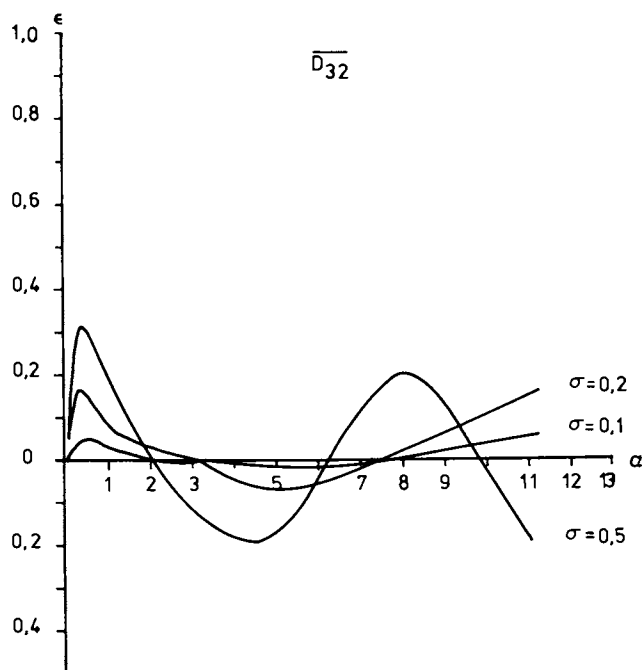


Fig. 3. Approximate behavior of the fractional error as a function of the mean size parameter  $\alpha_{32} = \pi D_{32}/\lambda$  and the fractional standard deviation  $\sigma$ . Where  $D_{32}$  is the mean volume to surface average particle diameter.



reference to figure 5. Assume that for a material having a gaussian particle size distribution and the extinction properties represented in the figure, measurements are to be taken at a wavelength  $\lambda'$  corresponding to a size parameter  $\alpha = 4$ . Note that, initially, most of the particle size distribution lies before the first extinction maximum. This implies that the weighting on  $D^2$  in equation 18 will increase together with the diameter squared. Therefore, the average diameter that satisfies equation 18 will correlate better with averages containing higher moments of the particle size distribution (ie: the turbidity average  $D_T$ ). Now assume that two more measurements are to be taken at wavelengths  $\lambda'/2$  and  $\lambda'/4$ . For this purpose the particle size distribution is mapped again on to the  $\alpha$  domain. Note that the particle size distribution has changed relative to the first measurement, the particle size distribution appears to have been shifted and broadened as the wavelength was reduced. Clearly, the result from changing the wavelength is a change in the range of values of  $Q(\alpha, m)$  weighting the  $D^2$  in equation 18 thus resulting not only in different values of the surface average extinction efficiency but also, in different values of the average diameter that will satisfy equation 18. As the wavelength is reduced, the distribution continues to shift until the large particle size regime is reached and the value of  $Q(\alpha, m)$  becomes independent of the shape of the particle size distribution. Increasing the variance of the particle size distribution will have a similar effect on the averages satisfying equation 18 since the inclusion of larger and smaller sizes will asymmetrically affect the weighting on  $D^2$ . An indication as to how different moments of the particle size distribution affect the calculation of the extinction efficiency can be obtained directly from the interpretation of  $Q(\alpha, m)$  for anomalous diffraction (ie:  $[m - 1] \ll 1$  and  $\alpha \gg 1$ ). The extinction efficiency for the anomalous diffraction case is given by<sup>1, 2</sup>

$$Q(\alpha, m) = 2 - 4 \left[ (\exp(-\rho \tan \beta) \cos \beta / \rho) (\sin(\rho - \beta) + (\cos \beta \cos(\rho - 2\beta) / \rho) + 4 (\cos^2 \beta / \rho^2) \cos(2\beta) \right] \quad (23)$$

where  $\tan \beta = k / (n - n_0)$  and  $\rho = 2\alpha(n/n_0 - 1)$ .

By first replacing equation 23 into 10, it can be readily shown, that the resulting integral can be expressed as a weighted sum of the moments of the particle size distribution

$$\int_0^{\infty} D^2 Q(\alpha, m) f(D) dD = 2 \left[ D_2 - (1/2) \sum_1^8 Kn(\lambda, m) \bar{D}_n \right] \quad (24)$$

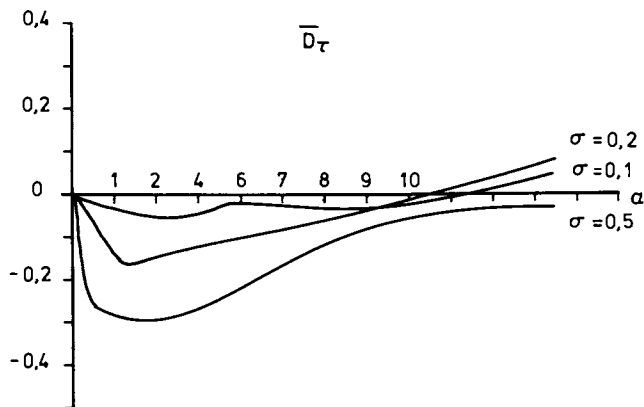


Fig. 4. Approximate behavior of the fractional error as a function of the mean size parameter  $\alpha \tau = \pi D_\tau / \lambda$  and the fractional standard deviation  $\sigma$ . Where  $D_\tau$  is the turbidity average particle diameter.

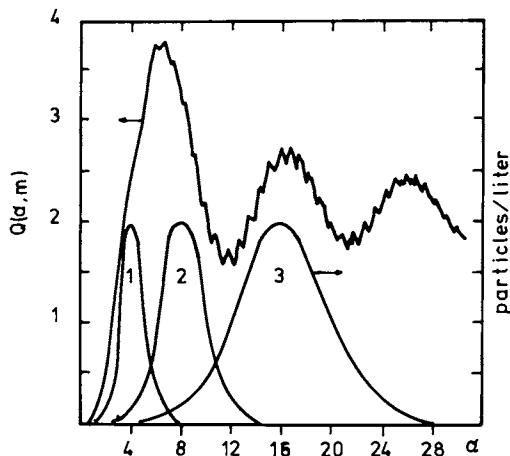


Fig. 5. Behavior of the particle size distribution relative to the extinction as function of the size parameter  $\alpha$ . 1) particle size distribution as seen at  $\lambda = \lambda'$ ; 2) particle size distribution at  $\lambda = \lambda'/2$ ; 3) particle size distribution at  $\lambda = \lambda'/4$ .

In this case, an eighth order approximation was used in order to include some of the higher moments of the distribution.  $Kn(\lambda, m)$  represents the weight for the  $m$ th moment of the size distribution. The values for  $Kn$  are given in Appendix II. A similar expression can be obtained in terms of the  $D_{3,2}$  average if Equation 24 is applied to  $Q(\alpha_{av}, m)$  in equation 19.

Note that the relative importance of the moments of the particle size distribution or the powers of  $D_{3,2}$ , as reflected by  $Kn(\lambda, m)$ , will vary as function of the optical constants and of the wavelength. Therefore, it is clear that, in the intermediate particle size regime, the measured extinction efficiency cannot be readily interpreted in terms of single combinations of moments of the particle size distribution. Furthermore, it is evident that the effective average particle diameter routinely determined from turbidity measurements will appear to be a function of the wavelength used in the experiments, as it can be observed in reported literature data<sup>3</sup>. The behavior of the error shown in figures 1-4 explains why there has been, in general, good correlation with the turbidity average particle diameter whenever the scattering equations have been applied to polydispersed systems.

### Discussion

The overall conclusion from the analysis of equation 18 over the complete domain of  $\alpha$  is that, in principle, information about the shape of the particle size distribution can be obtained directly from turbidity, or in general, from scattering measurements. However, the discriminating power of the measurements in terms of the particle size distribution depends upon the wavelength range selected for the analysis. The major difficulty in the interpretation of the data arises from the behavior of the extinction itself as function of the size parameter which causes the measurements "see" a different average at every wavelength.

In the large particle size regime, the interpretation of the average particle diameter as  $D_{3,2}$  is unambiguous. In the intermediate particle size regime, the effective average diameter  $D_{av}$  will vary as function of the wavelength. Measurements over a range of wavelengths will yield averages that are weighted according to the behavior of the scattering function over the corresponding size parameter range. However, the general formula given by equation 19 suggests that two parameters  $\alpha_{av}$  and  $D_{3,2}$ , can be used to interpret turbidity data over a wavelength range. The volume surface mean diameter will correspond to the particle size distribution whereas the  $\alpha_{av}$  will correspond to the average diameter "seen" by the measurements averaged over the wavelength range. This approach simplifies the analysis and interpretation of the scattering data for polydispersed systems considerably. For example, it is not necessary to calculate the mean surface scattering efficiency in the form suggested by Dobbins and Jizmagian. A single evaluation using  $\alpha_{av}$  and  $D_{3,2}$  yields the desired average efficiency. When optical constants are estimated from scattering data, the minimization problem is reduced to the estimation of: the optical constants  $\alpha_{av}$

and, one average particle diameter (ie:  $D_{3,2}$ ). Two moments of the particle size distribution, the second and the third can be obtained if the form of the particle size distribution is known. This is particularly important for the estimation of optical constants as functions of the wavelength, since only one evaluation of the extinction efficiency per parameter per iteration will be required and no prior knowledge of the shape of the particle size distribution is necessary.

In the small particle size regime, two equivalent formulations lead to the interpretation of the data in terms of ratios of moments of the particle size distribution or in terms of powers of the  $D_{3,2}$  average (equations 15 and 20). It is clear that in either case a sufficient number of terms in the series has to be included in order to account for the behavior of the extinction as function of  $\alpha$ . The number of terms required cannot be decided a priori, rather the data itself has to dictate how many terms in the power series approximation the measurements can detect.

The variation of the effective average diameter as function of the wavelength or as function of the variance of the particle size distribution is of great importance in the application of scattering measurements to the determination of molecular weights because typical molecular weight distributions are rather broad. For example, a polymer with a ratio  $M_w/M_n = 1.5$  has a fractional standard deviation equal to 0.71. For a 60 Å mean particle diameter and a gamma distribution,  $D_\tau = 210$  Å. The difference between  $\bar{D}_1$  and  $D_\tau$  indicates at least a three fold change in the magnitude of the size parameter thus requiring that high order terms be included in the measurement equation (ie: equations 15 or 20). Measurements at other wavelengths will clearly result in  $M_w$  appearing as a function of the wavelength if only the leading term is used. Finally, it should be noticed that if the  $D_{3,2}$  average is used for the interpretation of turbidity data, the resulting molecular weight average is the ratio  $\bar{M}_n/\bar{M}_{3,2}$  which is related to the molar surface area. The implications of this interpretation are currently being explored and they will be reported separately.

#### Acknowledgments

This research was supported by the NSF Initiation Grant RII-8507956. The author is indebted to Dr. J. Harwood from the University of Akron for his continuous encouragement and support.

#### REFERENCES

1. van de Hulst, H. C., "Light Scattering by Small Particles", 1957, Wiley, New York.
2. Kerker, M., editor., "Electromagnetic Waves", 1962, Pergamon Press, New York.
3. Kerker, M., "The Scattering of Light and Other Electromagnetic Radiation", 1969, Academic Press, New York.

4. Bohren, C. F.; Huffman, D. R., "Absorption and Scattering of Light by Small Particles", 1983, Wiley, New York.
5. Huglin, M. B., "Light Scattering from Polymer Solutions", 1972, Academic Press Inc. (London) LTD.
6. Deirmendjian, D., "Electromagnetic Scattering on Spherical Polydispersions", 1969, American Elsevier, New York.
7. Baltes, H. P., (Editor)., "Inverse Scattering Problems in Optics", 1980, Springer-Verlag, Berlin.
8. Gledhill, R. L., J. Phys. Chem., 1961, 66, 458.
9. Wallach, M. L.; Heller, W.; Stevenson, A. F., J. Chem. Phys. 1961, 32(2), 1796.
10. Maxim, D. L.; Klein, A.; Meyer, M. E.; Kuist, C. H.; J. Polym. Sci. Part C, 1969, 27, 195.
11. Husain, A.; Vlachopoulos, J.; Hamielec, A. E.; J. Liq. Chrom. 1979, 2(4), 517.
12. Zollars, R. L., J. Coll. Int. Sci., 1980, 74, 163.
13. Maron, S. H.; Pierce, P. E.; Ulevitch, I. N., J. Colloid Sci., 1963, 18, 470.
14. Dobbins, R. A.; Jizmagian, G. S., Opt. Soc. Amer., 1966, 56, 1345, 1351.
15. Bagchi, P.; Vold, R. D., J. Coll. Int. Sci., 1975, 53(2), 194.
16. Sorenson, H. W.; Alspach, D. L., Automatica., 1971, 7, 465.
17. Penndorf, R. B., J. Opt. Soc. Amer., 1962, 52, 896.
18. MAC'S Symbolic Manipulation System (Macysma), 1985, Symbolics Inc., Cambridge Massachusetts.

#### APPENDIX I

The coefficients of the power series expansion of the extinction efficiency, to a 5th order approximation, were derived by Penndorf (17) and independently at our laboratories using Macysma (18). The coefficients of the series are:

$$\Gamma_1' = \frac{24 nk}{(n^2 + k^2)^2 + 4(n^2 - k^2) + 4}$$

$$\Gamma_3' = \frac{4 nk}{15} + \frac{20 nk}{3 [ 4 (n^2 + k^2)^2 + 12 (n^2 - k^2) + 9]}$$

$$+ \frac{4.8 nk [ 7 (n^2 + k^2)^2 + 4 (n^2 - k^2 - 5) ]^2}{[(n^2 + k^2)^2 + 4(n^2 - k^2) + 4]^2}$$

$$\Gamma_4' = \frac{-192 n^2 k^2}{[(n^2 + k^2)^2 + 4(n^2 - k^2) + 4]^2}$$

$$\begin{aligned} \Gamma_s' &= \frac{6}{175} (P_1 R_2 + P_2 R_1) \\ &\quad - \frac{20nk [4(n^2 + k^2)^2 + 8(n^2 - k^2) + 21]}{21 [4(n^2 + k^2)^2 + 12(n^2 - k^2) + 9]^2} \\ &\quad + \frac{2}{225} \left( \frac{14nk}{9(n^2 + k^2)^2 + 24(n^2 - k^2) + 16} \right) \\ &\quad + \frac{3}{315} (2nk + 4nk(n^2 - k^2 - 3)) \end{aligned}$$

Where:

$$P_1 = \frac{(n^2 + k^2)^2 + n^2 - k^2 - 2}{Z}$$

$$P_2 = \frac{6nk}{Z}$$

$$\begin{aligned} R_1 &= \frac{(n^2 - k^2)^4 + 22(n^2 - k^2)^3 - 160(n^2 - k^2)^2 - 200(n^2 - k^2)}{Z} \\ &\quad + \frac{400 - 4n^2k^2 [24(n^2 - k^2) + 4n^2k^2 + 39]}{Z} \end{aligned}$$

$$\begin{aligned} R_2 &= \frac{2nk[2(n^2 - k^2)^3 - 12(n^2 - k^2)^2 + 205(n^2 - k^2)]}{Z} \\ &\quad + \frac{8n^2k^2(n^2 - k^2 + 9) - 198}{Z} \end{aligned}$$

$$Z = (n^2 + k^2)^2 + 4(n^2 - k^2) + 4$$

Replacement of the value  $\alpha = \pi D/\lambda$  into equation 17, yields equation 17a. Where the  $i$ th coefficient is now given by

$$\Gamma_i = \Gamma_i' (\pi/\lambda)^i$$

## APPENDIX II

This appendix reports the weights for the moments of the particle size distribution obtained from an eight order Taylor Series approximation to the scattering efficiency for the anomalous diffraction case

$$K_1 = -B (A_0 t - A_1)$$

$$K_2 = (B/2!)(A_0 t^2 - 2A_1 t - A_2)$$

$$K_3 = (-B/3!)(A_0 t^3 - 3A_1 t^2 - 3A_2 t + A_3)$$

$$K_4 = (B/4!)(A_0 t^4 - 4A_1 t^3 - 6A_2 t^2 + 4A_3 t + A_4)$$

$$K_5 = (-B/5!)(A_0 t^5 - 5A_1 t^4 - 10A_2 t^3 + 10A_3 t^2 + 5A_4 t - A_5)$$

$$K_6 = (B/6!)(A_0 t^6 - 6A_1 t^5 - 15A_2 t^4 + 20A_3 t^3 + 15A_4 t^2 - 6A_5 t - A_6)$$

$$K_7 = (-B/7!)(A_0 t^7 - 7A_1 t^6 - 21A_2 t^5 + 35A_3 t^4 + 35A_4 t^3 - 21A_5 t^2 - A_6 t + A_7)$$

$$K_8 = (-B/8!)(A_0 t^8 - 8A_1 t^7 - 28A_2 t^6 + 56A_3 t^5 + 70A_4 t^4 - 56A_5 t^3 - 28A_6 t^2 + 8A_7 t - A_8)$$

where  $t = 2\pi k/\lambda_0$

$$B = 4\cos(\beta)/\gamma^2$$

$$\gamma = 2\pi(n - n_0)/\lambda_0$$

The A coefficients can be generalized for even and odd indices

for n even  $A_n = (\cos(2\beta) - n)(\cos\beta)\gamma^n$

for n odd  $A_n = (\cos\beta \sin(2\beta) - n \sin\beta) \gamma^n$

RECEIVED November 12, 1986

## Chapter 12

# An Improved Disc Centrifuge Photosedimentometer and Data System for Particle Size Distribution Analysis

M. E. Koehler, R. A. Zander, T. Gill, Theodore Provder, and T. F. Niemann  
The Glidden Company, Dwight P. Joyce Research Center, Strongsville, OH 44136

An improved disc centrifuge photosedimentometer (DCP) was developed for use in the determination of the particle size and size distribution of latices, pigments and other particulates. Separation is based on Stokes Law for the sedimentation of particles in a centrifugal force field and does not rely on the use of particle size calibrants or standards. The DCP instrument provides accurate stable particle size analyses over a wide range of conditions while at the same time is rugged enough for heavy use in both a research and quality control environment. A stand-alone data collection, analysis and management system was developed both for routine quality control operation and for research use of the instrument.

The disc centrifuge photosedimentometer (DCP) is an instrument used to determine the particle size and size distribution of latices, pigments and other particulates. Separation is based on Stokes Law for the sedimentation of particles in a centrifugal force field. Particles are assumed to be spherical. In the most common mode of operation the separation takes place in a cylindrical cavity of known dimensions and containing a known volume of fluid. A dilute suspension of the particles of interest is injected onto the surface of the fluid while the disc is spinning and the particles sediment in the centrifugal force field radially outward past a detector system. The appearance time of the particle at the detector,  $t$ , in minutes is given by

$$t = \frac{k \eta \log_{10}(R_2/R_1)}{\Omega^2 \Delta \rho d^2} \quad (1)$$

0097-6156/87/0332-0180\$06.00/0  
© 1987 American Chemical Society



where  $D$  is the diameter of the particle in micrometers,  $R_1$  is the radius at the surface of the fluid in centimeters,  $R_2$  is the radius at the detector in centimeters,  $\Omega$  is the rotational speed of the disc in revolutions per minute,  $\eta$  is the viscosity of the fluid in poise,  $\Delta\rho$  is the density difference between the particles and the fluid in  $\text{gm/cm}^3$  and  $k$ , a collection of constant terms, is equal to  $6.299 \times 10^3$ . It can be seen then that the method relies only on measureable physical parameters and the use of particle size calibrants or standards is not required.

The goal of this work was to develop a DCP instrument which would provide accurate stable particle size analyses over a wide range of conditions while at the same time being rugged enough for heavy use in both a research and quality control environment. In addition a relatively inexpensive stand-alone system for data collection, analysis and management was needed for both routine quality control operation and for research use of the instrument.

This paper discusses the technical details of the instrument and data system. Instrument performance, methodology and comparative particle size analyses are discussed elsewhere in this volume (1,2).

### Experimental

Instrument. The instrument (3) is shown schematically in Figure 1. (A commercial version of the instrument described in this paper is now available from Brookhaven Instruments Corporation, Ronkonkoma, New York as the Brookhaven DCP-1000 Particle Size Analyzer.) It is based on the use of a variable ratio traction drive transmission (Kopp Model R1.0HS, Andantex USA Inc., 1800-T Brielle Ave., Wanamassa, Ocean Township, NJ 07712) coupled with a one-half-horsepower ac-motor operating at essentially constant speed. The rotational speed of the disc is selected manually by means of a dial and is continuously variable over a range from approximately 1,200 to 12,000 rpm. The rotational speed is continuously monitored by means of a digital tachometer located on the control module. The disc cavity is machined from a suitable plastic material, typically polymethylmethacrylate, and is mounted on a metal hub. The disc cavity is dynamically balanced over the operating speed range to insure vibration free operation. A Vortec cooler (Vortec Corporation, 10125 Carver Rd., Cincinnati, OH 45242) provides chilled air which cools the transmission as it passes through a heat exchanger in the transmission fluid and is then blown into the detector block assembly. This cooling prevents heat generated in the transmission and by the spinning disc cavity from warming the spin fluid during the course of a long analysis run.

Detection of the particles is accomplished by means of their attenuation of a light beam provided by a halogen lamp and collimated by two slit assemblies. A silicon photodiode and an operational amplifier circuit are used to monitor the light intensity. Adjustable gain and offset potentiometers are located on the control module. The signal can be displayed on a stripchart recorder and is monitored by means of a digital panel meter.

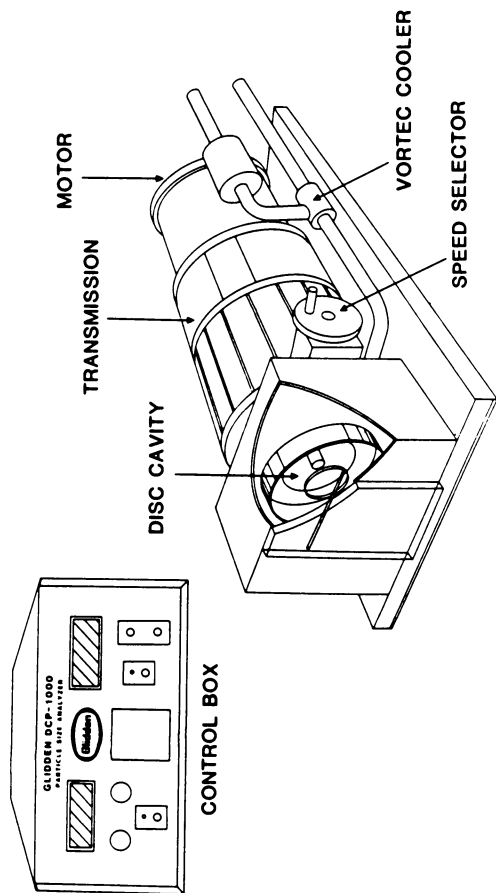


Figure 1. Schematic Drawing of DCP-1000 Particle Size Analyzer.

The analysis method employed is the patented external gradient method described in detail elsewhere (1,4). The overall instrument performance was evaluated using monodisperse polystyrene latex standards, covering a range from 0.176  $\mu\text{m}$  to 1.09  $\mu\text{m}$ , obtained from Dow Diagnostics, Indianapolis, Indiana.

**Calibration.** The instrument is calibrated by using a cathetometer to measure the diameter of the fluid surface with 5 ml and with 15 ml of water in the spinning disc cavity. Calibration was done with the disc cavity rotating at 5000 rpm. Variations in the diameter of the fluid surface as a function of rotational speed were found to be negligible. The detector block was aligned to the 5 ml-position of the disc cavity by placing 5 ml of water in the cavity, and adjusting the detector block position until a maximum attenuation of the light beam was observed indicating scattering by the meniscus. For a spin fluid volume of 15 ml with the detector at the 5 ml-position, the measured diameters at 5 ml and 15 ml yield  $R_1$  and  $R_2$  of equation (1) directly. At another spin fluid volume,  $V$ , these measured radii, at 5 and 15 ml,  $R_{5\text{ml}}$  and  $R_{15\text{ml}}$  are used to geometrically calculate the radius,  $R_1$ , of the fluid surface using equation (2).

$$R_1 = \left[ R_{5\text{ml}}^2 - \left( \frac{V - 5\text{ml}}{10\text{ml}} \right) (R_{5\text{ml}}^2 - R_{15\text{ml}}^2) \right]^{1/2} \quad (2)$$

A derivation of equation (2) is shown in the Appendix.

**Data System.** An IBM-PC desktop computer is interfaced to the instrument control module to provide automated data collection and analysis. The data collection and analysis programs are menu driven. A data management facility is an integral part of the data system. A modeling utility is provided to aid the operator in choosing the operating conditions (rotational speed, spin fluid volume, fluid density, etc.) for a sample. Programming is done in compiled BASIC and the 8087 math coprocessor is used to improve computational speed.

To initiate an analysis run, the operator interactively enters the experimental parameters and sample identification through the computer keyboard. When the sample injection is made the operator signals the computer to begin data collection by pushing a button located on the detector block. The raw data are plotted on the computer screen in real time during data collection. The operator ends data collection by use of a function key on the computer keyboard. Optionally, the computer can be set to stop data collection at a predetermined time.

Data analysis is interactive. The operator can control the slope sensitivity of a computer selected baseline, or can manually choose a baseline by means of a crosshair cursor on the raw data display. When the calculation is completed, the results are displayed on the screen. Plots of the raw data, and of the number, weight and surface differential and cumulative distribution can be displayed on the screen and printed at the operators option.

A data management system is an integral part of the program. This allows the operator to store experimental data on the computer's disks and to reanalyze stored data, or to simply review results without reanalysis. Using the cursor controls, the operator can select stored runs from the menu and print the results for those runs in tabular form. Selected runs can be deleted in a similar fashion.

### Results

The raw data trace for a mixture of 6 standard polystyrene latex microspheres is shown in Figure 2. This separation was done in 20 minutes at 10,450 rpm. While particle size data in the first few minutes is difficult to quantitate accurately with the DCP, this separation demonstrates the resolution capability of the instrument. Figures 3-7 show typical raw data, and number, surface and weight differential and cumulative distribution plots produced by the data system along with the corresponding report.

Data from a number of different particle size analysis instrumental methods including light scattering, field flow fractionation, hydrodynamic chromatography and microscopy were obtained for a series of polymethylmethacrylate latexes and were compared to DCP results (2). These and other comparative results have demonstrated the accuracy of the instrument and method. The reproducibility and precision of the instrument also were studied and are reported elsewhere (1).

The instrument has proven to be extremely reliable through many instrument-years of service in our laboratories. Routine maintenance consists only of an annual oil change for the traction drive.

### Conclusions

This improved instrument and the data system provide an accurate reliable means of particle size analysis of latex materials over a wide range of sample types and sizes.

### Appendix

The fluid volume is the difference between the volumes of the two cylinders of the same height having the radii of the outer and inner surfaces of the fluid and is given by

$$V_{\text{fluid}} = \pi h (R_B^2 - R_A^2) \quad (\text{A-1})$$

where  $R_B$  is the outer radius,  $R_A$  is the inner radius, and  $h$  is the height of the cylindrical section. Substituting for the case of the two measured radii at fluid volumes of 5ml and 15ml yields

$$V_{\text{fluid}} = 15\text{ml} - 5\text{ml} = \pi h (R_{5\text{ml}}^2 - R_{15\text{ml}}^2) \quad (\text{A-2})$$

which can be solved for  $h$  as

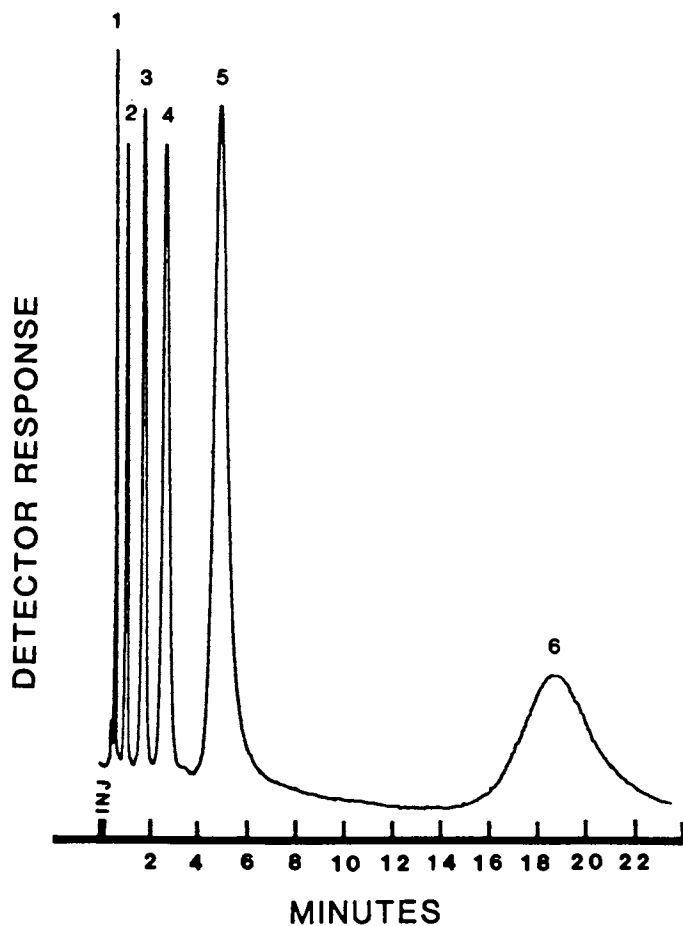


Figure 2. Raw Data Trace for a Mixture of Six Polystyrene Latexes 1 - 1.091  $\mu\text{m}$ , 2 - 0.822  $\mu\text{m}$ , 3 - 0.600  $\mu\text{m}$ , 4 - 0.497  $\mu\text{m}$ , 5 - 0.357  $\mu\text{m}$ , 6 - 0.176  $\mu\text{m}$ , Spin Fluid Volume 15 ml, Disc Speed 10,450 rpm.

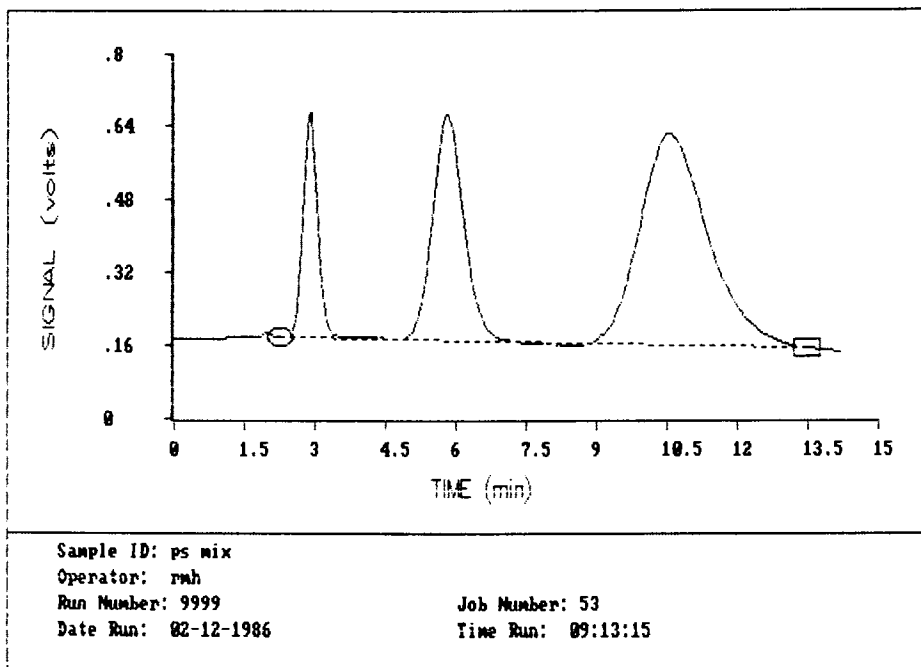


Figure 3. Plot from DCP-1000 Data System - Raw Data with Baseline.

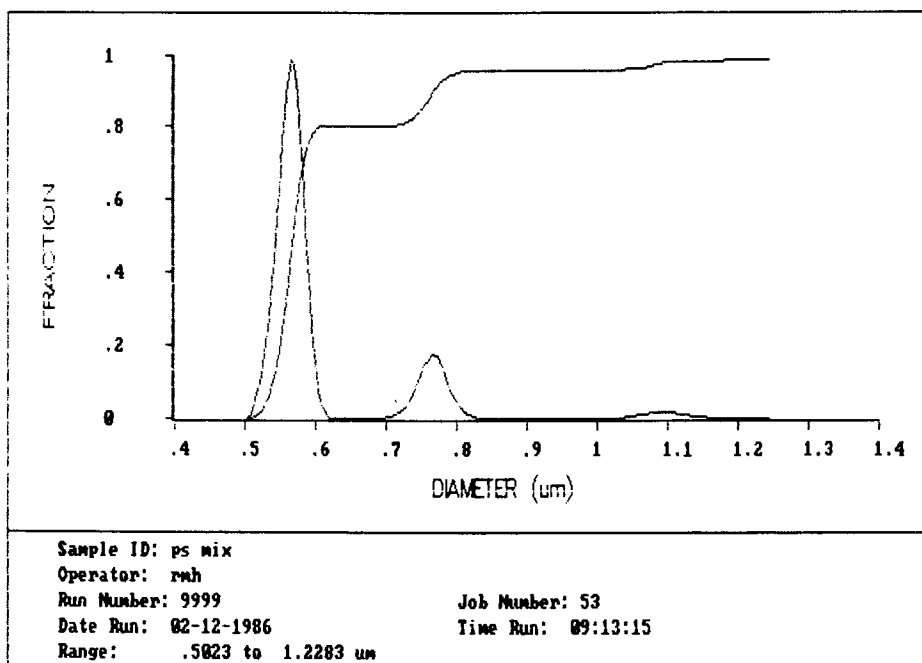


Figure 4. Plot from DCP-1000 Data System - Number Distribution.

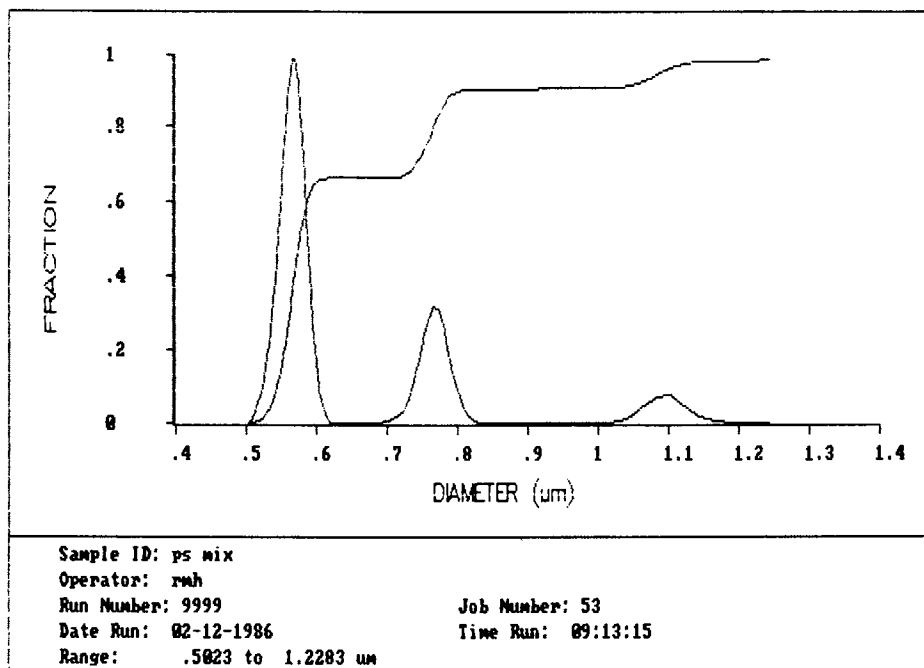


Figure 5. Plot from DCP-1000 Data System - Surface Distribution.

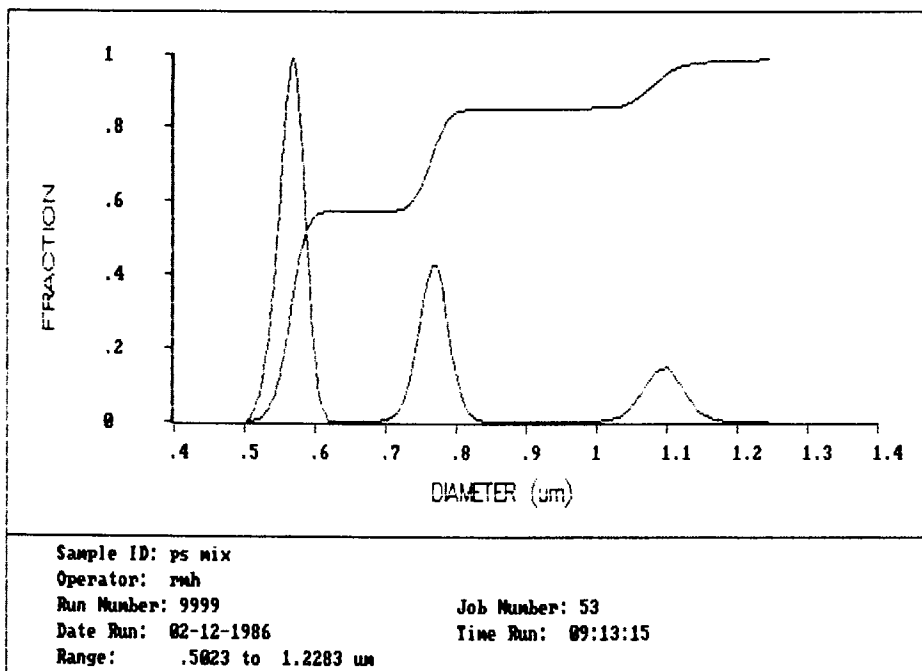


Figure 6. Plot from DCP-1000 Data System - Weight Distribution.



SAMPLE ID: ps mix

OPERATOR: rmh

RUN 9999

JOB 53

DATE RUN: 02-12-1986

TIME RUN: 09:13:15

ANALYSIS RESULTS

|                           |                          | STD DEV   |
|---------------------------|--------------------------|-----------|
| NUMBER AVERAGE (Dn)       | 0.6081 um                | 0.1089 um |
| SURFACE AREA AVERAGE (Ds) | 0.6545 um                | 0.1539 um |
| WEIGHT AVERAGE (Dw)       | 0.6907 um                | 0.1786 um |
| TURBIDITY AVERAGE (Dt)    | 0.7387 um                |           |
| PCS AVERAGE (Dp)          | 0.7912 um                |           |
| POLYDISPERSITY (Dw/Dn)    | 1.1358                   |           |
| SPECIFIC SURFACE          | 87307 cm <sup>2</sup> /g |           |

RUN PARAMETERS

|                  |                         |             |          |
|------------------|-------------------------|-------------|----------|
| DISC SPEED       | 4033 RPM                | TEMPERATURE | 20 C     |
| PARTICLE DENSITY | 1.05 g/cm <sup>3</sup>  | SPIN FL VOL | 15 ml    |
| SPIN FLUID       | WATER                   | SPIN FL VIS | 1.002 cp |
| SPIN FL DENSITY  | .9982 g/cm <sup>3</sup> |             |          |

BASELINE PARAMETERS

|               |              |              |           |
|---------------|--------------|--------------|-----------|
| SLOPE         | -.0021 v/min | INTERCEPT    | .1826 v   |
| STARTING TIME | 2.25 min     | ENDING TIME  | 13.45 min |
| HIGH DIAMETER | 1.2283 um    | LOW DIAMETER | .5023 um  |
| CURVE AREA    | 1.3232 v-min |              |           |

NOTE LINE

after another realignment ala MEK

Figure 7. Report from DCP-1000 Data System.

$$h = \frac{10\text{ml}}{\pi (R_{5\text{ml}}^2 - R_{15\text{ml}}^2)} \quad (\text{A-3})$$

For any other volume,  $V$ , having radius  $R_1$  at the fluid surface, one can then use  $h$  and one of the measured radii,  $R_{5\text{ml}}$ , to solve for  $R_1$  as follows,

$$V - 5\text{ml} = \pi \left( \frac{10\text{ml}}{\pi (R_{5\text{ml}}^2 - R_{15\text{ml}}^2)} \right) (R_{5\text{ml}}^2 - R_1^2) \quad (\text{A-4})$$

$$\left( \frac{V - 5\text{ml}}{10\text{ml}} \right) = \frac{(R_{5\text{ml}}^2 - R_1^2)}{(R_{5\text{ml}}^2 - R_{15\text{ml}}^2)} \quad (\text{A-5})$$

$$R_{5\text{ml}}^2 - R_1^2 = \left( \frac{V - 5\text{ml}}{10\text{ml}} \right) (R_{5\text{ml}}^2 - R_{15\text{ml}}^2) \quad (\text{A-6})$$

$$R_1 = \left[ R_{5\text{ml}}^2 - \left( \frac{V - 5\text{ml}}{10\text{ml}} \right) (R_{5\text{ml}}^2 - R_{15\text{ml}}^2) \right]^{1/2} \quad (\text{A-6})$$

yielding equation 2.

#### Literature Cited

1. Holsworth, R. M.; Provder, T.; Stansbrey, J. J. "A Novel External Gradient Formation Method for Disc Centrifuge Photo-sedimentometry Particle Size Distribution Analysis" This Volume.
2. Koehler, M. E.; Provder, T. "Comparative Particle Size Analysis" This Volume.
3. Koehler, M. E.; Provder, T.; Zander, R. A. U. S. Patent 4 311 039, 1982.
4. Holsworth, R. M.; Provder, T. U. S. Patent 4 478 073, 1985.

RECEIVED October 6, 1986

## Chapter 13

# External-Gradient-Formation Method for Disc Centrifuge Photosedimentometric Particle Size Distribution Analysis

R. M. Holsworth, Theodore Provder, and J. J. Stansbrey

The Glidden Company, Dwight P. Joyce Research Center, Strongsville, OH 44136

A novel and alternative method for making centrifugal disc photosedimentometric analyses has been developed which allows simplification of previous methods including an industry accepted method, the Buffered Line Start. In this new method the spin fluid/density gradient is formed external to the disc cavity and injected into the disc cavity while the disc is spinning at a predetermined speed. The externally formed spin fluid contains at least two miscible or partially miscible liquids of different densities in a substantially incompletely mixed condition. The External Gradient Method is evaluated and statistically compared to the Buffered Line Start method of analysis using a variety of particle sizes and latex types. The results of the statistical analysis are discussed relative to method type, sample type and size range, temperature and other operational variables.

The disc centrifuge photosedimentometer (DCP) has proved to be an excellent instrument for providing particle size and particle size distribution information to pigment and latex manufacturers and coatings formulators. The DCP operates by forcing particles radially outward through a spin fluid under high centrifugal force. As they move outwardly the particles are separated by size and/or density. At a specific radial distance the moving particles interrupt and attenuate a light beam, the intensity of which is measured by a photodetector. The particle size is related to the appearance time at the photodetector by means of Stokes' Law for centrifugation. The concentration of particles is obtained from the photodetector response and the application of Mie scattering theory.<sup>(1)</sup> A very important step in this operation is the formation of a density gradient within the spin fluid to allow a hydrodynamically stable separation of the suspended particles. An accepted method for forming this spin fluid density gradient within the disc cavity is the widely used and patented <sup>(2)</sup> Joyce-Loebl Buffered Line Start

0097-6156/87/0332-0191\$06.00/0  
© 1987 American Chemical Society

(BLS). This paper describes a novel and alternative method for performing DCP analyses and in particular a new procedure for the formation of the spin fluid density gradient external to the DCP disc. This new patented method (3), known as the External Gradient Method (EGM), will be compared to the BLS method of analysis. The quantitative precision of the results obtained with EGM and BLS will be compared by statistical analysis. In addition, qualitative advantages of the EGM over the BLS method will be given.

### Materials and Methods

The disc centrifuge used in this study has been described previously (4,5). (A commercial version of the instrument is now available from Brookhaven Instruments Corporation, Ronkonkoma, NY, as the Brookhaven DCP-1000 Particle Size Analyzer.) The latexes used in this study are monodisperse Dow polystyrene latex standards covering a range of sizes and two commercial latexes designated as #2 and #4, both of which had a broader dispersity than the polystyrene latex standards. All of the latex sample preparations analyzed in the statistical study were prepared in a similar manner. All the fluids were held in a thermostatically controlled temperature bath at 25°C. The temperatures at the beginning and end of each run were recorded.

For the EGM a hypodermic syringe with a volume usually greater than that of the total spin fluid, is used to form the density gradient external to the disc cavity. For example, if a total spin fluid of 15 ml is used in the analysis, 15 ml of the more dense fluid is drawn into the syringe followed by 1 ml of the less dense fluid. At this point the syringe contains two incompletely mixed miscible liquids. This density gradient, thus formed, is injected into the cavity of the spinning disc resulting in a spin fluid/density gradient ready for sample injection.

For the BLS, 15 ml of spin fluid (deionized (DI) water) were introduced, partly filling the disc cavity. Then, 1 ml of a 50% methanol-water solution, buffer fluid, was added while the centrifuge was running. The disc was decelerated for 0.40 to 0.60 seconds, depending on the sample, and reaccelerated to form the density gradient within the new spin fluid. The samples were made up in 50% methanol-water solution; 2 drops of latex to 25 ml of solution. The amount of sample injected into the disc cavity varied from 0.20 to 0.40 ml, depending on the sample. For the particle sizes and particle densities involved, the disc speed of 4000 rpm was convenient and used for all runs. For the EGM, the conditions were identical, except that the final spin fluid was created in the syringe, using 15ml of DI water and 1ml of 100% methanol, before being injected into the disc cavity. The samples were prepared and introduced into the disc cavity the same way for both methods.

The data for each run were acquired and stored every 5 seconds by a dedicated microprocessor. At the completion of a run the accumulated data were sent to a Digital PDP-11/44 minicomputer for computation and reporting. The baseline was automatically determined by the analysis software. These results were critically reviewed. The baseline was adjusted by the operator, when necessary, and the revised data calculated. These results were computed on the basis of the initial spin fluid temperature of 25°C.

The analyses of variance and covariance were carried out using BMDP P2V., BMDP Statistical Software, 1964 Westwood Blvd, suite 202 Los Angeles, CA 90025.

### Statistical Design

Preliminary studies indicated that the BLS and EGM gave very similar results. To substantiate these results, an experimental design was set up to compare the performance of the two methods with a rigorous, formalized set of experiments. The factors considered were (1) the two methods (METHOD), BLS and EGM, (2) two operators (OPERATOR), one with experience, the other never having used EGM before, (3) two similar disc centrifuge photosedimentometers (DCP), both at the same location, and (4) three typical latex samples (SAMPLE); #3, 0.497 $\mu$ m polystyrene standard and #2,  $D_w=0.282\mu$ m ( $D_w/D_n=1.03$ ) and #4,  $D_w=0.386\mu$ m ( $D_w/D_n=1.05$ ), both commercial latexes.

The experimental design was a 2x2x3 factorial with 4 Replicates plus two extra replicates per sample. Except for the four replicates, run in adjacent pairs, the order of all the runs was randomized. This resulted in 51 total runs for analysis in the statistical design.

It was not practical to include time explicitly as a fourth factor in the experimental design. However, some information could be obtained on this by comparing replicates run at random over the total time of the experiments with those run in pairs, one after the other. The total time span for running these experiments was a little more than a week. Four of the replicates for each sample were run in random order over this period, then a second replicate was paired with it and run immediately following the first. Finally, the last replicate for each sample was added at random. There were, then, nine replicates spread at random throughout the period, using the first of each of the paired replicates. There were, also, eight paired replicates run one after the other. The variances of these two sets of replicates for all the samples were then compared. The results indicate that absolutely no effect was discernable between the replicates that were run at random times and those that were run in pairs.

These results were analyzed using both Analysis of Variance and analysis of covariance with the change in temperature during the run, used as the covariate. Statistically, this is a fixed-effect model except for the covariate which is random. Analyses were also carried out on the individual samples, but the conclusions and residual mean squares were essentially the same as for the samples combined.

### Results and Discussion

The simplicity of operation of the EGM and its accuracy are best seen by comparing particle size distribution curves by the EGM and the BLS method and comparing data obtained from both methods. Figure 1 shows the separation of three latex standards by the BLS method. Twenty ml of water was used as spin fluid and 1 ml of 50% (V/V) methanol as a density buffer. A 0.25 ml sample of dilute latex ( $10^{-5}$

to  $10^{-6}$  g/l) was analyzed at a disc speed of 3586 rpm. It is obvious that the standards are separated with baseline resolution and that the reproducibility is very good. The EGM separation of the same latex sample, shown in Figure 2, also has excellent baseline resolution and reproducibility. The spin fluid consisted of 11 ml of water topped by a density gradient modifier consisting of 9 ml of water and 1 ml of methanol. The sample size was 0.25 ml and the disc speed was 3586 rpm. Particle size distributions shown in Figure 3 reveal that size separation by the two methods is virtually identical.

Figure 4 shows the results obtained on another sample containing four different standard latexes with particle sizes of 1.091, 0.822, 0.600 and 0.497 $\mu$ m, using a spin fluid of 11 ml of water topped with an external gradient of 9 ml of water and 1 ml of methanol and a disc speed of 3586 rpm. Peak appearance times of 3.6 minutes, 7.1 minutes, 12.5 minutes and 19 minutes correspond to calculated particle size values of 1.142, 0.813, 0.613 and 0.497  $\mu$ m respectively, which are in excellent agreement with the nominal values of the standards.

Results obtained on two different samples containing the four latexes mentioned above plus an additional polystyrene latex standard, namely 0.357 $\mu$ m, are shown in Figure 5. Using the same procedure described previously, in four separate experiments and using disc speeds of 4004, 6015, 8057, and 10,160 rpm, a distinct separation of the standards is seen over this wide range of Analyzer disc speeds.

Figure 6 shows the separation of the latex mixture shown in Figure 5 including an additional 0.176 $\mu$ m polystyrene standard. In this case, the externally prepared spin fluid/density gradient consisted of 15 ml of water and 1 ml of methanol and the disc speed was 10,450 rpm. Baseline separation and peak resolution are obtained over a decade of size range in less than 25 minutes.

The EGM has several advantages over the BLS: improved spin fluid density gradient stability at high disc speeds, e.g., 8,000 rpm to 10,000 rpm; successive sample injection without changing spin fluid, and the capability to change disc speeds during repeated injection without destroying the spin fluid/density gradient effectiveness. For example, disc speeds could be changed from 3,000 to 4,000, 4,000 to 5,000, and 5,000 to 6,000 rpm without upsetting the delicately balanced spin fluid density gradient needed for effective particle size analysis. This can not be done with the BLS. Note that for quantitative accuracy minor volume changes need to be accounted for after repeat injection. However, for qualitative analysis or "fingerprinting" this procedure is acceptable.

Subsequent experiments using dodecane (6) to inhibit evaporative cooling at the spin fluid/air interface have demonstrated even more improvement in baseline stability and run-to-run reproducibility when using the EGM.

### Statistical Analysis

Temperature control is an important factor in determining particle size by sedimentation methods. During a typical run changes in spin fluid temperature of 2-4°C were common. This temperature change (DELTEMP) was used as the covariate in the analysis of covariance.

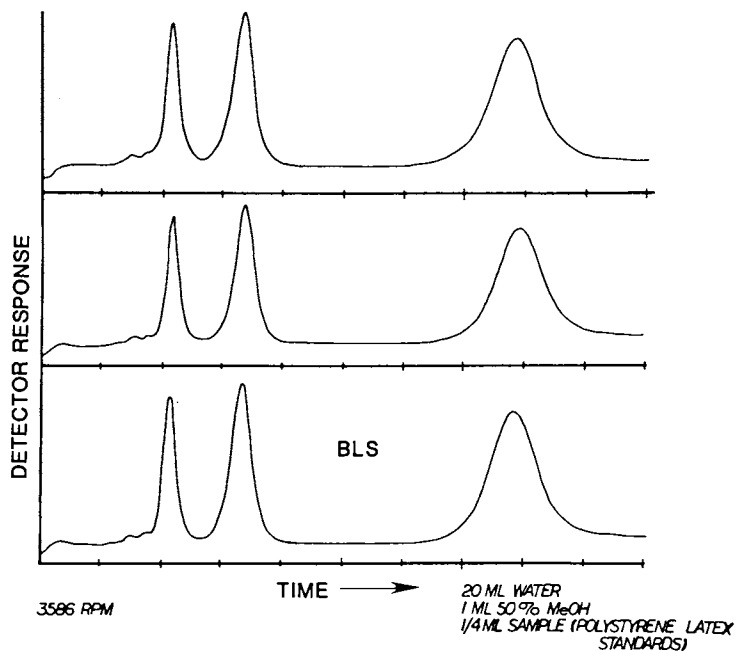


Figure 1. DCP separation of three latex standards by the BLS method.

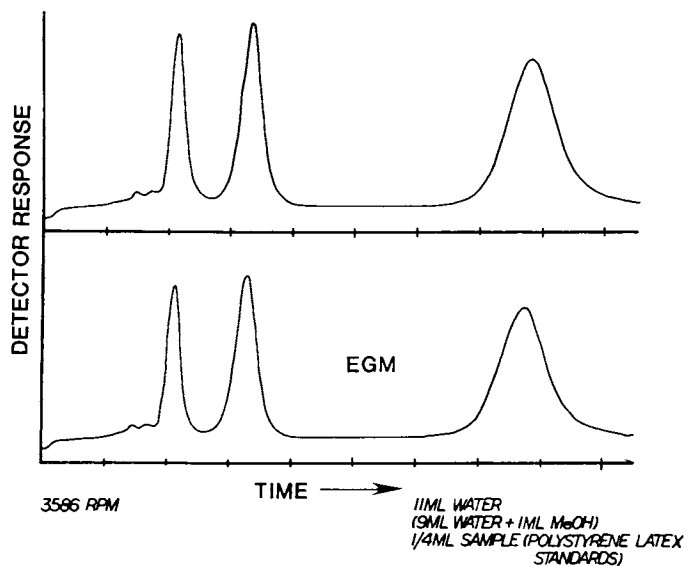


Figure 2. DCP separation of three latex standards by the EGM method.

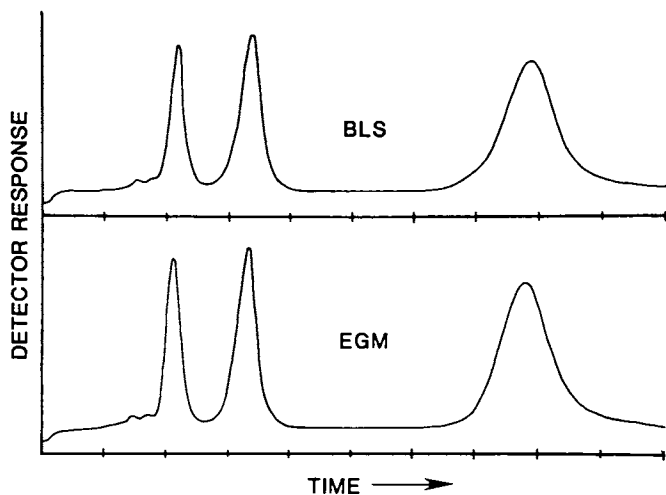


Figure 3. Comparison of the DCP separation of three latex standards by the BLS and EGM methods as seen in Fig.1 and Fig.2.

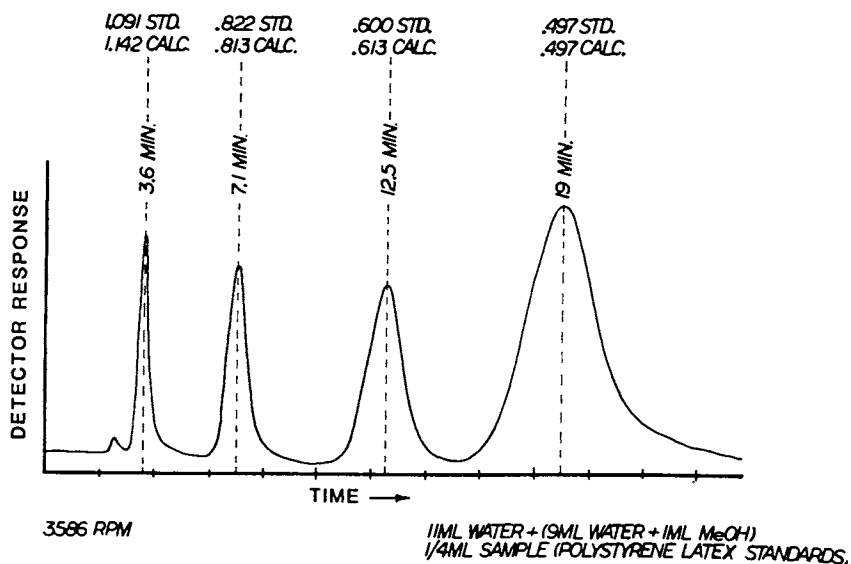


Figure 4. DCP separation of four latex standards by the EGM method showing nominal standard and calculated values.



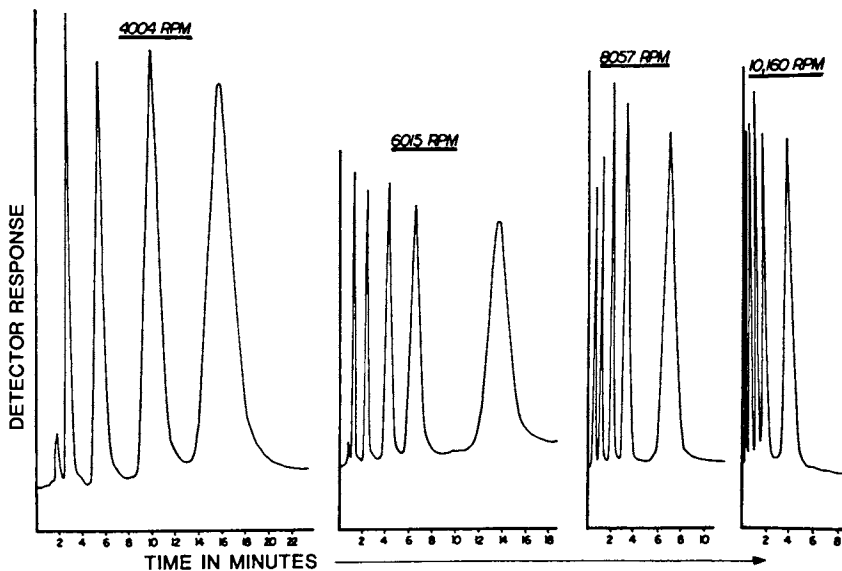


Figure 5. DCP separation of standard latexes at four different disc speeds by the EGM method.

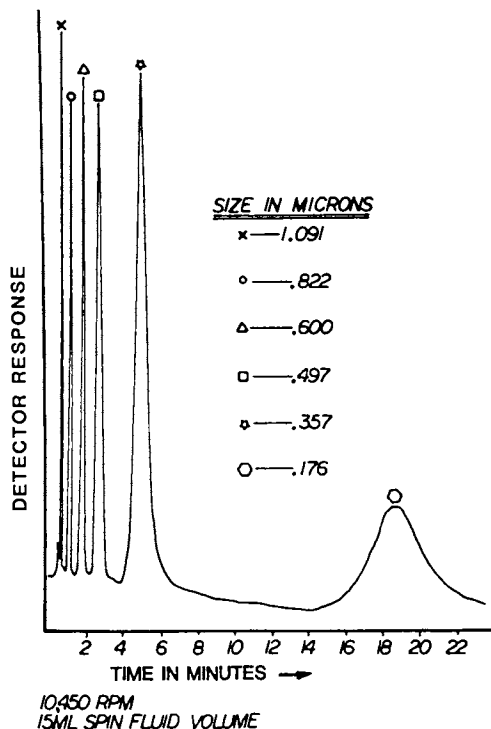


Figure 6. DCP separation of latex standards covering a decade of size range by the EGM method.

The magnitude of the temperature change seemed to have no effect. The results were almost identical when the runs with large temperature excursions were removed.

Analyses of covariance for both turbidity weight-average particle size ( $\bar{D}_w$ ) and polydispersity ( $\bar{D}_w/\bar{D}_n$ ) ( $\bar{D}_n$ , number-average particle size) were carried out. The Tables I and II show the results for the three samples combined.

TABLE I. ANALYSIS OF COVARIANCE FOR PARTICLE SIZE

| Source <sup>(a)</sup> | Degrees of Freedom | Sum of Squares | Mean Square | F       | Tail Prob. | Regression Coefficient |
|-----------------------|--------------------|----------------|-------------|---------|------------|------------------------|
| OPERATOR              | 1                  | 712.6          | 712.6       | 0.27    | 0.6067     |                        |
| SAMPLE                | 2                  | 13472409.6     | 6736204.8   | 2550.83 | 0.0000     |                        |
| DCP                   | 1                  | 17398.0        | 17398.0     | 6.59    | 0.0147     |                        |
| METHOD                | 1                  | 9005.5         | 9005.5      | 3.41    | 0.0733     |                        |
| OS                    | 2                  | 50763.4        | 25381.7     | 9.61    | 0.0005     |                        |
| OD                    | 1                  | 1313.9         | 1313.9      | 0.50    | 0.4852     |                        |
| SD                    | 2                  | 65119.9        | 32560.0     | 12.33   | 0.0001     |                        |
| OM                    | 1                  | 2443.6         | 2443.6      | 0.93    | 0.3427     |                        |
| SM                    | 2                  | 28501.4        | 14250.7     | 5.40    | 0.0091     |                        |
| DM                    | 1                  | 1297.9         | 1297.9      | 0.49    | 0.4879     |                        |
| DELTEMP               | 1                  | 128648.5       | 128648.5    | 48.72   | 0.0000     | 31.80684               |
| ERROR                 | 35                 | 92427.7        | 2640.8      |         |            |                        |
| TOTAL                 | 50                 | 13870041.9     |             |         |            |                        |

(a)The interaction effects are: OS, OPERATOR-SAMPLE; OD, OPERATOR-DCP; SD, SAMPLE-DCP; OM, OPERATOR-METHOD; SM, SAMPLE-METHOD; DM, DCP- METHOD.

TABLE II. ANALYSIS OF COVARIANCE FOR POLYDISPERSITY

| Source <sup>(a)</sup> | Degrees of Freedom | Sum of Squares | Mean Square | F      | Tail Prob. | Regression Coefficient |
|-----------------------|--------------------|----------------|-------------|--------|------------|------------------------|
| OPERATOR              | 1                  | 0.00039        | 0.00039     | 9.39   | 0.0042     |                        |
| SAMPLE                | 2                  | 0.00834        | 0.00417     | 100.51 | 0.0000     |                        |
| DCP                   | 1                  | 0.00015        | 0.00015     | 3.54   | 0.0681     |                        |
| METHOD                | 1                  | 0.00006        | 0.00006     | 1.53   | 0.2249     |                        |
| OS                    | 2                  | 0.00003        | 0.00002     | 0.37   | 0.6903     |                        |
| OD                    | 1                  | 0.00001        | 0.00001     | 0.19   | 0.6677     |                        |
| SD                    | 2                  | 0.00002        | 0.00001     | 0.23   | 0.7952     |                        |
| OM                    | 1                  | 0.00003        | 0.00003     | 0.70   | 0.4089     |                        |
| SM                    | 2                  | 0.00013        | 0.00007     | 1.62   | 0.2128     |                        |
| DM                    | 1                  | 0.00002        | 0.00002     | 0.59   | 0.4476     |                        |
| DELTEMP               | 1                  | 0.00003        | 0.00003     | 0.73   | 0.3982     | -0.00049               |
| ERROR                 | 35                 | 0.00145        | 0.00004     |        |            |                        |
| TOTAL                 | 50                 | 0.01066        |             |        |            |                        |

(a) See Table I for descriptions of the interaction terms.

Pooling the non-significant sums of squares with the residuals in the covariance tables above does not change the conclusions.

The important effects considered here are the METHOD and the ERROR. The two Methods are not significantly different for either the particle size or the polydispersity. The ERROR term, as will be shown later, is very nearly the same as the replication error.

The covariate, DELTEMP, is highly significant in the determination of the Particle Size. This indicates that temperature control, from the statistical point of view, is more important than has been previously considered. This is not surprising physically, in view of the temperature dependence of the spin fluid viscosity and the density terms contained in Stokes' Law. The cooling capacity of the two DCPs were known to be different. Both instruments had been physically recalibrated prior to running these experiments. Yet, there is some effect unaccounted for in the particle size analysis that leaves the two DCP instruments statistically somewhat different.

The three samples statistically were very different, both in particle size and polydispersity. In the case of the particle size determination, the two-factor interactions involving the SAMPLE were all significant, including the SAMPLE-METHOD interaction. Running the samples individually does not indicate why this might be. However, as noted below, the effects observed may be the result of different operator training, especially in determining the baselines. Yet, from practical considerations, the final variations are still acceptably small.

For polydispersity, as might be expected, SAMPLE was highly significantly different. Temperature, as shown by the very non-significant covariate term, has a negligible effect on the determination of polydispersity. However, for this set of data the operators were significantly different. This is possibly related to the individual judgement the operators make in repositioning the baseline. If this is correct, this effect should be reducible through better training of the operators. In spite of this difference, the standard errors of these determinations remain acceptably small.

The covariate, DELTEMP, in the analysis of covariance is very significant for particle size, but not at all significant for polydispersity. However, analysis of variance of both particle size and polydispersity gave a very different interpretation of the factors other than METHOD, which remained non-significant. In particular, the DCP instruments became extremely significant (expected) as did the OPERATOR (not expected). The strong, reasonable temperature effect, and the fact that the error terms agreed very well with the replication errors, led us to believe that the covariate analysis was the most meaningful interpretation of the data.

Since the methods have been established to be not significantly different, the other important question is the extent of variation of the measurements. It was previously established that the two methods had almost identical variances, so the following discussions are based on the two methods collectively. These results are summarized in Table III.

TABLE III. REPLICATION ERROR  
(Both Methods)PARTICLE SIZE,  $\bar{d}_w$ 

| SOURCE                 | DEGREES OF FREEDOM | STANDARD DEVIATION | COEFFICIENT OF VARIATION |
|------------------------|--------------------|--------------------|--------------------------|
| REPLICATES             |                    | ( $\mu\text{m}$ )  |                          |
| Sample 2               | 8                  | .0036              | 1.27 %                   |
| Sample 3               | 9                  | .0046              | 1.15                     |
| Sample 4               | 10                 | .0063              | 1.63                     |
| Mean of 2, 3, 4        | 27                 | .0051              |                          |
| RESIDUAL IN COVARIANCE |                    |                    |                          |
| Residual               | 35                 | .0051              |                          |
| Pooled Residual        | 40                 | .0052              |                          |

POLYDISPERSITY,  $\bar{d}_w/\bar{D}_n$ 

|                        |    |        |        |
|------------------------|----|--------|--------|
| REPLICATES             |    |        |        |
| Sample 2               | 8  | 0.0038 | 0.37 % |
| Sample 3               | 9  | 0.0079 | 0.77   |
| Sample 4               | 10 | 0.0045 | 0.43   |
| Mean of 2, 3, 4        | 27 | 0.0057 |        |
| RESIDUAL IN COVARIANCE |    |        |        |
| Residual               | 35 | 0.0064 |        |
| Pooled Residual        | 45 | 0.0062 |        |

The coefficient of variation gives a good measure of the reproducibility of these determinations. It is the standard deviation/mean reported as % variation. These figures of less than 2% for particle size ( $\bar{d}_w$ ), and less than 1% for polydispersity attest to the high capabilities of the methods.

In summary, the experimental design shows that (1) the samples selected were highly different, (2) temperature control is very important for precise measurement, and (3) there appears to be some operator effect in the determination of polydispersity. There are no interaction effects among operators, DCP instruments, and methods. For particle size measurement, however, different types of samples respond differently to the other factors in the experiment. In spite of this, the overall precision of the measurements by both the BLS method and the EGM is excellent.

### Conclusions

A novel approach to forming a density gradient for DCP analysis has been discussed. The EGM has been shown to be statistically equivalent to the BLS method and in the case of density gradient stability necessary for high speed separation the EGM has been shown, qualitatively, to have decided advantages.

The results obtained from the statistical analysis of the data were typical of other latices that have been analyzed. Analysis of variance indicated that there were no significant differences between (1) the two methods, (2) the two DCP's, (3) the two operators. Also, there were no significant interactions between these variables. The random errors in these experiments, in terms of standard deviations, were (1) for particle size,  $\bar{D}_w$ , 0.050 $\mu\text{m}$ , and (2) for polydispersity,  $\bar{D}_w/\bar{D}_n$ , 0.0065. The standard deviations of the two methods, individually, were almost identical.

### References

1. Provder, T., Holsworth, R. M., Div. of Org. Coatings and Plastics Chem. Preprint 36, 150(1976).
2. Jones, M. H., U. S. Patent No. 3,475,968, November 4, 1969.
3. Holsworth, R. M., Provder, T., U. S. Patent No. 4,478,073, October 23, 1984.
4. Zander, R. A., Koehler, M. E., Provder, T., U. S. Patent No. 4,311,039, January 19, 1982.
5. Koehler, M. E., Zander, R. A., Gill, T. T., "An Improved Disc Centrifuge Photosedimentometer and Data System", This Volume.
6. Coll, H., Searles, C. G., J. Coll. Inter. Sci., 1986, Vol 110, No. 1, 65.

RECEIVED October 6, 1986

## Chapter 14

# Improved Techniques in Disc Centrifugation

Hans Coll and Larry E. Oppenheimer

Research Laboratories, Eastman Kodak Company, Rochester, NY 14650

Results obtained from the disk centrifuge have been improved substantially by using preformed density gradients in the rotor fluid rather than the commonly used buffer-layer method, by protecting the fluid from evaporative cooling with a thin oil layer, and by the proper correction of the optical signal with the help of light-scattering theory. We have found that the oil-covered density gradient in the rotor is stable for hours, even at high rotor speeds, and several samples can often be injected consecutively onto the same gradient with no degradation in the results. Size distributions of spherical and near-spherical particles have been determined with great precision. The centrifugation method has been adapted for determining the hydrodynamic thickness of polymer layers (such as gelatin) adsorbed to colloidal particles. More recently, particle size analysis has been extended to nonspherical particles and to nonaqueous media.

The disk centrifuge is an excellent instrument for determining particle size distributions in the size range from several micrometers to somewhat below  $0.1 \mu\text{m}$ . For broad or especially multimodal size distributions, disk centrifugation is, overall, probably superior to any other sizing method for the aforementioned range. The only limiting requirement is a finite density difference between the particles and the suspending fluid.

The line-start method, which requires the particles to be more dense than the fluid, is generally used with the disk centrifuge. It has been recognized that stable sedimentation, as a rule, requires a density gradient in the spin fluid (1). The buffer-layer method (2) is most often used to generate this gradient, but at times it has been unreliable.

0097-6156/87/0332-0202\$06.00/0

© 1987 American Chemical Society

To investigate the effect of the density gradient on the stability of sedimentation in the disk centrifuge, we generated, externally, spin fluids containing well-defined density gradients (3). In this manner peak broadening was minimized and excellent reproducibility could be achieved. By introducing a thin layer of oil onto the meniscus of the spin fluid to prevent evaporation, we could use the same spin fluid for several hours, which, for a variety of samples, allowed multiple consecutive injections to be made through the oil layer.

The high precision of the disk centrifuge allowed the comparison of sedimentation velocities of colloidal particles with and without an adsorbed polymer layer, from which the hydrodynamic thickness of the adsorbed layer could be calculated (4). Here the disk centrifuge, giving complete size distributions, made the use of monodisperse samples unnecessary.

### Experimental

Experiments were done with a Joyce-Loebl Model III disk centrifuge-photosedimentometer (Vickers Instrument Co.). Preformed density gradients were made in a Lucite gradient apparatus (Buchler Instruments, Inc.) or in a similarly designed device made of glass (3). The two solutions were pumped into a near-vertical tube 1 cm I.D. x 35 cm long by using a peristaltic pump. The gradient was then injected from the tube into the spinning rotor by means of a piston. Figure 1 is a schematic of the gradient-forming system. Since Lucite is not wetted by water, 0.02% Pluronic L92 surfactant (BASF Wyandotte) was added to the aqueous liquids in the gradient maker.

Sucrose solutions were usually used as aqueous spin fluids. Nonaqueous media such as dodecane/hexadecane and diethylformamide/dimethylformamide mixtures have also been used. The quality of the gradients was confirmed refractometrically in separate experiments.

### Preformed Density Gradients

Samples containing pairs of polystyrene latexes with narrow size distributions were used to examine the effect of density gradient steepness on peak shape. Unstable sedimentation, characterized by poorly resolved, broad peaks, usually resulted when the samples were run by the buffer-layer method with 4% sucrose as the spin fluid. When the same samples were run in 20 mL of spin fluid with a preformed gradient from 0 to 4% sucrose (a 0/4% gradient), as shown in Figure 2a for a pair of latexes with nominal diameters of 0.45 and 0.765  $\mu\text{m}$ , sharp, well-resolved peaks were obtained. A 0/3% gradient also gave good separation (Figure 2b), but with a 0/2% gradient, the separation was severely degraded (Figure 2c). Additional experiments with truncated gradients (e.g., 4/7.5% sucrose) showed that this degradation occurs over a very narrow range of gradient densities. The latex pair was well separated in a 4/7.5% gradient but poorly separated in a 4.25/7.5% gradient with further degradation occurring in less steep gradients (Figures 3a-d).

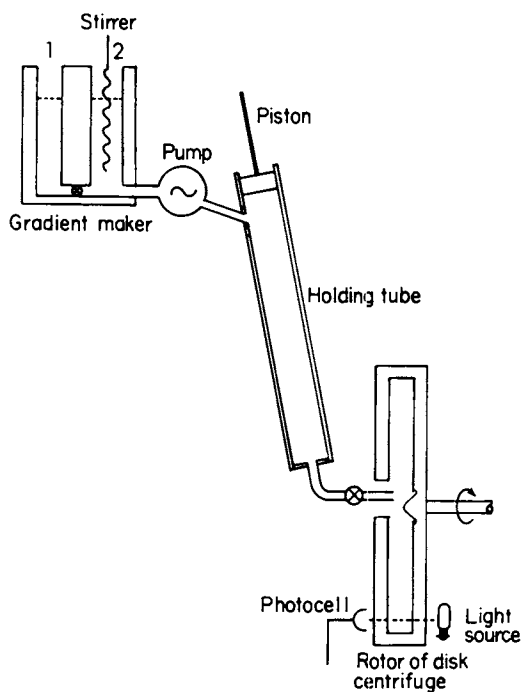


Figure 1. Schematic of the gradient-forming apparatus. Reproduced with permission from Ref. 3. Copyright 1985, Academic Press.



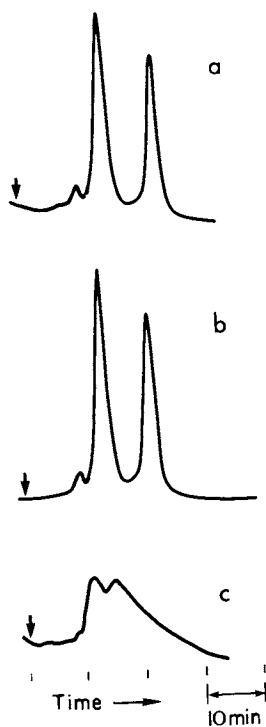


Figure 2. Sedimentation curves of polystyrene latexes with nominal diameters of 0.45 and 0.765  $\mu\text{m}$  disk centrifuged at 4000 rpm in 20 mL of spin fluid with gradients of (a) 0/4%, (b) 0/3%, (c) 0/2% sucrose. Reproduced with permission from Ref. 3. Copyright 1985, Academic Press.

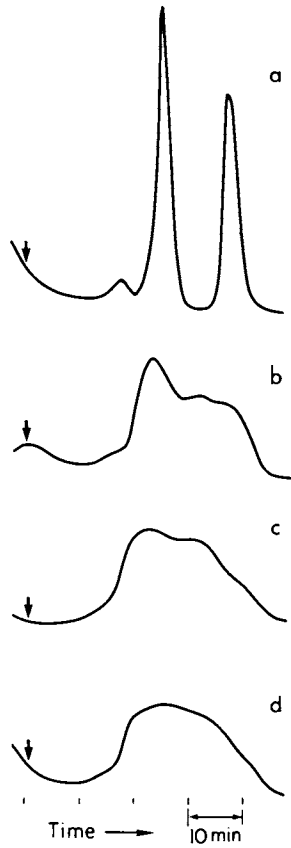


Figure 3. Sedimentation curves run as for Figure 2 but with gradients of (a) 4/7.5%, (b) 4.25/7.5%, (c) 4.5/7.5%, (d) 5/7.5% sucrose.

Gradient Protection

The preformed gradients in the spin fluid became unstable in less than 1 h if the rotor was run at high speed. The instability was characterized by the appearance of a large peak in the baseline after the centrifuge had been run for about 1 h with or without a sample having been injected into the rotor. If a sample was injected after the appearance of this baseline peak, a poor separation, such as that shown in Figure 4a, was always obtained. We attributed these phenomena to convective mixing of the spin fluid induced by evaporative cooling of the surface, with the baseline peak being caused by the transient refractive index inhomogeneity that would accompany such mixing. To suppress evaporation and the resultant cooling, we ran experiments in which the aqueous spin fluid was covered with 1 mL of *n*-dodecane. Good results were now obtained for samples injected after the spin fluid had been run for 3 h at 6000 rpm (Figure 4b).

The gradient-variation experiments described in the previous section were repeated with dodecane-protected gradients. Much shallower gradients gave stable sedimentation under these conditions. The latex mixture could be separated in a 0/1% gradient as well as in a 4/4.5% gradient. This confirmed that evaporative cooling of the spin fluid was the primary cause of convection and hence of unstable sedimentation.

Particle Size Distributions

Particle radii (*R*) are calculated from the sedimentation times (*t*) by means of the Stokes equation. For a spin fluid with density and viscosity gradients

$$R^2 = \frac{9}{8\pi^2 U^2 t} \int_{x_M}^{x_D} \frac{\eta_o dx}{(\rho - \rho_o)x} \quad (1)$$

where *U* is the rotor speed (revolutions per second),  $\rho$  is the particle density, and  $\rho_o$  and  $\eta_o$  are, respectively, the position-dependent density and viscosity of the spin fluid. The integration extends from  $x_M$ , the distance of the fluid meniscus from the axis of rotation, to  $x_D$ , the radial distance of the optical detector.

The concentration and hence the viscosity and density (of the aqueous sucrose, e.g.) at any point in the spin fluid are calculated from the concentrations and volumes in the gradient apparatus and the dimensions of the rotor.

The accuracy obtainable by using this approach can be seen from the results in Figure 5, which were obtained for polystyrene latexes with nominal diameters of 0.804 and 1.09  $\mu\text{m}$ . The diameters calculated from the peak positions were, respectively, 0.789 and 1.093  $\mu\text{m}$ , based on a measured density of 1.048 g/cm<sup>3</sup> for these latexes. The small peak at 1.3  $\mu\text{m}$  in Figure 5 is attributed to doublets of the 1.09- $\mu\text{m}$  latex. Although the ratio of the sedimentation times of these two peaks (1.09 and 1.3  $\mu\text{m}$ ) is close

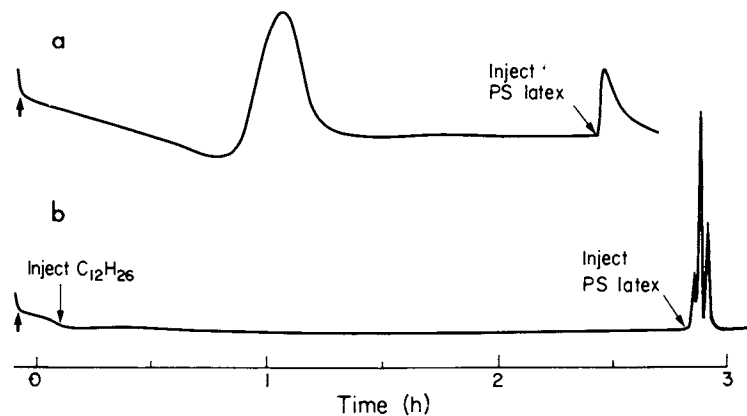


Figure 4. Effect of running a 2/6% sucrose gradient at 6000 rpm for ~3 h before sample injection (a) without oil protection, (b) with protection. Reproduced with permission from Ref. 3. Copyright 1985, Academic Press.

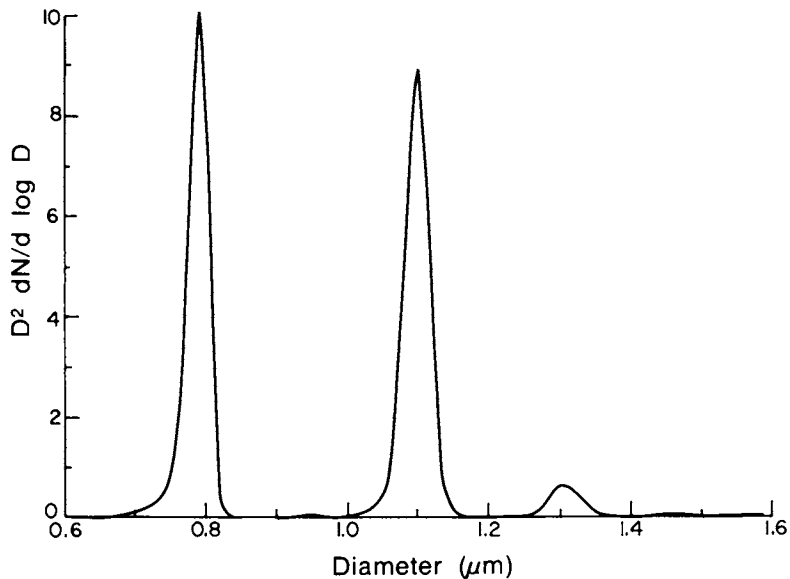


Figure 5. Particle size distribution of a mixture of polystyrene latexes with nominal diameters of 0.804 and 1.09  $\mu\text{m}$  obtained by disk centrifugation at 4000 rpm in a 1/4% sucrose gradient.

to the 0.7 predicted for doublets oriented parallel to the direction of sedimentation (1), we expect that Brownian motion would randomize the orientations of the aggregates. In this case the ratio of the sedimentation times would be somewhat below 0.7.

The instantaneous output of the detector ( $S$ ) can be related to the concentration of material of a given size by dividing by the extinction efficiency ( $Q_{\text{ext}}$ ) of the particles present in the detector (5).  $Q_{\text{ext}}$  is a function of the (known) particle size, the relative refractive index of the particles, and the wavelength-dependent optical response of the detection system. This treatment is exact only for spherical particles, but it is often used as an approximation for other shapes as well. For very narrow size distributions,  $Q_{\text{ext}}$  may be treated as a constant over the range of particle sizes, and this correction may be ignored. This is also the case for particles that are very large compared to the wavelength of light, where  $Q_{\text{ext}}$  approaches a constant value of 2. In addition, it has been shown that if the relative refractive index of the sample is sufficiently low ( $m < 1.25$ , e.g.) the wavelength sensitivity of the optical system and of  $Q_{\text{ext}}$  become unimportant, and calculations can be performed for a single wavelength ( $\sim 700$  nm for our instrument).

$S$  is related to the number concentration ( $N$ ) of particles viewed by the detector through

$$S = R^2 \pi N Q_{\text{ext}} L \quad (2)$$

where  $L$  is the path length. Since the size increment  $\Delta R$  sampled by the detector is proportional to  $R$ , the optically corrected distribution is a volume distribution (6, 7) with linear increment or an area distribution with logarithmic increment:

$$S/Q_{\text{ext}} = \text{const } R^3 \Delta N/\Delta R = \text{const } R^2 \Delta N/\Delta \log R \quad (3)$$

#### A Study Requiring High Precision: Determination of the Thickness of a Gelatin Layer Adsorbed on Silver Bromide

While examining time-dependent phenomena of silver bromide particles, we made many repeat measurements. With care, standard deviations could be kept below 1%. Figure 6, for instance, contains the diameters calculated from the peak maxima for 44 injections of a silver bromide dispersion. Four consecutive injections were made into the same dodecane-protected spin fluid, so that experiments in 10 different spin fluid gradients are represented here. Monitoring of the spin fluid temperature was required, since this variable affects both density and viscosity. Corrections were also made for the volume change of the spin fluid caused by successive injections (1, 3).

The ability to make very precise measurements has allowed us to use the disk centrifuge to determine the thickness of adsorbed gelatin layers on silver bromide particles (4). When particles are coated with an adsorbed polymer layer, the sedimentation time reflects the size and density of the particle core as well as the thickness and density of the adsorbed layer. An apparent (incor-

rect) size  $r$  can be calculated for such a particle by assuming that the density is uniform and equal to that of the core. The shell thickness ( $L$ ) is calculated from

$$L = R_c [(R_c/r)^2 - 1] \quad (4)$$

where  $R_c$  is the radius of the core particle. Values of  $R_c$  were measured after the adsorbed gelatin was removed from the particles by enzymatic digestion. Typical shifts,  $R_c - r$ , were  $\sim 0.1 \mu\text{m}$ .

Figure 7 contains the size distributions calculated for one sample before and after removal of the gelatin layer. A unique advantage of using a device that generates the whole particle size distribution, such as the disk centrifuge, is shown in Figure 8. Here, the gelatin-coated silver bromide is highly aggregated, leading to a multimodal size distribution. Nonetheless, it is possible to identify the peak corresponding to the unaggregated particles for comparison with the curve produced after the removal of the gelatin.

The layer thickness ranged from 0.025 to 0.15  $\mu\text{m}$ , depending on the sample, the ionic strength, and the pH of the spin fluid. Figure 9 shows plots of layer thickness as a function of spin-fluid ionic strength obtained for four silver bromide sols at pH  $\sim 6$ .

Similarly, we have measured the thickness of an adsorbed synthetic polymer layer on titanium dioxide particles in a hydrocarbon medium. Since the polymer could not be removed from the particles once adsorbed, the values for the bare particles were obtained by centrifuging aqueous dispersions of the titanium dioxide stabilized with an ionic surfactant.

### Nonspherical Particles

The sedimentation of isometric particles, such as cubes and octahedra, deviates only slightly from the Stokes equation. Significantly anisometric particles that can be approximated by ellipsoids of revolution are amenable to rigorous sizing by centrifugation if the axial ratios  $q$  are known. If the major semi-axis is  $a$  and the minor semi-axis is  $c$ , the sedimentation velocity  $dx/dt$  can be written as

$$dx/dt = \frac{2ac(\rho - \rho_o)\omega^2 x}{9\eta_o f(q)} \quad (5)$$

where  $\omega$  is the angular acceleration and  $f(q)$  is the friction factor, a function of the axial ratio. For a sphere,  $a = c$  and  $f(q) = 1$ . Given  $q$ , the appropriate friction factors can be calculated (8, 9), once it is recognized that particles with dimensions smaller than a few micrometers assume random orientations during centrifugation. Since  $q = c/a$ , the sedimentation time can be related to  $a$  and/or  $c$ . However, in the general case where the axial ratio is unknown, an independent assessment of  $a$  is not

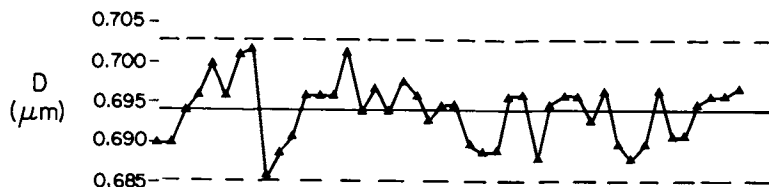


Figure 6. Reproducibility of peak positions for successive runs on a silver bromide sample centrifuged at 1500 rpm in 20 mL of a 4/8% sucrose gradient.  $N = 44$  injections,  $D = 0.694 \mu\text{m}$ ,  $\sigma = 0.55\%$ .

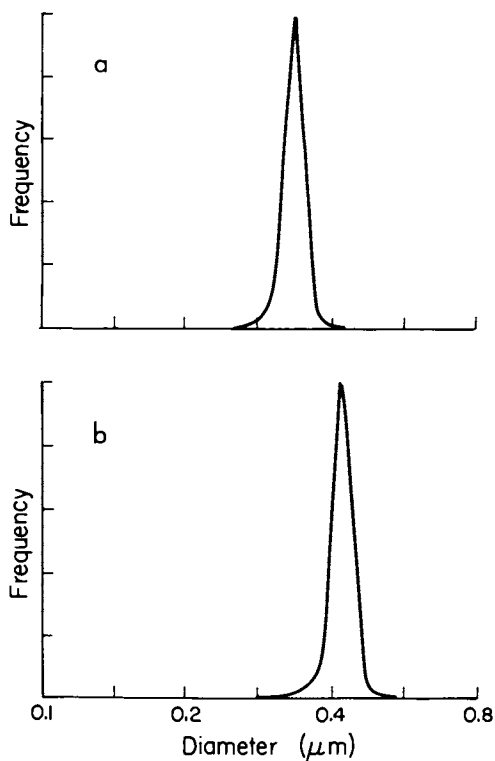


Figure 7. Apparent particle size distributions of a silver bromide dispersion (a) in 0.001 N  $\text{NaNO}_3$  with the gelatin layer intact, (b) after removal of the gelatin. Reproduced with permission from Ref. 4. Copyright 1985, Academic Press.

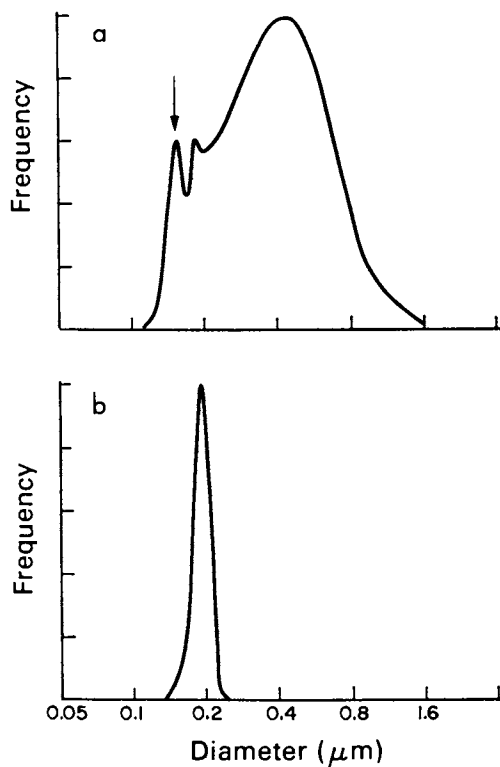


Figure 8. Apparent particle size distributions of a silver bromide dispersion (a) in 0.001 N  $\text{NaNO}_3$  with the gelatin layer intact, (b) after removal of the gelatin. The arrow in a indicates the peak for the unaggregated particles. Reproduced with permission from Ref. 4. Copyright 1985, Academic Press.



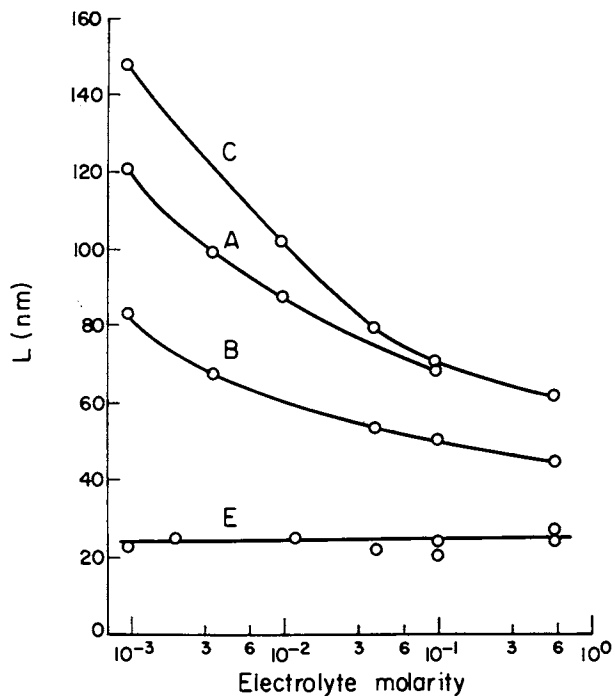


Figure 9. Gelatin-layer thickness versus spin-fluid ionic strength for four silver halide dispersions. The spin fluids contained  $\text{NaNO}_3$  and were adjusted to pH  $\sim 6$ . Reproduced with permission from Ref. 4. Copyright 1985, Academic Press.

possible. A special case is the oblate ellipsoid with  $a \gg c$ , a thin platelet, for which  $f$  approaches 0.65 and the product  $ac$  can be calculated from the sedimentation time.

### Conclusion

The stability of sedimentation in the disk centrifuge is greatly enhanced by the presence of a density gradient in the spin fluid, as evidenced by minimal peak broadening. A gradient with known properties can be formed externally and injected into the spinning rotor by using an apparatus such as the one described here or with an appropriately designed syringe device. Once injected, the density gradient is subject to degradation due to thermal gradients in the spin fluid caused by evaporative cooling at the meniscus. This effect can be suppressed by covering the spin-fluid surface with a thin layer of a nonvolatile oil such as dodecane. A density gradient protected in this manner can be used for several hours after injection into the rotor. Since many sample types can be introduced into the spin fluid through such an oil layer, consecutive runs can be made with the same spin fluid. The standard deviation in particle sizes calculated from peak positions can be reduced to <1% by using these techniques along with careful monitoring of the spin-fluid temperature.

The output of the disk centrifuge, a curve of optical density versus time, can be converted to a particle size distribution by using Stokes' law to convert the time axis to a size axis and by the application of light-scattering theory to calculate the particle frequencies from the optical densities. As described herein, one obtains mass distributions with linear size increments or the equivalent area distributions with logarithmic increments.

We have demonstrated that the high precision of the data allows the disk centrifuge to be used to determine the thickness of polymer layers adsorbed to dispersed substrates. Finally, although the analysis of disk-centrifuge data is exact for spherical particles, significant information can often be obtained for particles that can be treated as ellipsoids. When the axial ratio is known and constant, a distribution of sizes can be obtained.

### Literature Cited

1. Kaye, B. H. "Direct Characterization of Fineparticles"; Wiley-Interscience: New York, 1981.
2. Beresford, J. J. Oil Colour Chem. Assoc. 1967, 50, 594.
3. Coll, H.; Searles, C. G. J. Colloid Interface Sci., in press.
4. Coll, H.; Oppenheimer, L. E.; Searles, C. G. J. Colloid Interface Sci. 1985, 104, 193.
5. Oppenheimer, L. E., J. Colloid Interface Sci. 1983, 92, 350.
6. Allen, T. "Particle Size Measurement"; Chapman and Hall: London, 1968; pp. 122-124.
7. Coll, H.; Haseler, S. C. J. Colloid Interface Sci. 1984, 99, 591.
8. Tanford, C. "Physical Chemistry of Macromolecules"; Wiley: New York, 1961; pp. 324-328.
9. Happel, J.; Brenner, H. "Low Reynolds Number Hydrodynamics"; Prentice Hall: Englewood Cliffs, NJ, 1965.

RECEIVED June 27, 1986

## Chapter 15

# Measuring Particle Size Distribution of Simple and Complex Colloids Using Sedimentation Field-Flow Fractionation

J. Calvin Giddings, Karin D. Caldwell, and Harlan K. Jones

Department of Chemistry, University of Utah, Salt Lake City, UT 84112

This paper outlines the basic principles and theory of sedimentation field-flow fractionation (FFF) and shows how the method is used for various particle size measurements. For context, we compare sedimentation FFF with other fractionation methods using four criteria to judge effective particle characterization. The application of sedimentation FFF to monodisperse particle samples is then described, followed by a discussion of polydisperse populations and techniques for obtaining particle size distribution curves and particle densities. We then report on preliminary work with complex colloids which have particles of different chemical composition and density. It is shown, with the help of an example, that sedimentation FFF is sufficiently versatile to unscramble complex colloids, which should eventually provide not only particle size distributions, but simultaneous particle density distributions.

Sedimentation field-flow fractionation (sedimentation FFF) has recently emerged as a powerful and versatile technique for the characterization of simple and complex particle populations. In this technique, a particulate sample is entrained in a stream of liquid, subjected to a field acting perpendicular to the stream direction, and washed down the length of a thin flow channel (1). The rate at which particles are displaced downstream (measured by emergence times) can be related by exact theory to particle properties such as mass, size, and density (2). However, since different kinds of particles move at different velocities in this system, broad particle populations are sorted into a graded size (or mass) distribution along the length of the flow channel. Observation of the shape of the emerging distribution (recorded as a fractogram), together with theory, yields a particle size distribution curve (3-6).

0097-6156/87/0332-0215\$06.00/0

© 1987 American Chemical Society

Sedimentation FFF, applied in the above manner, yields highly detailed size distribution curves. It is convenient and accurate. Importantly, sedimentation FFF is a highly flexible technique. It can be adapted to nearly all particle types in virtually any suspending medium. It yields particle density as well as size and size distribution. Our recent work has shown that it can be used to probe both size and density distributions in complex colloids, defined as systems having colloidal particles of variable chemical composition. Complex colloids are important in many biological and environmental studies.

Clearly, sedimentation FFF is a separation technique. It is an important member of the field-flow fractionation (FFF) family of techniques. Although other members of the FFF family (especially thermal FFF) are more effective for polymer analysis, sedimentation FFF is advantageous for the separation of a wide assortment of colloidal particles. Sedimentation FFF not only yields higher resolution than nearly all other particle separation techniques, but its simple theoretical basis allows a straightforward connection between observed particle migration rates and particle size. Thus size distribution curves are readily obtained on the basis of theoretical analysis without the need for (and uncertainties of) calibration.

We note that sedimentation FFF, although a separation technique, is not a form of chromatography. Chromatography is universally defined as a method in which species are separated by differentially partitioning them between two phases, one stationary and one mobile (7). In all FFF methods, by contrast, separation is implemented within one phase, consisting of the liquid continuum within the flow channel. (We add here the observation that hydrodynamic chromatography is inappropriately named; separation in this system also takes place in the single liquid phase occupying the interstitial space of a packed column.)

In FFF systems, the separation along the flow axis is caused by the perpendicular field, whose crucial role is recognized by the word "field" in field-flow fractionation. The applied field interacts with entrained particles, forcing them to accumulate at one wall (the accumulation wall) of the channel. Since the flow velocity near any wall is reduced by frictional drag, the downstream displacement of the particles is retarded. Retardation (or retention) is greatest for those particles forced most closely to the wall. Consequently, particles are separated according to the different forces exerted on them by the applied field. These forces normally depend on particle size, leading to a size-based separation.

The sedimentation FFF process is illustrated in Figure 1. In this figure, the FFF channel, which has a ribbon-like rather than a tube-like configuration, is curved to fit within a centrifuge basket. The centrifuge is responsible for the sedimentation forces which impel particles toward the accumulation wall. Naturally, the largest and most massive particles are impelled by the greatest forces and end up closest to the wall, provided their density differs from that of the channel fluid.

The flow profile in the channel, shown in the figure, is parabolic in form. With this flow profile, the velocity approaches

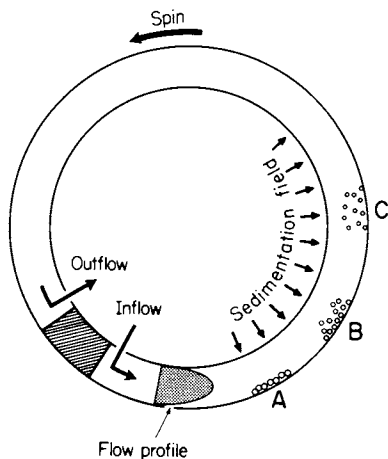


Figure 1. Separation of large (A) particles from intermediate-sized (B) and small (C) particles in a sedimentation FFF channel. The figure represents a side view of the channel, which is typically 0.0254 cm thick.

zero near the wall, reflecting the above-mentioned frictional drag. Consequently, the largest particles, hugging the wall most closely, are displaced most slowly down the channel. Separation ensues, as illustrated in the figure.

Sedimentation FFF is amenable to rather exacting theory (2). For laminar flow (which includes all FFF operation), the parabolic profile provides a concise description of the flow distribution. The sedimentation forces, which apply uniformly throughout the channel volume, are equally well-defined in terms of particle size, particle density, and fluid density. Thus migration rate can be rigorously related to particle size, as will be shown in the theory section.

Sedimentation FFF is applicable to particles ranging in size from about 0.01 to 1  $\mu\text{m}$ . A special form of sedimentation FFF termed steric FFF extends this range from 1  $\mu\text{m}$  to 100  $\mu\text{m}$  (8).

### Comparison of Particle Size Measurement Techniques

In order to provide context, we compare generally the FFF methodology with other approaches used for measuring particle size. Such comparisons are difficult because the efficacy of particle characterization depends on the special needs applicable to each sample. Thus sweeping generalizations must be looked at warily and applied with discretion. However, these generalizations help organize our thinking about such highly varied methodologies, and point us toward desired solutions.

For present purposes, particle characterization methods are divided into two major categories: those based on fractionation and those not. Some important techniques falling in these two categories are shown in Table I; other techniques are listed in a recent review (9).

Table I. Examples of major particle characterization techniques falling in two broad categories: fractionation and nonfractionation.

| Fractionation methods   | Nonfractionation methods  |
|---|---|
| field-flow fractionation (FFF):<br>sedimentation, flow, steric,<br>etc. | light scattering: classical,<br>turbidimetric, Fraunhofer,<br>quasi-elastic, etc. |
| disc centrifugation (DCF)   | neutron scattering  |
| hydrodynamic chromatography (HDC)                                       | electrozone   |
| size exclusion chromatography (SEC)                                     | electron microscopy   |
| sieving (SIV)   |   |

The nonfractionation techniques, by themselves, use a variety of phenomena to probe particle characteristics. In one class (e.g., most forms of light scattering), measurements are made on a large, nondifferentiated particle population. In another (e.g., electron microscopy and electrozone methods), results are based on a statistical averaging of measurements made for individual particles.

As a class, fractionation techniques have certain advantages and disadvantages. A limitation of the fractionation techniques is that adequate time must be taken to carry out the particle separation. While this time has been reduced to only a few minutes in some cases, it is still slow compared to the ideal case of using light as a probe, as in light scattering. (However, to acquire adequate data to characterize broad particle distributions, light scattering experiments must often be carried on for long periods of time.)

A general advantage of fractionation is that it breaks up broad particle populations into component fractions, making it possible to look at the components individually and to examine their role within and contribution to the overall population. Furthermore, each fraction typically contains a sufficient number ( $10^6 - 10^{10}$ ) of particles for valid statistical representation.

The advantages of fractionation are amplified by important characteristics which may or may not be possessed by individual fractionation techniques. Some of these important characteristics are:

1. High resolution. The wealth of detail about a particle population increases with the resolution between particle components.

2. Sample elution. With elution, detection is simplified and particle fractions can be collected and subjected to further characterization by additional fractionation steps, chemical analysis, electron microscopy, and other methods.

3. Exact theory. If particle properties can be related exactly to their observed behavior in the fractionation system, then the properties can be deduced directly from experimental results without the uncertainties of calibration procedures.

4. Adaptability and flexibility. A greater variety of particles can be treated and more of their properties measured if the fractionation system is applicable to a wide range of particle sizes, chemical types, and suspending media, and if fractionation conditions can be easily varied to yield complementary data under different conditions.

The four characteristics listed above are not all-inclusive. Other factors include speed and ease of operation. However, these factors are not as intrinsic to the method and are more subject to changes, improvements, and tradeoffs. Some of these factors will be discussed shortly.

In Table II, we show how the five fractionation techniques listed in Table I compare with respect to the four characteristics

Table II. Comparison of fractionation techniques with respect to four intrinsic features of major importance.

|     | resolution | elution | exact theory | flexibility |
|-----|------------|---------|--------------|-------------|
| FFF | high       | yes     | yes          | high        |
| DCF | high       | no      | yes          | medium      |
| HDC | low        | yes     | no           | low         |
| SEC | medium     | yes     | no           | low         |
| SIV | low        | no      | no           | low         |

listed above. The importance of these characteristics is discussed at greater length below.

Resolution is without question a key element in accurate and detailed particle characterization. Particle populations that cannot be resolved cannot, in any sense, be distinguished from one another. While deconvolution techniques can provide particle size distribution curves from low resolution systems, the deconvolution must be based on assumptions about instrumental band broadening and band shape. In general, any detailed information lost because of poor resolution cannot be recovered by mathematical manipulation alone. In all cases, the quality of a size distribution curve will increase with the intrinsic resolution exhibited by the system.

We note that FFF and disc centrifugation both achieve high resolution rankings in Table II. This comparable resolution has been predicted theoretically; any field (such as a sedimentation field) applied directly to a sample will lead to approximately the same resolution as found in an FFF system using the same field, providing the displacement distances are comparable (10). While in theory, resolution in FFF can be amplified by the arbitrary length of the separation path (channel length), in practice the two approaches have comparable levels of resolution.

The resolution achievable by a system depends upon the number of theoretical plates generated by that system and upon the selectivity of the system. The number of theoretical plates can be varied widely with separation path length, flow conditions, field strength, etc., and is thus highly variable. However, selectivity is a more intrinsic property of the fractionation method and serves as a basis of comparison of the different systems.

Size selectivity can be defined by the equation

$$S_d = \frac{d}{V} \frac{\ln V}{\ln d} = \frac{d}{V} \frac{dV}{d} \quad (1)$$

where  $V$  is particle velocity and  $d$  is particle diameter. This expression is applicable to both elution and nonelution systems. (For elution systems,  $V_r$  is generally used in place of  $V$  (11)). The usefulness of selectivity as an index of resolution follows if we note that a high  $S_d$  implies that a small increment in particle diameter  $\Delta d$  gives rise to a large increment in velocity  $\Delta V$ , which leads to highly resolved fractions. When the same small  $\Delta d$  is accompanied by a very small  $\Delta V$ , then discrimination is lost.

In Table III, we show the selectivities characteristic of four of the fractionation methods in their normal working range. Excluded from this list is sieving, to which the concept of selectivity is not applicable. For completeness, we have subdivided the FFF family into sedimentation FFF, thermal FFF, flow FFF, and steric FFF to show how the selectivity of each of these subtechniques compares to that of the other fractionation methods. The  $S_d$  values reported here differ from  $S$  values reported elsewhere (12), which refer to mass rather than size selectivity.

The second characteristic listed in Table II is elution. Elution provides a considerable advantage for detecting and processing the sample after the fractionation is complete.



Table III. Comparison of selectivity  $S_d$  for principal particle fractionation methods.

| method               | $S_d$       |
|----------------------|-------------|
| FFF:*                |             |
| sedimentation        | 3           |
| flow                 | 1           |
| thermal <sup>+</sup> | 1.2         |
| steric               | 0.5 - 1     |
| DCF                  | 2           |
| HDC                  | 0.02 - 0.03 |
| SEC <sup>+</sup>     | 0.03 - 0.22 |

\* values applicable when  $V \leq$  half of mean carrier velocity  $\langle v \rangle$ .

<sup>+</sup>For polymers where we consider particle diameter  $d =$  twice hydro-dynamic radius.

However, not all samples require elution, particularly if the application is routine.

The third characteristic entered in Table II reflects the exactness of the theoretical relationship between particle properties and experimental results. Except in special cases, a rigorous theoretical linkage will improve the quality of information derived from a fractionation experiment.

The final characteristic of Table II, flexibility, provides an index of a system's ability to cope with diverse particulate materials under varied circumstances. While flexibility is not important for repetitive runs of the same material, it is important for exploring new particle types, measuring new properties, evaluating accuracy, and for optimizing the speed and resolution associated with the particle characterization. FFF ranks highest for flexibility because of the large number of influential parameters subject to variation: field type, field strength, flow velocity, channel dimensions, and carrier properties. Field strength and flow velocity are especially important; both affect speed and resolution and can be played against one another for optimization. The variation of either property during a run can lead to a versatile approach called programming. We will show later that the variation of carrier density leads to the measurement of particle density.

It is interesting to compare the flexibility of three techniques--FFF, HDC, and DCF. In HDC, flow is a variable, but there is nothing equivalent to field strength to modulate the effect of flow; thus flowrates are not widely varied. In DCF, field strength can be varied, but there is no flow for compensating adjustments and there is little profit in varying conditions from one run to the next. In FFF, by contrast, both field and flow are widely and profitably varied to reach the desired goals of speed, accuracy, and redundancy.

### Theory

We have noted that the combination of regular geometry, uniform field strength, and well-defined parabolic flow, make possible a rigorous theoretical treatment to relate particle properties to experimental observations. This theory serves as the basis for particle characterization in sedimentation FFF (2). Here, we will briefly review the main theoretical concepts and some of the equations needed for particle size calculations.

We note first that immediately following the injection of a sample at the head of the channel, the flow of carrier is stopped briefly to allow time for the sample particles to accumulate near the appropriate wall. As the particles concentrate near the wall, the growing concentration gradient leads to a diffusive flux which counteracts the influx of particles. Because channel thickness is small (approximately 0.25 mm), these two mass transport processes quickly balance one another, leading to an equilibrium distribution near the accumulation wall. This distribution assumes the exponential form

$$c(x) = c_0 \exp(-x/\lambda w) \quad (2)$$

where  $c(x)$  is the concentration at elevation  $x$  above the wall,  $c_0$  is the concentration at the wall ( $x = 0$ ),  $w$  is the channel thickness, and  $\lambda$  is the retention parameter. Quantity  $\lambda$  is a dimensionless measure of the thickness of the equilibrium particle cloud;  $\lambda$  will vary from one particle size to another as a reflection of the fact that the force driving the particles toward the wall and the resultant cloud thickness is a function of particle diameter. Thus the dependence of  $\lambda$  on particle diameter  $d$  is ultimately responsible for particle separation.

Specifically, for sedimentation FFF,  $\lambda$  relates to  $d$  (along with field strength (acceleration)  $G$  and the difference  $\Delta\rho$  in density between the particle and the carrier) according to the expression

$$\lambda = 6kT/d^3 \Delta\rho\pi Gw \quad (3)$$

For nonspherical particles,  $d$  represents an effective diameter (the diameter of a sphere of equal volume).

Equation 3 can be rearranged as follows to yield  $d$  in terms of  $\lambda$

$$d = \left( \frac{6kT}{\Delta\rho\pi Gw\lambda} \right)^{1/3} \quad (4)$$

At the end of the stop-flow period in which the particle clouds reach equilibrium, flow is resumed and the particles are displaced downstream. The displacement velocity is characterized by the dimensionless retention ratio  $R$ , which is described by the equation

$$R = V/\langle v \rangle = V^0/V_r = 6\lambda[\coth(1/2\lambda) - 2\lambda] \quad (5)$$

This equation shows that  $R$  is given by the ratio of particle displacement velocity  $V$  to average carrier velocity  $\langle v \rangle$ , or equivalently to the ratio of channel void volume  $V_0$  to the retention volume  $V_r$ . Thus  $R$  is experimentally accessible because  $V_r$  is the measured volume required to displace a given particle size  $r$  through the channel. However, the equation also shows that  $R$  is related to  $\lambda$ , which is related to  $d$  through the previous equation. Thus a linkage is formed between particle diameter  $d$  and experimental retention volume  $V_r$ . It has been estimated that particle diameters accurate to 1-3% can be obtained by using this approach (2).

In practice, we use  $\lambda$  as an intermediate parameter in this calculation; a  $\lambda$  value can be obtained numerically from Equation 5 for each measurement of  $V_r$  and this value used to produce a particle diameter  $d$  from Equation 4.

We note that at high retention levels,  $R$  is given by the much simpler equation

$$R = 6\lambda \quad (6)$$

While the principal tool for particle characterization in sedimentation FFF is the foregoing equations applied to measured retention levels, additional particle information, particularly for narrow distributions, can be obtained through the measurement of band broadening.

Band broadening arises from three principal mechanisms, one of which depends on the mean velocity  $\langle v \rangle$  of the carrier and two of which are independent of  $\langle v \rangle$ . The latter two represent non-idealities in instrument and sample. The total variance of an eluting peak is the sum of variances contributed by each band-broadening mechanism. Expressed as plate height  $H$ , which is the total variance divided by column length  $L$  (12), the zone broadening is described by

$$H = \chi \frac{w^2}{D} \langle v \rangle + 81L \left( \frac{1}{R} \left( \frac{R^2}{36\lambda^2} + R - 1 \right) \right)^2 \left( \frac{\sigma_d}{d} \right)^2 + H_i \quad (7)$$

By refining column design, the instrumental band broadening  $H_i$  has been reduced to a level insignificant in comparison with the other terms of Equation 7. The nonequilibrium term, linear in carrier velocity  $\langle v \rangle$ , also depends on channel thickness  $w$  and inversely on particle diffusion coefficient  $D$ . The dependence of coefficient  $\chi$  on  $\lambda$  is well known, although the function is complex (14). Its limiting form is described by

$$\lim_{\lambda \rightarrow 0} \chi = 24\lambda^3 \quad (8)$$

The remaining (central) term on the right of Equation 7 is a polydispersity term. It accounts for the broadening which results from the actual fractionation of the different sized particles which make up the narrow sample. This term has a square dependence on the standard deviation in particle diameter  $\sigma_d$ .

The above equations may yield useful particle parameters. Thus both the standard deviation  $\sigma_d$  in particle diameter and diffusion coefficient  $D$  can be related to experimental  $H$  values. A procedure for obtaining particle information via this route will be detailed in our discussion of monodisperse particle populations.

### Monodisperse Particle Populations

Narrow particle fractions approaching a monodisperse distribution are particularly easy to treat and characterize when the above equations are applied to experimental data. Figure 2 shows an example of the elution profile (fractogram) obtained by running a mixture of four samples of "monodisperse" polystyrene latex beads. It is clear from the figure that a rather precise value of retention volume  $V_r$  can be identified with each bead size. With  $V_r$  known, it is easy to obtain  $R$  and  $\lambda$  from Equation 5 and thence particle diameter  $d$  from Equation 4. This operation, as noted, yields diameters accurate to approximately 1-3%.

As stated previously, additional information on the sample is obtainable from band broadening (plate height) measurements. If plate height is measured as a function of flow velocity at a fixed retention level, a linear relationship is obtained, as predicted by Equation 7. The slope of the line yields the diffusivity  $D$  of the sample, and the intercept provides the polydispersity  $\sigma_d$ . The  $D$  value translates into a value for the average particle diameter  $d$  via the Stokes-Einstein relationship

$$D = kT/3\pi\eta d \quad (9)$$

in which  $k$  is the Boltzmann constant,  $T$  the temperature, and  $\eta$  the viscosity of the carrier. Thus, a combination of retention and plate height measurements will, in theory, fully characterize a narrow sample of spherical particles, yielding particle diameter, polydispersity, and density, the latter by inserting  $d$  from Equation 9 into Equation 3 to obtain  $\Delta\rho$ . However, we note that parameters based on zone broadening measurements are presently less accurate than those based on retention measurements, so we seek additional information from retention.

Particle density can alternatively be evaluated from a set of retention measurements made in carriers of different density (15). Such density modifications are typically accomplished by successive additions of sucrose to the carrier. The observed retention values yield particle size and density through Equation 2. A rearrangement of this equation leads to a graphical procedure for size/density evaluation. The rearranged form is

$$\rho = \rho_s - \frac{6kT}{d^3\pi Gw} \cdot \frac{1}{\lambda} \quad (10)$$

Here,  $\Delta\rho$  from the original equation is explicitly expressed as  $\rho_s - \rho$ , the difference between the density  $\rho_s$  of the sample particle and the density  $\rho$  of the carrier. By plotting the reciprocal of the retention-derived  $\lambda$  against the density  $\rho$  of the carrier in which retention is observed, a line is obtained whose slope gives

the particle diameter and whose intercept yields its density. This method has been shown to yield accurate size and density values for monodisperse polystyrene latex spheres (15).

### Polydisperse Particle Populations

Most particulate samples of interest contain particles distributed over a broad size range. Sedimentation FFF sorts such polydisperse materials into nearly monodisperse populations. These are continuously eluted from the FFF channel beginning with the smallest particles and ending with the largest. A detector at the end of the channel monitors the particle content as a function of elution (retention) volume. A plot of detector response vs elution volume is shown in Figure 3. This plot is called a fractogram. The retention volume for each volume element, emerging at a specific value of  $V_r$ , can be converted to a value of retention parameter  $\lambda$  through Equation 5, which, in turn, can be used to calculate the particle diameter  $d$  of the fraction by means of Equation 4. Thus the theoretical rigor of sedimentation FFF makes it possible to assign a  $d$  value to each volume fraction. In the example shown in Figure 3, the assigned particle diameters calculated in this way are developed into a  $d$  scale paralleling the  $V_r$  scale. Note that the  $d$  scale is assigned purely by theory, requiring no calibration.

A fractogram with an auxiliary  $d$  scale like that shown in Figure 3 can be used directly to characterize polydisperse materials at a high level of resolution/detail. Small changes in particle populations, reflecting changes in environmental conditions or process control parameters, will be reflected immediately in the fractogram and can be distinguished by a comparison of fractograms. The particle diameter range over which any such change takes place can be directly identified from such a comparison. Using this approach, we have characterized diverse materials such as emulsions, protein particles, liposomes, and waterborne colloids.

The same general procedure applies to programmed sedimentation FFF. In programming, the field strength is reduced continuously during the run to condense broad particle distributions within a reasonable range of elution volumes. The general theory of programming (16) can be applied to construct a particle diameter scale for any fractogram obtained under arbitrary programming conditions. An example of programmed operation will be described by Kirkland et al. in another paper in this volume.

While the simple process of comparing fractograms with appended particle diameter scales will provide all the information needed in many particle characterization studies, the fractogram does not constitute a finished particle size distribution (PSD) curve. To obtain a quantitative PSD curve, corrections must be applied. The first correction, which we call a scale correction, is necessary because elution volume and particle diameter are not proportional to one another. Thus the particle content of a fixed volume of eluted sample will correspond to a different increment in  $d$  depending upon the point of collection. A simple correction factor, detailed elsewhere (3), can be applied to this scale problem.

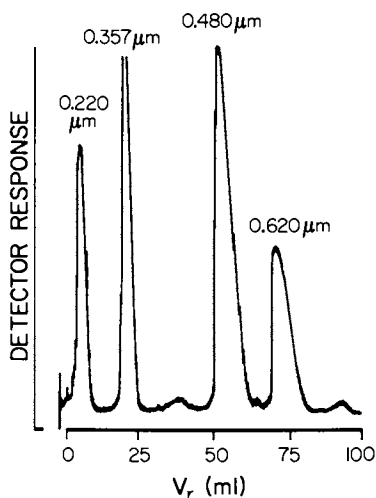


Figure 2. Fractionation of four samples of Dow polystyrene latex beads by sedimentation FFF. The nominal particle sizes are given in the figure. Flowrate = 12 ml/hr, channel thickness  $w = 0.0127$  cm, void volume  $V^0 = 2.0$  ml, and field strength  $G = 193.7$  gravities. Reproduced with permission from Ref. 20. Copyright 1980 John Wiley.

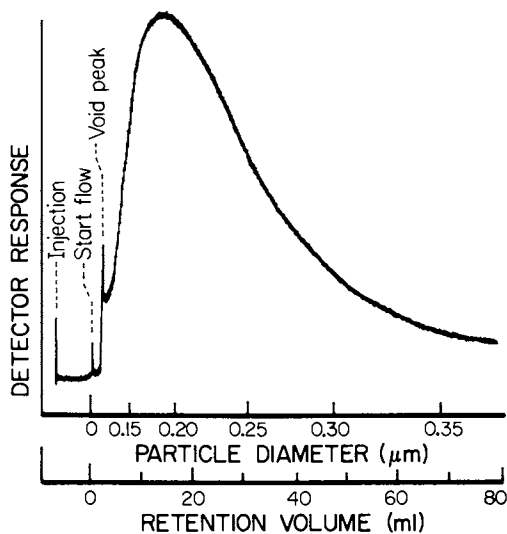


Figure 3. Fractogram of PVC latex with superimposed particle diameter scale. Field = 82.6 g, flow = 226 ml/hr,  $V^0 = 2.0$  ml, sample = 40  $\mu$ l of 6% PVC. Reproduced with permission from Ref. 20. Copyright 1980 John Wiley.

A second correction may be needed for distortions in the detector response. This is particularly true of the UV monitors commonly used for particle detection. While the signal for any given volume element is proportional to the particle content of that volume, the signal is sensitive to particle size and thus varies as we pass from one particle diameter to another. The UV monitor is essentially a turbidimetric detector whose signal increases significantly with particle diameter. Corrections based on the Mie theory of light scattering have been developed. However, a more suitable approach has been presented by Oppenheimer (17), who has used a special light scattering detector with a signal no longer dependent on particle size. With this detector, a second correction factor is no longer necessary.

While either the fully corrected PSD or the noncorrected PSD represented by the fractogram will provide all of the information needed by most users, sedimentation FFF is sufficiently versatile to provide more information if required. A useful approach is the physical collection of small fractions of size-sorted material. The fractions can then be subjected to a broad variety of tests using microscopic, chemical, or subsequent FFF procedures.

We have shown that fractions collected from broad particle distributions can be reinjected into the sedimentation FFF device for a second run (18). The emerging peaks are relatively narrow, reflecting their small particle size range. Quite obviously, a reinjected fraction run in a carrier of a different density will emerge at a different volume because of the effect of  $\Delta\rho$  on retention parameter  $\lambda$  (see Equation 3). The shift in retention volume (see next section) can be used to calculate the density of the particulate material exactly as outlined for monodisperse populations.

An alternate approach for determining particle density involves fraction collection followed by the application of quasi-elastic light scattering (QEL) to the fraction (19). The QEL technique is particularly effective in providing a mean particle diameter  $d$  for narrow particle distributions. With this  $d$  and the  $\lambda$  obtained from  $V_r$  (the volume at which the fraction was collected),  $\Delta\rho$  can be calculated directly from Equation 3. Addition of the known carrier density to  $\Delta\rho$  then yields the particle density  $\rho_p$ . Density values accurate to within a few percent have been obtained in a preliminary application of this technique (19).

### Complex Colloids

Earlier we described complex colloids as those having particles of variable chemical composition. Most colloids of biological and environmental origin and some of industrial origin are complex. These colloids represent a severe challenge for colloid characterization methods.

To obtain any depth of knowledge about complex colloids, information of two types must be obtained. First, particle size information must be acquired. Second, for any given particle size, information on the distribution of chemical components or on the distribution of some important property (like density) that

reflects chemical composition must be collected. The problem is actually a two-dimensional one, requiring far more information than is necessary to characterize chemically homogeneous colloids.

The versatility of FFF, combined with its facility for providing narrow fractions, makes this technique a prime candidate for the study of complex colloids. Work along this line has only recently started; consequently, we will provide only an outline sufficient to demonstrate applicability to complex colloids.

We return first to the process of fraction collection and note that subsequent testing often yields the second dimension of information. Interpretation is somewhat complicated by the fact that any single fraction will contain a variety of particles having different densities and different sizes. However, for a given fraction (given  $V_e$  and  $\lambda$  values), diameter  $d$  and density  $\Delta\rho$  are connected by Equation 3. Therefore, any subsequent test capable of yielding a second relationship involving  $d$  and/or  $\Delta\rho$  will yield information on both quantities. For example, if electron microscopy is used to determine the size distribution of particles within the fraction, then Equation 3 can be used to obtain a density distribution.

Similarly, collected fractions can be reinjected into the sedimentation FFF system operated with a different carrier density. The degree to which the retention volume for any particle type is shifted by this operation will depend upon the density of the particle. In theory, the shape of the fractogram following fraction reinjection will yield a density distribution curve for the fraction.

If the same measurements are made for each of several fractions collected along the elution volume axis, the density distribution for each fraction will be calculable. In this way, we envision the possibility of building up a true two-dimensional representation to characterize the particle mixture. In this representation, the particle concentration would be displayed as a function of particle diameter along one axis and particle density along another axis.

Considerable effort would clearly be needed to characterize complex colloids in such a complete way. In many cases, it is likely that one would only need to focus on a certain limited region of the size-density matrix, thus considerably reducing the experimental labor. In addition, other techniques (such as chemical analysis) might be brought into play to simplify the experiments and, at the same time, extend the information base. We are also examining an approach to the two-dimensional (size-density) characterization of complex colloids without the requirement for fraction collection.

The practicality of reinjection methodology for probing complex colloidal mixtures has only recently been demonstrated. In this experiment, a synthetic mixture of a polydisperse PVC colloid and a rather narrow polystyrene sample were subjected to fractionation, yielding the fractogram appearing at the top of Figure 4. A fraction containing both kinds of particles was then collected over the volume range indicated in the figure. This fraction was concentrated and then reinjected into a sedimentation FFF system whose carrier density was increased to approximately 1.03 g/ml by the addition of sucrose to the aqueous buffer. Because of the lower density (1.05 g/ml) and larger size of the polystyrene particles in the fraction, the buoyancy forces increase much more rapidly for these particles than for the denser (1.40 g/ml) PVC particles.

In Particle Size Distribution; Provder, T.;



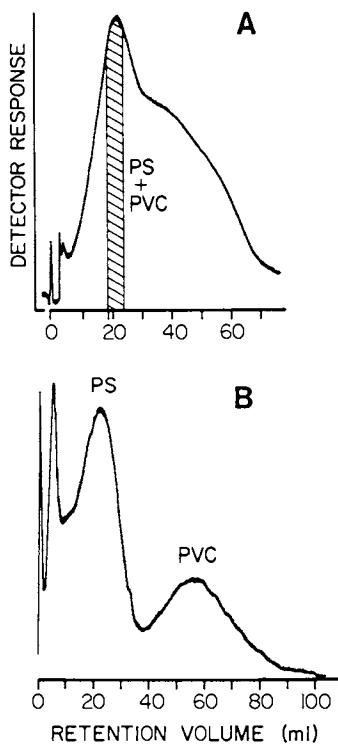


Figure 4. Cross-hatched area in fractogram A denotes a 5 ml fraction collected from a synthetic mix of polystyrene (PS) and polyvinyl chloride (PVC) run at 43.4 g with carrier density  $\rho = 1.00$  g/ml. Same fraction is rerun (B) at 111 g in carrier of density  $\rho = 1.03$  g/ml.

Consequently, the polystyrene peak is displaced to a much lower retention volume and is thus shifted away from the PVC peak, which is only slightly displaced. Consequently, these two chemical forms, although originally mixed, can be separated and independently characterized.

While many experimental challenges and data reduction problems must be dealt with in order to extend FFF methodology to important complex colloids, no fundamental barrier appears to exist which would block progress in this direction.

### Acknowledgments

This work was supported by contract number DE-AC02-79EV10244 from the Department of Energy.

### Literature Cited

1. Giddings, J.C.; Yang, F.J.F.; Myers, M.N. Anal. Chem. 1974, 46, 1917.
2. Giddings, J.C.; Karaiskakis, G.; Caldwell, K.D.; Myers, M.N. J. Colloid Interface Sci. 1983, 92, 66.
3. Yang, F.-S.; Caldwell, K.D.; Giddings, J.C. J. Colloid Interface Sci. 1983, 92, 81.
4. Yang, F.-S.; Caldwell, K.D.; Myers, M.N.; Giddings, J.C. J. Colloid Interface Sci. 1983, 93, 115.
5. Caldwell, K.D. In "Modern Methods of Particle Size Analysis"; Barth, H.G., Ed.; Wiley-Interscience: New York, 1984; Chapter 7.
6. Kirkland, J.J.; Rementer, S.W.; Yau, W.W. Anal. Chem. 1981, 53, 1730.
7. Commission on Analytical Nomenclature, Analytical Chemistry Division, International Union of Pure and Applied Chemistry, 1974, 37, 4.
8. Peterson, R.E., II; Myers, M.N.; Giddings, J.C. Sep. Sci. Technol. 1984, 19, 307.
9. Barth, H.G.; Sun, S.-T. Anal. Chem. 1985, 57, 151R.
10. Giddings, J.C. Sep. Sci. 1973, 8, 567.
11. Myers, M.N.; Giddings, J.C. Anal. Chem. 1982, 54, 2284.
12. Giddings, J.C. Pure & Appl. Chem. 1979, 51, 1459.
13. Karaiskakis, G.; Myers, M.N.; Caldwell, K.D.; Giddings, J.C. Anal. Chem. 1981, 53, 1314.
14. Giddings, J.C.; Yoon, Y.H.; Caldwell, K.D.; Myers, M.N.; Hovingh, M.E. Sep. Sci. 1975, 10, 447.
15. Giddings, J.C.; Karaiskakis, G.; Caldwell, K.D. Sep. Sci. Technol. 1981, 16, 607.
16. Yang, F.J.F.; Myers, M.N.; Giddings, J.C. Anal. Chem. 1974, 46, 1924.
17. Oppenheimer, L.E.; Mourey, T.H. J. Chromatogr. 1984, 298, 217.
18. Giddings, J.C.; Yang, F.-S. J. Colloid Interface Sci. 1985, 105, 55.
19. Caldwell, K.D.; Jones, H.K.; Giddings, J.C. Colloids and Surfaces, submitted.
20. Giddings, J.C.; Myers, M. N.; Caldwell, K.D.; Fisher, S.R. In "Methods of Biochemical Analysis"; Glick, David, Ed.; John Wiley & Sons, Inc.: New York, 1980; Vol. 26.

RECEIVED June 27, 1986

# Chapter 16

## Comparative Particle Size Analysis

M. E. Koehler and Theodore Provder

The Glidden Company, Dwight P. Joyce Research Center, Strongsville, OH 44136

A series of monodisperse PMMA latexes was synthesized and characterized with respect to refractive index, percent solids, and solution density. The particle size of each latex was analyzed by Disc Centrifuge Photosedimentometry (DCP), Sedimentation Field Flow Fractionation (SFFF), Hydrodynamic Chromatography (HDC), Quasielastic Light Scattering (QELS), Transmission Electron Microscopy (TEM), and turbidity. A comparison of the apparent particle size averages of the latexes as measured by each method showed that for small, more monodisperse latexes the various methods agree more closely than for larger diameter samples having higher polydispersities. The relative ordering of the apparent sizes by method is consistent. The light scattering methods gave higher apparent particle sizes, TEM the lowest number, while DCP and SFFF were in relatively good agreement in the center of the range. This is explained in terms of the assumptions made and the physical parameters measured by each method.

A variety of different instrumental methods are available for the measurement of the size and size distribution of particulates. These instruments utilize different physical phenomena as a means of assessing the particle size. Sedimentation methods measure a 'hydrodynamic' radius and require a knowledge of the density of the particle as well as the density and viscosity of the suspending fluid. Dynamic Light scattering methods measure the diffusion coefficient and tend to weight the measurement to larger particles and agglomerates. Hydrodynamic Chromatography (HDC) is a chromatographic method which separates particles on the basis of their diameter by their differential retention in the flow streams through the interstitial channels of a packed column. Transmission Electron Microscopy (TEM) allows the measurement of the particle

0097-6156/87/0332-0231\$06.00/0  
© 1987 American Chemical Society

size of hard particles. However, TEM is susceptible to distortion of soft particles, shrinkage of particles in the electron beam, and cannot readily ascertain if agglomeration has occurred. The turbidity method measures the apparent absorbance of a dilute suspension of particles and the apparent diameter of the scattering particles is calculated using classical light scattering theory (1).

The particles most frequently used as size standards are commercially obtained polystyrene latex microspheres. For sedimentation methods where knowledge of the density difference between the particle and the suspending fluid (water) is needed, the use of polystyrene as a standard material can be a serious problem due to the small magnitude of this density difference. For Sedimentation Field Flow Fractionation (SFFF), the apparent diameter is proportional to the cube root of the inverse of the density difference (2). For Disc Centrifuge Photosedimentometry (DCP) the apparent diameter is proportional to the square root of the inverse of the density difference,  $\Delta\rho$  (3). This is illustrated in Figure 1 which shows the relative error in apparent particle size as a function of the error in the assumed density of polystyrene latex in water for DCP and for SFFF. For example, from Figure 1 it can be seen that a 357 nm diameter latex particle with a nominal density of 1.057 g/cm<sup>3</sup> having an error of -20% in (-0.01 g/cm<sup>3</sup>) would result in an error of +12.4% in the DCP particle size diameter (+44 nm). The corresponding error in SFFF particle size diameter is +7.9% (+28 nm).

In order to make a better evaluation of the relative and absolute performance of various instruments, it was necessary to obtain well characterized, monodisperse latexes having a density greater than that of polystyrene. Polymethylmethacrylate<sub>3</sub> (PMMA) latex with a polymer density of approximately 1.21 gm/cm<sup>3</sup> was selected for this purpose.

A series of monodisperse PMMA latexes was synthesized and characterized with respect to refractive index, percent solids, and solution density. The particle size of each latex was analyzed by several different instrumental methods. The methods used include DCP, SFFF, HDC, Quasielastic Light Scattering (QELS), TEM, and turbidity.

### Experimental Methods

**Synthesis.** A series of latexes was prepared by semicontinuous emulsion polymerization of methyl methacrylate. A dialkyl ester of sodium sulfosuccinic acid surfactant yielded the narrow particle size distribution required. An ammonium persulfate/sodium metabisulfate/ferrous sulfate initiator system was used. The initiator was fed over the polymerization time, allowing better control of the polymerization rate. For the smaller size latexes (200 to 450 nm), a seed latex was prepared in situ by polymerizing 10% of the monomer in the presence of the ammonium persulfate. Particle size was adjusted by varying the level of surfactant during the heel reaction. As the exotherm of this reaction subsided, the monomer and the sodium metabisulfate/ferrous sulfate feeds were started and continued over approximately one hour. The

maximum particle size achievable by this method was 440 nm. To achieve larger particle sizes a latex of smaller size was used as the seed. Ammonium persulfate was then added at polymerization temperature, 80°C, and the additional level of monomer required to achieve the desired particle size was fed over 1.5 hours.

Analysis. The percent solids of each of the latexes was measured using a DuPont Model 950 Thermogravimetric Analyzer. Solution densities were determined using a Parr Mettler Model DMA-60 precision densitometer. The particle density was calculated from the solution density and the percent solids.

The DCP used was a variable speed unit developed in our own laboratory (3-6). (A commercial version of this instrument is now available as the Brookhaven DCP-1000 Particle Size Analyzer from Brookhaven Instruments Corporation, Ronkonkoma New York. SFFF measurements were performed using a prototype instrument provided by DuPont (7). (A commercial version of this instrument is now available as the DuPont SFFF-1000 Particle Size Analyzer.) HDC measurements were made by Micromeritics on their Model HDC-5600 FlowSizer instrument. QELS measurements were made on an instrument constructed by Professor Alex Jamieson at Case Western Reserve University (8). TEM measurements were made by the Pigments Division of SCM Corporation, Adrian Joyce Plant, Baltimore, Maryland. Turbidity measurements were made using a Bausch and Lomb Model Spectronic-20 spectrometer.

### Results

A comparison of the apparent particle size averages of the PMMA latexes as measured by each method is shown in Figure 2 (number averages, DN) and Figure 3 (weight averages, DW). These data, along with the particle density, the refractive index, the percent solids, and the polydispersity, (DN/DW), calculated as the ratio of the weight average particle size to the number average particle size, also are shown in Table 1.

### Discussion and Conclusions

Based on the TEM data, it appears that the small latexes are more monodisperse, and it can be seen that the various method agree more closely for those samples. In all cases however, the relative ordering of the apparent sizes by method is consistent. That is, the light scattering methods give higher apparent particle sizes, TEM gives the lower number, and the DCP and SFFF are in relatively good agreement in the center of the range.

Figures 4 and 5 show plots of the apparent number and weight averages determined by SFFF plotted against the corresponding data from DCP measurements. For perfect agreement, the data would lie along a line with slope of one with an intercept of zero. The deviation of these plots from linearity at larger particle sizes is probably due to a steric effect which occurs in SFFF when the particle diameter becomes a significant fraction of the channel thickness (2). The particle size limit above which the SFFF channel used in this work is expected to exhibit this effect is

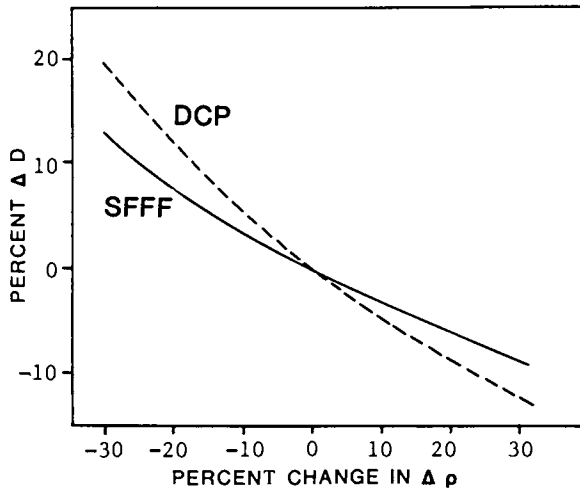


Figure 1. Relative Error in Particle Diameter vs. Relative Error in Density Difference - Polystyrene Latex in Water:  $d = 357 \text{ nm}$ ,  $\rho = 1.057 \text{ g/cm}^3$ .

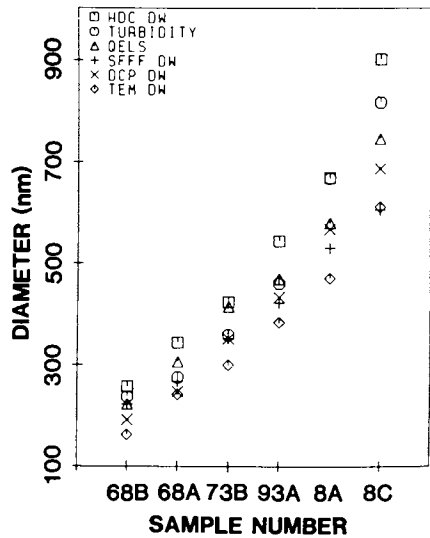
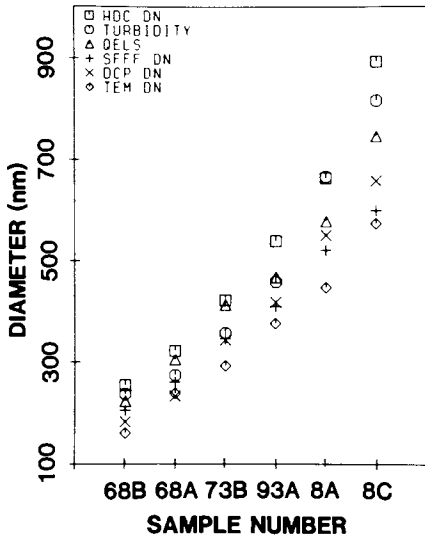


Figure 2 (left). Apparent Number Average, Turbidity, QELS Particle Sizes of PMMA Latexes.

Figure 3 (right). Apparent Weight Average, Turbidity, QELS Particle Sizes of PMMA Latexes.

TABLE 1  
PARTICLE SIZE AVERAGES FOR PMMA LATEXES

## DIAMETERS IN NANOMETERS

| SAMPLE ID | TEM |          | DCP |          | SFFF |          | HDC |          | TURBIDITY | QELS | % SOLIDS | SOLUTION DENSITY(g/cc) |
|-----------|-----|----------|-----|----------|------|----------|-----|----------|-----------|------|----------|------------------------|
|           | DN  | DW/DN    | DN  | DW/DN    | DN   | DW/DN    | DN  | DW/DN    |           |      |          |                        |
| 68B       | 160 | 162 1.01 | 182 | 192 1.05 | 205  | 222 1.08 | 255 | 257 1.01 | 237       | 223  | 24.56    | 1.221                  |
| 68A       | 239 | 241 1.01 | 233 | 247 1.06 | 261  | 267 1.02 | 322 | 342 1.06 | 275       | 305  | 23.05    | 1.213                  |
| 73B       | 293 | 298 1.02 | 344 | 351 1.02 | 346  | 350 1.01 | 422 | 423 1.00 | 357       | 413  | 22.59    | 1.218                  |
| 93A       | 377 | 383 1.02 | 418 | 432 1.03 | 410  | 421 1.03 | 540 | 542 1.00 | 459       | 468  | 26.20    | 1.211                  |
| 8A        | 448 | 469 1.05 | 550 | 566 1.03 | 521  | 529 1.02 | 664 | 668 1.01 | 667       | 578  | 26.26    | 1.217                  |
| 8C        | 574 | 611 1.06 | 658 | 686 1.04 | 600  | 605 1.01 | 893 | 901 1.01 | 817       | 746  | 9.88     | 1.221                  |

Average Particle Density = 1.215

Average Refractive Index = 1.48

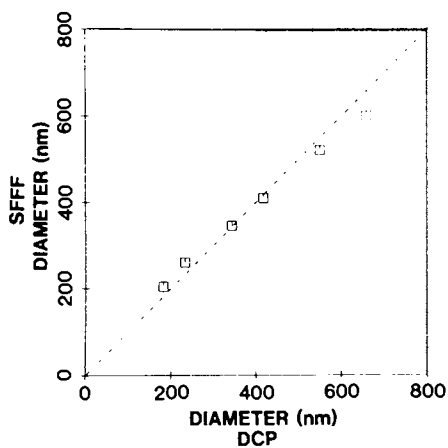


Figure 4. Apparent Number Average Particle Sizes of PMMA Latexes - SFFF vs. DCP.

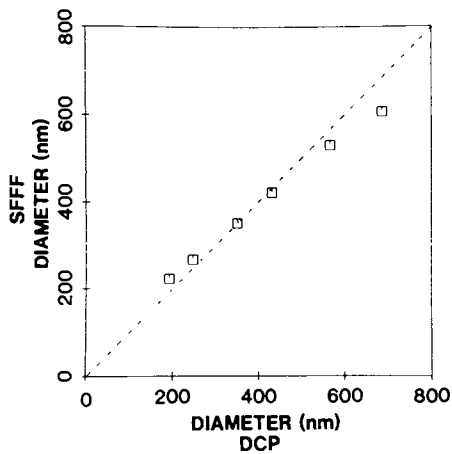


Figure 5. Apparent Weight Average Particle Sizes of PMMA Latexes - SFFF vs. DCP.



approximately 0.5  $\mu\text{m}$ . SFFF and DCP were found to be highly complementary methods. A higher particle size range is accessible to DCP and a lower range is accessible to SFFF. The methods yielded similar results in the region over which their ranges overlap. Both methods are capable of providing detailed distribution information over their respective ranges.

Figure 6 shows a comparison of the particle size distribution curves for samples 68-B and 8-A obtained by SEM, SFFF, and DCP, those methods directly yielding distribution information. For sample 68-B, based on the SEM number distribution, the sample is unimodal with a small shoulder on the large diameter side. The DCP number distribution curve shows the same characteristics. The SFFF number distribution curve appears to be broader and the small population of larger particles is not discernable. The shoulder on the smaller diameter side in the SFFF distribution appears to be an instrument artifact and occurred in the distributions of several samples.

For sample 8-A, shown in the same figure, the SEM number distribution indicates a broader distribution with a shoulder on the large particle size side and a tail with a hint of one or more secondary peaks on the small particle size side. The DCP number distribution for this sample shows asymmetry and a small shoulder on the large particle size side qualitatively similar to the SEM curve. On the small particle size side, the DCP shows a tail and a small peak, again qualitatively similar to the SEM curve. The SFFF number distribution curve for this sample does not show a shoulder on the large particle size side. While there is a shoulder on the small particle size side, the problem with artifactual peaks in this region with the SFFF instrument used makes it difficult to say if the tail and shoulder observed are real.

The average diameters obtained by HDC are consistently high. This may be due to a combination of a small calibration error and the relatively coarse (10 percent) spacing of size classifications used in the HDC quantification by Micromeritics.

The relative ordering of apparent particle sizes is not too surprising when one considers the assumptions made and the physical parameters measured by each method. What may be surprising is the large spread of values obtained for the slightly less monodisperse latexes. This demonstrates the need for caution when comparing particle size data obtained by different instrumental methods, especially for samples having broad particle size distributions. For accurate comparisons in these cases it is preferable to have both the size averages and the distribution curves.

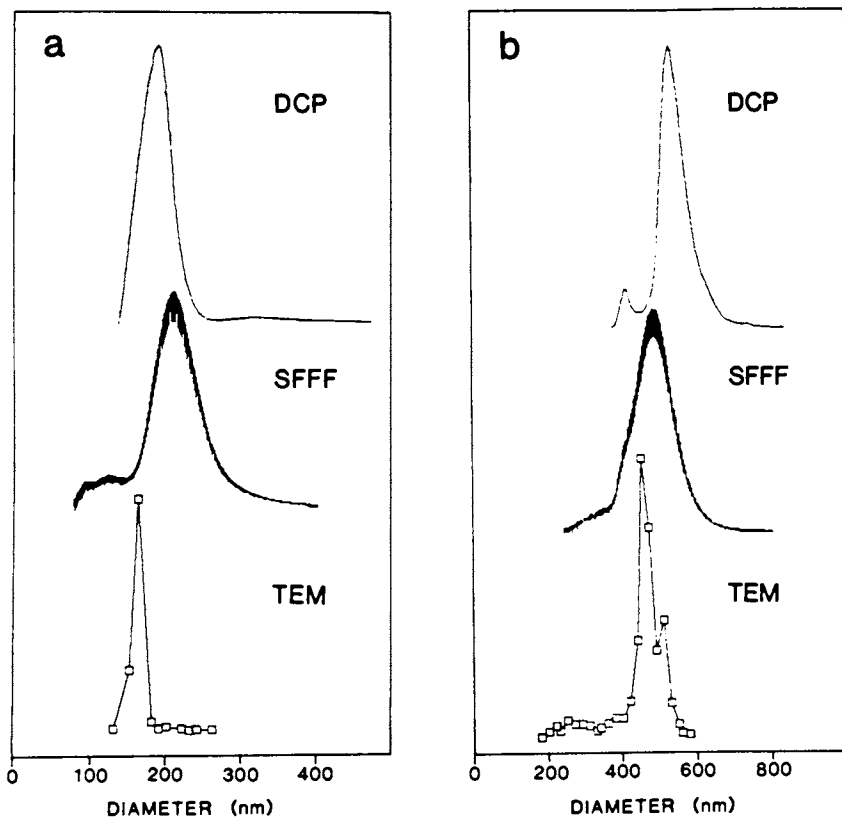


Figure 6. Comparison of Particle Number Distribution Curves by DCP, SFFF and TEM a)Sample 68-B b)Sample 8-A

Acknowledgments

The authors wish to acknowledge Sharon Kaffen for her synthesis of the PMMA latexes, Farrokh Malihi for QELS and turbidity measurements, C. M. Neag for percent solids analysis by thermogravimetry and C. B. Rakowski of SCM Pigments for the TEM measurements.

Literature Cited

1. Kerker, M. "The Scattering of Light and Other Electromagnetic Radiation"; New York, 1969; Ch. 7.32.
2. Caldwell, K. C. "Field-Flow Fractionation of Particles", In "Modern Methods of Particle Size Analysis", Chemical Analysis, Vol. 73; Barth, H. G., Ed.; Wiley: New York, 1984; Chapter 7.
3. Koehler, M. E.; Zander, R. A.; Provder, T.; Niemann, T. F. "An Improved Disc Centrifuge Photosedimentometer and Data System", This Volume.
4. Koehler, M. E.; Provder, T.; Zander, R. A. U. S. Patent 4 311 039, 1982.
5. Holsworth, R. M.; Provder, T. U. S. Patent 4 478 073, 1985.
6. Provder, T.; Holsworth, R. M. Div. of Org. Coatings and Plastics Chem. Preprint 1976, 36, 150.
7. Blaine, R. "New Applications and Techniques: Sedimentation Field Flow Fractionation", The TA Hotline, DuPont Company, Summer 1986, 5.
8. Malihi, F. B.; Provder, T.; Koehler, M. E. Journal of Coatings Technology, 1983, 55, 41-48.

RECEIVED October 6, 1986

## Chapter 17

# Measuring Particle Size Distribution of Latex Particles in the Submicrometer Range Using Size-Exclusion Chromatography and Turbidity Spectra

T. Kourti, A. Penlidis, J. F. MacGregor, and A. E. Hamielec

Department of Chemical Engineering, McMaster Institute for Polymer Production Technology, McMaster University, Hamilton, Ontario L8S 4L7, Canada

Turbidity spectra and size exclusion chromatography (SEC) are two techniques which could be used for the on- and off-line monitoring of polymer particle size during the polymerization. An experimental evaluation of the two techniques is reported herein and it is shown that they satisfactorily follow the change of the particle size during the reaction. Information from SEC analysis is exploited to experimentally evaluate the turbidity spectra technique and investigate its potential to be used as an on-line measurement of particle size for latex reactor control.

Particle number and particle size distribution (PSD) are key parameters in emulsion polymerization processes because they not only affect polymerization rate and polymer properties during the reaction, but they also determine application properties of the final latex such as stability, viscosity, film forming, and others. Efforts to manipulate these two important parameters during polymerization should precede any attempt to control latex reactor performance and therefore there is a need for on-line measurement of particle number and size distribution. Various techniques have been developed for the determination of PSD's of colloidal dispersions but these are often time consuming and unsuitable for on-line applications. Light scattering techniques are fast, simple, reproducible and thus seem to be promising for this purpose(1-2); chromatographic techniques can be used complementary for off-line measurements. The measurement techniques employed were turbidity spectra and size exclusion chromatography. The scope of this study is to investigate the ability of these two techniques to monitor latex particle growth during emulsion polymerization of vinyl acetate and to evaluate the potential of turbidity spectra to be used for on-line particle size measurements.

### TURBIDITY SPECTRA

#### Theoretical Background

The experimental simplicity of turbidity spectra is the main reason why the technique has received so much attention in the past years (1-5). Turbidity gives a measure of the attenuation of a beam of light traversing a dispersion of non-absorbing spheres:

0097-6156/87/0332-0242\$06.00/0  
© 1987 American Chemical Society

$$\tau = \frac{1}{\ell} \ln \frac{I_0}{I} \quad (1)$$

where  $I_0$  and  $I$  represent intensity of the incident and the emerging (from the scattering solution) beam, respectively, and  $\ell$  is the length of the optical path.

For a monodisperse suspension with  $N$  non-absorbing spherical particles per  $\text{cm}^3$ , in absence of multiple scattering, the turbidity,  $\tau$ , is given by:

$$\tau = N \frac{\pi D^2}{4} K \left( \frac{D}{\lambda_m}, \frac{n_p}{n_m} \right) \quad (2)$$

$K(D/\lambda_m, n_p/n_m)$ , the extinction coefficient, is in the general case a complicated function of the particle diameter  $D$ , the wavelength in the medium  $\lambda_m$ , and the refractive indices  $n_p$  and  $n_m$  of the particles and the medium, respectively.  $K$  can be calculated from the general Mie theory (3). For a polydisperse suspension:

$$\tau = N \int_0^{\infty} \frac{\pi D^2}{4} K \left( \frac{D}{\lambda_m}, \frac{n_p}{n_m} \right) f(D) dD \quad (3)$$

where  $f(D)$  is the suspension's normalized particle size distribution.

The concentration  $c$  of polymeric solids in the latex ( $\text{gr}/\text{cm}^3$  latex) is subsequently given by:

$$c = N \cdot \rho \int_0^{\infty} \frac{\pi D^3}{6} f(D) dD \quad (4)$$

where  $\rho$  is the particle density in  $\text{gr}/\text{cm}^3$ .

Combination of equations (3) and (4) gives a ratio, the specific turbidity, independent of  $N$ , as:

$$\frac{\tau}{c} = \frac{3}{2\rho} \frac{\int_0^{\infty} D^2 K \left( \frac{D}{\lambda_m}, \frac{n_p}{n_m} \right) f(D) dD}{\int_0^{\infty} D^3 f(D) dD} \quad (5)$$

It is evident from the above equation that for a known size distributional form,  $(\tau/c)$  is a function of the refractive index and density of the particles, the wavelength of the incident light and the parameters describing the particle size distribution.

Therefore, in principle, the parameters of the particle size distribution can be estimated from specific turbidity measurements at different wavelengths. This is not true, however, in the Rayleigh regime (i.e. small particles,  $(D/\lambda_m)$  less than 0.1). In this case, the extinction coefficient is proportional to  $(D/\lambda_m)^4$  and

$$\frac{\tau}{c} = L \frac{\int_0^{\infty} D^6 f(D) dD}{\int_0^{\infty} D^3 f(D) dD} = L \bar{D}_t^3 \quad (6)$$

where  $\bar{D}_t$  is a "turbidity" average particle diameter and  $L = 4\pi^4 \rho^{-1} \lambda_m^{-4} (m^2 - 1/m^2 + 2)^2$ ;  $m = (n_p/n_m)$ . It is clear from equation (6) that use of different wavelengths will not

provide additional information; hence, only a "turbidity" average diameter can be determined in the Rayleigh regime.

### Experimental

Poly(vinyl acetate) (PVAc) latexes produced by batch and continuous emulsion polymerization were used in this study. Details for the apparatus and the polymerization procedure can be found in Penlidis et al. (6,12,13). Samples taken during the reaction were subsequently analyzed to follow conversion- and particle growth-time histories. The batch experimental runs were designed to yield similar conversion-time histories but different particle sizes. Conversion was measured both off-line, by gravimetric analysis, and on-line using an on-line densitometer (a U-tube DPR-YWE model with a Y-mode oscillator with a PTE-98 excitation cell and a DPR-2000 electronic board by Anton Paar, Austria). A number of runs were repeated to check for reproducibility of the results. Four batch runs are described in Table I below and their conversion histories are plotted in Figure 1.

Table I. Classification of Batch Runs

| Run #                     | Emulsifier Level | Expected Particle Diameter |
|---------------------------|------------------|----------------------------|
| B7                        | low              | large                      |
| B10-B11<br>(replications) | medium           | medium                     |
| B8                        | high             | small                      |

A Bausch and Lomb Spectronic-20 spectrophotometer (and occasionally, a Hewlett-Packard 8450 A) was employed for the turbidity measurements (cell length 1.165 cm, bandwidth of 20 nm, wavelength from 380 to 580 nm). For the turbidity measurements, the samples were diluted with water saturated with emulsifier. The same degree of dilution was used for all the samples of the batch runs. A large number of measurements were repeated to check for reproducibility.

### Discussion of Turbidity Results

Specific turbidity histories for runs B7, B10 and B11 are shown in Figure 2. It is obvious that the results are consistent; the reproducibility obtained in runs B10 and B11 is clearly shown, while it is evident that the latex particles formed in run B7 are larger, as expected.

Specific turbidity histories are also plotted vs. dimensionless time for a continuous emulsion polymerization run: the samples were withdrawn from the second reactor of a continuous train where the first reactor is a small seeding reactor. Part A of Figure 3 shows the particle size behaviour during start up; all monomer, water, initiator and soap feedrates were kept constant until the process reached a steady state. In part B, the soap concentration in the seed reactor was increased; a decrease in the particle size was expected and it is clearly shown from the specific turbidity measurements.

Hopefully, it has become evident that specific turbidity gives consistent and reproducible qualitative results. Two approaches have been used to translate the specific turbidity measurements from the previously mentioned experiments into latex particle size:

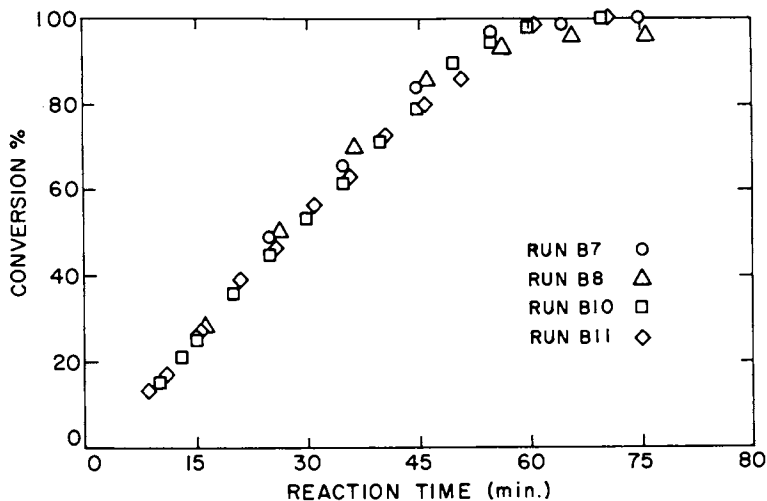


Figure 1. Conversion histories of the batch vinyl acetate emulsion polymerizations (similar recipes; only the emulsifier concentration is different).

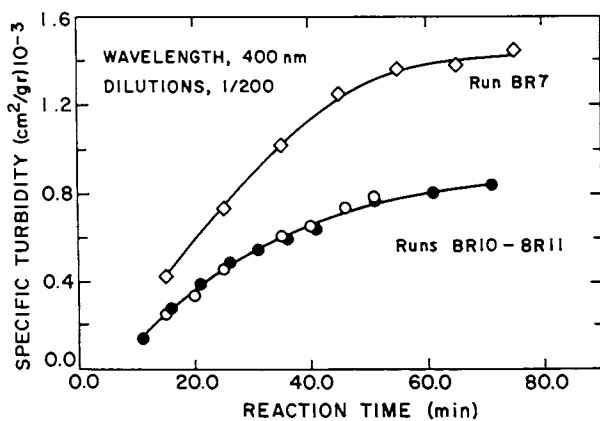


Figure 2. Specific turbidity behavior for three batch runs; runs B10-B11 are replications.

- (a) An approximate (apparent) diameter,  $\bar{D}_{ap}$ , was determined. This  $\bar{D}_{ap}$  corresponds to a monodisperse latex that would have given the same specific turbidity readings as the ones obtained and it is usually close to some average of the PSD (4,7,18).
- (b) Under the frequently valid in practice assumption that the latex PSD is well represented by the logarithmic normal distribution(2,18)

$$f(D) = \frac{1}{\sigma D (2\pi)^{1/2}} \exp(-(\ell_n D - \ell_n \bar{D})^2 / 2\sigma^2), \quad (7)$$

the parameters  $\bar{D}$  and  $\sigma$  of the distribution were determined by a non-linear least squares parameter estimation technique based on Marquandt's compromise procedure. The number and weight average diameters of the latex PSD were then calculated from

$$\begin{aligned} \bar{D}_N &= \bar{D} \exp(\sigma^2/2) \\ \bar{D}_w &= \bar{D} \exp(3.5 \sigma^2) \end{aligned} \quad (8)$$

Figure 4 shows contours of constant sum of squares in the space of the parameters  $\bar{D}$  and  $\sigma$ , for a set of specific turbidity measurements, from a batch run. The 95% approximate joint confidence region estimated as:

$$S(\sigma, \bar{D})_{0.95} = S(\sigma, \bar{D})_{\min} \left( 1 + \frac{p}{n-p} F_{0.05}(p, n-p) \right) \quad (9)$$

corresponds to a sum of squares equal to 0.25.  $S(\sigma, \bar{D})_{\min}$  is the sum of squares corresponding to the solution obtained by the search routine,  $p$  is the number of parameters that were estimated ( $p = 2$ ),  $n$  is the number of specific turbidity measurements ( $n = 6$ ),  $F_{0.05}(v_1, v_2)$  gives the upper 5% of an F-distribution with  $v_1, v_2$  degrees of freedom. A high negative correlation between  $\bar{D}$  and  $\sigma$  is evident. It is clear that a whole line of almost "equally good" pairs of estimates exists. The distributions which correspond to some of these "alternative" solutions (denoted by  $x$  in Figure 4) are plotted in Figure 5.

Although these results are not representative of batch reactor operation, where one would expect almost monodispersed latexes, and regardless of the fact that the distribution is changing as one moves along the confidence region, it was observed, however, that the estimated weight average diameter of these distributions was not affected by this shift. Furthermore, its numerical value remained close to that of  $\bar{D}_{ap}$  calculated in (a) under the monodisperse assumption, as shown in Figure 5 and Table II. Similar results were also observed (7) for poly(vinyl acetate) latexes with larger particles; all the "alternative" ( $\bar{D}, \sigma$ ) solutions in the elongated confidence region correspond to distributions with a constant weight average diameter which is numerically very close to the apparent diameter of the suspension, obtained under the monodisperse assumption.

The obtained weight average diameters can reasonably well follow the progress of the reaction as can be seen from Figure 6, where experimentally estimated weight average diameters are plotted with those theoretically predicted by a mathematical model for the batch emulsion polymerization of vinyl acetate.(6)

From the above discussion it has hopefully become clear that at the lower sub-micron range, for poly(vinyl acetate) latexes, specific turbidity measurements can provide a weight average particle diameter which is reasonably close to the apparent diameter resulting under the monodisperse assumption. These results were further verified with simulation studies; it was shown (7) that the maximum error introduced by assigning the  $\bar{D}_{ap}$  value to  $\bar{D}_w$  was ~4% for  $\bar{D}_{ap}$  values up to 4000 Å and polydispersities up to 1.5. Hence, when low polydispersity is expected, one might have fast, on-line particle size



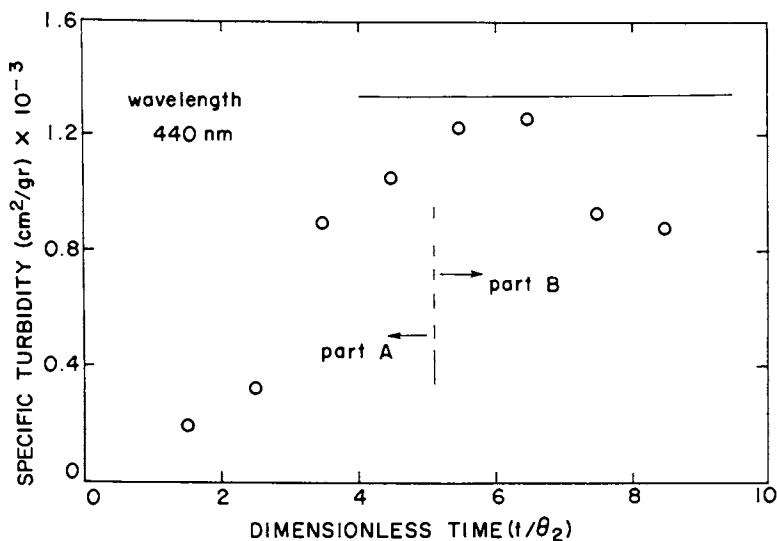


Figure 3. Specific turbidity measurements for the continuous run ( $\theta_2$  = residence time in the second reactor of the continuous train).

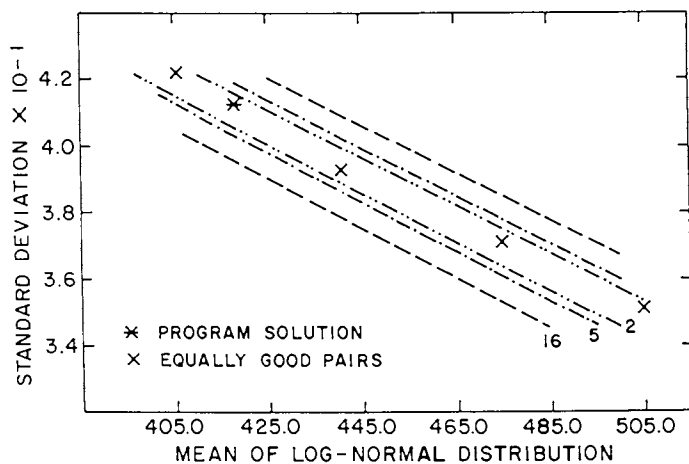


Figure 4. Contours of constant sum of squares ( $SS=16, 5, 2$ ) and possible, "equally good", alternative ( $\bar{D}, \sigma$ ) solutions.

American Chemical Society  
Library

1155 16th St., N.W.

Washington, D.C. 20036

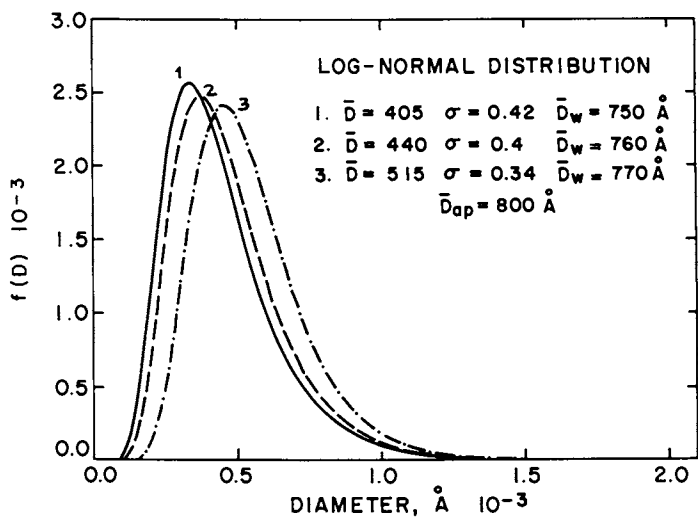


Figure 5. Particle size distributions corresponding to some alternative solutions (marked as x) of Figure 4.

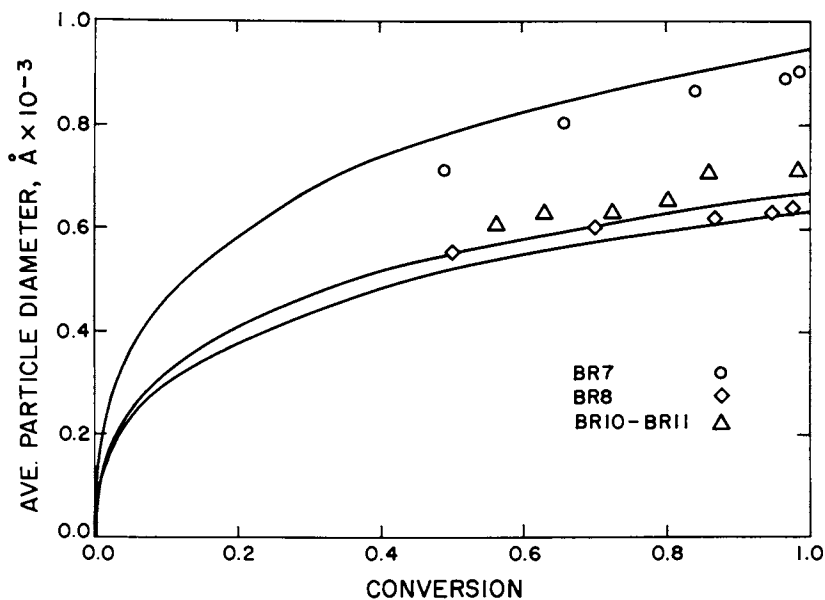


Figure 6. Particle growth histories for the batch runs; model predictions (continuous lines) and experimental data. Reproduced with permission from Ref. 6. Copyright 1985, Marcel Dekker Inc.

measurements by dispensing with parameter estimation and approximating the weight average diameter with  $\bar{D}_{ap}$ . In this case, concentration measurement (from on-line densitometer) and a turbidity measurement at one wavelength would provide sufficient data for the weight average diameter calculation.

Table II. Average Diameters from Specific Turbidity Method

| (Run B7, wavelengths: 400, 440, 480, 500, 560 nm) |              |                         |                            |
|---|--------------|-------------------------|----------------------------|
| Sample #  | Conversion % | $\bar{D}_w$ from (b), Å | $\bar{D}_{ap}$ from (a), Å |
| 5   | 49           | 715                     | 785                        |
| 6   | 66           | 805                     | 900                        |
| 7   | 84           | 870                     | 985                        |
| 8   | 97           | 890                     | 1020                       |
| 10  | 100          | 930                     | 1045                       |

\* $\bar{D}_{ap}$  should be closer to the true  $\bar{D}_w$  than  $\bar{D}_w$  from (b)

## SIZE EXCLUSION CHROMATOGRAPHY

### Theoretical Background

Particle chromatography using packed beds has attracted considerable attention of those interested in measuring particle size distribution of spherical particles in the submicron range (8,9,11,14,16). There exist two complementary approaches to the use of this technique, according to the packing material employed:

- Hydrodynamic Chromatography (HDC) utilizes non-porous packing and relies mainly on the velocity profile in the capillaries formed by the packing. Large particles are excluded from regions near the capillary wall, where the axial velocities are small and hence, on the average, experience a higher velocity and therefore a smaller retention volume.
- Size Exclusion Chromatography (SEC) utilizes porous packing material; steric exclusion of particles in suspension from the pores is an additional force for size separation. Suspended particles, smaller than the diameter in the pore, can diffuse into porous, giving an efficient mechanism of retardation and size separation.

Details concerning the hydrodynamic (HDC) and size exclusion chromatography (SEC) as applied to separate particle suspensions according to their size and an extensive literature review can be found in Penlidis et al. (9) and they will not be repeated here.

A detection system is connected to the outlet of the packed column for monitoring the particle concentration. The passage of an injected sample through the column and detector provides an output trace on the recorder, the chromatogram. A chromatogram can never fully represent the distribution of colloid sizes in the injected sample; instrumental spreading or axial dispersion causes elution of a single species to occur over a range of retention volumes. The contents of the detector cell are not monodispersed, but rather have a distribution that is likely to be unimodal, and it is often quite broad (14). Interpretation of a chromatogram must therefore account for the axial dispersion and involves an evaluation of instrumental spreading and correction of the detector response to obtain the true picture of the injected sample.

The detector response at retention volume  $v$ ,  $F(v)$ , can be expressed as (15)

$$F(v) = \int_0^{\infty} W(y) G(v, y) dy \quad (10)$$

where  $W(y)$  is the true chromatogram, that would have been obtained in the absence of axial dispersion, and  $G(v, y)$  is the normalized detector response for a truly monodisperse system with mean retention volume  $y$ ;  $G(v, y)$  is called the instrumental spreading function.

The solution of the above equation in order to obtain  $W(y)$  requires an appropriate form of the spreading function and the numerical values of its parameters. Furthermore, to convert  $W(y)$  into a size distribution requires a relationship between the mean retention volume  $y$  and the particle diameter  $D$  (i.e., a calibration curve).

Spreading Function. A general statistical shape function, which accounts for skewed chromatograms, initially proposed by Provder and Rosen (16), has been used:

$$G(v, y) = G_0(v, y) \left[ 1 + \frac{A3}{3!} H3(x) + \frac{A4}{4!} H4(x) \right]$$

where

$$G_0(v, y) = \frac{1}{\sqrt{2\pi\sigma^2}} \exp\left(-\frac{(v-y)^2}{2\sigma^2}\right) \quad (11)$$

$$x = \frac{(v-y)}{\sigma}$$

$$H3(x) = x^3 - 3x^2$$

$$H4(x) = x^4 - 6x^2 + 3 \quad (\text{Hermite polynomials})$$

and

$$A3 = \frac{\mu_3}{\mu_2^{3/2}} \quad A4 = \frac{\mu_4}{\mu_2^2} - 3.$$

$\mu_2$ ,  $\mu_3$  and  $\mu_4$  are the second, third and fourth moments of the distribution.  $A3$  is a measure of skewness and  $A4$  a measure of kurtosis.

Estimation of the Spreading Function. When the injected sample is monodispersed, peak broadening occurs solely due to axial dispersion; if  $y$  is the mean retention volume of the chromatogram, then the detector response is given by:

$$F(v) = WG(v, y) \quad (12)$$

where  $W$  is the area under the chromatogram. The parameters ( $\mu_2$ ,  $\mu_3$ ,  $\mu_4$ ) of the distribution can therefore be estimated from the heights of chromatograms of standard monodispersed latexes.

Calibration Curve. The chromatograms of standard monodisperse samples may be used to construct a calibration curve relating the particle diameter  $D$  with its mean retention volume,  $y$ , by:

$$\ln D = a + by + cy^2 \quad (13)$$

Solution for Axial Dispersion. With different degrees of success, numerous techniques have been proposed for solving equation (10). The most promising method seems to be that of Ishige et al. (10). It is a numerical method that does not require significant computing time.

The method uses the fact that any response  $F^*(v)$  always has a broader distribution than the input distribution  $W(y)$ . Hence, if a distribution  $F_i(v)$  is broader than  $F^*(v)$ , the assumed  $W_i(y)$  must be sharpened to give a response closer to  $F^*(v)$ . Using  $F^*(v)$  as the initial guess for  $W(y)$ , subsequent improved estimates are calculated by:

$$W_{i+1} = (F^*/F_i)W_i \quad (14)$$

where  $F_i$  is the chromatogram calculated using  $W_i$ . The procedure is repeated until  $F_i$  satisfies a convergence criterion.  $W_i(y)$  is always normalized before use.

Particle Size Determination. The corrected detector response at retention volume  $v$  is given as

$$W(v) \propto N(v)D^\gamma(v)K^\delta(v) \quad (15)$$

where  $N$  and  $K$  are the number concentration and extinction coefficient, respectively, of particles of diameter  $D$  at retention volume  $v$ ; indices  $\gamma$  and  $\delta$  are defined as follows:

$$\begin{array}{ll} \text{mass detector:} & \gamma = 3, \delta = 0 \\ \text{turbidity detector:} & \gamma = 2, \delta = 1. \end{array}$$

The extinction coefficient can be calculated from the general Mie theory (8).

The frequency distribution of the particle size is related to the number of particles eluting at volume  $v$  as follows:

$$f(D) dD = - \frac{N(v) dv}{\int_0^\infty N(v) dv}$$

or

$$f(D) = - \frac{N(v)}{\left( \int_0^\infty N(v) dv \right) (dD/dv)} \quad (16)$$

For a nonlinear calibration curve

$$\ln D = a + bv + cv^2$$

and

$$dD/dv = D(b + 2cv) \quad (17)$$

From equations (15-17):

$$f(D) = \frac{W(v)}{\left( \int_0^{\infty} \frac{W(v) dv}{D^{\gamma(v)} K^{\delta(v)}} \right) (dD/dv) D^{\gamma(v)} K^{\delta(v)}} \quad (18)$$

Average Diameters. After the frequency distribution has been obtained, the following average diameters can be calculated:

$$\text{number average:} \quad \bar{D}_N = \int_0^{\infty} D f(D) dD \quad (19a)$$

$$\text{weight average:} \quad \bar{D}_W = \frac{\int_0^{\infty} D^4 f(D) dD}{\int_0^{\infty} D^3 f(D) dD} \quad (19b)$$

$$\text{turbidity average:} \quad \bar{D}_t = \left( \frac{\int_0^{\infty} D^6 f(D) dD}{\int_0^{\infty} D^3 f(D) dD} \right)^{1/3} \quad (19c)$$

$$\text{surface average:} \quad \bar{D}_s = \left( \int_0^{\infty} D^2 f(D) dD \right)^{1/2} \quad (19d)$$

### Experimental

A dry packed column with porous material was used for the characterization according to size of the PVAc latex samples. The packing employed was CPG (Controlled Pore Glass), 2000 Å, 200-400 mesh size. Deionized water with 0.8 gr/lit Aerosol O.T. (dioctyl sodium sulphosuccinate), 0.8 gr/lit sodium nitrate and 0.4 gr/lit sodium azide served as the carrier fluid under a constant flowrate. The sample loop volume was 10 µl. A Beckman UV detector operating at 254 nm was connected at the column outlet to monitor particle size. A particle size-mean retention volume calibration curve was constructed from commercially available polystyrene standards. For reasons of comparison, the samples previously characterized by turbidity spectra were also characterized by SEC. A number of injections were repeated to check for the reproducibility of the method.

### Discussion of SEC Results

As a preliminary indication of the capability of SEC to qualitatively follow particle growth, the diameters corresponding to the peak retention volume were calculated directly from the calibration curve (without any correction for axial dispersion). "Peak" average particle diameters are plotted vs. conversion for the batch runs in Figure 7, where it is clearly shown that runs B10 and B11 are replications, with latex particles smaller than those produced from run B7, as expected. In the continuous run, shown in Figure 8,

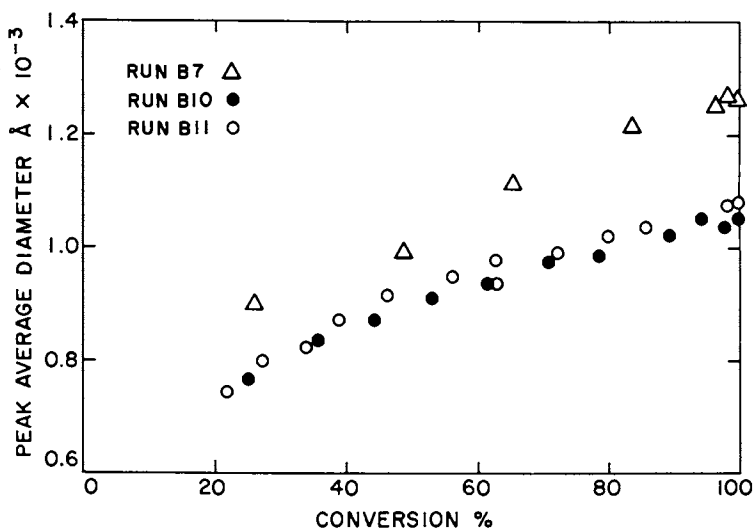


Figure 7. Size Exclusion Chromatography: peak average diameters for three batch runs with different emulsifier levels; runs B10 – B11 are replications.

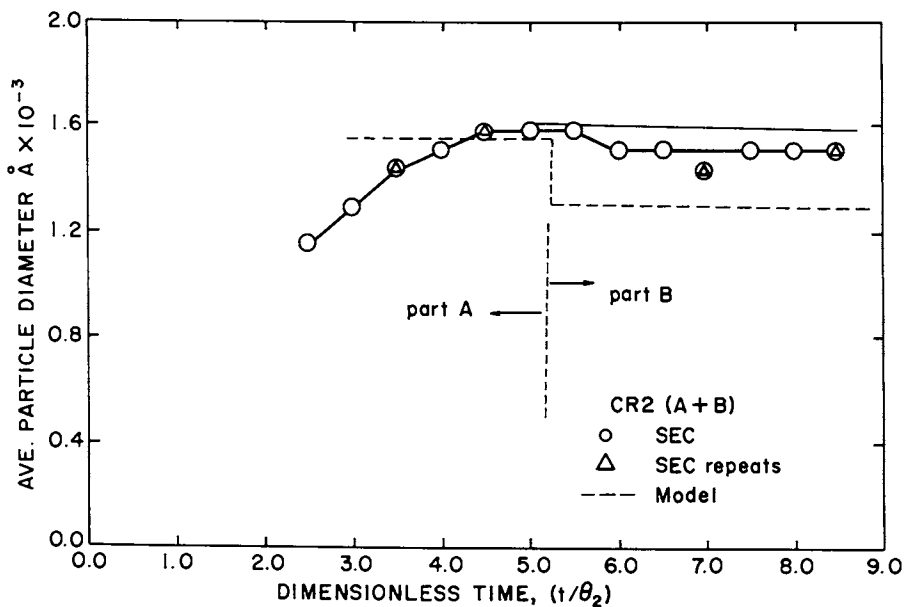


Figure 8. Size Exclusion Chromatography: peak average diameters for the continuous run (17). ( $\theta_2$  = residence time in the second reactor of the continuous train).

a decrease in the particle size is observed during part B, where the emulsifier concentration in the seeding reactor was higher than in part A (17). It can be seen that in both cases SEC followed the course of the reaction reasonably well.

The chromatograms of the several injected PVAc samples were corrected for axial dispersion (8-11) and number and weight average diameters were estimated. The resulting distributions and diameter averages showed that the latex samples from the batch runs were "almost" monodispersed (8). This was further supported by the fact that estimated average diameters were very close to the "peak" average diameters (Table III).

Table III. Average Diameters from SEC

| Sample # | Conversion % | Corrected                    |             | "Peak" Diameters |
|----------|--------------|------------------------------|-------------|------------------|
|          |              | $\bar{D}_N$<br>(from SEC, Å) | $\bar{D}_W$ |                  |
| B11-11   | 47           | 885                          | 890         | 920              |
| 13       | 63           | 920                          | 930         | 935              |
| 16       | 86           | 960                          | 980         | 1040             |
| 19       | 100          | 1010                         | 1020        | 1080             |
| B8-5     | 50           | 825                          | 830         | 860              |
| 6        | 70           | 890                          | 890         | 950              |
| 7        | 85           | 925                          | 935         | 980              |
| 10       | 100          | 940                          | 950         | 1020             |

SEC has been shown (7) to give satisfactory results for latexes with broad particle size distributions as well. The method is particularly useful (7) in the determination of distributions of small particles when specific turbidity would provide only a turbidity (or weight) average diameter.

### CONCLUSIONS

Turbidity measurements are simple, fast and reproducible. Specific turbidity can successfully follow the particle size evolution during the course of emulsion polymerization and can be translated into weight average diameters. A combination of an on-line spectrophotometer with an on-line densitometer (to obtain concentration) would provide the potential to estimate  $\bar{D}_w$  on-line, as well. An on-line determination of PSD's, for small particles however, would seem quite difficult due to the high correlation of their parameters. One should bear in mind that the above conclusions have been validated only for poly(vinyl acetate) latexes; the analysis is currently being extended to other systems, such as polystyrene and poly(methyl-methacrylate).

At low conversions, the presence of monomer results in false particle size when turbidity spectra is used (7). In this case, SEC can be used as a complementary technique since it can also successfully follow particle growth and therefore yield particle sizes.

Both of the above techniques seem to give consistent results in the detection of particle growth for latexes produced by continuous emulsion polymerization, as well. More details and results from this ongoing research will be published shortly.



LITERATURE CITED

1. Kiparissides, C.; MacGregor, J.F.; Singh, S.; Hamielec, A.E. CJChE 1980, 58, 65.
2. Zollars, R.L.; J. Colloid Interface Sci. 1980, 74, 163.
3. Heller, W.; Pagonis, W.J. J. Chem. Phys. 1957, 26, 498.
4. Meehan, E.J.; Beattie, W.H. J. Phys. Chem. 1960, 64, 1006.
5. Maxim, L.D.; Klein, A.; Meyer, M.E.; Kuist, C.H. J. Polym. Sci., Part C 1969, 27, 195.
6. Penlidis, A.; MacGregor, J.F.; Hamielec, A.E., Polym. Proc. Eng. 1985, 3 (3), 185.
7. Kourti, T.; MacGregor, J.F.; Hamielec, A.E. unpublished results.
8. Kourti, T. Technical Report, Dept. of Chem. Eng., McMaster University, Hamilton, Ontario, Canada, March 1984.
9. Penlidis, A.; Hamielec, A.E.; MacGregor, J.F. J. Liquid Chromat. 1983, 6(S-2), 179.
10. Ishige, T.; Lee, S.I.; Hamielec, A.E. J. Appl. Polym. Sci. 1971, 15, 1607.
11. Husain, A.; Hamielec, A.E.; Vlachopoulos, J. In "Size Exclusion Chromatography (GPC)"; Provder, Th., Ed.; ACS Symposium Series No. 138, American Chemical Society: Washington, DC, 1980; p. 47.
12. Penlidis, A.; MacGregor, J.F.; Hamielec, A.E., S. Proc. 189th ACS National Meeting, Division of PMSE, Miami Beach, Florida, April 1985, p. 484.
13. Penlidis, A.; MacGregor, J.F.; Hamielec, A.E., AIChE J. 1985, 31(6), 881.
14. Hamielec, A.E. In "Modern Methods for Particle Size Analysis", Barth, H.G., Ed.; J. Wiley & Sons, Inc.: New York, 1984; p. 251.
15. Tung, L.H. J. Appl. Polym. Sci. 1966, 10, 375.
16. Provder, T.; Rosen, E.M., Separation Science 1970, 5(4), 437; 1970 5(4), 485.
17. Penlidis, A.; MacGregor, J.F.; Hamielec, A.E. submitted for publication in AIChE J.
18. Kerker, M. "The Scattering of Light and Other Electromagnetic Radiation"; Academic Press: New York, 1969.

RECEIVED June 27, 1986

## Chapter 18

# Particle Size Distribution Analysis of Colloidal Latices Using Hydrodynamic Chromatography

Anthony W. Thornton, James P. Olivier, Cindy G. Smart, and Lee B. Gilman

Micromeritics Instrument Corporation, Norcross, GA 30093

The mass versus particle size distribution of several polymer latices with diameters in the range of 30 nm to 1500 nm was determined in less than 20 minutes using an integrated hydrodynamic chromatograph. Distributions obtained were compared with those found by other particle sizing techniques such as electron microscopy to verify validity of the technique. The instrument employed was able to analyze latices reproducibly with different optical properties, even though some of the injected particles may have been trapped within the column. Latex properties were correlated with particle size distribution data to illustrate the benefit of this particle sizing technique.

Particle size distribution of a latex has a pronounced influence on its rheological properties, storage stability, and film forming capabilities (1). In addition, latex particle size distributions provide information on polymerization mechanisms and kinetics (2), and provide a means of polymerization control (3,4).

It is often difficult to define the size of a particle, especially one with an irregular shape. Latex particles suspended in an aqueous phase are often nearly perfect spheres. For this case, particle size can be described accurately using a single dimension, usually the diameter. The diameter of latex particles can be determined accurately using microscopy (usually transmission electron microscopy) if clusters of latex spheres or severely deformed particles are excluded. Latex particle diameters are determined relative to the space between rulings on a calibrated grid. Similar calibrations exist for a number of other techniques available for determination of latex particle size distributions (5,6). These techniques include photon correlation spectroscopy, disk centrifuge photosedimentometry, sedimentation field flow fractionation, and hydrodynamic chromatography, (HDC). The

0097-6156/87/0332-0256\$06.00/0

© 1987 American Chemical Society

accuracy of any one of these techniques can be specified based upon theoretical models or calibration using latices that have been sized by microscopy. The capabilities of one of these methods, HDC, is the subject of this paper.

Hydrodynamic chromatography was originally described by Small (7) in 1974. A number of publications have appeared since then which describe the separation mechanism and sample detection methods used with HDC (5, 8-18). In addition, Van Gilder, et. al. (19) used HDC as the primary particle sizing technique in research on the particle size versus viscosity relationship of high solids paper coating latices.

The original HDC apparatus used columns packed with polymeric ion exchange spheres and standard liquid chromatography components to separate latex particles according to size. The device was calibrated using latices whose particle size had been determined by microscopy. Elution time was found to vary regularly, although not linearly, with particle size. Unfortunately, several hours were required for each size analysis. Subsequent developments (14, 18) have largely overcome this drawback.

Hydrodynamic chromatography was commercialized by Micromeritics Instrument Corporation in 1984. The FlowSizer HDC 5600 is an integrated, computer controlled liquid chromatograph consisting of an eluant delivery system, a sample injection valve, a size separation column, a sample detector, and an eluant volume measuring device (see Figure 1). Size analysis begins with injection of a latex sample into a flowing stream of eluant which passes through the separation column. The latex particles separate inside the column such that large particles exit before small particles. Presence of sample in the eluant is monitored as it exits the column using an ultraviolet light detector with wavelength fixed at 254 nm. Consideration of data treatment and instrument design is required to understand how the hydrodynamic chromatograms are converted into accurate, high resolution latex particle size distributions.

### Accuracy in HDC

Data Treatment. Hydrodynamic chromatograms can be represented as the convolute integral of three particle size dependent functions. This is shown in Equation 1:

$$F(V) = \int_{V_2}^{V_1} \{W(y) G(V,y) K(y)\} dy \quad (1)$$

where  $F(V)$  is the sample detector response versus eluant volume since injection,  $V$  (the sample chromatogram);  $W(y)$  is the mass of particles which make up the sample with mean elution volume  $y$ ;  $G(V,y)$  is the band broadening function describing spreading of the band of particles with mean elution volume  $y$  as it passes through the chromatograph;  $K(y)$  is the detector response for a given concentration of particles with mean elution volume  $y$ ; and  $V_1$  and  $V_2$  define the eluant volume window during which all particles in the sample elute. This equation is similar to that used by Tung for describing gel-permeation chromatograms (20).

A mathematical technique known as deconvolution can be used

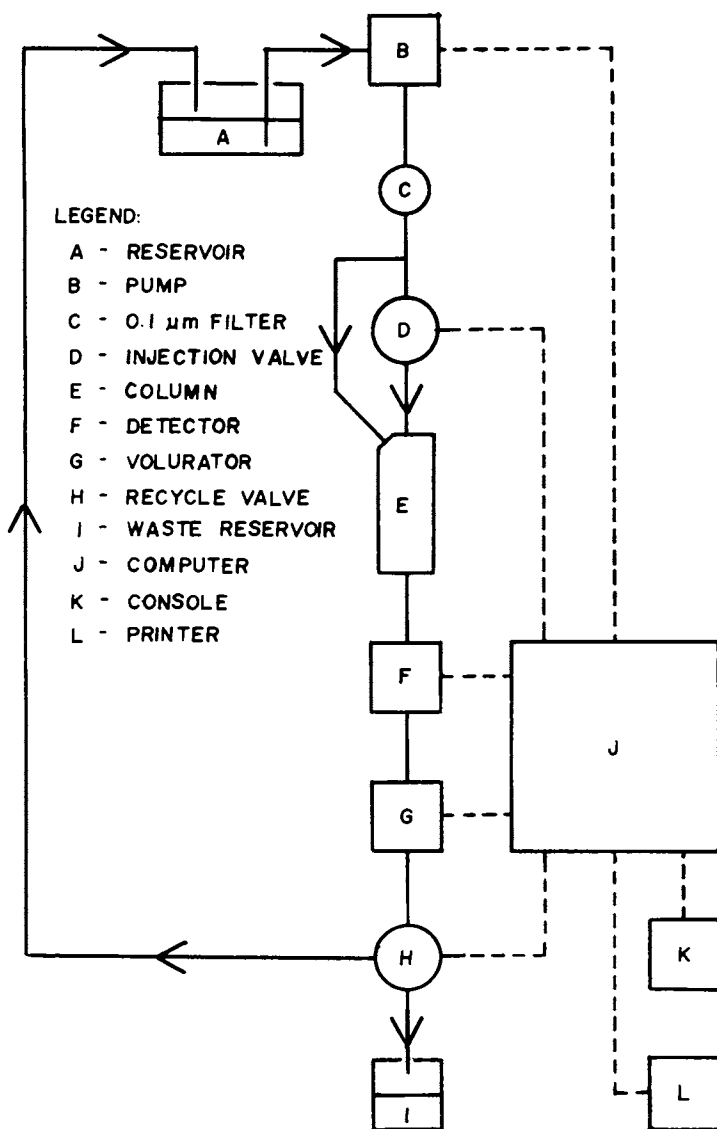


Figure 1. Block diagram of commercial hydrodynamic chromatograph. Solid lines indicate fluid flow path. Broken lines indicate data communication. Arrows indicate fluid flow direction.

to interpret chromatographic data and solve the convoluted integral based on known information. This allows recovery of some resolution lost due to the overlap of sample bands, and determination of the mass-based particle size distribution. The measured chromatogram,  $F(V)$ , is represented as a sum of chromatograms of monodisperse materials that fall within the analytical limits of the instrument, and whose size, band broadening and light refraction characteristics are known. An infinite number of latex peak models could be generated for the analysis range of HDC. However, summing a large number of peak models becomes quite time consuming. The FlowSizer therefore uses 100 peak models during deconvolution. A linear combination of varying amounts of all these peak models is summed to regenerate the actual chromatogram obtained. An iterative process, non-negative least squares analysis (21, 22), is used to insure that the best fit of the data is obtained. The relative amount of each peak model used is then converted to the mass fraction of material having the particle size of the models used in evaluating the unknown sample chromatogram.

Equation 1 can be replaced with the finite sum:

$$F(V) = \sum_{i=1}^{100} W_i G(V)_i K_i \quad (2)$$

where  $W_i$  is the mass of particles with mean elution volume corresponding to chromatogram  $i$ ,  $G(V)_i$  is the broadening function for particles making up chromatogram  $i$ , and  $K_i$  is the detector response factor for those particles.  $F(V)$  is measured during a particle analysis,  $G(V)_i$  is determined during instrument calibration, and  $K_i$  values are measured for polystyrene latices of known size. Therefore, deconvolution of Equation 2 gives the values of  $W_i$ . The particle size versus mean elution volume calibration is then used to convert  $W_i$  values into the particle size distribution of the sample.

The band broadening function  $G(V)_i$  can be determined for several particle sizes by analyzing latex samples of known particle size which have very narrow size distributions, and then mathematically modeling the shape of the resulting chromatographic peaks. The function can then be interpolated for particle sizes between those corresponding to the known latices. The relationship between particle diameter and  $y$ , the mean elution volume of the particles, is the particle size versus elution volume calibration. As discussed earlier, an HDC is calibrated using polystyrene latices, but the calibration is valid for other latices (23), and even non-latex materials. (Colloidal gold that had been sized at 40 nm by electron microscopy was detected at 39 nm using the FlowSizer.)

$K_i$ , the detector response factor, describes the signal generated when particles are present in the eluant as it transits the detector flow-through cell. Detector response arises primarily from scattering of light by the latex particles (15), although a small contribution from light absorption by the sample may occur (16). Polystyrene latex standards of known size and concentration were used to determine  $K_i$  factors for conversion of detector response into mass concentration information.

The quality of the deconvolution results will be limited by the quality of the given data. Chromatographic data,  $F(V)$ , must be collected under the same conditions as the calibration data. Detector response must change linearly with sample concentration within the operating range of the chromatograph. If not,  $K_1$  values will not be constant for a given particle size, and calculated mass percent values will not be reliable. The eluant volume measuring device must give reproducible elution volume information. If not, data will not be collected in the same window,  $V_1$  to  $V_2$ , or at the same eluant volume values  $V$ , resulting in incorrect particle size assignment. Sample injection and elution must be reproducible. If not, the detector response will not truly represent the injected sample, and calculated particle size distributions will be inaccurate. Calibration samples must be monodisperse and of known size. If not, band broadening functions,  $G(V)_1$ , and particle size versus elution volume,  $y$ , calibrations will be inaccurate. The hydrodynamic chromatograph and its operating conditions must be designed to satisfy each of these conditions to insure that accurate, reproducible particle size distributions are determined.

Instrument Design. The FlowSizer consists of HPLC components housed in a single cabinet and interfaced to an internal, dedicated computer. This design helps to minimize "dead volumes" in the flow paths and electrical noise on sample data lines. The elapsed volume measuring device, the VoluRator, is connected to the detector flow outlet. The VoluRator generates a series of pulses proportional to the volume of fluid leaving the detector. The repeatability of the VoluRator was determined to be  $\pm 0.5\%$  coefficient of variance of measured elution volume (24). Repeatability of this magnitude will insure that detector data are always collected at the same elapsed volume values, regardless of eluant flow rate.

Calibration Samples. Monodisperse polystyrene latices are available with known, narrow particle size distributions. Coefficients of variance about the mean diameter are typically less than 6% of diameter measured using electron microscopy (25). HDC typically cannot resolve differences in diameter of only 6%. Therefore, these polystyrenes are sufficiently narrow to be used as HDC calibration reference samples. However, doing so may result in incorporation of a systematic error in the particle size versus elution volume calibration, arising from known electron microscopy errors of as much as  $\pm 5\%$  for particles below 1  $\mu\text{m}$  (26). Therefore, accuracy can only be stated as relative to electron microscopy results for the calibration samples. FlowSizer performance specifications have been reported elsewhere (27) with diameter and mass percent results within  $\pm 5\%$  of those determined by electron microscopy for a series of these monodisperse polystyrene latices.

This investigation will show that reproducible particle size distributions are possible using hydrodynamic chromatography, even though a portion of the injected sample may be trapped within the column matrix. In addition, it will illustrate the effects of using fixed  $K_1$  factors for different types of latex whose scattering and absorbing characteristics differ from those of polystyrene. These two areas determine whether or not mass percent particle size

distributions can be obtained using HDC and do not appreciably affect the ability of HDC to give mean particle diameters. It is the ability of HDC to determine the size distributions of samples, and not just mean diameters, which makes it a valuable analytical technique.

### Experimental

Particle size distributions and peak areas of injected latices were determined using a standard FlowSizer HDC 5600, Micromeritics Instrument Corporation, Norcross, Georgia. The column was replaced with a single open tube during a portion of percent recovery testing. Polyvinyl chloride extinction coefficients were substituted for polystyrene coefficients during a portion of the  $K_i$  factor testing. Ten monodisperse polystyrene latices were purchased from Duke Scientific Corporation, Palo Alto, California. A particle size distribution, determined using transmission electron microscopy (TEM), was obtained for each latex (see Table I, first and second columns).

The concentration of each latex was determined gravimetrically. Three 1.0 ml samples of each latex were weighed to the nearest 0.1 mg. The samples were placed in a vacuum oven (55° C, -100 kPa) for two hours. The dried samples were allowed to cool to room temperature in a desiccator and weighed again to the nearest 0.1 mg. Weight percent values were calculated for the three samples of each latex. The arithmetic mean of the three weight percent values and the standard error of the means for each latex are listed in the third and fourth columns, respectively, of Table I.

Table I. Polystyrene Latices Used in Mass Recovery Testing

| Latex Distribution <sup>a</sup> |                         | Latex Concentration <sup>b</sup> |                     |
|---------------------------------|-------------------------|----------------------------------|---------------------|
| Mean Diameter (nm)              | Standard Deviation (nm) | Weight Percent (%)               | Estimated Error (%) |
| 43                              | 7.5                     | 12.9                             | 0.1                 |
| 91                              | 5.8                     | 10.38                            | 0.02                |
| 176                             | 2.3                     | 10.79                            | 0.03                |
| 198                             | 3.6                     | 10.49                            | 0.02                |
| 261                             | 3.1                     | 10.40                            | 0.02                |
| 305                             | 8.4                     | 10.91                            | 0.08                |
| 624                             | 5.2                     | 10.77                            | 0.03                |
| 804                             | 4.8                     | 9.86                             | 0.09                |
| 913                             | 5.9                     | 10.2                             | 0.1                 |
| 1091                            | 8.2                     | 10.6                             | 0.1                 |

a. Mass-weighted distribution based on microscopy data supplied with sample.

b. Based on three gravimetric determinations.

Particle Retention in Column. Each polystyrene latex was agitated and a 1.0 ml aliquot of each was diluted with FlowSizer eluant. Final sample concentrations ranged from 0.05% to 1.0% (by weight), depending on latex particle size, in order to generate chromatographic signals in the linear range of the detector. Diluted samples were placed in a low power ultrasonic bath (Ultrasonics, Plainview, New York) for 60 seconds just prior to injection. Peak areas were determined for each injection. Each sample was injected until three consecutive areas differed by less than two percent from one value to the next.

Equation 3 was used to calculate mass percent of sample recovered,  $M_r$ , for each sample:

$$M_r = \frac{A_c}{A_t} \frac{C_t}{C_c} \times 100 \quad (3)$$

where  $A_c$  is the average of the determined areas from the last three injections of each sample through the packed column; similarly,  $A_t$  is the mean of the last three areas determined for injections through the open tube; and  $C_c$  and  $C_t$  are the concentrations of the sample injected through the column and open tube, respectively. The mass % recovered for each sample, and an estimate of the error in each value, are given in Table II, second and third columns, respectively.

Table II. Results of Percent Recovery Testing

| Sample<br>Mean<br>Diameter <sup>a</sup><br>(nm) | Recovered              |                           | Retained     |                            | Area<br>Coefficient<br>of Variance <sup>b</sup><br>(%) |
|---|------------------------|---------------------------|--------------|----------------------------|--|
|   | Mass<br>Percent<br>(%) | Estimated<br>Error<br>(%) | Mass<br>(ug) | Estimated<br>Error<br>(ug) |  |
| 43  | 100                    | 1                         | 0.00         | 0.00                       | 0.7  |
| 91  | 95                     | 4                         | 1.75         | 0.08                       | 1.0  |
| 176   | 82                     | 2                         | 3.8          | 0.1                        | 1.1  |
| 198   | 72                     | 2                         | 17.6         | 0.6                        | 1.1  |
| 261   | 62                     | 2                         | 22.5         | 0.8                        | 1.5  |
| 305   | 64                     | 2                         | 47           | 1                          | 0.5  |
| 624   | 78                     | 3                         | 122          | 5                          | 1.7  |
| 804   | 72                     | 2                         | 208          | 7                          | 1.2  |
| 913   | 70                     | 2                         | 193          | 6                          | 0.9  |
| 1091  | 61                     | 3                         | 880          | 50                         | 0.1  |

a. From Table I.

b. Based on last three injections of each sample.

Equation 4 was used to calculate the mass of sample retained in the column,  $M_t$ , of each of the ten latices:

$$M_t = \sum_{i=1}^n \frac{M_r A_i C_c V_L}{(100) A_c} \quad (4)$$

where  $A_i$  is the area of the  $i$ th injection of the sample;  $n$  is the total number of injections of the sample; and  $V_L$  is the volume of the injection loop (10 uL for the FlowSizer). Substitution of Equation 3 into Equation 4 followed by cancellation of terms gives:



$$M_t = \sum_{i=1}^n \frac{A_i C_t V_i}{A_t} \quad (5)$$

The mass of each sample retained and an estimate of the error of the calculated value are given in Table II, fourth and fifth columns, respectively.

**Effects of Detector Response Function.** Two synthetic blends were made using three of the polystyrene latices (91 nm, 176 nm and 1091 nm). A sample of commercially available acrylic latex and one of butadiene latex were obtained and diluted with eluant. The two blends and two commercial samples were each analyzed using the FlowSizer with each of two different detector response functions. The results obtained with the two different functions are given in Table III and Figure 2.

The two response functions used are illustrated in Figure 3. The polystyrene response function was determined using monodisperse latices of known size, along with curve fitting routines. Polystyrene detector response arises from both absorbance and scattering of incident ultraviolet light. The polyvinyl chloride response curve was calculated according to Mie's theory (15) using complex refractive index values given by Nagy (28). Polyvinyl chloride detector response arises almost exclusively from scattering of incident ultraviolet light.

Table III. Comparison of HDC Particle Size Distributions Obtained Using Different Detector Response Functions

| Type of Distribution | Absorbance and Scattering  |                    | Scattering Only            |                    |
|----------------------|----------------------------|--------------------|----------------------------|--------------------|
|                      | Mean Diameter of Mode (nm) | Mass % in Mode (%) | Mean Diameter of Mode (nm) | Mass % in Mode (%) |
| Narrow               |                            |                    |                            |                    |
| Monomodal            | 136.3                      | 100.0              | 135.7                      | 100.0              |
| Resolved             | 89.6                       | 46.1               | 90.1                       | 75.8               |
| Bimodal              | 1029.0                     | 53.9               | 1046.0                     | 24.2               |
| Overlapped           | 90.3                       | 53.0               | 90.7                       | 54.9               |
| Bimodal              | 165.5                      | 47.0               | 165.0                      | 45.1               |

### Results and Discussion

**Particle Retention in Column.** The results listed in Table II indicate that a significant proportion of the latices with diameters above 200 nm is retained within the HDC column. However, the percent recovered for each sample is very reproducible once the column is conditioned. The last column of Table II lists the coefficient of variance (CV) of the measured areas for the last three injections of each sample. Such low CV values are possible only if the same amount of sample is reaching the detector for each injection. Percent retention of latex within the column must be repeatable, and therefore, predictable. Any predictable (systematic) error which may affect calculated results can be eliminated. The effects of sample retention can be overcome by multiplying  $K_1$  (extinction coefficient) by percent recovery for each sample and using

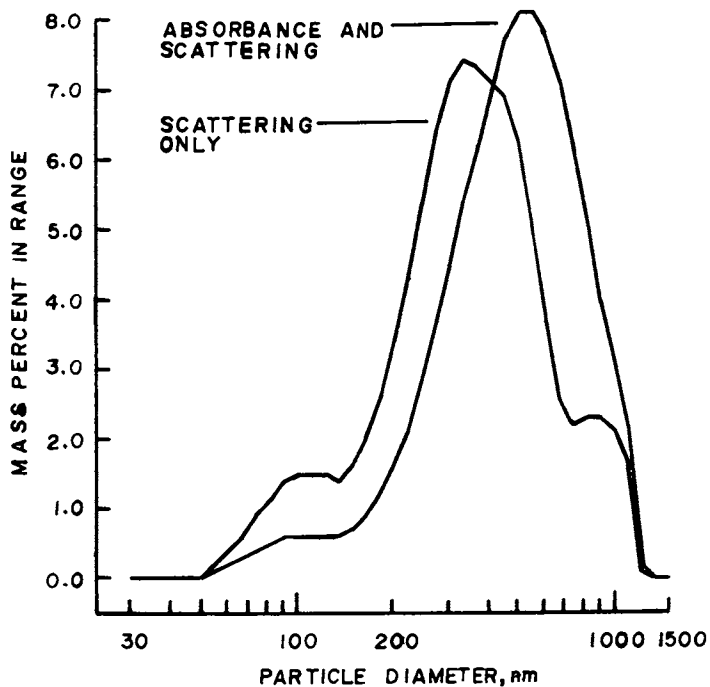


Figure 2. Particle size distribution of a commercially available polybutadiene latex calculated using different detector response functions.

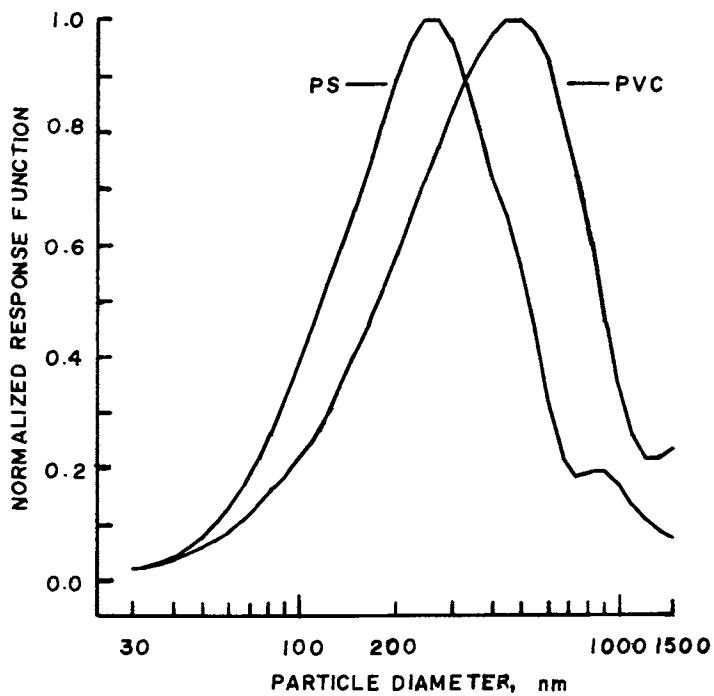


Figure 3. Detector response functions for polystyrene (PS) and polyvinyl chloride (PVC) for 254 nm incident light.

the result as an effective extinction coefficient,  $K_i'$ . Equation 2 can then be rewritten as:

$$F(V) = \sum_{i=1}^n W_i G(V)_i K_i' \quad (6)$$

to include the effects of sample retention. Deconvolution of Equation 6 will then give accurate, reproducible particle size distributions, even though some of the injected sample is retained within the column.

Effects of Detector Response Function. The detector response functions for polystyrene latices and polyvinyl chloride latices differ significantly due to absorbance of ultraviolet light by the polystyrene particles. The polyvinyl chloride particles absorb essentially no light at 254 nm. The effects of using different detector functions in Equation 6 depend on the type of sample distribution determined. The detector response does not vary appreciably over the small size range of a narrow monomodal acrylic latex. Therefore, changing detector response functions has little effect on the calculated particle size (see Table III). The sizes of modes in a well resolved bimodal polystyrene sample (91 nm and 1091 nm) are similarly not affected by changing response functions, although the relative mass in the two modes is affected significantly. However, if the two modes are close together in size (91 nm and 176 nm), or overlap, even the relative mass in the two modes is not affected greatly. This is again due to the small variation in response function over the width of the bimodal distribution.

The response function varies significantly over the width of a broadly distributed sample. Figure 3 illustrates particle size distributions determined for the polybutadiene sample. The results are significantly different, with better definition of modes present in the distribution found using the non-absorbing response function. The mean diameters of the two distributions are 513 nm and 405 nm for the polystyrene and polyvinyl chloride functions, respectively. Polybutadiene is expected to absorb very little light at 254 nm. Therefore, the scattering only results would be expected to best represent the sample. It should be noted that the effects of using different response factors are greatest for broad sample distributions.

The examples shown in this investigation are extreme due to significant differences in the absorbance characteristics in the two response functions. The differences between the distributions in Figure 3 and Table III can be used as a guide to the maximum magnitude of error expected in HDC particle size distributions if the response function used does not correspond to the optical properties of the latex sample.

## Applications

Quality Control of Latex Polymerization Using Hydrodynamic Chromatography. Latex polymers are most commonly manufactured in a large vessel with all the product being removed at the end of the polymerization reaction. This so-called batch polymerization process

yields a latex product which has slightly differently properties for each batch. Manufacturers typically blend two or more batches of latex together to insure a more uniform product. In addition, latices may be blended to obtain desirable properties as contributed by different sizes of latex particles (19). Latex manufacturers will also on occasion blend small quantities of poor quality batches with good products and still obtain a mixture with acceptable properties. In the past, blending of latices was monitored primarily by viscosity measurements, surface tension measurements, and end use tests. Although useful, such tests give no insight into why a particular batch of material behaves in a given way. Thus, valuable guidance in how to correct a problem in blending or polymerization is often not available. Particle size analysis of the latex can often yield insight into why a particular batch of material is not acceptable. In many cases, batch polymerizations require enough time that particle size can be monitored by HDC as the latex is being made. This will allow action to be taken to correct some polymerization problem and thus to obtain good quality product.

Two commercially produced polystyrene latices were analyzed using HDC. The manufacturer reported that the two batches exhibited different rheological properties. Both samples originally had a viscosity in the expected range. However, upon storage for a few hours, the viscosity of one sample increased to an unacceptable value. Both batches were determined to have the same concentration of non-volatile material (percent solids). Size analysis by HDC revealed that the good batch of latex was bimodal as expected. The manufacturer had blended together two separate batches of material (each having one size mode) to obtain the good material. The unstable latex was found to contain three modes. Two of the three modes were found at the same diameters as for the good material. The third mode was found at a larger particle size. In addition, the relative amount of material found in the second mode was much greater for the unstable sample. Table IV compares the results found for the two samples. The increased viscosity of the unstable latex appears to result from an increase in the amount of large size material with time. This indicates that smaller sized latex particles were agglomerating during storage to yield larger size particles. Cause for this agglomeration was not disclosed but could have resulted from several factors in the polymerization recipe or operation of the polymerization equipment.

Table IV. Comparison of Results Obtained by HDC for Two Batches of a Commercially Available Polystyrene Latex

| Mode | Good Sample        |                  | Unstable Sample    |                  |
|------|--------------------|------------------|--------------------|------------------|
|      | Mean Diameter (nm) | Mass Percent (%) | Mean Diameter (nm) | Mass Percent (%) |
| A    | 133.2              | 62.2             | 136.2              | 55.4             |
| B    | 251.2              | 37.8             | 248.1              | 42.1             |
| C    | -                  | -                | 463.4              | 2.5              |

Quality Control of Purchased Latices Using Hydrodynamic Chromatography. Two different commercially available acrylic copolymer latices were purchased by a ceramics manufacturer for use as a binder for casting thin ceramic films. Although different products, the two latices were believed to have similar properties when used in this process. Analysis of these two acrylics by HDC indicated the reason for this similarity. Figure 4 shows that the two latices do indeed have similar particle size distributions, although one has a slightly higher mean particle diameter. With this particle size information, additional sources of latex for this application can be screened and qualified at lower cost and more rapidly than end use tests.

### Conclusion

The results reported herein indicate that hydrodynamic chromatography is an accurate, reproducible technique for latex particle size distribution analysis. Typical analysis requires 15-20 minutes to complete and reproducibility is generally better than  $\pm 5\%$  for both reported particle size and mass percent. Latex particle size distributions found using HDC provide useful information about end use performance of many types of material (see Table V).

Table V. Materials Analyzed by Hydrodynamic Chromatography

|                                 |  |
|---------------------------------|--|
| Polystyrene                     | Ethylene-vinyl acetate copolymer             |
| Polybutadiene                   | Methyl-methacrylate-butyl acrylate copolymer |
| Polyvinyl acetate               | Acrylonitrile-butadiene-styrene terpolymer   |
| Polyvinyl chloride              | Styrene-butadiene-acrylic terpolymer         |
| Poly 2-vinyl pyridine           | Acrylonitrile-butadiene-acrylic terpolymer   |
| Polytetrafluoroethylene         | Styrene-butadiene-vinyl pyridine terpolymer  |
| Polychlorobutene                | Poly dimethylsiloxane emulsion               |
| Polymethyl-metacrylate          | Hydrocarbon tackifier emulsion               |
| Styrene-butadiene copolymer     | Rosin tackifier dispersion                   |
| Vinyl acetate-acrylic copolymer | Carbon black dispersion (oil furnace black)  |
| Vinylidene chloride copolymer   | Colloidal gold                               |

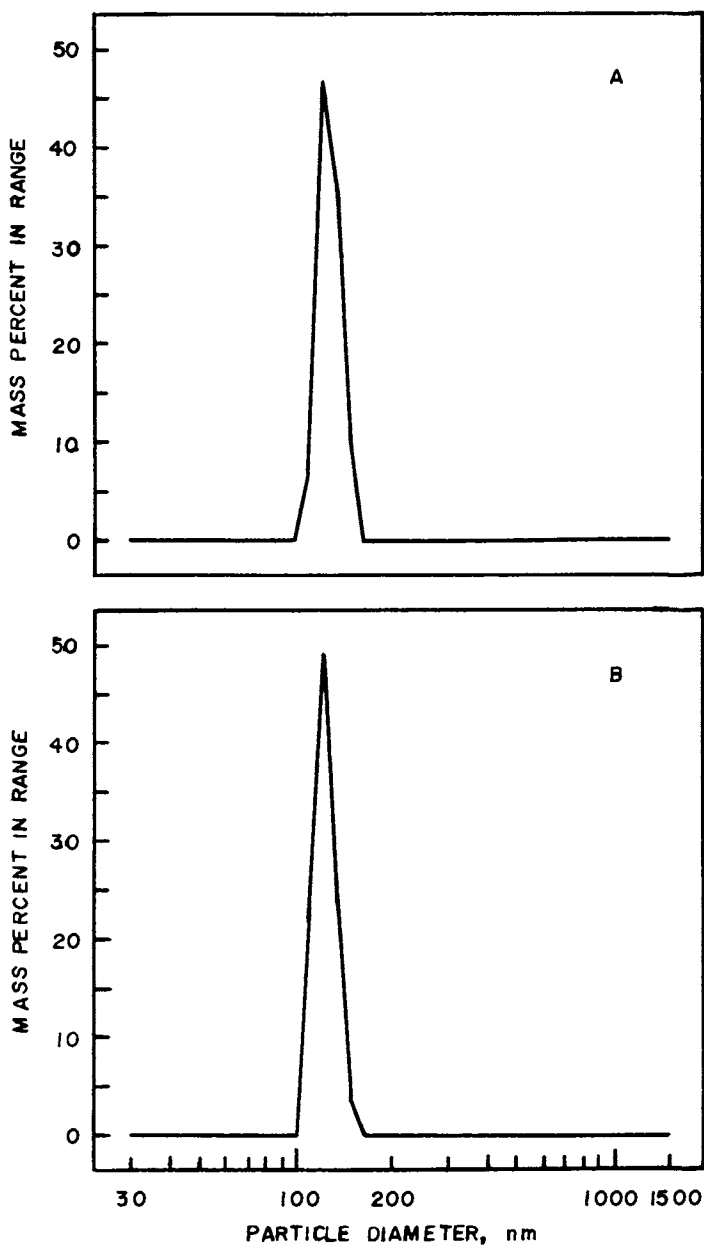


Figure 4. Particle size distribution of two different commercially available acrylic binders mean diameter = 121 nm (A), 127 nm (B).

Acknowledgments

The authors wish to express their gratitude to Shandra L. Shields of Micromeritics for performing the experiments described in this paper.

Literature Cited

1. Tadros, T. F.; Vincent, B. In "Encyclopedia of Emulsion Technology"; Becher, P., Ed.; New York: Marcel Dekker, 1983; Vol. I, pp. 129-285.
2. Lichti, G.; Gilbert, R. G.; Napper, D. H. J. Polym. Sci., Polym. Chem. Ed. 1983, 21, 269.
3. Van Gilder, R. L.; Langhorst, M. A. Proc. ACS Division of Polymeric Materials: Science and Engineering 1985; Vol. 53, pp. 440.
4. Schork, F. J. Lecture Notes In "Advances in Emulsion Polymerization and Latex Technology"; Compiled by El-Aasser, M. S.; Emulsion Polymers Institute, Lehigh University, 1984; Vol. I, Lecture 7.
5. McHugh, A. J. CRC Critical Reviews in Analytical Chemistry 1984, 15, Issue 1, 63.
6. Barth, H. G., Ed. "Modern Methods of Particle Size Analysis"; New York: John Wiley and Sons, Inc., 1984.
7. Small, H. J. Coll. and Inter. Sci. 1974, 48, 147.
8. Small, H.; Saunders, F. L.; Solc., J. Adv. Coll. Inter. Sci. 1976, 6, 237.
9. Silebi, C. A.; McHigh, A. J. AIChE J. 1978, 24, 204.
10. Stoitsits, R. F.; Poehlien, G. W.; Vanderhoff, J. W. J. Coll. and Inter. Sci. 1976, 57, 337.
11. McHugh, A. J.; Silebi, C. A.; Poehlein, G. W.; Vanderhoff, J. W. "Colloid and Interface Science"; Kerker, M., Ed.; New York: Academic Press, 1976; Vol. IV, pp. 549-562.
12. Mullins, M. E.; Orr, C. International Journal of Multiphase Flow 1979, 5, 79.
13. Silebi, C. A.; McHugh, A. J. J. Appl. Polym. Sci. 1979, 23, 1699.
14. McGowan, G. R.; Langhorst, M. A. J. Coll. and Inter. Sci. 1982, 89, 94.
15. van de Hulst, H. C. "Light Scattering by Small Particles"; New York: Dover Publications, Inc., 1981; Chapter 18. Originally published by John Wiley and Sons, Inc., 1957.
16. Silverstein, R. M.; Bassler, G. C.; Morrill, T. C. "Spectrometric Identification of Organic Compounds" 3rd ed.; New York: John Wiley and Sons, Inc., 1974; p. 234.
17. Barth, H. G.; Sun, S. T. Anal. Chem. 1985, 57, 151R.
18. Thornton, T.; Maley, R.; Gilman, L. In "Polymer Latex II"; London: The Plastics and Rubber Institute, 1985; paper 14.
19. Van Gilder, R.; Lee, D. I.; Purfeerst, R.; Allswede, J. TAPPI 1983, 66, No. 11, 49.
20. Tung, L. H. J. Appl. Polym. Sci. 1966, 10, 375.
21. Morrison, I. D.; Grabowski, E. F.; Herb, C. A. Langmuir 1985, 1, 496.
22. Lawson, C. L.; Hanson, R. J. "Solving Least Squares Problems"; Englewood Cliffs, NJ: Prentice-Hall, 1974.
23. Nagy, D. J.; Silebi, C. A.; McHugh, A. J. J. Coll. and Inter. Sci. 1981, 79, 264.



26. Davidson, J. A.; Haller, H. S. J. Coll. and Inter. Sci. 1974, 47, 459.
27. Thornton, T.; Gilman, L. Proc. ACS Division of Polymeric Materials: Science and Engineering, 1985; Vol. 53, p. 426.
28. Nagy, D. J. Ph.D. Thesis, Lehigh University, PA, 1979, p. 218.
24. Ball, D.; Thornton, T. "Advantages of Direct Measurement of Retention Volume in Liquid Chromatography and Size Exclusion Chromatography"; 32nd Pittsburgh Conference on Analytical Chemistry and Applied Spectroscopy, Atlantic City, NJ, 1981; paper 357.
25. Bangs, L. B. "Uniform Latex Particles"; Indianapolis, IN: Seragin, Inc., 1984; pp. 14-15.

RECEIVED July 29, 1986

## Chapter 19

# Application of High-Speed, Integrated, Computerized, Hydrodynamic Chromatography for Monitoring Particle Growth During Latex Polymerization

R. L. Van Gilder<sup>1</sup> and M. A. Langhorst<sup>2</sup>

<sup>1</sup>Designed Latexes and Resins, The Dow Chemical Company, Midland, MI 48640

<sup>2</sup>Analytical Laboratory, The Dow Chemical Company, Midland, MI 46840

The computerized hydrodynamic chromatograph (HDC) technique has been used successfully to detect agglomeration and new-particle generation as significant deviations from the controlled particle growth during latex polymerizations. It was possible to use this high speed integrated computerized HDC technique to determine when these deviations started and how the growth pattern developed during the polymerization. Transmission electron micrograph data supported the results by the computerized HDC analysis.

In the earlier publications (1,2) it was shown how hydrodynamic chromatography (HDC) could be applied in the study of polymer latexes to determine particle-size. An improved technique for the HDC was developed which utilized higher efficiency and resolving power columns to significantly reduce the analysis time (3). A high speed integrated computer was included in this improvement so that both particle-size and particle-size distribution of latexes could be quantified in the relatively short period of time. This high speed computerized version of the HDC has been used extensively for measurements on the final latex.

There is considerable interest in monitoring an emulsion polymerization by following the growth rate of latex particles. It is well known that in addition to a well-controlled particle growth pattern significant deviations can result from particle association or nucleation during the growth stage. A method which would define when such deviations occur during the latex polymerization would be of obvious value and would lead possibly to more efficient optimizations of different latex polymerizations.

Information on particle growth during either a seeded polymerization or during the growth stage of an un-seeded polymerization at different degrees of conversion also could enhance the understanding of the kinetics. In earlier work (4,5) the rate of polymerization, for polystyrene latexes primarily, has been related to the latex particle diameter and the total number of particles in the reactor. It would be useful to obtain kinetic data and develop the kinetic relationships for styrene (S)-butadiene (B) latexes.

0097-6156/87/0332-0272\$06.00/0

© 1987 American Chemical Society

In this publication monitoring of different particle growth patterns during latex polymerizations using the high speed computerized HDC will be described for S/B latexes. Kinetic information will not be dealt with in this paper.

### Experimental

The carboxylated S/B latexes were prepared by an emulsion polymerization process. Samples were taken throughout the runs for analysis on the computerized HDC. The latex particle-size and particle-size distribution was determined using an integrated, high speed chromatograph technique using the delayed marker injection (3). An eluant composition was chosen for HDC measurements so that changes in the hydrodynamic volume of the carboxylated S/B latexes were insignificant (2). The reactor samples were diluted with this eluant upon removal from the reactor followed by injection into the computerized HDC, and elution through the column. The data from the detector was stored in the computer and mathematically treated using the integrated high speed computer system to yield the particle-size and particle-size distribution data. This entire procedure for each reactor latex sample required a relatively short period of time, approximately fifteen minutes.

Prior to the measurements of the different reactor latex samples the computerized HDC was calibrated for particle-size using the standard procedure (3) and also for particle-size distribution quantification. For the particle-size distribution calibration two different particle-size monodisperse carboxylated S/B latexes were polymerized. Various mixtures of these latexes were prepared by blending the large 2100Å and the small 700Å latexes in different ratios by weight: 60/40, 70/30, 80/20 and 90/100 respectively. These prepared latex blends were then measured using the HDC technique.

Transmission electron microscopy (TEM) analysis (6-8) was used also to characterize the latexes in this particle growth monitoring study. The electron micrographs were taken at a magnification of 30,000X.

### Results and Discussion

#### Calibration of the Computerized HDC for Particle-Size Distribution.

The particle-sizes and particle-size distribution of the two monodisperse carboxylated S/B latexes are shown in the hydrodynamic chromatograms of Figure 1. The average diameters of the large,  $D_L$ , and the small,  $D_S$ , relatively monodisperse latexes were 2100Å and 720Å respectively.

The relative amount of each latex ( $V_L$ ,  $V_S$ ) in the different blends, as determined by HDC are shown in Figures 2 and 3. There was excellent correlation between the actual and the measured quantities of each component in the different binary mixtures. This calibration for particle-size distribution demonstrated that the computerized HDC could be used to determine the relative amount of each latex in the various binary mixtures within 1%.

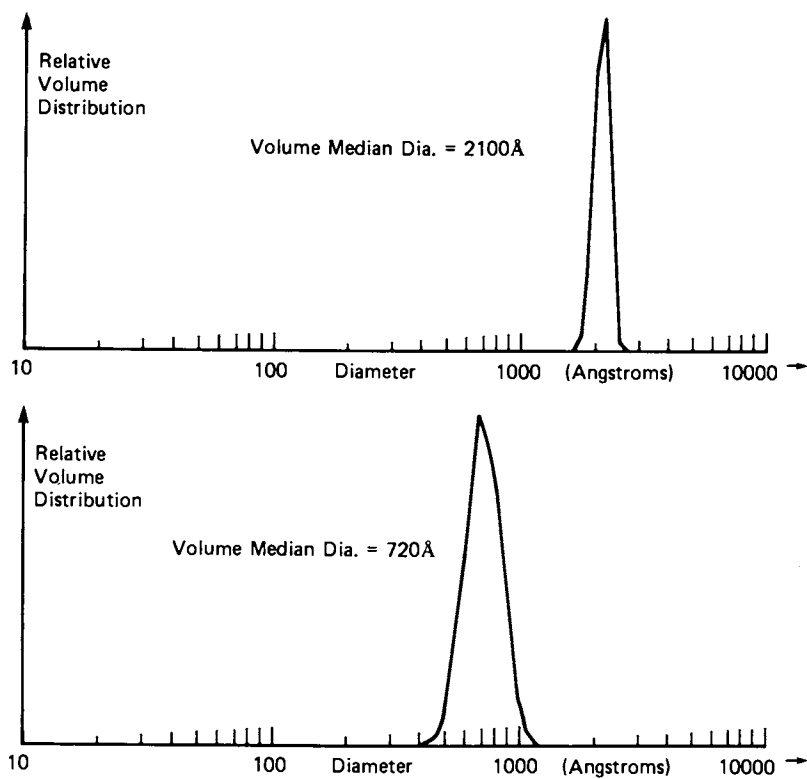


Figure 1. S/B latex particle-size distribution via HDC. Reproduced with permission from Ref. 11. Copyright 1983 Tappi J.

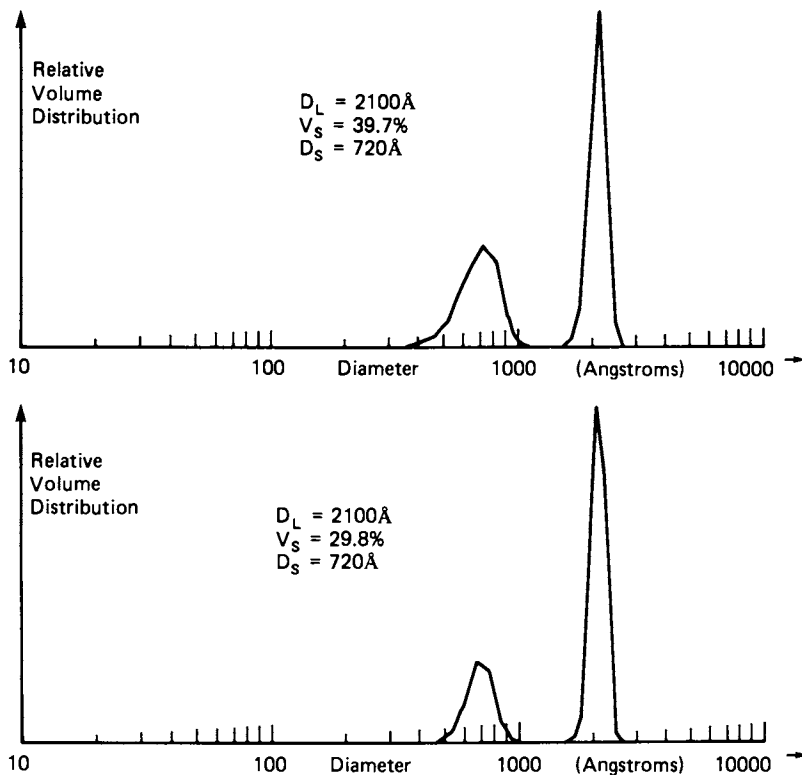


Figure 2. S/B latex particle-size distribution via HDC. Reproduced with permission from Ref. 11. Copyright 1983 Tappi J.

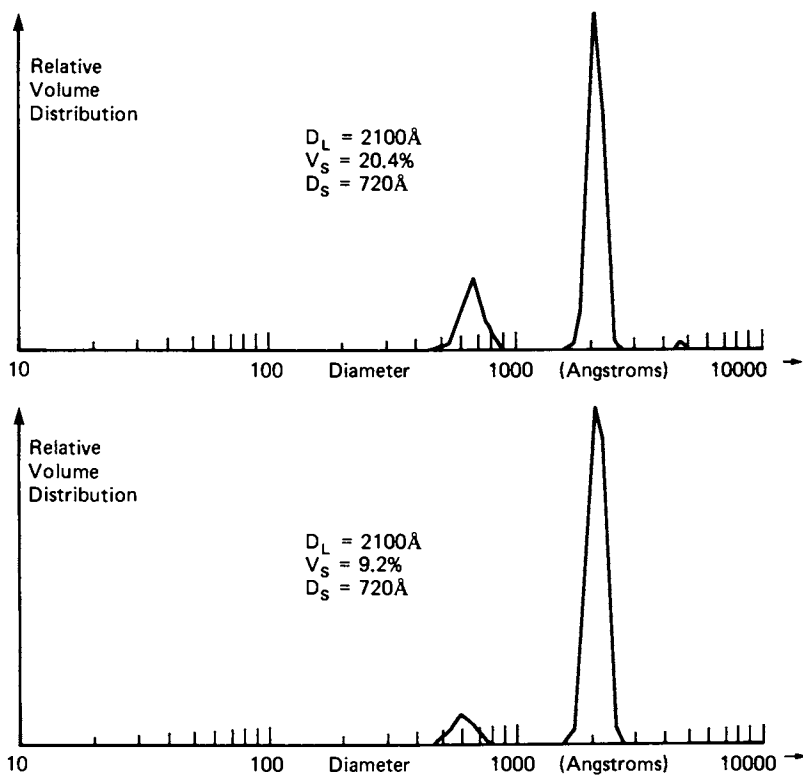


Figure 3. S/B latex particle-size distribution via HDC. Reproduced with permission from Ref. 11. Copyright 1983 Tappi J.

Also it should be noted that this computerized HDC analysis for particle-size measurements of these latexes was within 2% of that measured by TEM. Since the particle-size determinations by the two different methods were in close agreement it was accepted that the HDC eluant composition was minimizing the particle-swelling phenomenon of the carboxylated S/B particles.

#### Computerized HDC for Monitoring the Latex Emulsion Polymerization Particle Growth Patterns.

When particle-size and particle-size distribution assessments are required during the latex polymerizations to provide information on the particle growth patterns the size that is most pertinent is the in-situ particle-size. As a result of this, certain widely used methods of particle-size determination are considered unacceptable. For instance in electron microscopy the polymer is removed from its aqueous environment, sometimes being chemically modified and always dried before measurement. The latex particle-sizes may be quite different from that in their original aqueous environment. Light scattering methods utilize the latex in its natural environment. Light scattering methods utilize the latex in its natural environment. However complications do result in light scattering if compositional changes take place in the polymer phase.

Since the eluant in the HDC can be varied widely in composition this method appeared to be the most appropriate for in-situ measurements of particle-size. In this work the effective particle-size was desired. In general when carboxylated S/B latexes are involved the changes in apparent diameter are due to swelling of the latex particles by water from the continuous phase. This swelling can result when the carboxyl groups, as shown in Figure 4, become neutralized as the pH of the latex is raised and water associates to a greater extent with the resulting ionized sites. As mentioned previously the choice of HDC eluant composition becomes important in order to minimize these swelling effects.

All conventional latex polymerizations can be divided into two stages: a nucleation stage in which all the particles are formed and growth stage in which the formed particles grow to a larger size with no further nucleation. In a seeded emulsion polymerization a fixed number of particles in the form of a seed latex are added to the reactor. Monomer and initiator are added then to this seed latex and the particles grow to a larger size. For both the seeded and un-seeded types the number of particles should remain constant, during the growth stage without new particle generation or agglomeration of existing particles.

First, consider a polymerization with a well-controlled growth stage.

The aim point in particle-size for this latex polymerization was 2200Å. Sampling the reactor latex at an early interval A and analyzing the sample by computerized HDC method showed that the latex was relatively monodisperse and at the expected average particle diameter (Figure 5). This monodispersity in the particle-size distribution as well as the expected particle growth continued through later intervals B and C (Figure 5). The final particle-size of the latex agreed well with the expected diameter. The latex

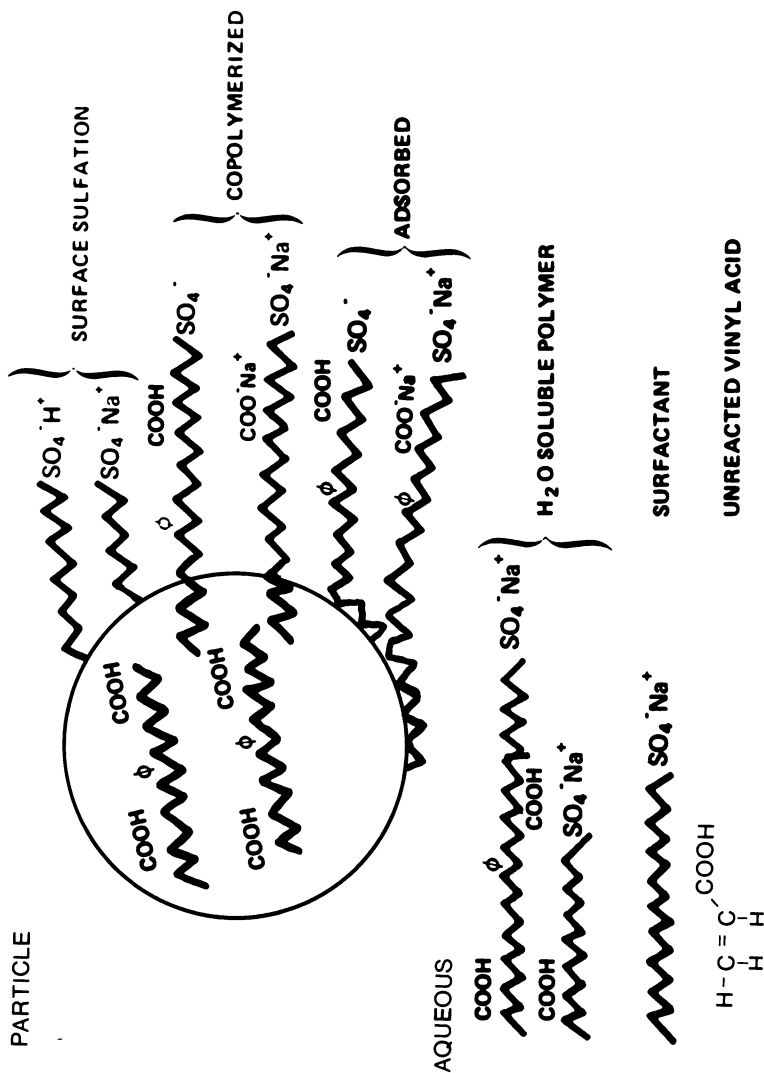


Figure 4. Styrene-butadiene latex (carboxylated-persulfate initiated).



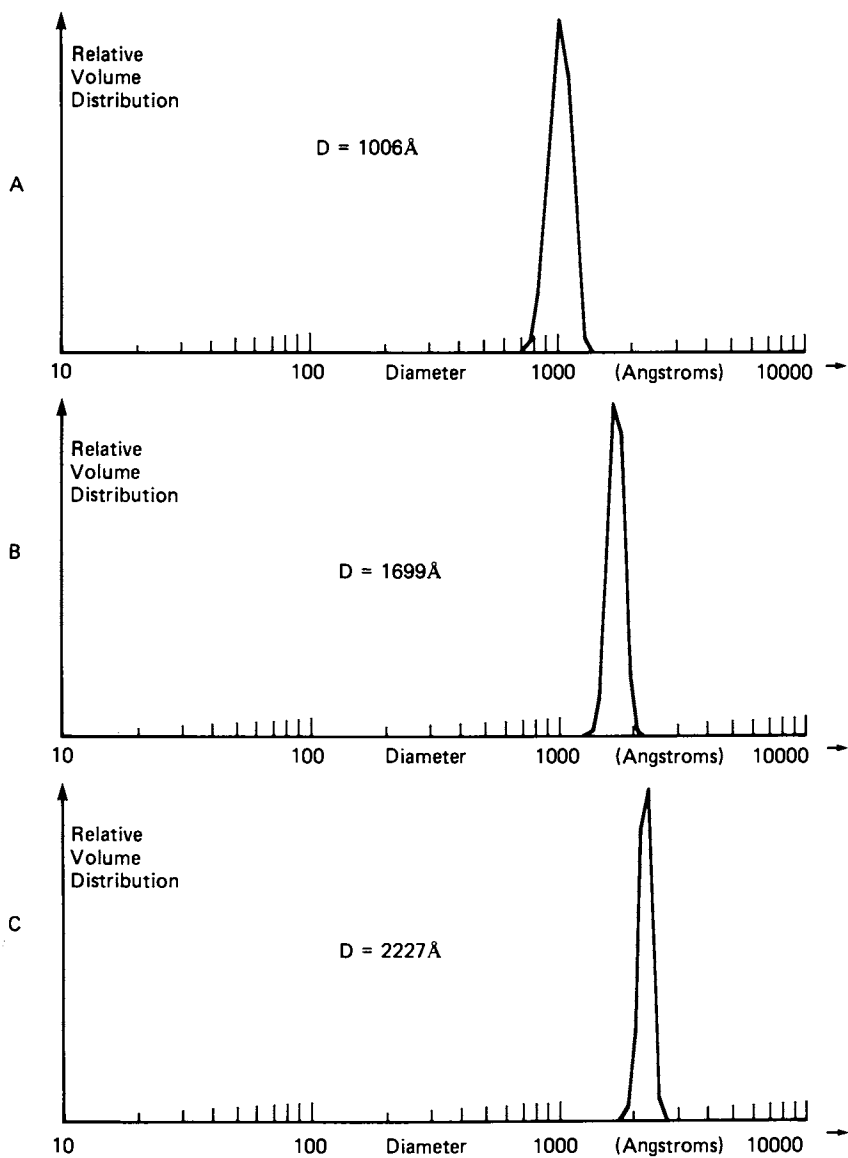


Figure 5. S/B latex particle-size distribution by HDC.

films of the different reactor latex samplings were homogeneous and did not indicate any noticeable signs of instability or coagulum formulation due to the method of reactor sampling. As a result the reactor sample and the corresponding particle growth data which was generated was interpreted to be very representative. The transmission electron micrograph data, shown in Figure 6, verified that the particles were uniform in size and spherical in shape thus excluding the possibility of any noticeable destabilization and establishing the fact that this latex polymerization was a well-controlled particle growth case.

The second particle growth pattern was derived from a latex polymerization that was carried out using a simple electrolyte addition to the reactor.

Monitoring the polymerization by the computerized HDC indicated that the particle-size distribution was relatively monodispersed at an early interval A (Figure 7). However, at a later interval B (Figure 7) the particle-size distribution became skewed towards the large particle-size range. This resulted in a multi-component broad particle-size distribution of the final latex, as shown at interval C in Figure 7. Certain particle populations were larger than that expected. It was speculated that there was some loss of the stabilization charge layer on the particles due to the electrolyte addition (9,10). When this phenomenon started to occur possibly the existing particles associated with each other to form different size aggregates. Electron micrographs of this latex (Figure 8) supported this explanation since a considerable number of the latex particles were no longer spherical and appeared to consist of distinct aggregates. There was some indication of new particle generation occurring also.

In the third instance the HDC monitoring of a supposedly monodisperse latex indicated skewing of the particle-size distribution this time toward the lower particle-size range. HDC analysis of the latex at an early interval A again indicated a relatively monodisperse particle-size distribution (Figure 9). At a later interval B the main particle population had increased in average diameter significantly over that of interval A with a small (1000A) particle-size fraction also appearing (Figure 9). As this polymerization continued, the small and large particle-size components both increased in size with the volume fraction of the small component also increasing. The two particle-size fractions merged into a skewed particle-size distribution, as shown by the later interval C chromatogram in Figure 9. It is possible that the unexpected newly generated particles resulted from the particular conditions used in this polymerization.

It is also possible that the unexpected newly generated particles were relatively unstable and tended to associate with those of the main population. The main particle population average diameter, as a result, was larger than that expected and the distribution deviated significantly from the desired monodispersity.

The particle growth data that was generated by the computerized HDC analysis can be combined with the conversion-polymerization time data (Figure 10) to yield the total number of particles  $N_T$ , in the reactor at various intervals of sampling (4,5). This is another way to represent the degree of control in the particle grow-up. In this work the total number of particles,  $N$ , was plotted as a function of polymerization time in Figure 11. For the controlled particle growth

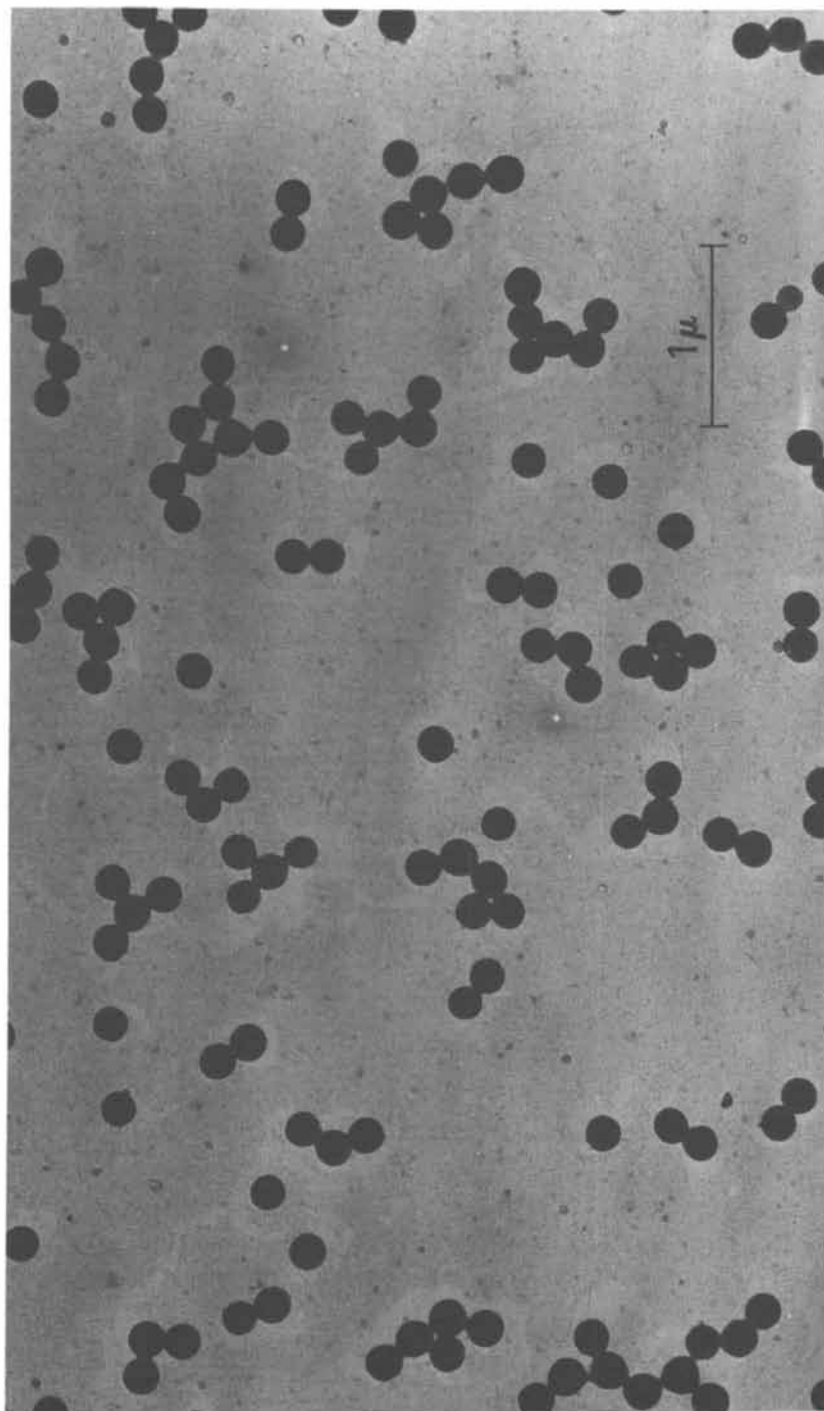


Figure 6. Monodisperse latex.

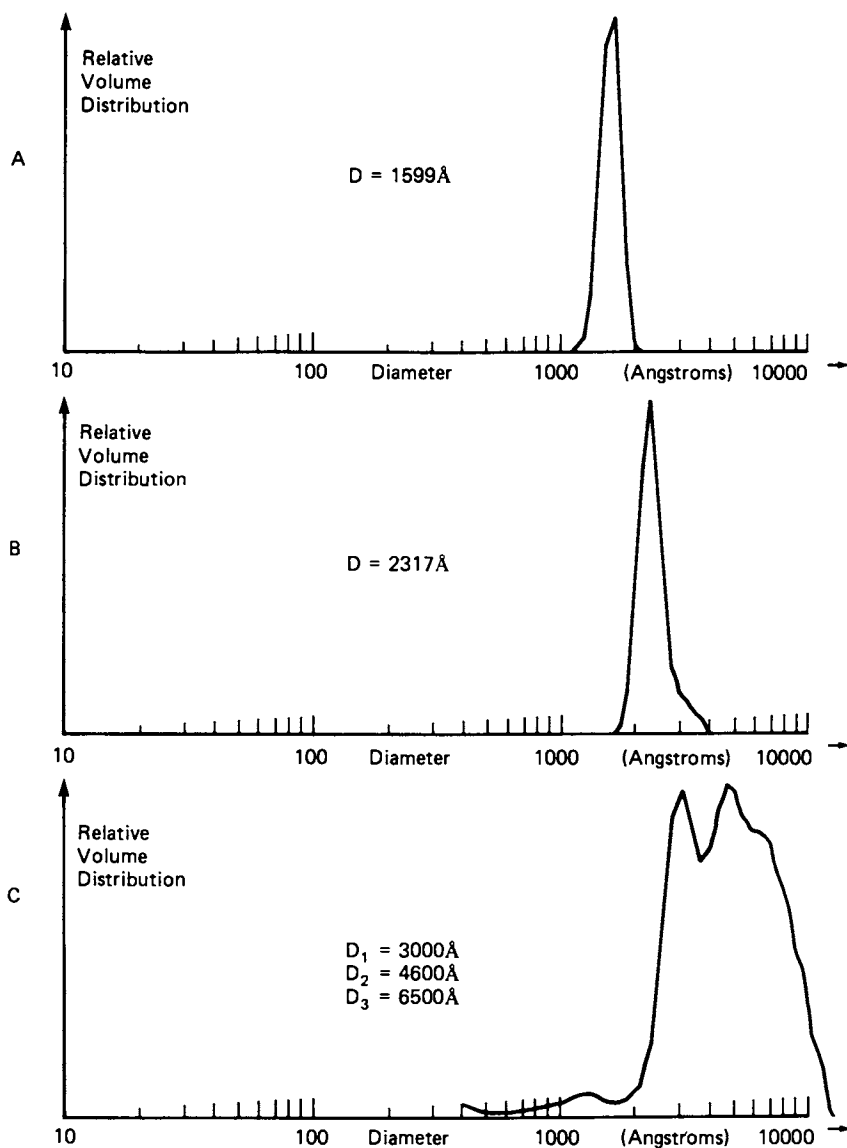


Figure 7. S/B latex particle-size distribution by HDC.

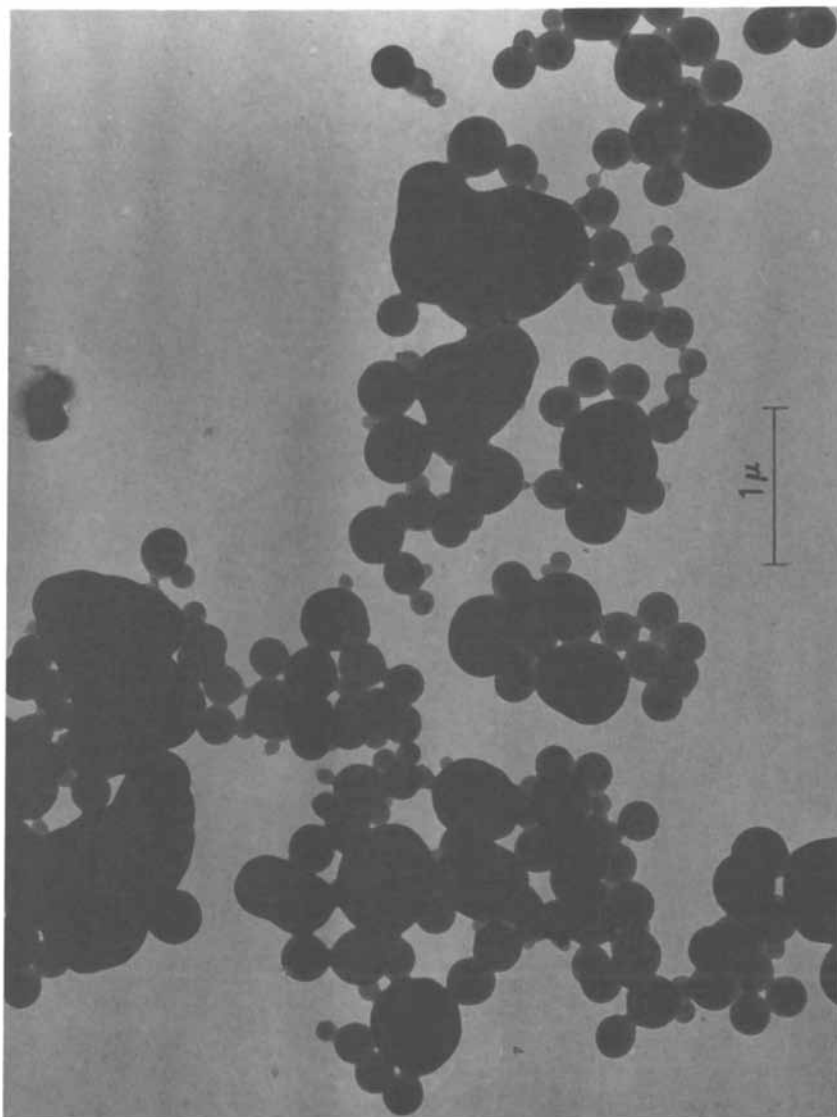


Figure 8. Multi-component latex particle-size distribution.

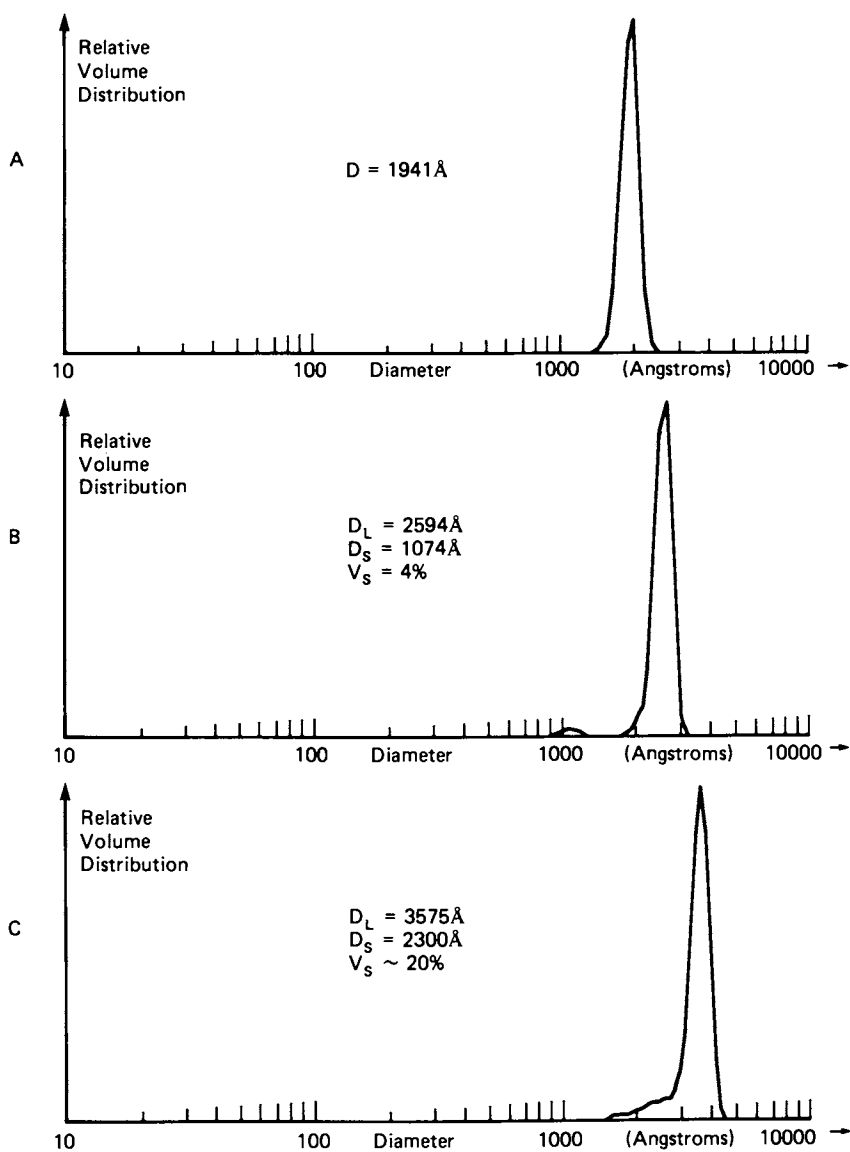


Figure 9. S/B latex particle-size distribution by HDC.

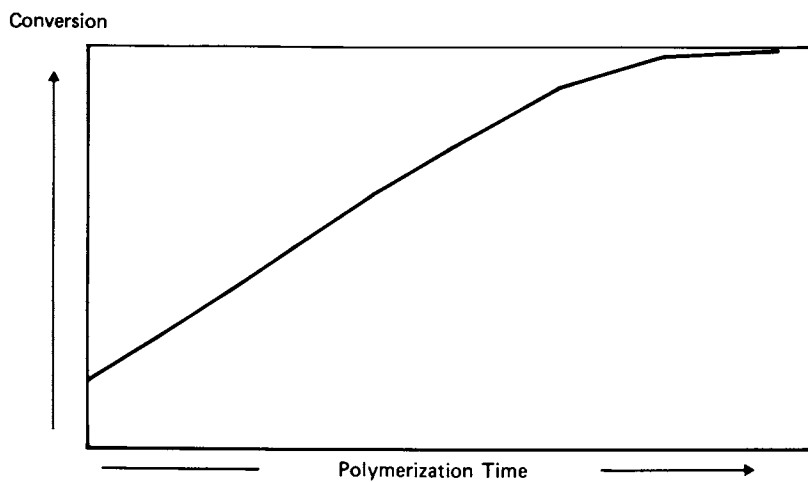


Figure 10. 2200 A monodisperse S/B latex conversion profile.

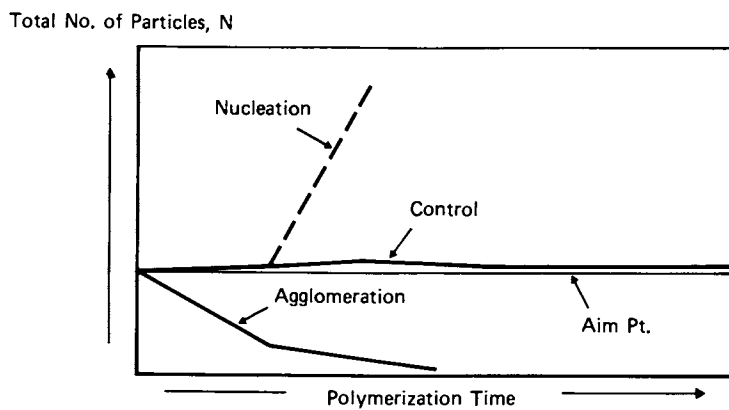


Figure 11. Standard S/B latex polymerization.

situation there was good agreement between the aim-point and the calculated total number of particles from the experimental data on particle-size and conversion. As could be expected the total number of particles,  $N_T$ , decreased for the case involving agglomeration and increased when new particles were generated. It is possible that both agglomeration and new particle-generation could occur during the same polymerization, as was indicated in the second particle growth case described above. As a result the total number of particles could change significantly depending upon which phenomenon was predominating.

### Conclusions

The computerized HDC technique was used to quantify the relative amounts of the large 2100Å and small 700Å monodisperse latexes in different binary mixtures. The HDC measurements for the relative amounts of the two components were within 1% of the actual amounts.

In addition to the measurement of the final particle diameter and particle size distribution the computerized HDC was used to monitor the particle growth pattern during the latex polymerization. The data generated from this monitoring technique showed that very significant departures from the controlled particle-growth pattern did occur in different types of polymerizations. Both agglomeration and new particle generation were detected as deviations in this work.

### Literature Cited

1. H. Small, J. Colloid Interfac. Sci., 48 (1974) 147.
2. H. Small, F. L. Saunders, J. Solc., Advances in Colloid and Interfac Sci., 6 (1976) 237-266.
3. G. R. McGowan and M. A. Langhorst, J. Colloid Interfac. Sci., 89, No. 1 (1982).
4. J. W. Vanderhoff, J. F. Vitkuske, E. B. Bradford and T. Alfrey, Jr., J. Polym. Sci. 20, 225 (1956).
5. C. I. Kao, D. P. Gundlach, and R. T. Nelsen, J. Polym. Sci.: Polym. Chem. Ed. 22, 3499 (1984).
6. W. E. Brown, J. Appl., Phys. 18, 273 (1947).
7. E. A. Willson, J. R. Miller and E. H. Rowe, J. Phys. Colloid Chem. 53, 357 (1949).
8. E. B. Bradford and J. W. Vanderhoff, J. Colloid Sci. 14, 543 (1959).
9. J. Gregory, Trans. Faraday Soc. 65, 2260 (1969).
10. J. Gregory, J. Colloid Interface Sci., 42, 448 (1973).
11. R. Van Gilder, D. I. Lee, R. Purfeerst, and J. Allswede, Tappi J. 60, 11 (1983).

RECEIVED September 18, 1986



## Chapter 20

# Particle Recovery in Hydrodynamic Chromatography

B. M. Secchi<sup>1</sup>, D. L. Visioli, and C. A. Silebi

Chemical Engineering Department and Emulsion Polymers Institute, Lehigh University,  
Bethlehem, PA 18015

Mass recovery of a dispersion of colloidal particles after separation by hydrodynamic chromatography or HDC is necessary to accurately determine particle size distributions and to apply HDC to dispersions containing particles larger than 200 nm. The effects of ionic strength, superficial velocity, particle diameter, and repeated injections on mass recovery have been studied. The prevailing mechanism of particle capture is shown to be interception rather than Brownian diffusion. Mass recovery is improved by using an eluant having ionic strength higher than traditionally used but still well below the critical micelle concentration of the surfactant used. Superficial velocity affects mass recovery only if the dispersion contains particles larger than 300 nm; in this case recovery is improved by lowering superficial velocity. Mass recovery of particles larger than 200 nm increased by injecting a sample up to five times, additional injections produced a constant recovery.

The knowledge of particle size and particle size distribution is fundamental in several fields and finds many applications of industrial interest. For example, pigments are examined routinely for the presence of large particles of aggregates which may adversely affect texture, gloss, and opacity (1). Several techniques have been applied in order to determine average particle size distribution, such as light scattering, sieving and filtration, centrifugation, and scanning electron microscopy. All of the above methods present advantages and disadvantages, time consuming operation being one of the most common and limiting disadvantages.

In recent years particle chromatography has developed dramatically as a simple and versatile method for particle size determination. The size fractionation of colloidal particles by chromatograph-

<sup>1</sup>Current address: Experimental Station, Polymer Products Department, E. I. du Pont de Nemours & Co., Inc., Wilmington, DE 19898

ic methods can be divided into four main areas: porous and non-porous packing chromatography, open capillary chromatography, and field flow fractionation. The technique which uses non-porous packing, developed originally by Small (2), is known as hydrodynamic chromatography (HDC). HDC was found by Nagy (3) to have higher efficiency than porous packing chromatography due to excessive peak broadening in the latter. The higher efficiency of HDC is typified by the large number of theoretical plates, typically an order of magnitude greater with HDC than with porous packing chromatography. In HDC, separation of colloidal particles takes place under the influence of two mechanisms: the laminar velocity profile developed by the eluant in the interstitial volume of the packed column according to the mechanism advanced by DiMarzio and Guttman for the separation of polymer molecules in capillary tubes (4); and (2) the attractive and repulsive interactions between the colloidal particles in the sample and the packing material. HDC columns packed with 20 $\mu\text{m}$  (20000 nm) spherical particles have been used to separate colloidal particles in the range of 30 nm to 500 nm; using a packing having larger diameter extends the upper limit to 2000 nm. However, using larger packing significantly reduces separation efficiency, mainly due to an increase in the axial dispersion and also to reduced separation factor.

Particle size distribution as well as an average particle size can be determined by HDC. One of the main limitations to an accurate determination of the particle size distribution (PSD) as well as to the range of applicability of HDC is the low mass recovery due to capture of particles bigger than 200 nm. Silebi and McHugh (5), in their analysis of the determination of particle size distribution by HDC, concluded that size distributions could be calculated accurately only for systems with particle sizes below about 300 nm due to poor recovery of larger particles.

Several studies have been conducted on particle capture by collectors of different shapes. Among the first studies were those of Albrecht (6), and Kaufman (7), who investigated the capture of airborne particles flowing past simple collector geometries. In packed columns, particle capture can be quantified in terms of the filter coefficient,  $\lambda$ , defined by:

$$\lambda = \frac{1}{L} \ln \frac{C_0}{C_f} \quad (1)$$

where  $C_0$  and  $C_f$  are the number of particles that enter and exit the column, and  $L$  is the length of the packed column.

The efficiency of a single collector,  $\eta$ , is defined by:

$$\eta = \frac{C_{i-1} - C_i}{C_{i-1}} \quad (2)$$

where  $C_{i-1}$  and  $C_i$  are the concentration of the influent and effluent streams at the  $i$ -th collector.

The relationship between the filter coefficient and the single collector efficiency is obtained by combining the preceding two equations:

$$\lambda = \frac{3(1 - \epsilon)}{2D_{pk}} \ln(1 - \eta) \approx \frac{3(1 - \epsilon)}{2D_{pk}} \eta \quad (3)$$

where the front factor is equal to the reciprocal of the length of a single collector. Particle capture in packed columns has variously been attributed to several mechanisms, i.e., sedimentation, Brownian diffusion, and interception. Sedimentation is not an important mechanism for the capture of submicron particles having nearly the same density as the medium (8). The total collector efficiency is the sum of the contributions from each of these mechanisms:

$$\eta_1 = \eta_s + \eta_{Br} + \eta_1 \quad (4)$$

In the case of Brownian diffusion and interception, particle capture is enhanced by London attractive forces and reduced by electrostatic double layer repulsive forces.

i. Brownian Diffusion. Brownian diffusion is considered to be one of the most important mechanisms for capture of submicron particles, becoming in the absence of electrostatic effects almost the sole mechanism governing capture of particles smaller than 200 nm in diameter (9). The Brownian diffusion coefficient  $D$  of a particle with diameter  $d_p$  may be represented by the Stokes-Einstein equation (10):

$$D = \frac{kT}{3\pi\mu d_p} \quad (5)$$

where  $T$  is the absolute temperature,  $k$  is the Boltzmann constant, and  $\mu$  is the viscosity of the medium.

Pfeiffer (11) analyzed flow through assemblages of spheres, deriving an expression of the collector efficiency:

$$\eta_{Br} = 4.0 A_s^{1/3} \frac{D^{2/3}}{d_p k v_s} \quad (6)$$

where  $v_s$  is the average superficial velocity and  $A_s$  is a dimensionless function of the column void fraction. Happel (12) derived the following expression for  $A_s$ :

$$A_s = \frac{2(1-P^5)}{2 - 3P + 3P^5 - 2P^6} \quad (7)$$

where  $P = (1-\epsilon)^{1/3}$ . Equation 6 doesn't show any dependence on the ionic strength as it ignores the influence of London attraction forces and double layer repulsion. Ruckenstein and Prieve (13) carried out analyses of deposition of submicron particles by Brownian diffusion in the presence of double layer repulsion. They incorporated the spatial variation of the diffusivity due to hydrodynamic interaction with the collector. They obtained numerical solutions for collection by spheres and cylinders and compared theory with experiments of Hull and Kitchener (14). The large discrepancies between theory and experiment were attributed to the extreme sensitivity of predicted collection to small variations in the surface chemical parameters.

ii. Interception. Another mechanism often invoked for particle capture is interception. This mechanism assumes that the center of a small nondiffusing spherical particle follows exactly an undisturbed

fluid streamline near a larger collector until the particle and collector touch, whereupon the particle is retained by contact adhesion (14). Hydrodynamic resistance between particle and collector, which results from the forced drainage of the viscous fluid from the narrowing gap during approach, is ignored, as is the finite reach of strong attraction through universal intermolecular forces. The error is considered negligible, as these opposing effects tend to compensate each other. For a spherical collector Yao et al. (8) derived the following expression for the contribution of interception to the collector efficiency:

$$\eta_1 = 1.5A_s N_R^2 \quad (8)$$

where  $N_R$  is the interception number, given by the ratio of particle to packing diameter ( $d_p/D_{pk}$ ). For small particles, interception predicts that the rate of collection by all collectors is proportional to the square of particle diameter. The few experimental data reported by these authors gave instead a variation of the filter coefficient with the first power of the suspended particle size.

Later Tien and Payatakes (15), in their study of the deposition of colloidal particles, developed a mathematical model which included in one expression the contributions by Brownian diffusion, interception with London attraction, and gravitational field. The most general form of their expression is:

$$\eta = 4A_s^{1/3} N_{Pe}^{-2/3} + 0.72N_{Lo}^{1/8} N_R^{15/8} + 0.0024A_s N_G^{1-2} N_R^{-0.4} \quad (9)$$

where  $N_{Pe}$ ,  $N_{Lo}$  and  $N_G$  are the dimensionless Peclet, London and Gravitational numbers defined by:

$$N_{Pe} = \frac{D}{D_{pk} v_s}$$

$$N_{Lo} = \frac{4H}{9n\mu v_s d_p^2} \quad (10)$$

$$N_G = \frac{g(\rho_p - \rho) d_p^2}{18\mu v_s}$$

where  $H$  is the Hamaker constant,  $g$  is the acceleration of gravity,  $\rho_p$  and  $\rho$  are the densities of the particle and the medium respectively.

Tien and Payatakes assumed the different mechanisms to be independent (no interaction effects). Prieve and Ruckenstein had already demonstrated the validity of this assumption (16).

### Experimental

The HDC flow system used is very similar to many of today's liquid chromatograph units. A schematic diagram of the HDC apparatus is shown in Figure 1. The eluant consists of a solution of sodium lauryl sulfate at concentrations ranging from 1 to 10mM (millimolar) in distilled deionized water. A trace of formaldehyde is added to the eluant to avoid bacterial growth in the column. Prior to use, the

eluant is filtered through a 1.0 micron Nucleopore filter membrane to prevent extraneous material from fouling the system. The eluting solution is delivered to the columns at constant flow rate using a Milton Roy Mini-Pump. The column is glass tubing which is 9mm ID and 110 cm long, it is slurry-packed with styrene divinyl benzene beads having mean particle diameter of 20  $\mu\text{m}$ . The packing height is 97 cm. The void volume  $\epsilon$  is 0.37. The detector is a Laboratory Data Control Model 1202 variable wavelength UV-visible spectrophotometer having wavelength range 190-690 nm which contains a dual-path cell with flow-type configuration. A dual-beam (sample-reference) optical system is used to compensate for solvent absorbance and source energy variation. The output from the detector is monitored on a Linear instruments Model 385 strip chart recorder.

Mass recovery is calculated by comparing the peak area resulting from injection of a sample through the column with the peak area from injection of an identical sample through a by-pass. The areas under the chromatogram have been measured with a Zeiss MOP-3 (modular system for quantitative digital analysis). Mass recovery is evaluated from the following expression:

$$\% \text{ recovery} = \frac{100(\text{peak area})_c(\text{CS})_b(Q)_c(\text{OD})_c}{(\text{peak area})_b(\text{CS})_c(Q)_b(\text{OD})_b} \quad (11)$$

where CS is the chart speed of the recorder, Q is the volumetric flow rate, OD is the optical density range, and the subscripts c and b refer to the column and the bypass respectively. The filter coefficient is calculated from equation 1 where  $C_f/C_o$  is the % recovery.

## Results

In the present work, mass recovery has been tested at different flow rates and ionic strengths for several particle diameters. The dependence on superficial velocity is reported in Figures 2 to 5. Recovery is improved as surfactant (sodium lauryl sulfate) concentration is increased from 1 to 6mM where maximum recovery of the larger particles is attained.

Recovery of particles with larger diameter (i.e., 357 and 450nm) is increased to a limiting value by injecting them several times (generally after 4 or 5 injections)(Figure 6). Hence the relationship between recovery and superficial velocity is drawn using 'steady state' maximum recovery values. Smaller sized latexes did not exhibit this behavior. This variation in recovery with number of injections can be explained by saturation of the available adsorption sites. This adsorption is reversible, since the recovery values return to the initial value if a sufficiently long time interval (e.g., 4 hours) elapses before injecting another sample. The occasional appearance of phantom peaks when a chromatographic system which has not been in use for a few hours or more is restarted further indicates that desorption has occurred.

The particle size distribution of a sample containing particles larger than 300 nm has been determined using the algorithm developed by Silebi and McHugh (5). Figures 7 and 8 show the PSD obtained after injecting the sample several times. As a result of the increase in recoveries of larger particles after successive injections of the sample, the computed PSD and average particle sizes are shifted toward larger particle sizes.

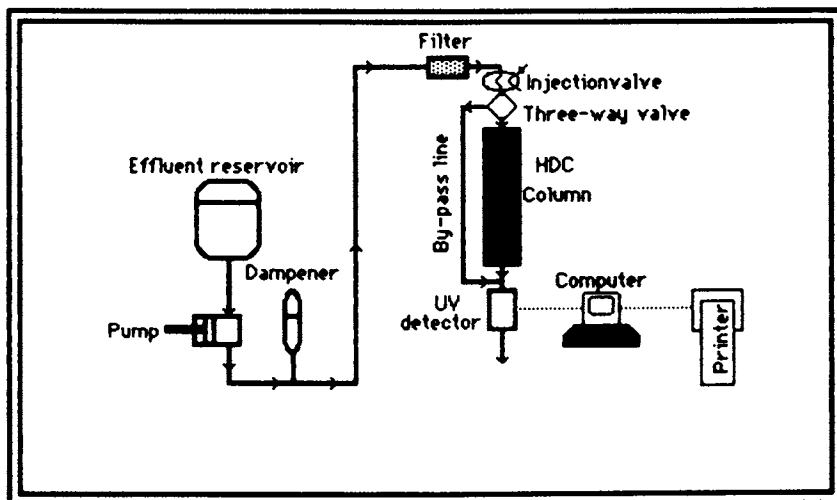


Figure 1. Schematic diagram of experimental system.

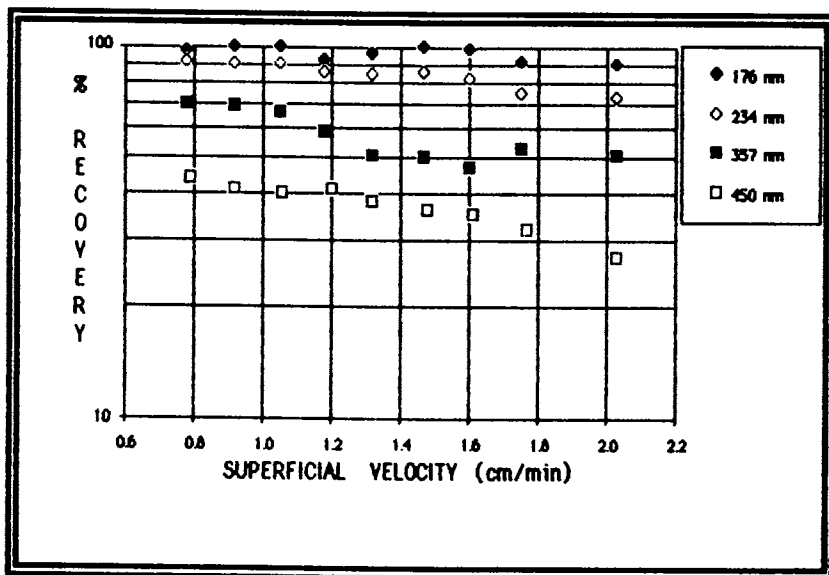


Figure 2. Effect of Superficial velocity on particle recovery for various particle diameter at a surfactant concentration of 1 mM SLS.

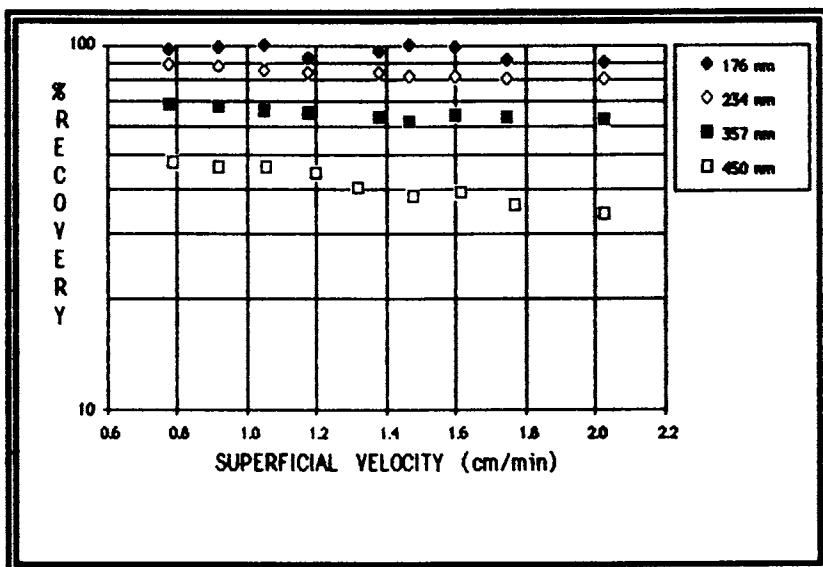


Figure 3. Effect of Superficial velocity on particle recovery for various particle diameter at a surfactant concentration of 3 mM SLS.

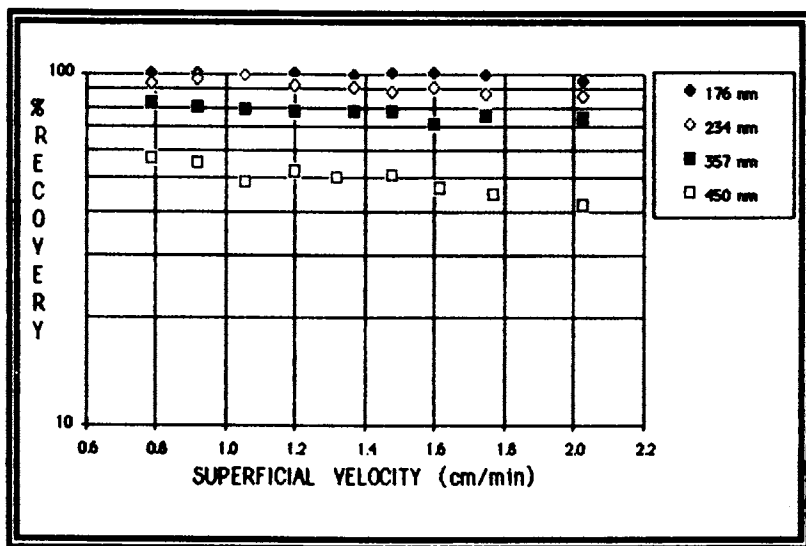


Figure 4. Effect of Superficial velocity on particle recovery for various particle diameter at a surfactant concentration of 6 mM SLS.

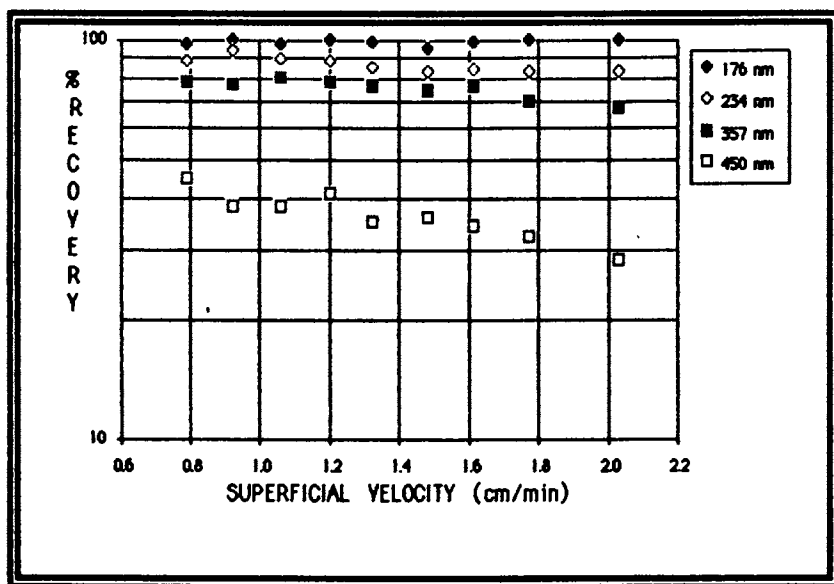


Figure 5. Effect of Superficial velocity on particle recovery for various particle diameter at a surfactant concentration of 10 mM SLS.

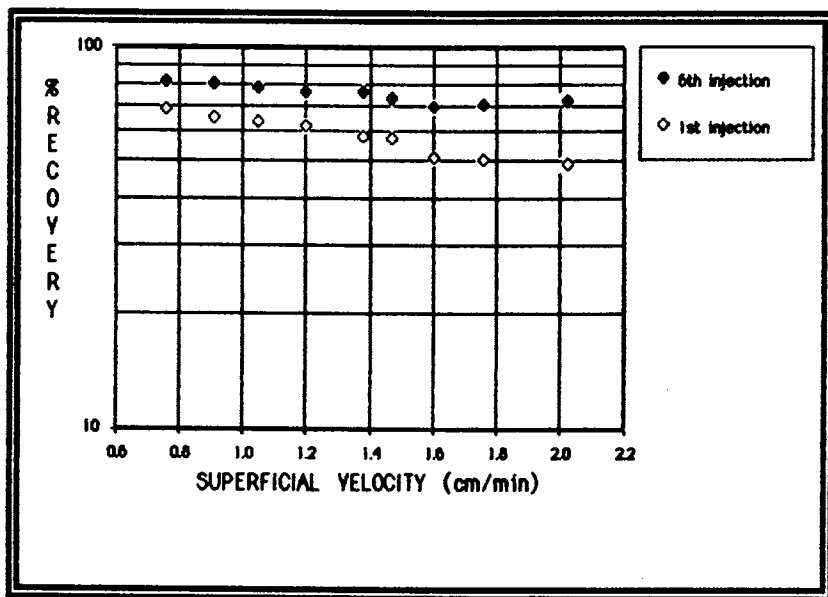


Figure 6. Variation of recovery with successive injections of a 357 nm polystyrene latex at a surfactant concentration of 6mM SLS.



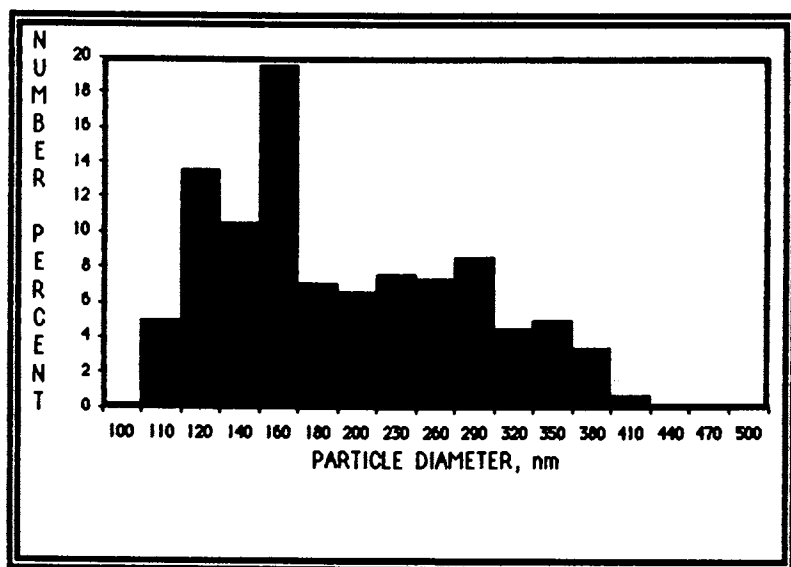


Figure 7. Calculated PSD of a polystyrene sample after its first injection.

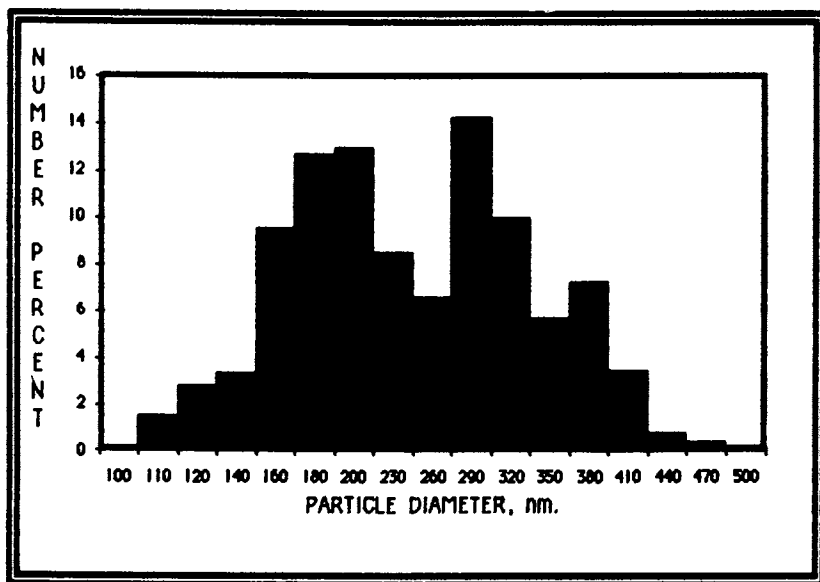


Figure 8. Calculated PSD of a polystyrene sample after its fourth injection.

### Discussion

With the system and the latexes used,  $N_R$  is always smaller than 0.09, so equation 9 can be applied to the HDC system, and hence theoretical values of the filter coefficient can be calculated by using equation 3. Evaluation of the sedimentation term was found to be negligible in our system.

Figure 9 shows that the experimentally determined filter coefficient as a function of the interception number was 3 to 6 orders of magnitude smaller than the theoretical prediction of Payatakes et al. (17) in the case where electrostatic effects were ignored. However, electrostatic forces due to the double layer effect are certainly present in the HDC system, since the packing material is an ion exchange resin and the eluant is a dilute solution of an electrolyte. This phenomenon will affect mainly the mechanism of capture by Brownian diffusion, as the random motion of the particles is insufficient to overcome the repulsion; whereas the hydrodynamic forces which contribute to particle capture by interception will not be affected to the same extent. The inverse relationship between superficial velocity and recovery observed also indicates that interception is the controlling mechanism, since increasing the superficial velocity increases the hydrodynamic forces, resulting in decreased recovery. If particle capture by Brownian diffusion were the controlling mechanism, recovery should improve at higher velocity. This indicates that, in the presence of electrostatic repulsion, particle capture by Brownian diffusion should be negligible: this is confirmed by comparing the experimentally determined relationship between the filter coefficient and the particle diameter with the theoretical relationship derived by considering only interception (Figure 10). The theoretical and experimental relationships show the same functional dependence, but the experimental values are one to three orders of magnitude smaller. Indeed, Payatakes' numerical calculations also show that the value of  $\eta$  is 3 orders of magnitude smaller when electrostatic repulsion effects are important. In Payatakes' work, the double layer number, defined as  $a/K^{-1}$  where  $a$  is the radius of the colloidal particle and  $K^{-1}$  is the Debye length (often loosely called the double layer thickness), is used as a measure of the importance of electrostatic effects. Payatakes showed that electrostatic effects are important when the double layer number is less than 1000; our experimental system certainly operates in this regime, since, our calculated values of the double layer number range from 8 to 150.

### Conclusions

Increasing surfactant concentration from the 1 mM SLS usually used to a higher concentration which is still below the critical micelle concentration (e.g., 8 mM) greatly improves the particle recovery. For example, 45% recovery is found for particles with average diameter of 450 nm using 6 mM SLS eluant, whereas less than 30% recovery is obtained for the same latex using 1 mM SLS. A straight calibration curve with little loss of resolution is obtained when the eluant's ionic strength is increased.

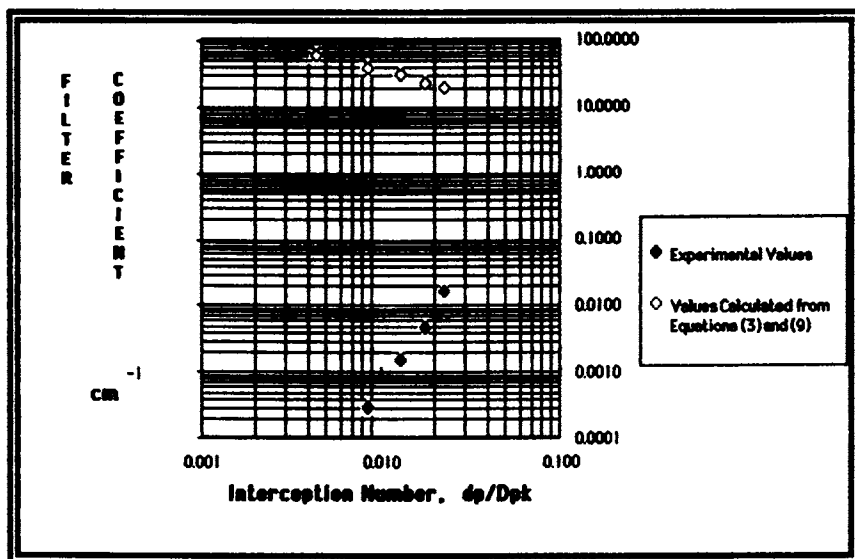


Figure 9: Theoretical and Experimental Values of the Filter Coefficient for a surfactant concentration of 10 mM SLS and a superficial velocity of 2 cm/min.

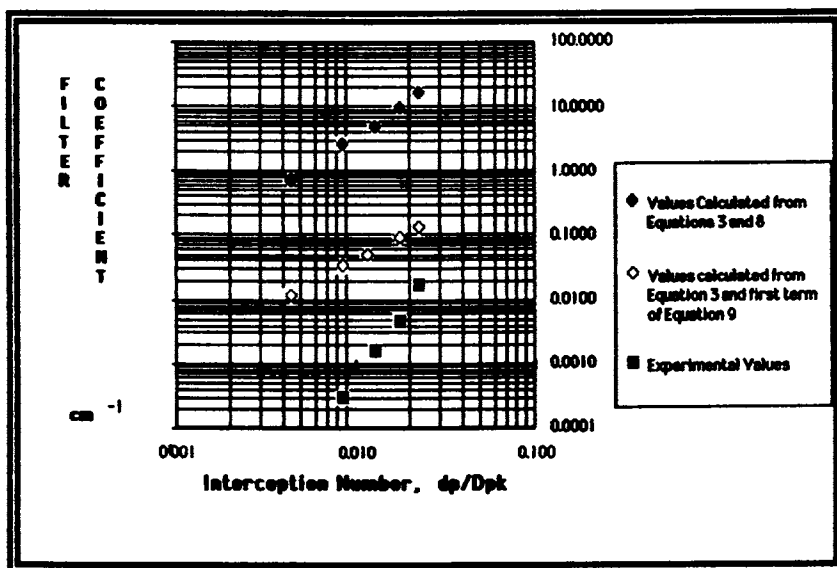


Figure 10: Theoretical and Experimental Values of the Filter Coefficient for a surfactant concentration of 10 mM SLS and a superficial velocity of 2 cm/min.

When higher ionic strength eluant is used, flow rate does not significantly affect mass recovery if the particle diameter is less than 200 nm. For larger particles, mass recovery is maximum at low flow rate (0.6 to 0.8 ml/min. i.e., superficial velocity of 0.9 to 1.3 cm/min).

Mass recovery of larger particles is increased by repeatedly injecting samples of the same latex onto the column. Since it is most difficult to determine the particle size distribution of samples having average particle diameter greater than 200 nm, the accuracy of determining particle size distribution for these samples can be improved by injecting the sample four or five times. Because of the exponential dependence of particle recovery upon the length of the column, the use of shorter columns will result in higher recoveries of the larger particles. The minimum value of the filter coefficient as a function of the ratio of particle diameter to packing diameter indicates that recovery of large particles can be enhanced by using a packing with higher average diameter (e.g., 30  $\mu\text{m}$ ). However, resolution for small particles is poorer if the average packing diameter exceeds 20  $\mu\text{m}$ .

Particle capture occurs through an interception mechanism. Because of the strong electrostatic forces operating in the experimental system, the contribution of Brownian diffusion to particle capture is negligible.

#### Literature Cited

- (1) Cadle, R. D. "Particle Size Determination"; Interscience Publisher, New York, 1955; p.13.
- (2) Small, H.; J. Colloid and Interface Sci., 1974, 48, 147.
- (3) Nagy, D. J., Ph.D. Thesis, Lehigh University, Bethlehem, Pa., 1979.
- (4) DiMarzio, E. A. and Guttman, C. M., Macromolecules, 1970, 3, 131.
- (5) Silebi, C. A., and McHugh, A. J., J. Appl. Poly. Sci., 1979, 23, 1699.
- (6) Albretch, F., Phys. Z., 1931, 32-48.
- (7) Kaufman, A., Verein Deutsches Ing., 1936, 80, 593.
- (8) Yao, K. M., Habibian, T., and O'Melia, C. R., Env. Sci. Tech., 1971, 5, 1105.
- (9) Cookson, J. T., J. Env. Sci. Tech., 1970, 4, 128.
- (10) Bird, R. B., Steward, W. E., and Lightfoot, E.N., "Transport Phenomena", John Wiley & Sons, New York, 1960.
- (11) Pfeiffer, R., Ind. Eng. Chem., 1964, 3, 380.
- (12) Happel, J.J., AIChE, 1959, 5, 174.
- (13) Ruckenstein, E., and Prieve, D. C., J. Chem. Soc. Farad. Trans. 2, 1973, 69, 1522.
- (14) Hull, M., and Kitchener, J.A., Trans. Farad. Soc., 1966, 62, 1638.
- (15) Tien, C., and Payatakes, A. C., AIChE J., 1979, 25, 737.
- (16) Prieve, D. C., and Ruckenstein, E., AIChE J., 1974, 20, 1178.
- (17) Payatakes, A. C., Rajagopalan, R., and Tien, C., J. Coll. and Int. Sci. 1974, 49, 321.

RECEIVED August 4, 1986

## Author Index

- Annappagada, A., 133  
Beddow, J. K., 2  
Berger, E. J., 89  
Bott, S. E., 74  
Caldwell, Karin D., 215  
Chang, K., 89  
Chang, Y. S., 30  
Chu, Benjamin, 115  
Coll, Hans, 202  
Ford, James R., 115  
Frock, Harold N., 146  
Garcia-Rubio, L. H., 161  
Giddings, J. Calvin, 215  
Gill, T., 180  
Gilman, Lee B., 256  
Grabowski, E. F., 89  
Gulari, Erdogan, 133  
Gulari, Esin, 133  
Hamielec, A. E., 242  
Herb, C. A., 89  
Hester, R. D., 62  
Holsworth, R. M., 191  
Jang, B. Z., 30  
Jawad, B., 133  
Jones, Harlan K., 215  
Koehler, M. E., 180,231  
Kourti, T., 242  
Langhorst, M. A., 272  
MacGregor, J. F., 242  
Mettille, M. J., 62  
Morrison, I. D., 89  
Niemann, T. F., 180  
Olivier, James P., 256  
Oppenheimer, Larry E., 202  
Penlidis, A., 242  
Provdor, Theodore, 180,191,231  
Ray, W. Harmon, 105  
Secchi, B. M., 287  
Silebi, C. A., 287  
Smart, Cindy G., 256  
Stansbrey, J. J., 191  
Stock, Ruth S., 105  
Thornton, Anthony W., 256  
Tscharnuter, W. W., 48  
Vaidya, R. A., 62  
Van Gilder, R. L., 272  
Visioli, D. L., 287  
Weiner, B. B., 48  
Xu, Renliang, 115  
Zander, R. A., 180

## Subject Index

- A
- Accuracy of particle sizing  
HDC, 57-61  
PCS, 54,55f
- Acrylic binders, particle size distributions, 269f
- Adaptability, fractionation techniques for particle characterization, 219,221
- Airy formula, intensity distribution of the Fraunhofer diffraction pattern, 148
- Algorithm, inversion, for obtaining particle size distributions from QELS data, 91-94
- American Society for Testing and Materials, standard tensile test, 34
- Angular dependence of the scattering intensity, particle sizing using PCS, 81,83f,84
- Angular light scattering, particle sizing, 146-159
- Autocorrelation (AC) function  
Brownian particles of uniform size and shape, 77  
determination of particle size distributions, 119-120  
monodisperse samples, 60,134  
particle sizing using QELS, 90-91  
relation to polymer MWDs, 63  
relation to the first-order AC function, 62
- Averages of particle size, polydisperse particulate systems, 161-178
- B
- Band broadening  
HDC, 259-260  
sedimentation FFF, 223
- Batch polymerization, latex, 266-267
- Bentonite suspensions  
dynamic light-scattering measurements, 124-125,126f

## Author Index

- Annappagada, A., 133  
Beddow, J. K., 2  
Berger, E. J., 89  
Bott, S. E., 74  
Caldwell, Karin D., 215  
Chang, K., 89  
Chang, Y. S., 30  
Chu, Benjamin, 115  
Coll, Hans, 202  
Ford, James R., 115  
Frock, Harold N., 146  
Garcia-Rubio, L. H., 161  
Giddings, J. Calvin, 215  
Gill, T., 180  
Gilman, Lee B., 256  
Grabowski, E. F., 89  
Gulari, Erdogan, 133  
Gulari, Esin, 133  
Hamielec, A. E., 242  
Herb, C. A., 89  
Hester, R. D., 62  
Holsworth, R. M., 191  
Jang, B. Z., 30  
Jawad, B., 133  
Jones, Harlan K., 215  
Koehler, M. E., 180,231  
Kourti, T., 242  
Langhorst, M. A., 272  
MacGregor, J. F., 242  
Mettille, M. J., 62  
Morrison, I. D., 89  
Niemann, T. F., 180  
Olivier, James P., 256  
Oppenheimer, Larry E., 202  
Penlidis, A., 242  
Provdor, Theodore, 180,191,231  
Ray, W. Harmon, 105  
Secchi, B. M., 287  
Silebi, C. A., 287  
Smart, Cindy G., 256  
Stansbrey, J. J., 191  
Stock, Ruth S., 105  
Thornton, Anthony W., 256  
Tscharnuter, W. W., 48  
Vaidya, R. A., 62  
Van Gilder, R. L., 272  
Visioli, D. L., 287  
Weiner, B. B., 48  
Xu, Renliang, 115  
Zander, R. A., 180

## Subject Index

- A
- Accuracy of particle sizing  
HDC, 57-61  
PCS, 54,55f
- Acrylic binders, particle size distributions, 269f
- Adaptability, fractionation techniques for particle characterization, 219,221
- Airy formula, intensity distribution of the Fraunhofer diffraction pattern, 148
- Algorithm, inversion, for obtaining particle size distributions from QELS data, 91-94
- American Society for Testing and Materials, standard tensile test, 34
- Angular dependence of the scattering intensity, particle sizing using PCS, 81,83f,84
- Angular light scattering, particle sizing, 146-159
- Autocorrelation (AC) function  
Brownian particles of uniform size and shape, 77  
determination of particle size distributions, 119-120  
monodisperse samples, 60,134  
particle sizing using QELS, 90-91  
relation to polymer MWDs, 63  
relation to the first-order AC function, 62
- Averages of particle size, polydisperse particulate systems, 161-178
- B
- Band broadening  
HDC, 259-260  
sedimentation FFF, 223
- Batch polymerization, latex, 266-267
- Bentonite suspensions  
dynamic light-scattering measurements, 124-125,126f

- Bentonite suspensions--Continued  
static light-scattering  
measurements, 123-124,126f
- Bimodal distribution  
according to the Mie theory and  
Rayleigh-Debye  
approximation, 81,82f  
determination of MWDs, 68,70f  
intensity-weighted particle size  
distribution, 86f  
measurement of particle size  
distribution of latex  
particles, 110t  
measurements using different  
light-scattering  
techniques, 138-143
- Broad distributions, use in particle  
sizing, 52,54
- Brownian diffusion, as a  
particle-capture mechanism, 289
- Buffered line start (BLS), DCP  
particle size distribution  
analysis, 192-196
- Butadiene-styrene latices  
HDC monitoring of particle growth  
during polymerization, 272-286  
particle size distributions  
determined by HDC, 273-284
- C
- Calibration  
computerized HDC for particle size  
distribution analysis, 273-277  
DCP, 183  
HDC, samples used, 260-261  
size-exclusion chromatography, 250
- Cancer and normal cells, physical  
meaning, 25,28
- Chromatography, definition, 216
- Coincidence versus flocculation,  
emulsion systems, 95,100
- Coefficient of variation of scattering  
intensities, PSL spheres, 78
- Coefficients of the power series  
expansion of the extinction  
efficiency, 177-178
- Collector efficiency, HDC, 288-290
- Colloid(s), determination of particle  
size distributions by  
sedimentation FFF, 215-230
- Colloidal latices, particle size  
distribution analysis by  
HDC, 256-268
- Computerized HDC  
calibration for particle size  
distribution analysis, 273-277  
monitoring particle growth during  
latex polymerization, 277-286
- Constrained regularization method, to  
solve the Fredholm integral  
equation, 64
- CONTIN, use in particle sizing  
calculations, 78
- Conversion histories, vinyl acetate  
emulsion polymerizations, 245f
- Conversion profile, monodisperse  
latex, 285f
- Correctness of the solution,  
determination of MWDs, 71
- Correlator channels, particle sizing  
using PCS, 57-58
- Correlator hardware limitation,  
particle sizing using PCS, 54,56
- Covariance for particle size and  
polydispersity, DCP  
studies, 198-200
- Crazing in HIPS  
initiation and propagation, 41-44  
relation to rubbery-phase  
morphology, 39,41,42f
- D
- Data correlation, particle size  
determinations using angular light  
scattering, 157,158-159f
- Data system, determination of particle  
size distributions by DCP, 183-184
- Data transformations, particle sizing  
using PCS, 56-59
- Data treatment, HDC, 257-260
- Decaying exponential function,  
Brownian particles of uniform size  
and shape, 77
- Deconvolution  
particle sizing using PCS, 57  
use to interpret HDC  
data, 257,259-260
- Degree of separation, rubber  
particles, 32
- Density, monodisperse particle  
systems, 224
- Density gradients, effect on  
sedimentation curves of  
PSL, 203,205-206f
- Detector response  
effects of function on generated  
particle size  
distributions, 263-266
- HDC  
factor, 259-260  
versus eluent volume, 257,259  
size-exclusion  
chromatography, 249-250
- Diameter, average particle  
calculation from turbidity  
measurements, 161-178  
determination by sedimentation  
FFF, 222  
determination by size-exclusion  
chromatography, 252-254  
latex samples, 246

- Diffusion constant, spherical particles, 77
- Diffusivity, monodisperse particle systems, 224
- Disc centrifugation, improved techniques for determining particle size distributions, 202-214
- Disc centrifuge photosedimentometer description, 180-181, 191 schematic, 182f
- Disc centrifuge photosedimentometry (DCP)  
particle size distribution analysis, 180-201, 231-238  
separation of latex standards  
BLS method, 193-196  
EGM method, 194-197
- Disc-shaped particle, scattering factor, 123
- Disc thickness, calculation, 128
- Dispersion, rubber particles, 32-34
- Dispersion index, two dimensions, 33
- Distribution(s), particle size--See Particle size distributions
- Distribution averaging, inversion algorithm for obtaining particle size distributions from QELS data, 93
- Distribution parameters, effect of baseline errors, 60t
- Dust, effect on PCS, 51-52, 53f
- Dynamic light scattering (DLS)  
bentonite suspensions, 124-125, 126f  
measurement of particle size distributions of latex particles, 105-113  
particle size analysis, 231-238  
theory, 119-121  
use to determine macromolecular polydispersity, 62-72  
See also Photon correlation spectroscopy (PCS), Quasi-elastic light scattering (QELS)
- E
- Efficiency of a collector, HDC, 288-290
- Electric field AC function, relation to intensity distribution of particle size, 107
- Electrical polarizability difference, orientational polarizability, 118
- Electronics, light scattering, 154, 156f
- Elution, fractionation techniques for particle characterization, 220-221
- Elution volume of particles, HDC, 259-260
- Emulsifier concentrations, effect on particle size distributions of emulsion systems, 95, 96-97f
- Emulsion polymerization latex, HDC monitoring of particle growth patterns, 277-286  
specific turbidity histories, 244, 245f, 247f
- Emulsion systems, particle size distributions, study by QELS, 89-103
- Energy  
collection of particles of different sizes, 135  
falling on a particle, Fraunhofer diffraction, 135  
scattered by one sphere, 135
- External gradient method (EGM), DCP particle size distribution analysis, 191-201
- Extinction efficiency  
coefficients of the power series expansion, 177-178  
fractional errors between surface average and calculated values, 168-171, 173f
- Mie theory, 162  
turbidity measurements of polydisperse particulate systems, 165
- F
- Field-flow fractionation, sedimentation--See Sedimentation  
field-flow fractionation (sedimentation FFF)
- Filter coefficient, HDC, 296, 297f
- Fineness, rubber particles, 32-33
- Flexibility, fractionation techniques for particle characterization, 219, 221
- Flocculation versus coalescence, emulsion systems, 95, 100
- Flow profile, FFF channel, 216-218
- Fluid volume, calculation, 190
- Flux differences of particles per unit volume, 152, 153f
- Forward scatter, to measure particle size, 150
- Fourier equation, morphological analysis, 3
- Fractional errors, between surface-average extinction efficiency and calculated extinction, 168-173
- Fractionated distributions, use in particle sizing, 50-51
- Fractionation techniques for particle characterization advantages and disadvantages, 219 characteristics, 219-221



Fractionation techniques for particle characterization---Continued  
types, 218t

#### Fractograms

latex beads, 226f  
polystyrene sample, 229f  
poly(vinyl chloride) colloid, 229f

#### Fraunhofer diffraction pattern analysis

particle size measurements of monodisperse systems, 137  
particle size requirements, 133-134  
theory, 135-136

#### Fraunhofer light scattering, to determine particle size, 146-150

Fredholm integral equation, methods used to solve, 63-66,67f

#### Free-radical distributions, determination of MWDs, 68,70f

### G

Gelation layer adsorbed on silver bromide, determination of thickness, 209-213

Generalized exponential function fit method, to solve the Fredholm integral equation, 66,67f

Geometry of a PCS measurement, 76f

Gradient-forming system, DCP, 204f

Gradient protection, DCP, 207,208f

Gravitational number, HDC collector efficiency, 290

Gray level, texture analysis, 6-7

Gyraton, radius of, definition, 119

### H

High-impact polystyrene (HIPS), spatial dispersion of rubber particles, 30

High-speed, integrated, computerized HDC, monitoring particle growth during latex polymerization, 272-286

#### Hydrodynamic chromatography (HDC)

accuracy, 257-261  
applications, 266-268  
background, 257  
description, 288  
diagram of apparatus, 258f,292f  
materials analyzed, 268t  
monitoring particle growth during latex polymerization, 272-286  
particle recovery, 287-298  
particle size distribution analysis, 231-238,249,256-258

### I

Image analysis, rubber particles in HIPS, 34-35,38-41

Index of refraction---See Refractive index

#### Intensity

as a function of angle, polystyrene-water system, 106f  
light scattered by a sphere, definition, 56  
relation to the refractive index difference in two orthogonal directions, 116

#### Intensity distribution

particle sizing by PCS, 79  
relation to electric field AC function, 107

Intensity-weighted particle size distribution of a bimodal distribution, 86f

Interception, as a particle-capture mechanism, 289-290

Interference pattern resulting from the scattering of two particles, PCS, 76f

Invariant texture morphology descriptors, texture analysis, 6-7

Inversion, definition, 6

Inversion algorithm for obtaining particle size distributions from QELS data, 91-94

Inversion scattering problem, treatment, 163

### K

Kodak distribution results, particle size distributions of latex particles, 110t

### L

Laser light scattering (LLS)  
comparison with TEB, 127-131  
determination of macromolecular polydispersity, 62-72  
determination of MWDs of polymers in solution, 115-116  
diagram of instrumentation, 117f

#### Latex

colloidal, particle size distribution, 256-268  
emulsion polymerization particle growth patterns, 277-286  
particle size distributions  
determination by DCP, 207-209  
determination by DLS, 105-113  
measurement in the submicrometer range, 242-254

## Latex--Continued

- PMMA
  - analysis, 233
  - particle size averages, 235t
  - synthesis, 232-233
- polybutadiene, particle size
  - distribution, 264f
- polymerization, quality control
  - using HDC, 266-267
- polystyrene--See Polystyrene latex (PSL)
- poly(vinyl chloride), sedimentation
  - FFF, 225,226f
- spheres
  - bimodal distributions of suspensions
    - containing, 140-143f
  - trimodal distributions of suspensions
    - containing, 143-144f
- standards
  - DCP separation by the BLS method, 193-196
  - DCP separation by the EGM method, 194-197
- Light energy, due to a particle, 135
- Light scattering
  - angular, determination of particle size, 146-159
  - determination of particle size distributions, 133-145
  - dynamic--See Dynamic light scattering (DLS)
  - experimental use of table, 121
  - laser--See Laser light scattering (LLS)
  - measurement of particle size, application, 157
  - measurement systems, 154-156
  - quasi-elastic--See Quasi-elastic light scattering (QELS)
  - static--See Static light scattering
- Line width
  - obtained from polarized DLS measurements, 124
  - PCS, calculation, 128
- Logarithmic normal distribution, latex particles, 246
- London number, HDC collector efficiency, 290
- Mie equation, particle sizing using PCS, 80-84
- Mie factor correction, effect on constrained regularization solutions for bimodal distributions, 111f
- Mie scattering
  - determination of particle size, 150-154
  - diagram of effects that cause, 106f
- Mie theory
  - extinction efficiency, 162
  - relation of turbidity to characteristics of suspended isotropic spherical particles, 162
- Mixture analysis, physical meaning, 25,26-27f
- Molecular weight distributions (MWDs)
  - generation using generalized exponential functions, 66,68
  - polymers, measurement by DLS, 62-72
- Moments of particle size distributions, polydisperse systems, 161-178
- Monodisperse latex
  - conversion profile, 285f
  - particle size analysis, 231-238
  - transmission electron micrograph, 281f
- Monodisperse particle populations, sedimentation FFF, 224-225,226f
- Monodisperse spheres
  - sizing by PCS, 49
  - turbidity, 134
- Monodisperse suspensions
  - particle size measurements, 136-138
  - turbidity, 243
- Morphological analysis
  - methods available, 31
  - particulate material, 2-29
  - theory, 4-5
- Multicomponent latex, transmission electron micrograph, 283f
- Multiple-angle detection, use for submicrometer particle sizing by PCS, 58,59f,74-88
- Multiple-pass analysis, inversion algorithm for obtaining particle size distributions from QELS data, 92

## M

- Macromolecular polydispersity, determination from DLS data, 62-72
- Mass fraction distribution of particle size, determination, 107-108
- Mass percent of sample recovered, HDC, 262-263
- Mass recovery testing, use of PSL, 261t

## N

- Nonfractionation methods, particle characterization, 218t
- Non-negative constraint, inversion algorithm for obtaining particle size distributions from QELS data, 92

- Non-negative least squares method  
 results, measurement of particle  
 size distributions of latex  
 particles, 112,113f
- Nonspherical particles,  
 sedimentation, 210,214
- Normal distributions, determination of  
 MWDs, 68,69f
- Normalized correlation function,  
 relation to the distribution of  
 decay constants, 63
- Normalized dispersion index,  
 definition, 34
- Not-roundness, physical meaning, 7,12f
- Number distribution  
 particle sizing by PCS, 79  
 PSL as determined by DCP, 186f
- O
- Operator independence, determination  
 of MWDs, 72
- Optical constant, definition, 119
- Optical retardation  
 definition, 116  
 rise and decay curves, relation to  
 particle rotational  
 motion, 116,118
- Optics for light scattering, 154,155f
- Orientalational polarizability, relation  
 to electrical polarizability  
 difference, 118
- P
- Particle(s)  
 calculation of radii from  
 sedimentation times, 207  
 capture in packed columns, 288-290  
 density in monodisperse particle  
 systems, 224  
 detection by DCP, 181  
 diameters  
 calculation from turbidity  
 measurements, 161-178  
 determination by sedimentation  
 FFF, 222  
 disc-shaped, scattering factor, 123  
 latex, growth histories, 248f  
 measurement of surface area, 148-149  
 measurement of volume, 149  
 monitoring of growth during latex  
 polymerization by HDC, 272-286  
 recovery in HDC, 287-298  
 retention in column, HDC, 262-266
- Particle size  
 comparison of measurement  
 techniques, 218-221  
 DCP studies, analysis of  
 covariance, 198-200
- Particle size--Continued  
 determination  
 by angular light  
 scattering, 146-159  
 by light scattering,  
 advantages, 133  
 by PCS  
 use of multiple-angle  
 detection, 74-88  
 uses and abuses, 48-61  
 by size-exclusion  
 chromatography, 251-252  
 dimensionless, definition, 107  
 measurements  
 monodisperse systems, 136-138  
 polydisperse systems, 138-145  
 monodisperse PMMA latices, 231-238  
 physical meaning, 7-10
- Particle size distributions  
 colloid, analysis by sedimen-  
 tation FFF, 215-230  
 colloidal latices, analysis by  
 HDC, 256-268  
 determination  
 by computerized HDC, 273-277  
 by DCP, 180-190  
 by DLS, 62-72,105-113  
 by light-scattering  
 techniques, 133-145  
 by sedimentation FFF, 222-224  
 emulsion systems, 94-100  
 latex particles, measurement in the  
 submicrometer range, 242-254  
 obtained using different detector  
 response functions, 263t  
 PMMA latices, 238f  
 polydisperse particulate systems,  
 calculation from turbidity  
 data, 161-178  
 polystyrene samples, 291,295f  
 PSL, analysis by DCP, 207-209  
 rubbery phase in a toughened  
 plastic, assessment, 30-44  
 silver bromide dispersions, 210-213  
 standard deviations, 33  
 submicrometer emulsion systems,  
 study by QELS, 89-103
- Particle size histogram, PLS  
 spheres, 85,86f
- Particulate material, size, shape,  
 and texture analysis, 2-29
- Peak broadening, inversion algorithm  
 for obtaining particle size  
 distributions from QELS  
 data, 93-94
- Peclet number, HDC collector  
 efficiency, 290
- Performed density gradients, effect on  
 sedimentation curves of  
 PSL, 203,205-206f
- Photon correlation, theory, 134

- Photon correlation spectroscopy (PCS)  
 advantages and disadvantages for  
   particle sizing, 48,75  
 particle size distributions in  
   colloidal suspensions, 115-131  
 particle size measurements  
   monodisperse systems, 136-137  
   polydisperse systems, 138-143  
 particle size requirements, 133  
 particle sizing, uses and  
   abuses, 48-61  
 submicrometer particle sizing, use  
   of multiple-angle  
   detection, 74-88  
See also Dynamic light scattering,  
 (DLS), Quasi-elastic light  
 scattering (QELS)
- Photosedimentometry, disc  
 centrifuge--See Disc centrifuge  
 photosedimentometry (DCP)
- Plastic, rubbery phase, assessment of  
 particle size distribution and  
 spatial dispersion, 30-44
- Polybutadiene latex, particle size  
 distribution, 264f
- Polydisperse suspensions  
 particle size measurements, 138-145  
 sedimentation FFF, 225-227  
 turbidity, 135,243
- Polydispersity, DCP studies, analysis  
 of covariance, 198-200
- Polymer latices, particle size  
 distribution analysis, 256-268
- Polymerization, latex  
 HDC monitoring of particle  
   growth, 272-286  
 quality control using HDC, 266-267
- Poly(methyl methacrylate) (PMMA)  
 latices  
 particle size analysis, 231-238  
 synthesis, 232-233
- Polynomial subdistribution method, to  
 solve the Fredholm integral  
 equation, 64
- Polypropylene, rubbery phase  
 morphology, 37f
- Polystyrene  
 detector response functions, 265f  
 high-impact, spatial dispersion of  
 rubber particles, 30
- Polystyrene latex (PSL)  
 calibration of HDC, 260-261  
 DCP determination of particle size  
 distributions, 184-189,207-209  
 HDC analysis, 267  
 mass recovery testing, 261t  
 microspheres, use as size  
   standards, 232,234f  
 sedimentation curves, 205-206f  
 sedimentation FFF, 224,226f
- Polystyrene latex (PSL)--Continued  
 spheres  
   coefficient of variation of  
     scattering intensities, 78  
   particle size histogram, 85,86f  
 Polystyrene-water system, intensity as  
 a function of angle, 106f
- Poly(vinyl chloride)  
 detector response functions, 265f  
 sedimentation FFF, 225,226f  
 size and density determinations, 51t
- Power series expansion of the  
 extinction efficiency,  
 coefficients, 177-178
- Q
- Quality control using HDC, latex  
 polymerization, 266-267
- Quasi-elastic light scattering (QELS)  
 advantages for emulsion  
 studies, 89-90  
 background, 90-91  
 characterization of colloidal-sized  
 particles, 48-61  
 determination of particle size  
 distributions, 89-103  
 particle size analysis, 231-238  
See also Dynamic light scattering,  
 (DLS), Photon correlation  
 spectroscopy (PCS)
- R
- Radius  
 of a fluid surface, DCP  
   calculation, 183  
 of a particle, calculation from  
   sedimentation times, 207  
 of gyration, definition, 119
- Rayleigh-Debye approximation, bimodal  
 distribution, 81,82f
- Rayleigh ratio, solution of  
 polydisperse nonabsorbing  
 particles, 118-119
- Reflection, definition, 5
- Refractive index  
 definition, 150  
 differences of particle  
   fractions, 118  
 effects on particle size  
   measurements, 154t
- Reinjection, sedimentation  
 FFF, 227-228
- Residual porosity, physical  
 meaning, 14,18t
- Resolution, fractionation techniques  
 for particle  
 characterization, 219-220

- Response function, detector, effects  
on generated particle size  
distributions, 263-266
- Retention ratio, sedimentation  
FFF, 222-223
- Rotation, definition, 5
- Rotation-reflection, definition, 6
- Roughness indicator, physical  
meaning, 14,16f
- Rubber-modified polymers,  
structure-property  
relationships, 31
- Rubber particles, degree of  
dispersion, 32-34
- Rubber toughening in HIPS polymers,  
basic mechanism, 41,43
- Rubbery phase, toughened plastic,  
assessment of particle size  
distribution and spatial  
dispersion, 30-44
- Rubbery-phase morphology, HIPS  
general discussion, 35,36-37f  
relation to crazing, 39,41,42f
- S
- Scattering efficiency, polydisperse  
particulate systems, 168
- Scattering intensity  
Mie equation, 80  
per particle as a function of  
particle diameter, 81,82-83f  
Rayleigh regime, 80
- Sedimentation  
curves for PSL, 205-206f  
isometric particles, 210,214  
particle size analysis, methods  
used, 231-238
- Sedimentation field-flow fractionation  
(sedimentation FFF)  
colloids, 215-230  
description, 215-216  
monodisperse particle  
populations, 224-225,226f  
particle size  
analysis, 50-51,231-238  
polydisperse particle  
populations, 225-227  
process, schematic, 217f
- Shape, definition, 2
- Shape analysis, particulate  
material, 2-29
- Shape analyzer, morphological features  
measured, 3
- Shape classifier, physical  
meaning, 7,11f
- Shape composition, physical  
meaning, 14,17f
- Shape descriptors, physical  
meaning, 7-28
- Shape distribution, physical  
meaning, 14,17f
- Shape symmetry, physical  
meaning, 14,19-24f
- Shape term, definition, 4
- Side scatter, measurement of particle  
size, 152
- Silver bromide, determination of  
thickness of absorbed gelatin  
layer, 209-213
- Size analysis, particulate  
material, 2-29
- Size dependence of the scattered  
intensity, light-scattering  
techniques, 138
- Size-exclusion chromatography  
measurement of particle size  
distributions of latex  
particles, 249-254  
plots of peak average  
diameters, 253f  
theoretical background, 249-250
- Size parameter  
particles, 152  
polydisperse particulate  
systems, 168-171,173f
- Size selectivity, fractionation  
techniques for particle  
characterization, 220-221
- Size term, definition, 4
- Skewed distributions, determination of  
MWDs, 68,69f
- Sodium lauryl sulfate, effect on HDC  
particle recovery, 291,292-294f
- Spatial dispersion of rubbery phase in  
a toughened plastic, 30-44
- Specific turbidity  
definition, 243  
emulsion  
polymerizations, 244,245f,247f
- Spherical particles, AC function, 134
- Spreading function, size-exclusion  
chromatography, 250
- Standard deviation of the distribution  
of particles in a mixture, 33
- Static light scattering  
measurements of bentonite  
suspensions, 123-124,126f  
theory, 118-119
- Statistical analysis, BLS and EGM  
studies of particle size  
distributions, 193-194,198-200
- Statistical properties of descriptors,  
morphological analysis, 5
- Statistical terms, texture analysis, 6
- Steric effect, sedimentation FFF  
measurement of particle size, 233
- Stokes-Einstein equation  
Brownian diffusion coefficient of a  
particle, 289

- Stokes-Einstein equation--Continued  
 single-particle diffusion  
   coefficient and the hydrodynamic diameter of a particle, 90
- Stokes equation, calculation of particle radii, 207
- Stress-field overlap, HIPS, 43-44
- Styrene-butadiene latices  
 HDC monitoring of particle growth during polymerization, 272-286  
 particle size distributions determined by HDC, 273-284
- Submicrometer emulsion systems, particle size distributions, QELS studies, 89-103
- Submicrometer particle sizing by PCS, use of multiple-angle detection, 74-88
- Sucrose density gradients, effect on sedimentation curves of PSL, 203,205-206f
- Sulfonation, effect on particle size of polystyrene-divinylbenzene, 50
- Superficial velocity, effect on HDC particle recovery, 291,292-294f
- Surface area, particles, measurement, 148-149
- Surface distribution, PSL as determined by DCP, 187f
- Surface of separation, rubber particles, 32
- Surface scattering efficiency  
 definition, 164  
 polydisperse particulate systems, 168
- Surfactant concentrations  
 effect on HDC particle recovery, 291,292-294f  
 relation to diameter and surface area of internal phase of emulsion system, 95,98-99f
- Suspensions, monodisperse, particle size measurements, 136-138
- Swelling  
 styrene-butadiene latices, 277-278f  
 sulfonated  
   polystyrene-divinylbenzene, 50f
- Swollen particles, sizing by PCS, 50
- Symmetry operations  
 morphological analysis, 5-6  
 texture analysis, 6
- T
- Taylor series approximation of the scattering efficiency to determine the weights for the moments of particle size distributions, 178
- Temperature, effect on particle size determinations, 194,198-200
- Tensile deformation, HIPS, 34
- Textural analysis, particulate material, 2-29
- Textural descriptors  
 morphological, major types, 6-7  
 physical meaning, 7-28
- Textural symmetry, definition, 6-7
- Texture, definition, 6
- Theory, fractionation techniques for particle characterization, 219,221
- Thickness  
 absorbed gelatin layers on silver bromide particles, 209-213  
 equilibrium particle cloud, sedimentation FFF, 222
- Transient electric birefringence (TEB) apparatus, experimental use, 121  
 comparison with LLS, 127-131  
 diagram of instrumentation, 117f  
 measurement parameters, 125,127  
 particle size distributions in colloidal suspensions, 115-131  
 theory, 116-118
- Translational diffusion coefficient for spheres, 60
- Transmission electron micrographs  
 monodisperse latex, 281f  
 multicomponent latex, 283f
- Transmission electron microscopy  
 HIPS, 35  
 particle size analysis, 231-238
- Trimodal distribution measurements  
 using different light-scattering techniques, 139,143-144f,145
- Turbidity  
 characterization of suspended isotropic spherical particles, 162  
 definition, 242-243  
 monodisperse systems  
   in the large particle size regime, 165  
   of nonabsorbing spheres, 134  
   particle size analysis, 231-238  
 polydisperse systems  
   general discussion, 135  
   in the large particle size regime, 166  
   in the small particle size regime, 167  
   measurements, 161-178  
 relation to powers of the particle diameter, 165  
 relation to ratios of moments of the particle size distribution, 165  
 relation to surface mean diameter and mean surface scattering efficiency, 164

Turbidity--Continued

spectra  
 particle size distributions of  
 latex particles, 242-249  
 particle size measurements  
 of monodisperse systems, 137  
 of polydisperse systems, 139-145  
 particle size requirements, 134  
 theoretical background, 242-244  
 theory, 134-135

## U

Ultramicrotomy, HIPS, 35

## V

Vinyl acetate emulsion  
 polymerizations, conversion  
 histories, 245f

Volume, particles, measurement, 149  
 Volume distribution, particle sizing  
 by PCS, 79

## W

Wavelength, turbidity measurements,  
 effect on particle size  
 distributions, 172-174

Weight distributions  
 particle sizing by PCS, 79  
 PSL as determined by DCP, 188f

## Z

Zimm plot, bentonite suspensions, 126f

*Production by Cara Aldridge Young  
 Indexing by Karen McCeney  
 Jacket design by Pamela Lewis*

*Elements typeset by Hot Type Ltd., Washington, DC  
 Printed and bound by Maple Press Co., York, PA*